Development of Tau Polarimetry for Measuring Beam Polarization in e^+e^- Colliders

by

Caleb Dennis Miller
B.Sc., UNBC, 2013
M.Sc., Queens University, 2016

A Dissertation Submitted in Partial Fulfillment of the
Requirements for the Degree of

DOCTOR OF PHILOSOPHY

in the Department of Physics and Astronomy

Development of Tau Polarimetry for Measuring Beam Polarization in e^+e^- Colliders

by

Caleb Dennis Miller
B.Sc., UNBC, 2013
M.Sc., Queens University, 2016

Supervisory Committee

Dr. J. Micheal Roney, Supervisor
(Department of Physics and Astronomy)

Dr. Robert Kowalewski, Departmental Member
(Department of Physics and Astronomy)

Dr. Katherine Elvira, Outside Member
(Department of Chemistry)

Abstract

The Belle II experiment is considering the addition of longitudinal polarization to the e^- beam of SuperKEKB. The addition of beam polarization would allow for a number of world leading electroweak precision measurements, and the dominant uncertainty in these future measurements is expected to be how well the average beam polarization is known. The development of the Tau Polarimetry technique provides a highly precise way for detectors at e^+e^- colliders, at a centre-of-mass energy of 10.58 GeV, to determine the average beam polarization in data collected. As Belle II is in the process of collecting a significant data-set and maximizing the detector performance, the Tau Polarimetry technique has been developed and demonstrated on the resemblant *BABAR* detector. To enable Belle II to take high luminosity data, which is required for the additional physics enabled by the beam polarization, the beam backgrounds must be well modelled and understood. Thermal neutron detectors have been deployed to monitor neutron backgrounds arising from the high energy beams. The calibration, operation, and analysis of the data collected from these detectors is presented in this dissertation. In addition to the background studies, the Belle II detector sensitivity to electroweak asymmetries with polarized beams has been carried out with state-of-the-art Monte Carlo generators and the results compared with leading theoretical calculations. The development of Tau Polarimetry at *BABAR* is the primary focus of the dissertation and the expected statistical and systematic limitations are established. This work provides a road map for the application of Tau Polarimetry at Belle II and the sensitivity expected.

Table of Contents

Acknowledgements

This dissertation is the work of many years and I'd like to thank a those who supported me through the process:

My wife, Allison Weick, and my daughter, Esther Weick Miller, for putting up with my efforts to complete it.

My supervisor, Michael Roney, for his mentorship and guidance.

My fellow graduate students, for eating, drinking, and playing board games.

Original Contributions

As the research presented in this dissertation is based on data collected by large collaborations of people it is important to define the line between collaborative effort and original work. The main dissertation body begins with the theory motivations behind the Chiral Belle upgrade which provided an opportunity to work with theorists and compare/validate the calculations of electroweak parameters from different groups. This involved using simulation code to recreate the experimental process of measuring the parameter and comparing the results, this also provided the opportunity to work with the theorists to add features to the simulation code.

The next section of the dissertation describes the efforts to measure beam backgrounds at SuperKEKB, this work was based on the work of a previous graduate student and analysis techniques developed by them and the Belle II group. The chapter (Chapter 5) begins with a discussion of the detectors present in the background team, collectively BEAST II, and the Phase 1 results. The original work begins with the calibration of the neutron detectors at UVic and improvements to the data taking process. This work led to designing and sourcing materials to deploy the detectors in new locations around KEK. The chapter also presents original analysis of the beam backgrounds detected by the neutron detectors and development of a more robust fitting technique than the one used by the background group. During the extent of this dissertation work, I remained the primary contact for the detectors to the background team which included maintaining the detectors and providing summary data files for further analysis. In addition to the work of providing the detectors as a service to the Belle II collaboration, I took on multiple data collection shifts, operating the Belle II detector as it collects collision information.

The primary focus of the dissertation is the development of the Tau Polarimetry technique. This is an entirely original work developed using the data collected by the *BABAR* collaboration.

Chapter 1

Introduction

1.1 Motivations

The experimental apparatus at the heart of modern particle physics are particle colliders. By accelerating particles to relativistic speeds and colliding them within specialized detectors, specific processes can be studied in minute detail or exotic forms of matter can be created. These experiments come to fruition through the combined effort of hundreds, if not thousands, of people to design, build, calibrate, and analyze the detector and the data it collects. Each of these steps is crucial to end up with a well-understood apparatus which can produce precise and valuable results. The main goal of these experiments is to look for evidence of physics not described by the Standard Model (SM), the theory describing all subatomic interactions, via precision measurements and searches for new phenomena. The SM is known to be incomplete as it only describes three of the four fundamental forces, electromagnetism, weak nuclear force, and the strong nuclear force. In addition to it's lack of description for the fundamental force of gravity, the SM lacks an explanation for the neutrino mass ordering, has no source of CP violation that could cause the matter-antimatter asymmetry in the universe, and offers no candidates for dark matter or dark energy. Even with these shortcomings, the SM has been an extremely powerful theoretical model of particles and the interactions between them. In performing the highly precise measurements and searches for new phenomena, physicists hope to find a hint of the limitations of the SM and inform a future, more complete, theory.

The Belle II experiment and it's associated accelerator, SuperKEKB, are currently in the process of reaching their design functionality. Once reached, SuperKEKB will deliver e^+e^- collisions to the Belle II detector at an unprecedented rate, over $40\times$ more than its predecessors. This will enable Belle II to make a number of world leading precision measurements in many areas of the SM; However, one area of the SM Belle II is not well equipped to study is

asymmetries arising in the electroweak sector, and so a proposed upgrade, colloquially called the 'Chiral Belle' project, has been suggested to extend the physics reach of Belle II.

1.2 Outline

To begin the discussion, Chapter 2 presents the SM concepts and experimental particle physics terminology required to fully engage with the material presented in this dissertation. The addition of beam polarization to SuperKEKB is expected to allow Belle II to significantly improve the precision to which a number of electroweak parameters in the SM are known[1]. Chapter 3 discusses the physics motivations for the Belle II upgrade and the theory work being done in preparation for it. In particular, the left-right asymmetry (the difference in cross-section for left and right polarized beams) for the $e^+e^- \to e^+e^-$ process (Bhabha process) and the $e^+e^- \to \mu^+\mu^-$ process (muon-pair) has had recent improvements in the precision of the theory calculations. The Chapter compares these theory calculations to independent theory calculations, implemented as two Monte Carlo simulation algorithms (KKMC for the muon-pairs and ReneSANCe for the Bhabhas), to determine the level of agreement between them and identify optimal fiducial requirements to optimize a future measurement.

As Belle II was in the commissioning stages when the analyses in this dissertation began, the *BABAR* experiment data was used as a testing environment for studies requiring high statistics. The *BABAR* experiment is similar in design to Belle II, both operating as e^+e^- colliders at 10.58 GeV, and it's expected any lessons learned at *BABAR*, such as the attainable statistical and systematic uncertainties in an analysis, will largely translate to Belle II. Chapter 4 describes the similarities and function of the two detectors.

As part of the effort to bring Belle II online and be able to make high quality physics measurements the effects of backgrounds arising from the accelerated beams needed to be understood. One of the background types that can arise from the beams are "thermal" neutrons. High energy neutrons produced in the beam pipe or from secondary interactions of produced particles behave much like a gas and spread throughout the beam tunnels and detector region. As these neutrons bounce around they lose kinetic energy until they reach a thermodynamic energy ($\frac{1}{2}mv^2 = \frac{3}{2}k_BT$, where k_B is the Boltzmann constant), which is referred to as thermal neutrons. By detecting these neutrons and comparing the density of them to simulations under different beam operation environments, the physical sources can be identified and projections for the scaling of the backgrounds can be made. Chapter 5 discusses the calibration, deployment, and analysis of data collected by neutron detectors

during the commissioning phase of SuperKEKB and Belle II.

As the precision with which the average beam polarization is known is expected to dominate the systematic uncertainties of the electroweak measurements enabled by polarized beams, a precision technique to determine the polarization will improve the future measurements. Chapters 6 and 7 discuss the development of a new technique to precisely measure the beam polarization, Tau Polarimetry, with two independent approaches at *BABAR*. This technique is a novel concept and Chapter 6 focuses on the development of extracting a pure $\tau^{\pm} \to \pi^{\pm}\overline{\nu}_{\tau}$ decay selection as this was assumed to be the most sensitive τ decay. This chapter goes in depth on a variety of studies of systematic uncertainties effecting the study eventually resulting in finding a uncontrolled bias which could not be identified. The analysis was transitioned to extracting the polarization measurement from the $\tau^{\pm} \to (\rho^{\pm} \to \pi^{\pm}\pi^{0})\overline{\nu}_{\tau}$ decay which appeared to be unaffected by the bias. This process and the results of the precision measurement are the focus of Chapter 7. With the level of precision demonstrated by Tau Polarimetry it is expected that Chiral Belle will be able to make measurements of a number of SM parameters, using most of the final state fermions produced in Belle II ($e^{+}e^{-}$, $\mu^{+}\mu^{-}$, $\tau^{+}\tau^{-}$, $c\bar{c}$, $b\bar{b}$), that will be substantially more precise than the current measurements of the SM values for those parameters. Finally Chapter 8 summarizes the dissertation conclusions.

Chapter 2

Standard Model and Experimental Particle Physics Concepts

2.1 The Standard Model

The SM is a mathematical description of the interactions between particles; however, it's quite often more useful to describe it phenomenologically as a more intuitive way to approach and understand it. From this perspective the SM is a list of particles and forces, and their relative interaction strengths. The typical way to represent this is in a grid, grouping particles (and forces) by their similarities as represented in Figure 2.1. The groupings of particles in the SM are a natural starting point to discuss the SM. Each particle in the SM is first grouped as either a fermion or a boson based on whether they obey the Pauli exclusion principle or not. The fermions are further broken down into quarks and leptons as well as three generations of pairs of quarks and pairs of leptons.

2.1.1 Fermions

The feature separating quarks and leptons is the strong force, which only acts on quarks. The quarks and leptons exhibit three generations of increasing mass, with higher mass versions of each particle having similar but not identical properties and couplings. The higher generation particles are unstable (with neutrinos being an exception) and will quickly decay to first generation particles. The up and down quarks comprise most of the matter we're familiar with, such as protons and neutrons and the atoms they compose. Protons and neutrons can be considered bound-states of quarks, where a proton is composed of two up quarks and a down quark (uud), while a neutron is two down quarks and an up quark (udd). Quarks can also combine in pairs to form mesons (as opposed to 3-quark "baryons") such as the pion ($u\overline{d}$). The leptons come in two distinct types of particles. First the charged leptons such as

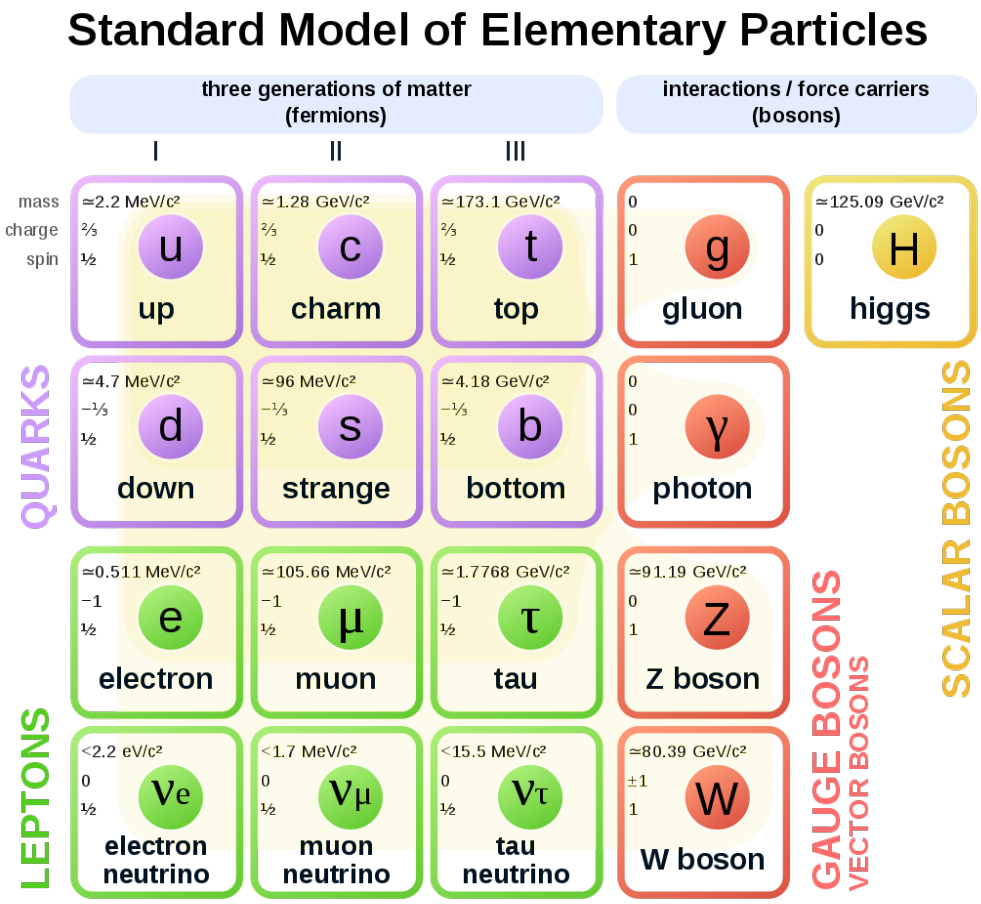

Figure 2.1: Standard Model particles, with individual masses, electric charge, and intrinsic angular momentum (spin) listed[2]. Anti-matter particles and colour charge states not shown for simplicity.

the electron, and second the neutrinos. The charged leptons consist of the electron, muon and τ particles of which muon and τ are both unstable and decay, the muon relatively slowly ($\sim$2 μs) and the τ quickly ($\sim$1 ps). Notably the muon only decays to an electron while the τ can decay to both leptons and quarks due to its sufficient mass.

The last group of fermions, the neutrinos, are somewhat unique as they aren't very well understood in the SM. Their nature, including whether they are the same type of fermion as the others, is still an active field of research. However, in this dissertation we can assume the neutrinos are classical neutrinos (i.e. no mass and the following consequences) as the effects of neutrino oscillations or undiscovered heavier neutrinos would have no measurable effects in this analysis. As this dissertation focuses on a property of τ decays, neutrinos are prevalent throughout the analysis as charged lepton decays always produce an associated

neutrino. Neutrinos are not detected by the experiment but carry away kinetic energy which lowers the total "visible" energy in events which produce them.

2.1.2 Bosons and Fundamental Forces

The fundamental bosons are often called force carriers as they are each associated with a fundamental force and only interact with particles which experience the force. For a particle to interact with a force it must carry the associated "charge" of the force.

Photon and the Electromagnetic Force

For the electromagnetic force the associated boson is the photon and the fundamental charge is the electric charge (referred to as just charge throughout the dissertation). This means for a particle to interact with the photon it must have an electric charge.

W, Z, and the Weak Force

For the weak nuclear force (or weak force) there are 3 associated bosons, the neutral Z^0 boson and two electrically charged $W^{\pm}$ bosons. The weak force is the only parity violating force, meaning it treats left and right-handed particles differently; where left and right handed refers to how the angular momentum of the particles is orientated with respect to the momentum vector. $W^{\pm}$ bosons will only interact with left handed particles while the Z boson will interact with all particles. This preference to interact with only one type of particle gives rise to the asymmetries discussed in Chapter 3.

Gluons and the Strong Force

The strong nuclear force (or strong force) has 8 associated bosons known collectively as gluons. The associated charge of the strong force is referred to as a "colour" charge. Whereas the electric charge has only 1 distinct charge, which varies between positively, negatively, and neutrally charged; the strong force has 3 distinct charges. In order to describe these different states the colours red, green, blue, and colourless(neutral) are somewhat arbitrarily used to describe them. Colour charge is only present in the quarks and gluons and the quark-bound states are always in a combination that results in an overall colourless charge (red + anti-red = colourless, red + blue + green = colourless).

2.2 Particle Physics Terminology used in this Dissertation

In order to fully engage with the analyzes presented in this dissertation a familiarity with common phrases and concepts used in particle physics is required. This Section is included to describe these concepts.

2.2.1 Antimatter

Antimatter particles are identical to their matter counterparts except that each SM charge(quantum number) is flipped. So for an electron, its antimatter particle, the positron, has a positive electric charge. When a particle collides with it's antimatter particle an annihilation occurs. This annihilation results in a pure energy state which rematerializes into another matter-antimatter pair. Any matter-antimatter pair with a combined mass less than the original state energy can be produced. This process allows e^+e^- colliders to produce a variety of final states for study.

2.2.2 Accelerating Particles

For the purposes of this Section, SuperKEKB and Belle II will be discussed though these terms are not unique to them. The role of the SuperKEKB is to deliver a large number of collisions of accelerated particles to Belle II, and doing so in a way which produces a minimal amount of background radiation. SuperKEKB collides electrons and positrons (e^+e^-) at a centre-of-mass energy ($\sqrt{s}$) of 10.58 GeV, which is the mass of the $\Upsilon(4S)$ meson, a bound state of a b and anti-b quark pair. SuperKEKB is designed to optimize the production of the $\Upsilon(4S)$ meson as the study of b-quark physics is one of the major focuses of Belle II. A major goal of SuperKEKB is to provide a higher density of e^+e^- crossings (and therefore more collisions) than ever previously achieved. The standard measurement for this is called luminosity and is in units of: number of particles per unit area per second. As the accelerator delivers a large quantity of collisions the amount of delivered beam is summarized as a time-integrated luminosity ($\mathcal{L}$, in units of inverse area). The eventual goal of Belle II is to collect at least 40000 fb^{-1} (1 fb^{-1} = 10^{-39} cm^{-2}).

2.2.3 Particle Production

In the collision of high energy particles a plethora of particles can be produced in the final state (subject to a number of conservation principles). The most important determinant is the available mass/energy in the collision, so for e^+e^- collisions at 10.58 GeV all quarks and

leptons, except the top quark which is too massive, can be produced in matter-antimatter pairs. The likelihood of producing a particular matter-antimatter pair is typically represented as a cross-section (units of area). This is a particularly useful way to express the probability as when multiplied by the integrated luminosity you arrive at the expected number of events in the data-set. As an example, at $\sqrt{s} = 10.58$ GeV the cross-section for $e^+e^- \rightarrow \tau^+\tau^-$ process is 0.919 nb; In a 40000 fb^{-1} data-set, 36.8 billion $\tau^+\tau^-$ final states are expected. The vast majority of of particles generated in this way will go on to produce secondary particles either through decaying, strong, or radiative effects. For 2nd and 3rd generation particles there are typically a variety of possible decay paths available. Each decay path has a certain probability of occurring (Branching fraction), and in a large dataset each likely decay path is present.

2.2.4 Particle Detection

After a collision occurs with Belle II a number of steps occur before an analyst can use the data. In order for an event to be saved the detector makes a "trigger" decision. This trigger decision is designed to maximize the amount of e^+e^- collisions recorded by the detector while minimizing background events from either beam interactions, or cosmic sources. Once the detector receives a trigger decision the raw detector information is saved and undergoes "reconstruction". The reconstruction process takes the raw detector data and builds particle candidates and event information for analysts to use.

Chapter 3

Chiral Belle Upgrade Project Motivations and Theory

3.1 Introduction

The Chiral Belle upgrade is a proposal to add polarization to the electron beam of SuperKEKB. This upgrade would allow Belle II to make a number of precision measurements in the electroweak sector. This project is being developed by an international team which has published a white paper as part of the SNOWMASS Community Planning Exercise[1]. This Chapter will summarize the physics motivations behind the project.

3.1.1 Electroweak Asymmetries

Due to the presence of the weak force, the $e^+e^- \to f\overline{f}$ process has an asymmetry in the cross-sections for left-handed and right-handed beam polarizations. This left-right asymmetry (A_{LR}) is defined as[3, 4]:

$$A_{LR} = \frac{\sigma_L - \sigma_R}{\sigma_L + \sigma_R} \propto \frac{sG_F}{\alpha} g_A^e g_V^f \langle P_e \rangle \tag{3.1}$$

Where σ_{LR} is the left and right handed cross-sections respectively, G_F is the Fermi constant, s is square of the centre-of-mass energy, α is the fine structure constant, g_A^e is the neutral current axial coupling of the electron, g_V^f is the neutral current vector coupling of the fermion, and $\langle P_e \rangle$ is the average beam polarization defined as:

$$\langle P_e \rangle = \frac{1}{2}\left[\left(\frac{N_L^e - N_R^e}{N_L^e + N_R^e}\right)_{\mathbf{L}} - \left(\frac{N_L^e - N_R^e}{N_L^e + N_R^e}\right)_{\mathbf{R}}\right] \tag{3.2}$$

Where N_{LR}^e refers to the actual number of left or right handed electrons in the data-set, and **LR** refers to the left or right nominal polarization of the e^- beam. Switching the beam polarization between left and right polarization is a necessity for having a left and right polarized data set from which to extract A_{LR}.

Importantly the size of the A_{LR} that can be measured is directly proportional to the average beam polarization. Chiral Belle intends to achieve a 70% polarized beam and measure it with a 0.5% level of precision.

3.1.2 Physics Reach

Assuming Chiral Belle meets its goals, Belle II expects to set world leading measurements of the neutral current vector couplings. Table 3.1 shows the current world averages and the projected level Belle II could reach with 20 ab^{-1} (1 ab^{-1} = 1000 fb^{-1}) of data. In addition

Final State Fermion	Current World Average	Chiral Belle Sensitivity
b-quark	-0.3220±0.0077	±0.002
c-quark	+0.1873±0.0070	±0.001
tau	-0.0366±0.0010	±0.001
muon	-0.03667±0.0023	±0.0007
electron	-0.3816±0.00047	±0.0009

Table 3.1: Current world averages and projected sensitivity of Belle II for measuring g_V^f, where f is the final state fermions[1].

to measuring the neutral current couplings a precision measurement of A_{LR} would also allow Belle II to extract a measurement of the weak-mixing angle ($\sin^2\theta_W$), as the two parameters are related.

$$A_{LR} \propto T_3^f - Q_f \sin^2\theta_W \tag{3.3}$$

$$g_V^f = T_f^3 - 2Q_f \sin^2\theta_W \qquad g_A^f = T_f^3 \tag{3.4}$$

Where T_3^f is the 3rd component of the weak isospin, and Q_f is the electric charge of the fermion. A precise measurement of $\sin^2\theta_W$ is attractive for Belle II as it would allow for a similar constraint on $\sin^2\theta_W$ as was done at LEP but at $\sqrt{s}$ = 10.58 GeV rather than the Z-pole ($\sqrt{s}$ = 91.19 GeV). This would provide the most stringent experimental constraint on the energy dependence of $\sin^2\theta_W$, which is predicted in the SM. Deviations in the energy dependence, 'running', of $\sin^2\theta_W$ from the SM would be evidence of new physics. One such deviation would be the presence of a new 'dark sector' Z^0 boson that induces parity violation effects outside the predictions of the SM. Figure 3.1 shows the existing and planned measurements of $\sin^2\theta_W$ as well as the potential effect of the existence of a new dark Z^0.

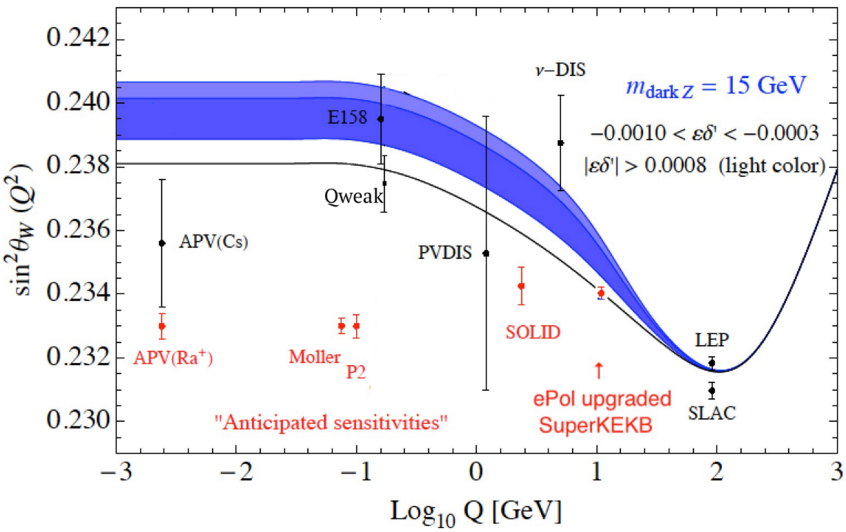

Figure 3.1: Plot of $\sin^2\theta_W$ under the SM, existing measurements (black), and planned measurements (red). Adapted from Figure 3 of Reference [5]. The blue band represents the presence of a 15 GeV dark Z-boson under a range of coupling parameters.

3.2 A_{LR} at Belle II

As part of the ongoing efforts to introduce beam polarization to Belle II there has been a number of recent theoretical results improving the precision of the theoretical calculations of A_{LR} for the electron and muon final state[4, 6]. From an experimental viewpoint it's important to understand if the theory calculations embedded within the Monte Carlo simulation code used for the processes under study are consistent with independent calculations. If significant deviations are found, it would require improvements to the calculations. This chapter discusses efforts to compare simulations with next-to-next-leading-order (NNLO) capable MC generators with the recent theory results.

3.3 Validation of Calculations of A_{LR} in $e^+e^- \to \mu^+\mu^-$ at Chiral Belle

The calculation of the asymmetry in muons was published in 2020[6] and is the first time A_{LR} has been precisely calculated at $\sqrt{s} = 10.58$ GeV. In order to validate and compare the results of the calculation, the asymmetry was found with `KKMC` [7], and the comparison was included in the publication. For the $e^+e^- \to \mu^+\mu^-\gamma$ process, shown in Figure 3.2, the Born level A_{LR} is shown in Equation 3.5[6].

$$A^0_{LR} = -\frac{2s}{m_Z^2}\left[a_e v_\mu + a_\mu v_e \frac{6(\cos a + \cos b)}{2\cos a \cos b + \cos 2a + \cos 2b + 8}\right] \tag{3.5}$$

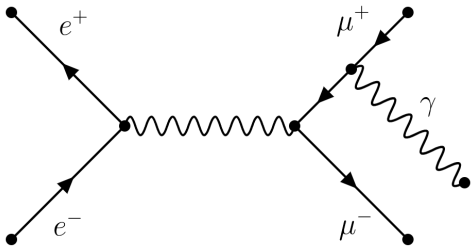

Figure 3.2: Feynmann diagram of the s-channel $e^+e^- \to \mu^+\mu^-\gamma$ process.

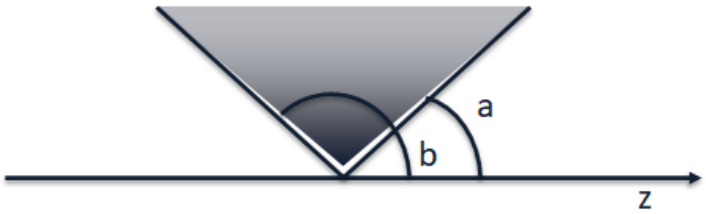

Figure 3.3: Angular acceptance between a and b, where angles are measured from the initial state electron momentum axis.

Where s is the square of the centre-of-mass energy, and m_Z is the Z-boson mass. $a_{e,\mu}$ and $v_{e,\mu}$ are related to the neutral current couplings as $a_f = g_A^f/(2\sin\theta_W\cos\theta_W)$ and $v_f = g_V^f/(2\sin\theta_W\cos\theta_W)$. a and b refer to the angular acceptance of the selection as shown in Figure 3.3.

3.3.1 KKMC Generator Settings

In order to ensure the generator produces comparable results, the following parameters are changed from their default settings to match the values used in Ref. [6]. The decay width of the W, and the top quark is set to 0. The following masses are set, $m_h = 125$ GeV, $m_u = 69.83$ MeV, $m_d = 69.84$ MeV, $m_c = 1.2$ GeV, $m_s = 0.15$ GeV, $m_t = 174$ GeV, $m_b = 4.6$ GeV. The centre-of-mass energy is set to 10.577 GeV. The lepton masses are set to $m_e = 0.510998910$ Mev, $m_\mu = 0.105658367$ GeV, and $m_\tau = 1.77684$ GeV. Additionally the generator is set to only produce results where the final state muons are within the angular acceptance of $b > \theta_\mu > a$, where b is 170° and a is 10°.

3.3.2 MC Production

The production was carried out by setting the beam polarization, to either fully left-handed or fully right-handed and requiring a muon-pair final state, and in order to perform the comparison, two billion $e^+e^- \to \mu^+\mu^-\gamma$ events were generated with KKMC. A feature of the theory calculations is a maximum photon energy, Ω. In the KKMC simulations multiple photons can be emitted so in order to achieve an analogous requirement $\Omega_{\texttt{KKMC}} = \frac{\sqrt{s}}{2}\left(1 - \frac{s'}{s}\right)$ is defined. Where s is the square of the centre-of-mass energy and s' is the square of the invariant mass of the muon pair. Unless otherwise specified $\Omega = \Omega_{\texttt{KKMC}} = 2$ GeV throughout this section.

3.3.3 Comparison of Observables

Figure 3.4 shows the first comparisons between theory and simulation where the differential cross section and A_{LR} has been calculated for particular values of $\cos\theta$. As these parameters cannot be calculated at specific values in simulation, the events are grouped in bins of $\cos\theta$, 0.125 in width. The points displayed in Figure 3.4 show the values calculated for the grouped bins with the points centred on the mean value of $\cos\theta$ for the events in each bin. In order to better capture the finite nature of simulation, the cross-section and A_{LR} values are integrated across a fiducial acceptance. Figure 3.5 shows this as the angular acceptance is extended from some minimal value to the full fiducial acceptance. Note that as the integration extends the acceptance the initial events populate every bin that comes after and therefore the points are not statistically independent. Next the forward-backward asymmetry ($A_{FB} \equiv \frac{\sigma_{\cos\theta>0} - \sigma_{\cos\theta<0}}{\sigma_{\cos\theta>0} + \sigma_{\cos\theta<0}}$) was determined under two different integration choices. First a symmetric angular acceptance between 90° and a (forward: $a < \theta < 90°$, backward: $90° < \theta < 180° - a$), and second as a function of the minimum acceptance value of Ω. The forward-backward asymmetry seen in Figure 3.6 shows an offset of a few percent between the theory calculations and the KKMC results. The authors of Ref. [6] suggest this is likely due to the difference in approaches related to the number of photons allowed in the final state. A final comparison is done again on the cross-sections and A_{LR} but as a function of Ω acceptance rather than θ. Figure 3.7 shows the cross-sections at $\theta = 90°$ and integrated across the full angular acceptance. Figure 3.8 shows the A_{LR} distributions for the same conditions.

As A_{LR} at $\theta = 90°$ is an infinitesimal point the acceptance for charged muons generated by KKMC is set to $70° < \theta < 110°$, a region over which the A_{LR} dependence on $\cos\theta$ is linear to a good approximation, as can be seen in Figure 3.4. From Figure 3.8, the agreement between theory and simulation between 1 GeV and 3 GeV is strong. The region is also relatively

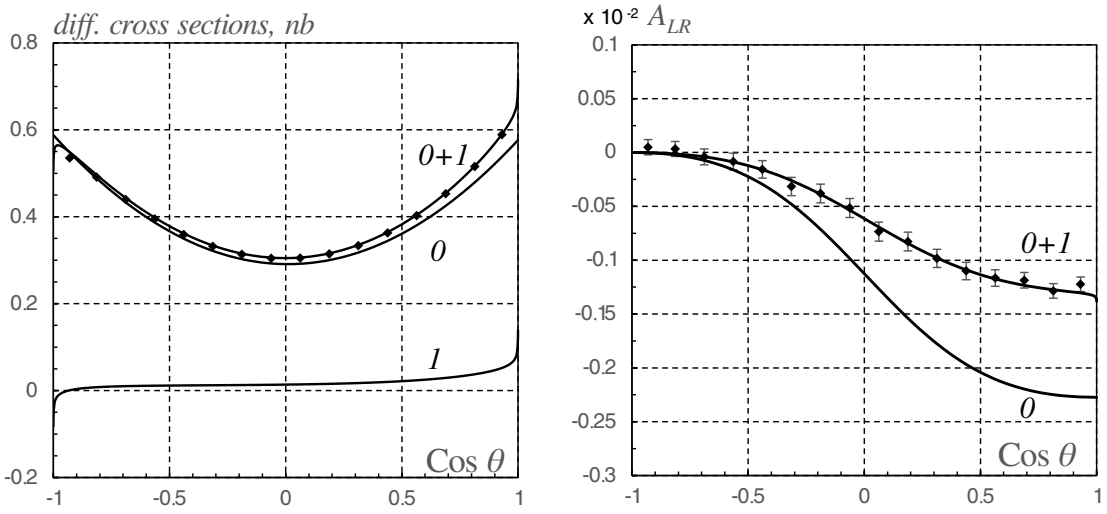

Figure 3.4: $e^+e^- \to \mu^+\mu^-\gamma$ observables; Left: unpolarized NLO corrected (0+1), Born (0), and their difference (1); differential cross sections vs scattering angle θ. Right: the polarization Born asymmetry (0) and asymmetry taking into account the NLO EWC (0+1) vs scattering angle $\cos\theta$, KKMC Monte Carlo points are integrated in $\cos\theta$ bins 0.125 in width. Calculations are done at an Ω cut of 2 GeV. The points are the results obtained from running the KKMC Monte Carlo generator as described in the text, where the error bars represent the statistical errors from the number of Monte Carlo events generated.

flat and suggests future experimental results would benefit from operating in this regime to reduce uncertainty coming from the A_{LR} dependence on radiative effects. Accounting for the statistical uncertainties arising from the finite KKMC samples, the absolute KKMC statistical uncertainty on A_{LR} is $\pm 1.9 \times 10^{-5}$. It should also be noted that as Ω approaches zero there is significant deviations between the theory and simulation. The paper authors suggest this is due to infrared divergences that KKMC is able to address while the theory calculations do not.

3.3.4 A_{LR} in $e^+e^- \to \mu^+\mu^-\gamma$ Conclusions

The addition of the KKMC simulated comparisons was an important addition to the theory paper. The results demonstrate the need for precision calculations and theoretical understanding of the left-right asymmetry in preparation for future measurements. The results were also able to identify energy and fiducial regimes where the future Chiral Belle analyses can be relatively insensitive to any dependence of the asymmetry in response to radiative effects. With the successes found in performing simulation studies for the muon final state, the next section covers a similar study carried out for the electron final state ($e^+e^- \to e^+e^-\gamma$).

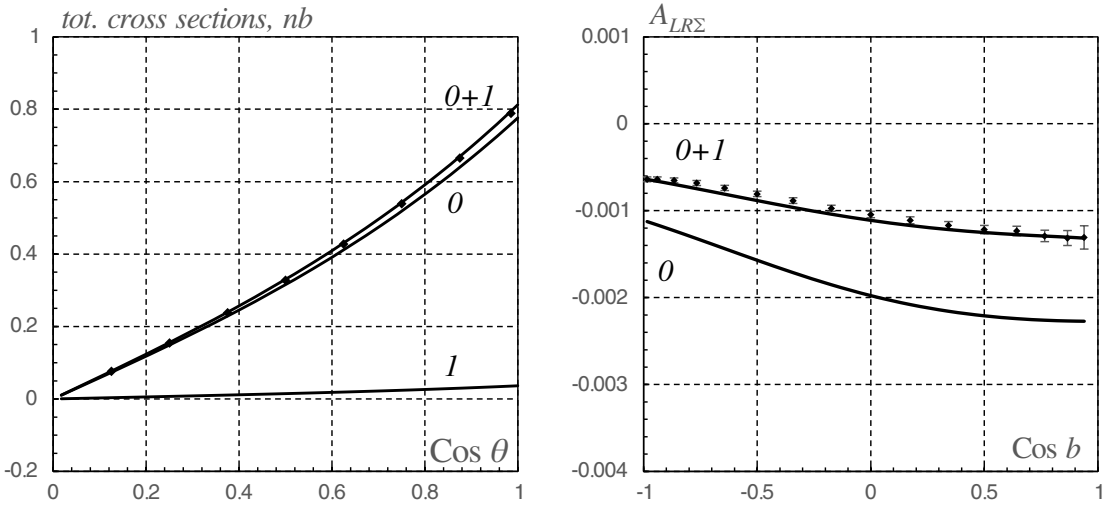

Figure 3.5: $e^+e^- \to \mu^+\mu^-\gamma$ observables; Left:unpolarized NLO corrected (0+1), Born (0), and their difference (1). Left: total cross-section vs symmetric angular acceptance ($-\cos\theta$ to $\cos\theta$). Right: the left-right integrated Born asymmetry (0) and asymmetry taking into account the NLO EWC (0+1) vs angular acceptance ($\cos b$ to $\cos 10^\circ$). Calculations are done at an Ω cut of 2 GeV. The points are the results obtained from running the KKMC Monte Carlo generator as described in the text, where the error bars represent the statistical errors from the number of Monte Carlo events generated.

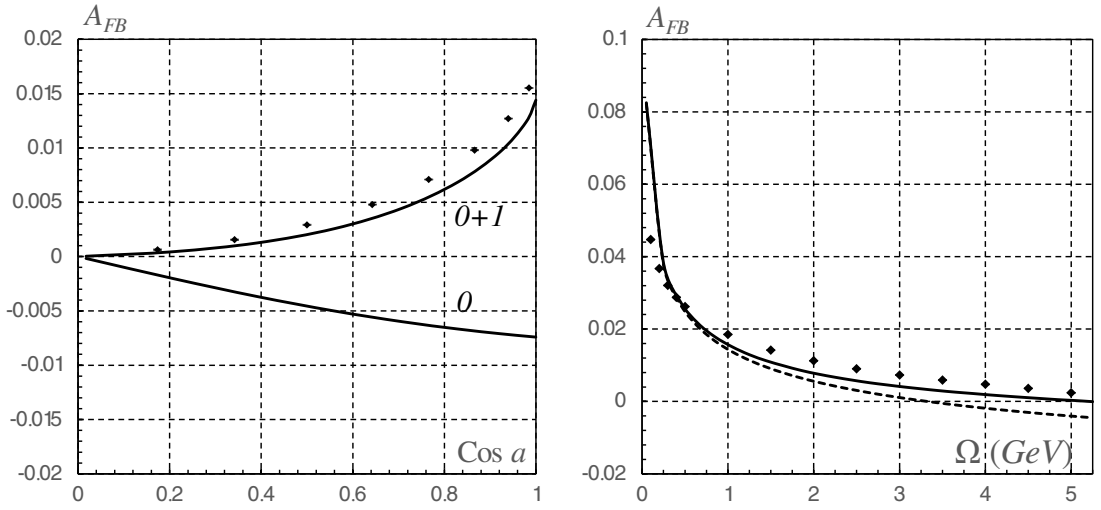

Figure 3.6: $e^+e^- \to \mu^+\mu^-\gamma$ observables; Left: the forward-backward Born asymmetry (0) and asymmetry taking into account the NLO EWC (0+1) vs angle a at an Ω cut of 2 GeV. Right: Calculations in two approaches: soft photon (dashed line) and hard photon (solid line), the NLO corrected forward-backward asymmetry at $|\cos\theta| < \cos 30^\circ$. The points are the results obtained from running the KKMC Monte Carlo generator as described in the text, where the error bars represent the statistical errors from the number of Monte Carlo events generated.

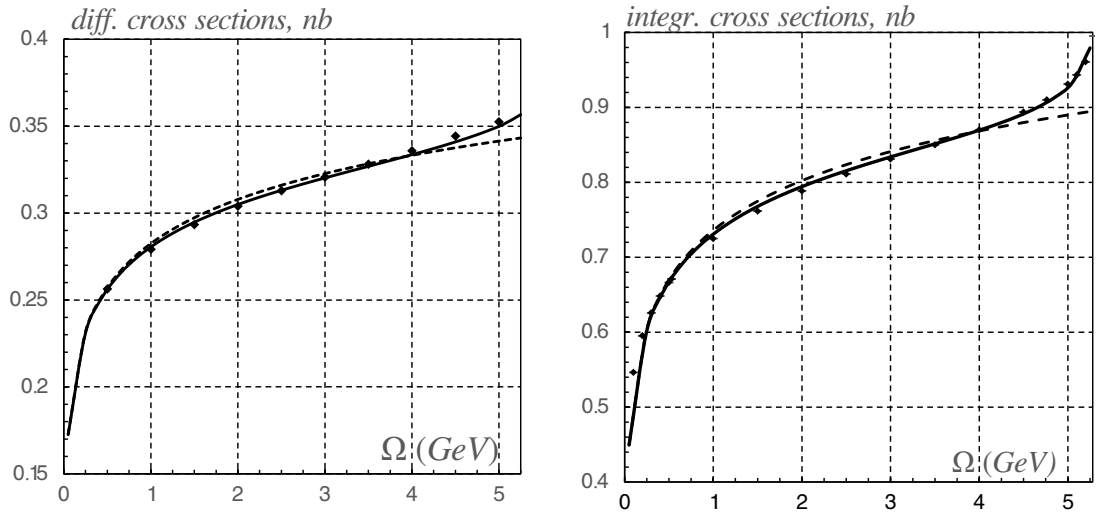

Figure 3.7: Calculations in two approaches: soft photon (dashed line) and hard photon (solid line) for the $e^+e^- \to \mu^+\mu^-\gamma$ process. Left: The NLO corrected unpolarized differential cross section at $|\cos\theta| < \cos 30^\circ$ vs Ω. Right: the NLO corrected unpolarized integrated cross section at a=10° to b=170° vs Ω. The points are the results obtained from running the KKMC Monte Carlo generator as described in the text, where the error bars represent the statistical errors from the number of Monte Carlo events generated.

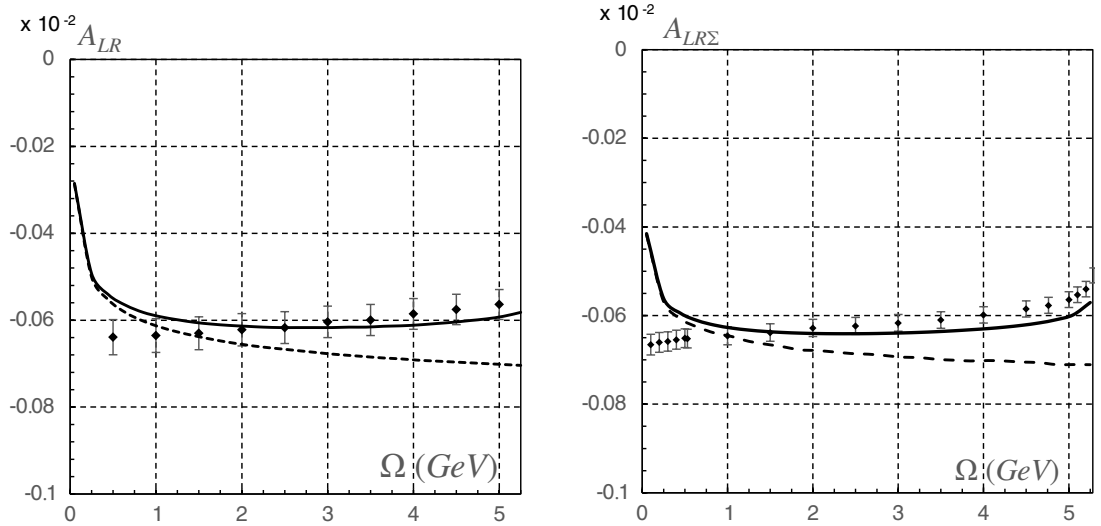

Figure 3.8: Calculations in two approaches: soft photon (dashed line) and hard photon (solid line) for the $e^+e^- \to \mu^+\mu^-\gamma$ process. Left: the NLO corrected polarization asymmetry at θ=90°, KKMC Monte Carlo integrated between 70° and 110°. Right: the NLO corrected integrated asymmetry from a=10° to b=170°. The points are the results obtained from running the KKMC Monte Carlo generator as described in the text, where the error bars represent the statistical errors from the number of Monte Carlo events generated.

3.4 Validation of Calculations of A_{LR} in $e^+e^- \to e^+e^-\gamma$ at Chiral Belle

For the $e^+e^- \to e^+e^-\,\gamma$ process (Bhabha process) both the s-channel and t-channel processes play a large role in the value of A_{LR}. These processes are illustrated in Figures 3.9 and 3.10 respectively. For Belle II the centre-of-mass energy of 10.577 GeV is well below the Z-pole

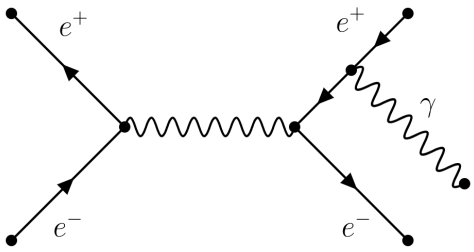

Figure 3.9: Feynman diagram of the s-channel $e^+e^- \to e^+e^-\gamma$ process.

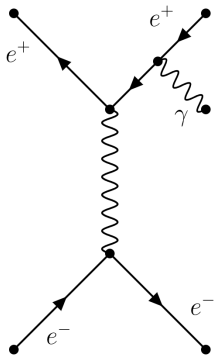

Figure 3.10: Feynman diagram of the t-channel $e^+e^- \to e^+e^-\gamma$ process.

and as such the production cross-sections are dominated by γ mediators. At Born level this leads to an A_{LR} form as seen in Equation 3.6[4].

$$A^0_{LR} = \frac{4v_e a_e s s_a^2}{m_Z^2} \times \frac{c_a(21 + c_a^2) + 12l_a}{c_a(c_a^4 + 26c_a^2 - 75) - 24s_a^2 l_a} \tag{3.6}$$

Where v_e and a_e are related to the vector and axial couplings as shown in the section above, s is the square of the centre-of-mass energy, s_a is $\sin a$, c_a is $\cos a$, and l_a is $\ln \frac{1-c_a}{1+c_a}$, where a represents the angular acceptance between a and 180°-a. This section describes the work done to generate $e^+e^- \to e^+e^-$ events with a polarized electron beam, and comparisons to the theoretical work contained in Reference [4].

3.4.1 ReneSANCe MC Generator

In order to carry out this study a new MC generator was required as the KKMC generator does not simulate the $e^+e^- \to e^+e^-$ process. The typical generators used by Belle II to simulate the Bhabhas do not support polarized beams. The ReneSANCe MC generator[8] was published a few months before this study began and contained all the necessary features. Originally the generator did not include the functionality to produce results for only a single polarized beam, requiring both beams to be equally polarized. After contacting the authors, Renat Sadykov and Vitaly Yermolchyk, a new version with this functionality was released. In order to generate the events needed for an A_{LR} calculation ReneSANCe provides two options. First events can be generated within a defined angular acceptance for a certain electron beam state and the production cross-section is included in the output. From the produced events angular cuts can be made on the electron to produce sub-selections, and by repeating this process with the other beam state A_{LR} measurements at various angles of final state electron selection can be produced. This is the approach taken for the aforementioned A_{LR} muon study. Unfortunately due to the exponential behaviour of the Bhabha cross-section near the $\cos\theta = 1$ direction, the computational requirements to produce significant statistics for $\cos\theta_{e^-} < 0.8$ were too large. The second approach that can be taken with the ReneSANCe generator is a direct calculation of the A_{LR} numerator or denominator. This allows for A_{LR} at various acceptance angles to be quickly calculated at the sacrifice of having access to any individual Bhabha events. Due to the significantly reduced computational demand, and high precision for all acceptance angles, this method was used for this section.

3.4.2 Generator Settings

As the ReneSANCe default settings do not match the SM values used if Ref. [4], the following changes to SM parameters were made. The width of the W, and the top quark is set to 0. The following masses are set, $m_h = 125$ GeV, $m_u = 69.83$ MeV, $m_d = 69.84$ MeV, $m_c = 1.2$ GeV, $m_s = 0.15$ GeV, $m_t = 174$ GeV, $m_b = 4.6$ GeV. The centre-of-mass energy is set to 10.577 GeV and the soft photon cutoff, ω, is set to 0.002. Additionally the angular acceptance of the positron is set to be $|\cos\theta_{e^+}| < 0.94$.

3.4.3 A_{LR} Comparison

The plot of interest in Ref. [4] is the integrated A_{LR}. Which integrates the electron as $\int_{-\cos a}^{\cos a} d\sigma$, where a is the angle between the initial and final state electron. Extracting the data points from Figure 3 of Ref. [4] allows us to produce an overlaid plot as seen in Figure

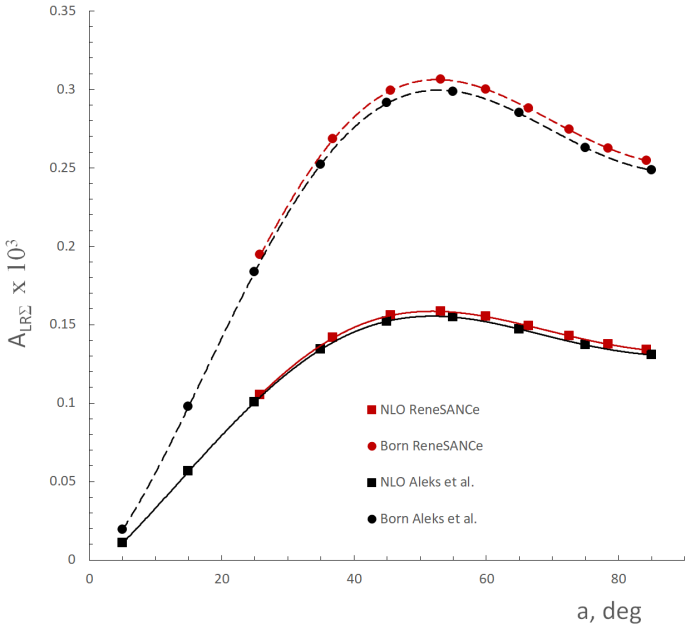

Figure 3.11: Comparison of A_{LR} in Bhabhas for an angular acceptance of $a < \theta < 180° - a$. Theory results in black, MC simulation in red. The NLO results are in good agreement, however the difference in the Born level variables suggests a difference in definition remains.

3.11. This shows strong agreement across the parameter space. Interestingly it also shows that ReneSANCe produces a higher value for A_{LR} in both the Born and NLO (Next to leading order) calculation. In both cases the ReneSANCe value are ∼2% higher, corresponding to $8{\times}10^{-6}$ in the NLO value and $4{\times}10^{-6}$ in the Born value. The source of the discrepancy is unclear.

3.4.4 $\sin^2\theta_W$ Sensitivity

In order to determine the sensitivity to $\sin^2\theta_W$ the value of the mass of the W-boson is varied in the generator. This is done through the Born level definition of $\sin^2\theta_W$, $\sin^2\theta_W{=}1-\frac{m_W^2}{m_Z^2}$, as recommended by Sadykov and Yermolchyk [9]. The PDG mass of the W-boson, 80.377 GeV[10], is varied by ±12 MeV and ±60 MeV to study the effect on the A_{LR} value. Figure 3.12 shows the shifts in A_{LR} as the value of m_W is varied. A consistent behaviour in both the NLO and Born level results where a larger value of m_W gives a larger A_{LR} value is observed. Figure 3.13 shows just the NLO distribution normalized by the PDG m_W distribution. This highlights the consistent behaviour across the parameter space (Both figures include error bars given by the ReneSANCe generator, however they are too small too be seen at this scale).

m_W(GeV)	$A_{LR}\times10^3$	$\Delta A_{LR}\times10^3$	$\sin^2\theta_W$	$\Delta\sin^2\theta_W$
80.379	0.146409	-	0.223013	-
80.391	0.144296	-0.002213	0.222781	-0.000232
80.367	0.148623	0.002214	0.223245	0.000232
80.439	0.157520	0.011112	0.221853	-0.001160
80.319	0.134424	-0.011984	0.224173	0.001159

Table 3.2: Relationship between value of A_{LR} and $\sin^2\theta_W$ as a function of W-boson mass. The Δ columns show the deviation from the SM values (m_W=80.3379 GeV).

The shifts in A_{LR} can be converted to shifts in $\sin^2\theta_W$ using the Born level definition. This is done by selecting the value of a which gives the largest value of A_{LR}, $\cos a = 0.6 (a = 53.1°)$. Table 3.2 shows the comparison of A_{LR} and $\sin^2\theta_W$. These numbers suggest that an A_{LR} measurement with a total uncertainty of 0.5% would make a result in a $\sin^2\theta_W$ 1.2× more precise than the current world average from this single measurement mode. From the A_{LR} variations it is extrapolated, using $1/\sqrt{N}$, that $\sim 2\times10^{11}$ Bhabha events would be required for the needed level of precision. Using the acceptance window of $|\cos a| < 0.6$, ReneSANCe returns a production cross-section of 40.8 nb. Using this cross-section with the required number of events results in a requirement for a dataset on the order of 50 ab^{-1}.

3.4.5 $\sin^2\theta_W$ Sensitivity with A_{LR} from Bhabhas at Chiral Belle

The A_{LR} studies with ReneSANCe have verified the shape and overall size of the A_{LR} calculations carried out in the theory calculations. There are a few small differences especially in the Born level calculation that need to be addressed before the results can be published, which is a future goal for this analysis. The sensitivity studies show an uncertainty of 0.000232 on a $\sin^2\theta_W$ measurement is required to meet the current 1σ uncertainties in the SM. In order to estimate the sensitivity Belle II will have with 50 ab^{-1} of data, angular acceptance for the Belle II luminosity paper, $|\cos\theta| < 0.819$[11], is used to find the ReneSANCe A_{LR} value of 0.00015 for that acceptance. The luminosity paper also provide the production cross-section for the angular acceptance to be 17.4 nb, and the efficiency to be 0.3593. Next assuming a 70% polarized beam is achieved and measured to with 0.5% ($\delta\langle P_e\rangle = 0.005$) accuracy the expected error on the A_{LR} measurement can be estimated as follows.

$$N_{e^+e^-} = \varepsilon\mathcal{L}\sigma = (0.3593)(50\text{ab}^{-1})(17.4\text{nb}) = 3.13\times10^{11}\text{events} \tag{3.7}$$

$$\delta A_{LR} = \frac{1}{\sqrt{N_{e^+e^-}}} \qquad A_{LR}^{\text{meas}} = \langle P_e\rangle A_{LR} = 0.000105 \tag{3.8}$$

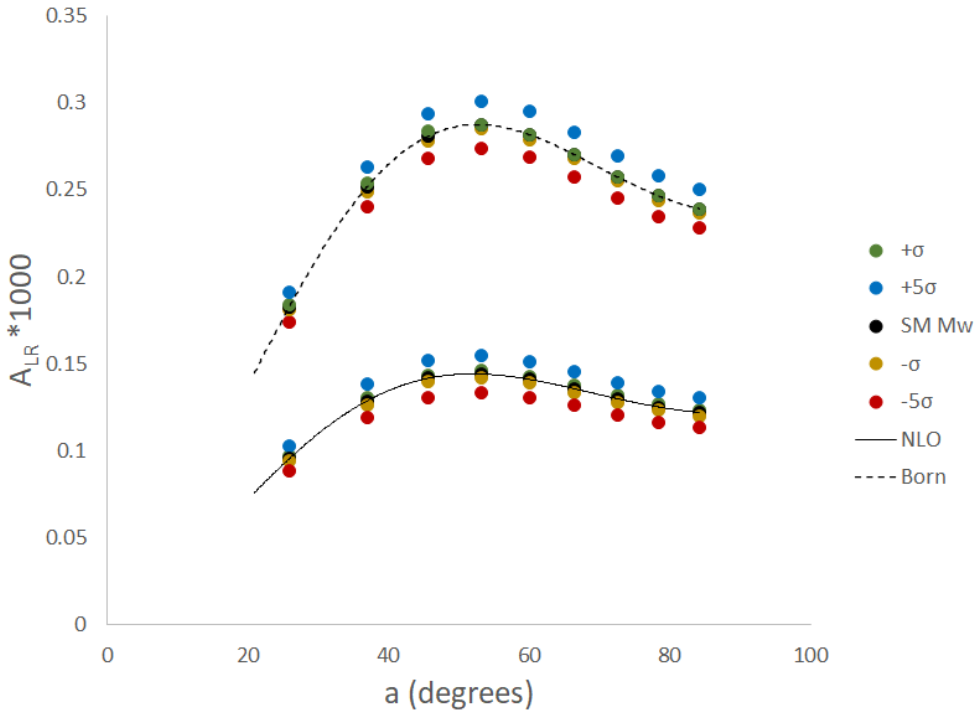

Figure 3.12: A_{LR} in Bhabhas for an angular acceptance of $a < \theta < 180° - a$. The series show the sensitivity in A_{LR} as m_W changes.

$$\delta^{\text{rel}} A_{LR}^{\text{meas}} = \sqrt{\left(\frac{\delta A_{LR}}{A_{LR}^{\text{meas}}}\right)^2 + (\delta\langle P_e\rangle)^2} = 0.0178 \tag{3.9}$$

$$\Delta A_{LR}^{\text{meas}} = A_{LR}(\delta^{\text{rel}} A_{LR}^{\text{meas}}) = 2.66 \times 10^{-6} \tag{3.10}$$

Which is very similar to the value of 2.21×10^{-6} shown in Table 3.2 for a 1σ fluctuation in the m_W mass. To estimate the accuracy of the $\sin^2\theta_W$ measurement, the shifts in A_{LR} and $\sin^2\theta_W$ observed in Table 3.2 are assumed to be linearly related. The average of the four ratios $(\frac{\Delta\sin^2\theta_W}{\Delta A_{LR}})$ is 103.9 and all of the ratios are near it in value suggesting the linear assumption is good. Under this assumption the sensitivity achievable at Belle II can be estimated as:

$$\delta\sin^2\theta_W = \delta A_{LR}\frac{\Delta\sin^2\theta_W}{\Delta A_{LR}} = 0.000277 \tag{3.11}$$

This value is about a factor of 3 larger than the current world average uncertainty, ±0.00010[10]. Should Belle II do a global fit including information from all $e^+e^- \to f\overline{f}$ processes, the final precision can be estimated using this result and the projected uncertainties from Table 3.1 to be ~ 0.00015.

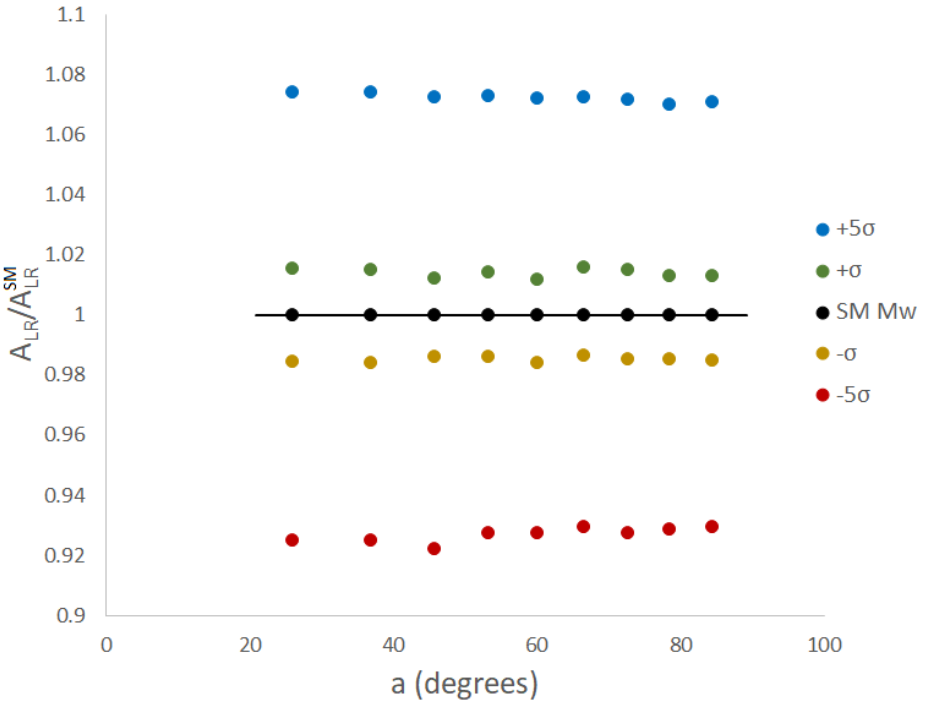

Figure 3.13: $A_{LR}/A_{LR}^{\mathrm{SM}}$ in Bhabhas for an angular acceptance of $a < \theta < 180° - a$. The series show the sensitivity in A_{LR} as m_W changes.

3.4.6 A_{LR} in $e^+e^- \to e^+e^-\gamma$ Conclusions

The A_{LR} studies on the Bhabha process has shown the two theory approaches are in relatively good agreement, differing by 2%. Interestingly the 2% offset appears in both the Born and NLO level calculations suggesting a difference in definition rather than an inherent difference in the two. At this time the source of the discrepancy is unknown and will likely require input from both Aleksejevs *et.al.*, and Sadykov and Yermolchyk to identify. A sensitivity study of the expected uncertainty revealed Belle II could reach a competitive measurement of $\sin^2\theta_W$ from the Bhabha A_{LR} alone with 50 ab^{-1} of data.

Chapter 4

General Purpose B-Factory Detectors

4.1 *BABAR* and Belle II

BABAR and Belle II are both general purpose detectors constructed to detect events produced from e^+e^- collisions at or near 10.577 GeV. Due to the similar purpose and lessons learned at *BABAR* that informed the design of Belle II, the detectors are very similar and analyses developed on one should largely translate directly to the other. PEP-II (*BABAR*'s accelerator) and SuperKEKB both delivered/deliver e^+e^- collisions at a centre-of-mass energy of 10.577 GeV, the minimum energy required to produce free B mesons, also referred to as the $\Upsilon(4S)$ resonance. The general purpose classification of *BABAR* and Belle II refers to their ability to detect, track, and measure a wide variety of particles produced in e^+e^- collisions. This chapter will describe the sub-detectors that make this possible and compare the similarities between the detectors.

4.2 Detector Overview

Both detectors are built in radial layers encircling the beampipe in a barrel-like fashion. Each layer provides complimentary information to help build up a complete picture of a collision event. The layer closest to the beam pipe identifies the point of origin of the particles (vertex detection), in Belle II this layer has two subsystems names the PXD and VXD, while in *BABAR* it is called the SVT. The next layer tracks the direction and momentum of charged particles through a low density gas, the CDC in Belle II and the DCH in *BABAR*. Both Belle II and *BABAR* include thin low density detectors as the next layer, with the primary purpose being the identification of the particle type (PID). In Belle II there are two subsystems, TOP and ARICH, while *BABAR*'s subsystem is called DIRC. The next layer is a high density electromagnetic calorimeter, acting as a backstop for electrons and photons

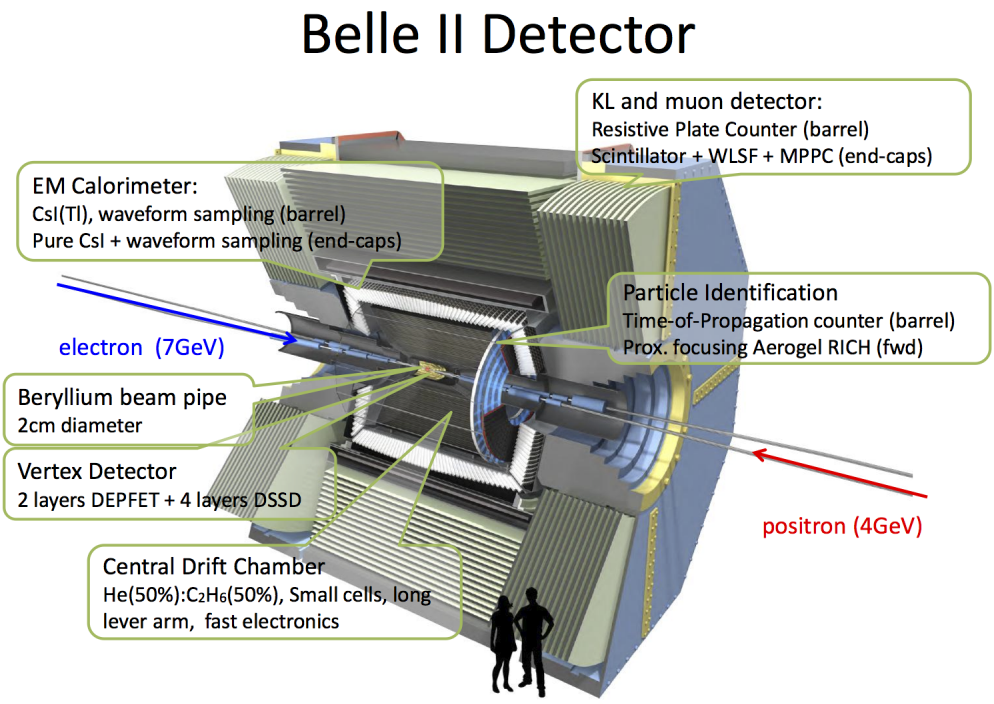

Figure 4.1: Cross-section of the Belle II detector with sub-detector systems labeled[12].

and provides a measurement of the total energy, the ECL in Belle II and the EMC in *BABAR*. These radial layers are all contained within a magnetic yoke which provides a solenoidal 1.5 T magnetic field and instrumented iron flux return plates. These instrumented flux return plates detect any particles which punch through the rest of the detector. This subsystem is called the KLM in Belle II and the IFR in *BABAR*. A cross-section of the Belle II detector is shown and Figure 4.1, and the *BABAR* detector in Figure 4.2. Tables 4.2 and 4.1 summarize the detectors and their main roles, to be defined after, for both *BABAR* and Belle II.

4.2.1 Coordinate System

Both *BABAR* and Belle II employ the same coordinate system both in Cartesian and spherical coordinates where the interaction point (IP) is always defined as the origin. In Cartesian coordinates the positive z-axis is aligned with the direction of the electron beam and defines a forward, positive z, and a backward, negative z, region. The y-axis is aligned vertically, with increasing y corresponding to increasing height. The x-axis increases horizontally with distance from the centre of the accelerator ring. In spherical coordinates, r is distance from the origin, θ is the angle with respect to the z-axis, and ϕ is the angle with respect to

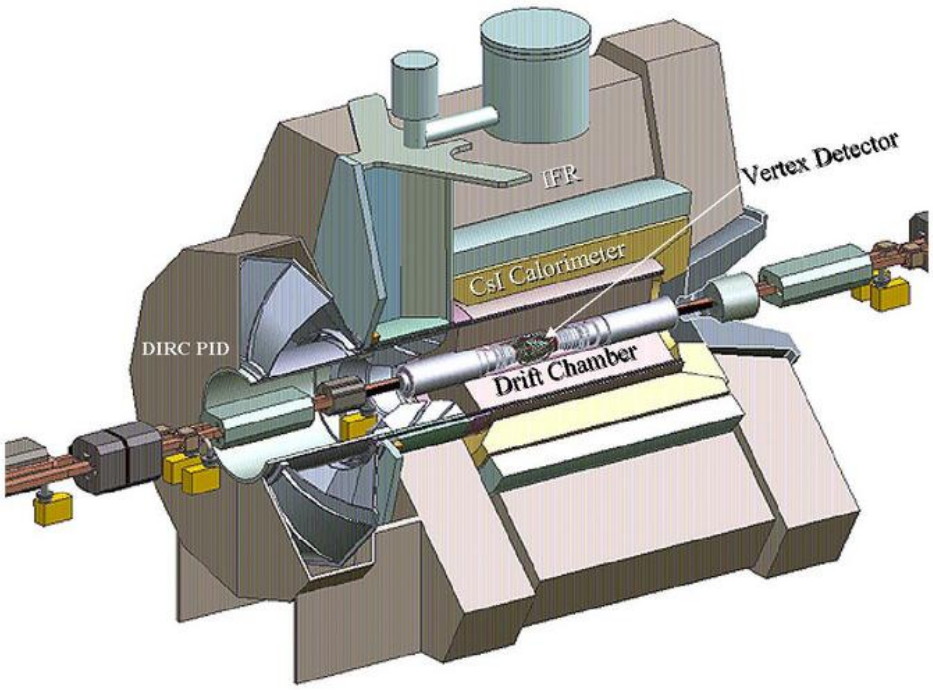

Figure 4.2: Cross-section of the *BABAR* detector[13].

Detector	Primary Measurement
PXD	Vertex Detection
SVD	Vertex Detection
CDC	$\vec{p}$,Charge,dE/dx
TOP	Particle Identification
ARICH	Particle Identification
ECL	Electromagnetic Energy, Hadronic Tagging
KLM	Hadronic Showers and Muon ID

Table 4.1: List of Belle II Detector Systems[14]

Detector	Primary Measurement
SVT	Vertex Detection
DCH	$\vec{p}$,Charge,dE/dx
DIRC	Particle Identification
EMC	Electromagnetic Energy
IFR	Hadronic Showers and Muon ID

Table 4.2: List of *BABAR* Detector Systems[15]

the x-axis. In general when discussing the detector design and locations the lab frame of reference is used unless otherwise specified. When discussing particles and event selection criteria, the centre-of-mass frame is used unless otherwise specified. The detector coverage and a conversion between lab frame and centre-of-mass frame angles for Belle II is shown in Section 4.2.2.

4.2.2 Belle II protractor

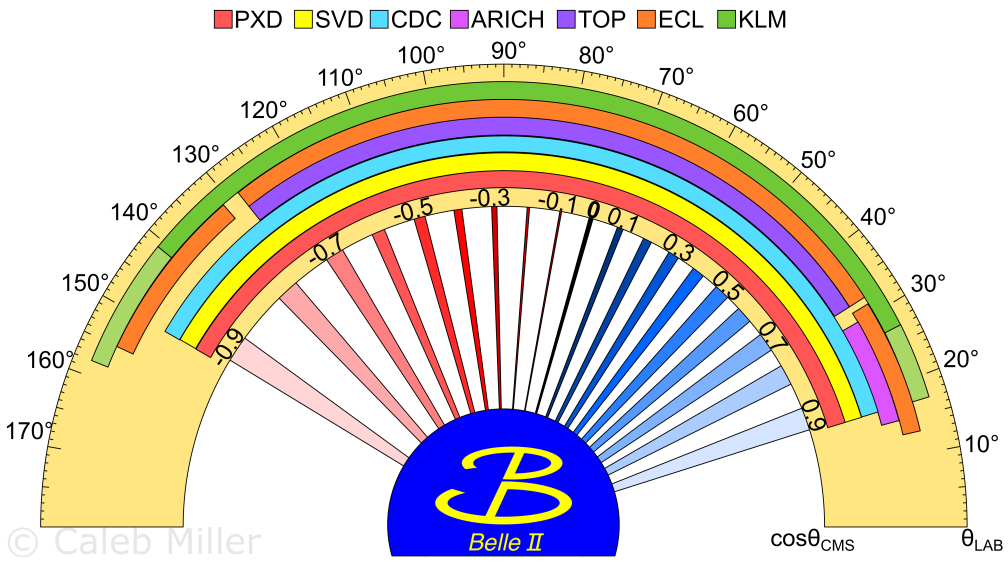

Figure 4.3: Belle II angular boost protractor with sub-detector coverage. Lab frame angles and their corresponding centre-of-mass frame $\cos\theta$ values.

4.3 Vertex Detection

Reconstruction of the origin point of particles in the detector is provided by a vertex detector. This allows particles originating from external sources, such as cosmic rays or beam backgrounds, to be removed from the event. For collisions which produce pairs of short-lived particles, i.e. decay within the beam pipe, the vertex detector can often reconstruct two separate decay vertices thereby sorting out which detected particles come from the same decay. At *BABAR* this is done by the Silicon Vertex Tracker (SVT) and at Belle II this is done with

two sub-detectors, the PiXel Detector (PXD) and the Silicon Vertex Detector (SVD). These sub-detectors are described in more detail below.

4.3.1 SVT

The SVT at *BABAR* consisted of 5 layers of double-sided silicon strips. The strips were laid out parallel to the beam pipe and each layer is composed of multiple strips wrapping around the beam pipe in a barrel-like configuration. The first three layers surround the beam pipe in a cylindrical layout, with a distance of 32 mm, 40 mm, and 54 mm from the expected beam collision point. The outer two layers were cylindrical for most of their coverage but approach the beam pipe at $\sim 45^\circ$ near the end of their coverage. These layers were further out from the beam pipe at 125 mm, and 142 mm respectively. This spacing assists with tracking of the particles through the SVT. *BABAR* reported a vertex resolution of 55 μm in the x-y plane, and 65 μm in the z-direction[15].

4.3.2 PXD

The innermost sub-detector of Belle II is the PXD. The PXD is composed of silicon transistors which are 50 μm thick, and are 50μm$\times$50μm in size. This small size has a few advantages over the more typical strip detectors. The primary advantage is the smaller detector size will experience less activity per sensor and this allows for greater ability to read out information and discriminate between events. The other advantage is the small localization of the sensor which when coupled with the 2 layers present allows for a very accurate determination of the origin point of a particle.

4.3.3 SVD

The SVD is the next part of the Belle II vertex detection system. The SVD is composed of 4 layers of silicon detectors that range from 4 cm to 14 cm from the beam pipe. In order to reduce the cost and cabling requirements, strip detectors are used in place of pixels. The strips are about 12cm long by 6 cm wide. The total thickness of the detectors is on the order of 300 μm. With these two systems (PXD and SVD) working in tandem, the Belle II collaboration expects to resolve vertices with an accuracy of $\sim$5 μm in the r-ϕ direction and $\sim$10 μm in the z direction[14].

4.4 Charged Particle Tracking

Particle tracking is an essential part of general purpose detector, and both *BABAR* and Belle II employ drift chambers to accomplish this. Drift chambers are filled with a low density gas and are crisscrossed by wires that pick up ionization left in the wake of charged particles. By tracking charged particles accurately as they traverse a drift chamber, a number of key features can be identified. First, as the particles move through the magnetic field they will curl in a direction dependent on their electric charge. This curl also has an intrinsic radius which is defined by the particle's momentum. The drift chambers can also make a measurement of the rate at which the particle is losing energy(dE/dx) which depends on the speed of the particle and when combined with the momentum measurement, provides information about the mass of the particle. Finally, the drift chambers play a role in the trigger decision of the detector, which decides if an event is interesting enough to record. At *BABAR* the drift chamber was called the DCH while at Belle II it is referred to as the CDC.

4.4.1 DCH

The DCH at *BABAR* was a cylindrical tube, 3 m long and 1.6 m in diameter. The interior was instrumented with 28,768 wires which provided up to 40 spatial and ionization loss measurements for particles travelling through the DCH. The cylinder was also filled with a gas mixture of 80% helium and 20% isobutane. This mixture was chosen for it's long interaction length (807 m), which means most particles won't scatter off gas particles, and has a decent dE/dx resolution of 6.9%.

4.4.2 CDC

The CDC at Belle II by contrast is slightly larger, 2.4 m in length and 2.2 m in diameter. The interior contains 56,576 wires and a gas that is 50% helium and 50% ethane (C_2H_6). This mixture was carried over from the predecessor experiment, Belle, however a number of other candidate gases were considered. The helium ethane mixture was chosen for it's proven performance in Belle, which exhibited long interaction lengths, and good position and energy loss resolution. Belle II has reported an expected dE/dx resolution of $\sim$10%[14].

4.5 Particle Identification

Both *BABAR* and Belle II use Cherenkov detectors to improve the ability of the experiments to correctly identify charged particles. Cherenkov radiation is produced when a particle

is moving faster than the speed of light in a medium, which occurs for most high energy particles travelling through the detector. Cherenkov radiation is somewhat analogous to a sonic boom, but with a cone of light produced rather than sound. The relationship between the speed of the particles and the opening angle is given by $\cos\theta = 1/(n\beta)$, where n is the refractive index and $\beta = v/c$. This speed measurement can be coupled with the momentum measurement from the drift chamber to extract the particle mass, which is primarily used to separate kaons from pions, but also feeds into the electron, muon, and proton identification.

4.5.1 DIRC

The Cherenkov detector at *BABAR* was composed of synthetic fused silica bars which acted as both the radiator and light pipe for transporting the Cherenkov radiation to a light sensitive collector. These bars wrapped around the cylinder of the detector, between the DCH and EMC, in a barrel like way and light emitted within them was internally reflected and eventually entered a water tank on the backwards side of the detector. The light then traveled through roughly 1 m of water, which allowed the light to spread apart further to improve the angular resolution. The light was then collected at one of some 10752 PMTs. *BABAR* has reported an angular resolution of 2.5 mrad was achieved and at a momentum regime of 3 GeV/c was able to separate kaons and pions at a 4.2σ significance. In addition to this, *BABAR* was able to measure the particle flight times to within 1.7 ns which provides a secondary measurement on the particle velocity.

4.5.2 TOP and ARICH

Belle II has deployed two independent Cherenkov detectors, one around the barrel region similar to *BABAR* called Time Of Propagation (TOP) detector, and another in the forward end-cap called the Aerogel Ring Imaging CHerenkov (ARICH) detector. The TOP detector also uses synthetic fused silica bars as radiators and light tubes, but instead of a water tank uses very dense multi-channel plate photomultiplier detectors(MPC-PMT) fused directly onto the silica bar. Belle II has reported an expected performance of 1.8 mrad in angular resolution at 3 GeV/c and a design timing resolution of 25 ps, with a expected performance of better than 50 ps. The kaon-pion separation is expected to be similar to the *BABAR* performance. The ARICH system uses aerogel as a radiation material instead of fused silica, and detects the full Cherenkov ring rather than just the opening angle of it. This is done by placing avalanche photo-diodes 20 cm behind the aerogel radiators. With this setup ARICH expects to achieve an angular resolution of 3.1 mrad, and assuming a background

free environment, could separate 4 GeV pions and kaons at a 5σ significance[14].

4.6 Electromagnetic Calorimeter

The electromagnetic calorimeters of both *BABAR* and Belle II are made up of rectangular crystals, roughly 10x10x30 cm, of thallium doped cesium iodide (CSI(Tl)). Electrons and photons which enter the calorimeter create showers of secondary electrons and photons and are fully stopped within the crystals. Muons tend to only leave a trail of ionization as they pass through the calorimeter and the rest of the detector. Hadronically interacting particles such as pions, protons, and neutrons tend to deposit a fraction of their energy in the calorimeter. These energy depositions result in light being produced which is detected by photodiodes attached to the back of the crystals. This energy measurement is essential for identifying electrons, measuring the event energy from both charged and neutral particles, and plays a role in the trigger decision of the detectors.

4.6.1 EMC

The ElectroMagnetic Calorimeter (EMC) at *BABAR*was made up of 5,760 crystals in the barrel region and 820 crystals in the forward region. Together they covered an angle from 15.8° to 141.8° which represents 90% of the angular space in the centre-of-mass.

4.6.2 ECL

At Belle II the Electromagnetic CaLorimeter (ECL) was designed to be an improvement in two major ways. First the CSI(Tl) crystals in the ECL are aligned slightly away from pointing directly at the IP, this significantly reduces the chance a particle slips between the cracks of two crystals. Second, the backwards endcap was also covered in crystals which increases the detector coverage. At Belle II 6,624 crystals are used in the barrel, and 2,112 in the endcaps for a total coverage of 12.4° to 155.1°, which corresponds to a 95% angular coverage. The ECL also reads out digitized waveforms which it uses to distinguish between hadronic and electromagnetic energy depositions. This is done through analysis of the pulse shape collected by the calorimeter and is the first time a high energy physics experiment has done this[16].

4.7 Flux Return

Surrounding the calorimeters at both *BABAR* and Belle II are multiple layers of iron plates which act as flux returns for the magnetic field. Muons, pions, and kaons can pass through the calorimeter depositing only a small amount of their total energy. By adding scintillator material between the iron plates, particles which generate showers within the iron plates can be detected. This detection can provide additional information about the type of particle detected as well as a veto for cosmic rays and other non-collision events. Both *BABAR* and Belle II implement resistive plate chambers (RPCs) to accomplish this. RPCs consist of charged plates with a gas gap between them. As charged particles transverse the gas, ionization streams are created which are detected as a pulse in the readout electronics.

4.7.1 IFR

The instrumented flux return(IFR) at *BABAR* contained 19 layers of active detectors and covered a total area of $\sim$2000 m^2. The RPCs used two bakelite (phenolic polymer) sheets coated in graphite for the charged plates, and were connected to an 8 kV supply. The plates were separated by a 2mm gap. During operation the IFR had a 90% μ-tagging efficiency and a 6-8% $\pi^{\pm}$ misidentification rate[15].

4.7.2 KLM

At Belle II the kaon-long and muon detector(KLM) contains 15 layers of detectors. Belle II also implements a 2mm gap in the RPCs and fills the gaseous volume with a mix of HFCs, argon, and butane-silver gas. The RPCs used in Belle II were recovered from the Belle experiment however the plates in the forward and backward endcaps were found to be under-performing and were replaced with scintillators instead. The Belle II collaboration has projected a 89% μ-tagging efficiency with a 1.3% $\pi^{\pm}$ fake rate.

Chapter 5

Thermal Neutron Beam Background Characterization

5.1 Commissioning and Background Modeling

As the SuperKEKB beamline and Belle II were upgrades to the KEKB collider and Belle detector, a variety of commissioning Phases were planned in order to bring the systems back online and begin initial calibrations. The first commissioning Phase (Phase 1) was a test of the SuperKEKB beamline without the final focusing magnets or Belle II in place. The rings were connected with a temporary beam pipe in place of Belle II and a variety of background monitoring detectors were placed around the beamline. This set of monitoring detectors (known as BEAST II) were in place for a few months of beam running and during that time the operators worked with the KEK(高エネルギー加速器研究機構) accelerator team to study the effect of beam parameters on backgrounds and make predictions about the expected backgrounds in future Phases. Phase 2 was completed in 2018 and included the Belle II detector, excluding the PXD and SVD (collectively known as the VXD), with the final focusing magnets. The goal of Phase 2 was to test backgrounds with collisions to ensure background rates in Phase 3 would be safe for the operation of the VXD. Phase 3 began in early 2019, and includes the full Belle II detector, the main goal of Phase 3 is to reach the design luminosity of the accelerator and begin collecting data for physics analysis.

Commissioning Phase	Dates	Conditions
Phase 1	2016	Temporary Beampipe in place of Belle II
Phase 2	2018	Belle II except the VXD
Phase 3	2019 to present	Full operations

Table 5.1: Summary of the commissioning phase for SuperKEKB and Belle II.

5.1.1 The BEAST II Detectors In Phase 1

^{3}He

The four ^{3}He thermal neutron detectors were deployed around the future interaction point and their contributing measurement is the thermal neutron rate. Neutrons can be produced as secondary particles from a variety of background sources and can take a comparatively long time compared to the other backgrounds to subside. The total neutron background is important for Belle II detectors such as ARICH which has limits on the neutron flux it can withstand.

TPC

Four TPCs (Time Projection Chambers) were deployed in Phase 1 and were positioned beside the ^{3}He detectors. Each TPC is capable of measuring the directionality of fast neutrons as well as other heavy particles such as alphas. This is useful for determining the approximate source of backgrounds as well as providing another measure of the neutron rate.

Crystals

The crystal system was a mix of thallium doped cesium iodide crystals(CsI(Tl)), pure cesium iodide(CsI), and Lutetium-yttrium oxyorthosilicate (LYSO). There were 6 of each scintillator type deployed in Phase 1. The crystal's were used to measure the energy spectrum of the electromagnetic backgrounds and the different crystals were compared for their respective efficiencies and robustness as possible upgrades to the Belle II ECL.

BGO

The 8 Bismuth germanium oxide(BGO) crystals were in place to monitor the amount of electromagnetic dose. Most backgrounds produce electromagnetic particles and the total dose is especially important for the TOP detector.

PINs

The PIN system is comprised of 64 diodes comprised of an **I**ntrinsic semiconductor sandwiched between P and N type semiconductors (PIN). The PIN detectors are sensitive to each particle that passes through it and is able to make very fast measurements. With this the PIN detectors provided the instantaneous dose at multiple positions. This is useful for

determining the location of the loss positions as well as sending the accelerator team a fast notification in the case of a sudden spike in beam backgrounds.

Diamonds

The diamond system was a set of 4 detectors placed near the interaction point to monitor the dose received. The diamonds sensors were in place to predict the dose received by the future PXD and SVD. During the commissioning of Belle their equivalent of the SVD was severely damaged during beam commissioning and so diamonds played the role of a monitor on these conditions and during Phase 2 acted as a beam abort system if backgrounds got too high.

CLAWS

The CLAWS detector was a system of 8 plastic scintillators. The system was designed to monitor the background rate of a single bunch as it passed through the interaction region. When a new bunch of electrons or positrons was injected into the large ring it had a relatively high background rate as particles which are less centralized in the bunch were lost. CLAWS monitored how many additional backgrounds were caused by the new bunch and determined how many loops were required before a bunch was acceptable to use in physics collisions.

QCSS

The QCSS system was a series of scintillators which were being prototyped to be attached to the final focusing magnets(QCS) during Phase 2. The QCSS was highly efficient at detecting charged particles and take up little space. It was deployed in Phase 1 to help monitor beam losses and was planned for Phase 2 as a beam loss monitor that could be used to help optimize collimator positions.

5.1.2 The BEAST II Detectors In Phase 2

After the completion of Phase 1 the Belle II detector was rolled into place on the beam line. The Phase 2 commissioning was planned to run for around 5 months. With the final focusing magnets in place the accelerator team could also now begin testing collisions which meant BEAST II still had a role in monitoring backgrounds associated with this. Phase 2 saw the return of some of the detector systems with addition of a few new ones. ^{3}He, TPCs, PINs, Diamonds, and CLAWS continued from Phase 1. The Crystals and BGO were replaced with

the presence of the Belle II detector itself, and the QCSS suffered from a loss of personnel and wasn't able to continue into Phase 2. Two new detector systems joined for Phase 2:

FANGS

The FANGS detector was a series of silicon detectors that function similarly to the SVD. The purpose of FANGS was to monitor the energy distribution of incoming particles and more importantly extrapolate the measured occupancy, the fraction of the detector active at any given time, to how much occupancy the SVD and PXD will experience in similar conditions.

PLUME

The PLUME detector was a new type of detector with a variety of capabilities. The detector itself was composed of two boards of detectors. Each board has a set of pixel sensors of each side. This allowed PLUME to do basic tracking of particles that pass through the detector and determine directionality. The main goal in Phase 2 was to test and prototype the detector technology while also providing measurements of the expected occupancy in the PXD and SVD.

5.2 Thermal Neutron Detection with ^{3}He

When choosing a detector medium for counting thermal neutrons with proportional detectors there are usually three main considerations. First, the cross section for capturing thermal neutrons; second, the energy, or Q value, of the capture event; and third, the cost of the medium. The three most commonly used mediums are ^{3}He, ^{6}Li, and ^{10}B. Table 5.2 shows the relevant physical parameters for the three gases.

Gas	σ (barns)	Q value (keV)
^{3}He	5332	764
^{6}Li	941	4780
^{10}B	3840	2790

Table 5.2: Comparison of detector mediums commonly used in thermal neutron detection.

For highly efficient neutron detection, ^{3}He is the best medium due to the high capture cross section. For the thermal neutron detectors deployed in Belle II a cylindrical detector, 20 cm long and 5 cm in diameter, filled with ^{3}He was used. Equation 5.1 shows the relevant

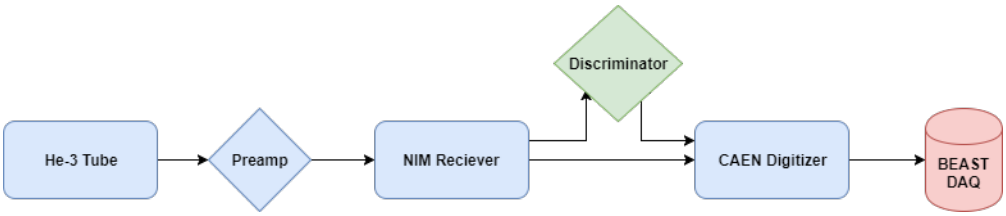

Figure 5.1: Data flow path for the ^{3}He BEAST II system.

reaction where both byproducts ionize the gas and produce a portion of the total measured amplitude. By conservation of momentum the proton($^1_1$H) has a higher kinetic energy of 573 keV while the triton($^3_1$H) carries away the other 191 keV.

$$^3_2\mathrm{He} + ^1_0\mathrm{n} \rightarrow ^3_1\mathrm{H} + ^1_1\mathrm{H} + 764\mathrm{keV} \tag{5.1}$$

In order to collect the signal from the detected neutrons a readout system was designed at the University of Victoria. The signal is obtained by applying a high voltage to a sense wire running through the centre of the tube. When the produced protons ionize the gas, they produce secondary electrons and positively charged ions. The electrons move towards the positively biased sense wire and accelerate when they experience an increasing electric field as they get closer to the wire. These accelerated electrons then further ionize the gas, releasing more electrons, which also accelerate and further ionize the gas, a process that repeats itself repeatedly in a process called avalanching. The signal on the wire is produced when the ions produced in the avalanche drift away from the wire and induce a signal on the wire. The pulse is then amplified by a preamplifier attached directly to the detector. The amplified signal is passed through a receiver unit before the analog pulse is recorded by the digitizer and passed to the Data AcQuisition (DAQ) computer. This process is summarized in Figure 5.1. An additional feature shown in the figure is the addition of a discriminator. The discriminator was added to the DAQ chain to improve the event detection efficiency as is further discussed in Section 5.5. Four of these detectors were deployed in Phase 1 of Belle II as part of the BEAST II commissioning detector. The purpose of the BEAST II detector was to provide an evaluation of the simulation for beam conditions and inform the collaboration as to the actual amount of secondary radiation present around the beam line. The main sources of this secondary radiation in Phase 1 commissioning was determined to be caused by collisions of the beam with residual gases and Touschek scattering. These background sources are further explained in Section 5.14. The detectors were then deployed again in Phase 2, being mounted in the 'dockspace' (a gap between the ECL and exterior

shielding), to monitor beam conditions as well as study the same backgrounds as in Phase 1 with the addition of luminosity dependent backgrounds.The detectors have remained at Belle II through Phase 3 as long term background monitors. One detector will continue inside Belle II, until the PXD requires the space for it's DAQ modules, while the other detectors have been installed in the beam line.

5.3 Phase 1 Results

The thermal neutron measurements in Phase 1 were used to study the backgrounds contributing to neutron production. The BEAST II group published the results of this study in Reference [17]. In addition to the BEAST II paper, additional details of what was done with the ^{3}He neutron detectors can be found in Reference [18]. One of the results of interest, which led to continuing the research with the ^{3}He neutron detectors was the relationship found between simulation and measured rates as can be seen in figure 5.2. The results in

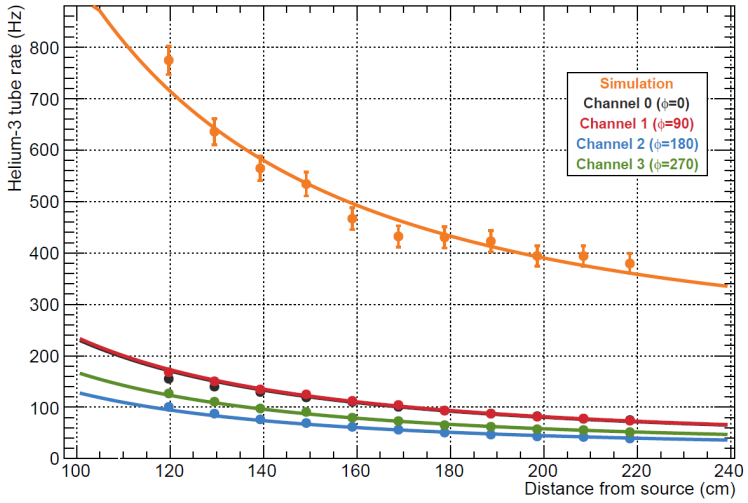

Figure 5.2: Comparison of neutron rates measured at UVic and predicted by simulation.[18]

figure 5.2 were measured using a 168 GBq AmBe neutron source at UVic. The discrepancy between the data and simulation was used to calibrate the detectors and correct the data measured during the Phase 1 running.

5.4 Phase 2 Goals

One of the goals for this research was to lower the discrepancy between signal and simulation as seen in Figure 5.2. In addition to this, a calibration at higher rates was desired to match

more closely with the rates expected in during the Phase 2 calibration of Belle II. In order to accomplish this the tubes were recalibrated by the author at UVic, and the shielding used in Reference [18] to lower the neutron rates was removed. As mentioned above, a discriminator was added to the DAQ chain and is described in Section 5.5.

5.5 Discriminator

In order to reduce the discrepancy between the observed rates and the simulation a discriminator was added to the readout chain to try and reduce any possible pileup effects. This addition immediately produced an increase in overall rates as well as improved sensitivity to changes in distance from the source. As the threshold for accepting a pulse as signal can be adjusted a study was done to choose the optimal threshold. Figure 5.3 shows how the rates are effected by the threshold voltage. 300 mV was chosen as the threshold setting to avoid the exponential growth of noise seen at low thresholds. In addition to this the measured rate through the discriminator was approximately equal to the analog measured rate (indicated as 'CAEN', the colloquial name of the readout component) at this setting which gave a backup method to determine the rate should something fail during operation. Finally, Figure 5.4 shows the improved rates obtained from the four detectors. With this improved efficiency, the focus of the research shifted to studying the cause of the spread in the measured neutron rates, as well as any other systematic uncertainties which may affect the system.

5.6 Temperature Effects

As the temperature around the detectors was not recorded during Phase 2 the effect of temperature on the measured neutron rate was studied. This was expected to have some effect on the measured rates, as the signal multiplication caused by gas amplification is dependent on the pressure of the gas. The temperatures measurements were taken with a thermocouple in the neutron source room at UVic over night. Figure 5.5 shows the relationship between temperature and neutron rate measured over a temperature change of $\sim 10°$C. The fit results in a slope of 2.87 ± 0.1 Hz/°C. Assuming this scales with the neutron rate, this gives an increase of $0.32\pm0.01\%$/°C in the neutron rate. Early Phase 3 measurements suggest the temperature in the dockspace varies by around 5°C. This adds a systematic uncertainty of approximately 2% to the neutron rates.

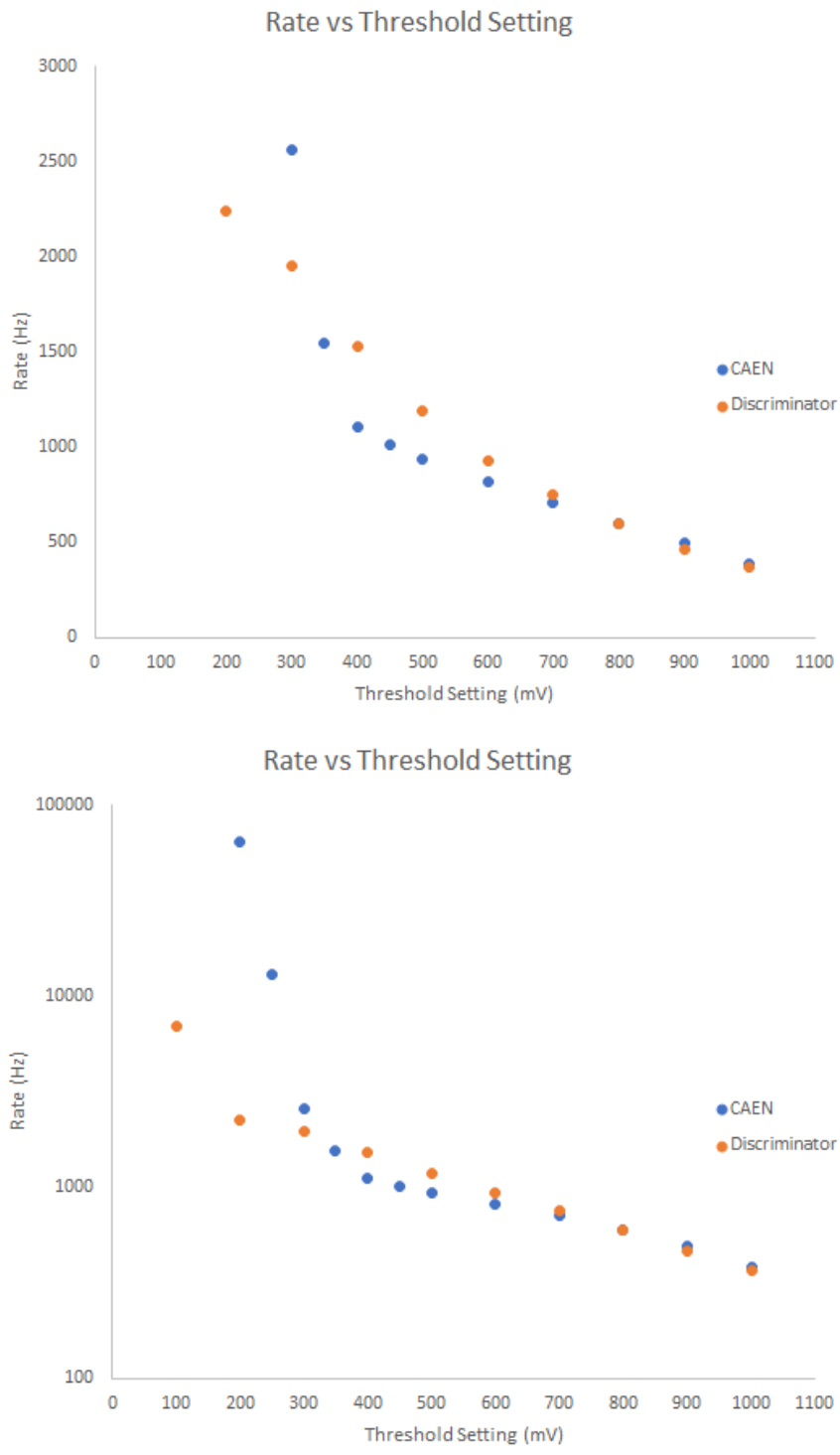

Figure 5.3: Neutron rate vs. discriminator threshold, linear scale(Top), and log scale(Bottom).

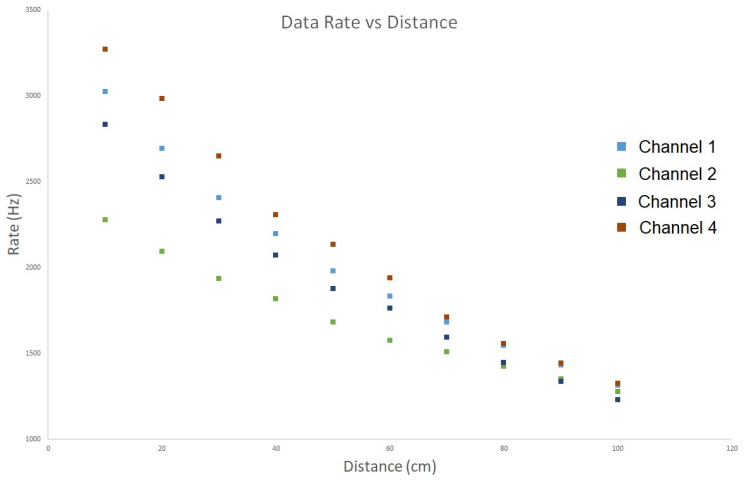

Figure 5.4: Neutron rate vs. distance with the discriminator added to the DAQ chain.

5.7 Voltage Effects

It was noticed during the calibration of the Phase 1 data that there was a discrepancy in the pulse amplitude spectra between data and calibration. The detectors were tested with a range of voltages at UVic and this effect was properly calibrated for. Further investigation showed the voltage supply used in Phase 1 was off by about 30 Volts. This was shown to be mostly due to a faulty probe used in calibrating the supply, but it is also possible the voltage dropped during the course of Phase 1 data taking. To remove this uncertainty the voltage will be monitored every second in Phase 2 with a DATAQ high speed DAQ as seen in Figure 5.6.

5.8 Simulation and Validation

In order to calibrate the detectors for use in Belle II the neutron source at the University of Victoria was simulated with GEANT4[20, 21]. Two separate tests were carried out. The first was to simulate the detectors at various distances from the source. This allows for the efficiency of the detector at various neutron fluxes to be calculated. The second test was measuring and simulating the neutron flux at various positions around the neutron source itself. The neutron source at UVic in composed of a high activity AmBe source (168GBq) encased in a cube of graphite measuring 1.85 metres on each side. Figure 5.7 shows the position of the detectors with respect to the graphite. The simulation was used in the Phase

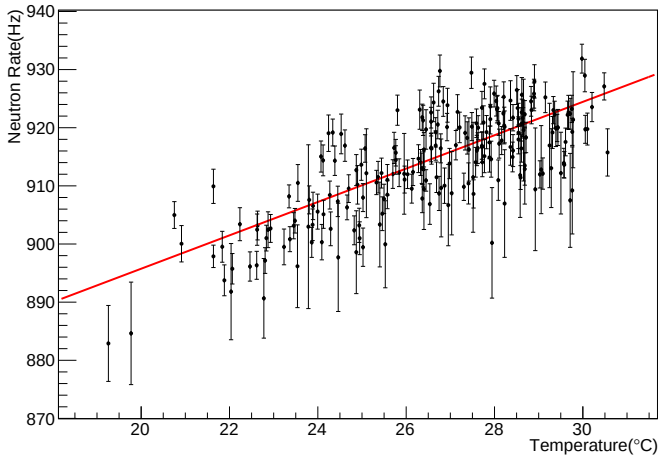

Figure 5.5: Neutron rate as function of temperature.

Figure 5.6: Voltage monitor used in Phase 2 [19].

1 to calibrate the detectors for the results published in the Phase 1 BEAST II paper[17]. The details of the simulation were improved for use in Phase 2. The changes include a more accurate boron concentration, and a more accurate description of the physical shape of the source shielding. These improvements to the simulation were studied and implemented by Sam de Jong[18].

5.9 Detector Comparison

Noticing the slight difference between the final results, evident in Figure 5.4, the tubes were each tested independently in 3 different arrangements. In each of the three setups the preamplifier and DAQ channel associated with Detector 4 was used. The first setup consisted of each detector placed on a table near the source approximately 50 cm from the

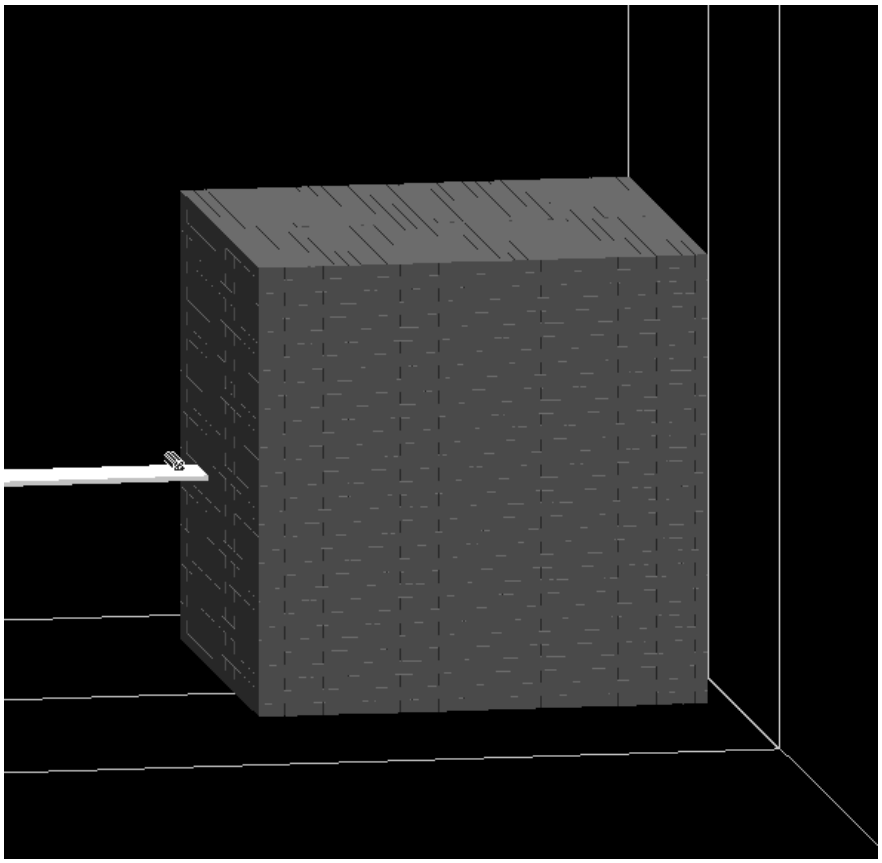

Figure 5.7: GEANT4 simulation of graphite pile with detector on table.

neutron source. The second setup was with the detectors approximately 10 cm from the neutron source, and finally the third setup was remaining at 10 cm and placing a block of shielding between the detector and neutron source. The average rates collected in these setups is shown in Table 5.3. Three of the tubes display an expected level of variance given the manufacturer's tolerances while the fourth detector is well outside. The reason for this large deviation is not well understood, but is not a large concern as the lower efficiency can be calibrated out. Table 5.4 shows the results of Table 5.3 scaled relative to Detector 4.

	Setup#1	Setup #2	Setup #3
Detector 1	2044.3 ± 2.5	3135.2 ± 1.8	1469.4 ± 1.2
Detector 2	2207.3 ± 2.5	3283.4 ± 1.9	1639.3 ± 1.2
Detector 3	2184.0 ± 2.6	3248.0 ± 1.8	1631.4 ± 1.1
Detector 4	2143.6 ± 2.4	3244.2 ± 1.7	1596.0 ± 1.4

Table 5.3: Neutron rate in Hz measured in each tube for 3 distinct configurations.

	Setup #1	Setup #2	Setup #3	Average
Detector 1	0.954 ± 0.002	0.966 ± 0.001	0.921 ± 0.002	**0.947 ± 0.019**
Detector 2	1.030 ± 0.002	1.012 ± 0.001	1.023 ± 0.002	**1.023 ± 0.008**
Detector 3	1.019 ± 0.002	1.001 ± 0.001	1.014 ± 0.002	**1.014 ± 0.009**
Detector 4	1	1	1	**1**

Table 5.4: Neutron detection efficiency relative to detector 4.

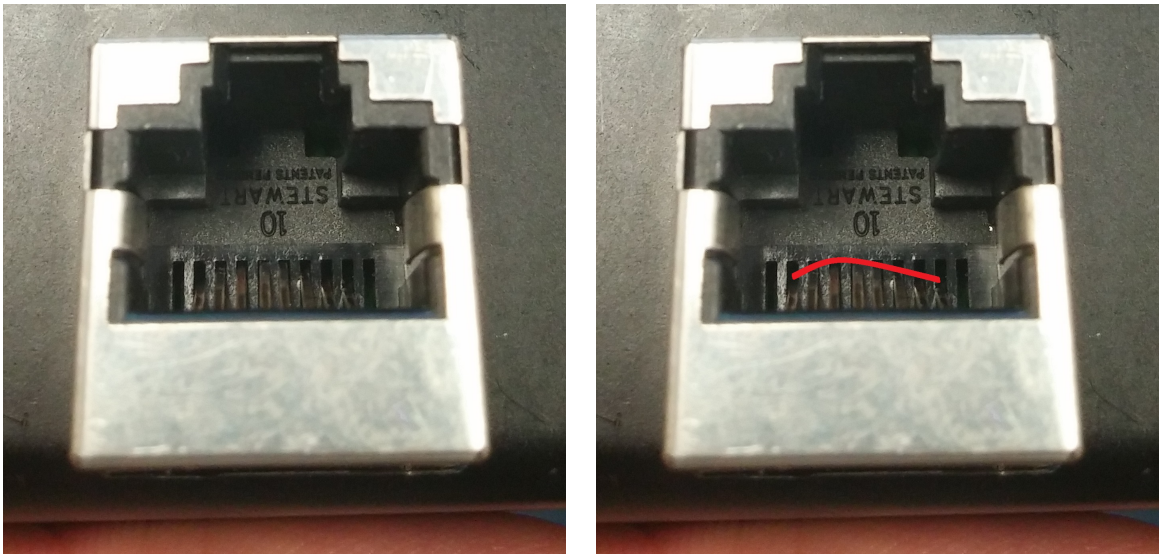

Figure 5.8: Damaged data port (Left), if undamaged all metallic pins should aligned and not depressed. Same port with visual aid showing the damage/curvature of the pin alignment (Right).

5.10 Preamplifier Damage

During the new calibration of the neutron detectors a strong dependence on the signal path was noted. This was eventually determined to be due to damage on the preamplifier modules. The pins for the cat 5 cable were bent likely resulting in a poor connection as shown in Figure 5.8. New preamplifiers were ordered, however due to time constraints the detectors had already been shipped to Japan. In order to test the new preamplifiers, pulses were simulated with a pulse generator to test similarities in amplification and acceptance. The preamplifiers were found to have subtle differences which result in a 2% systematic uncertainty on the measured rates. This is entirely acceptable as it will not be a limiting uncertainty.

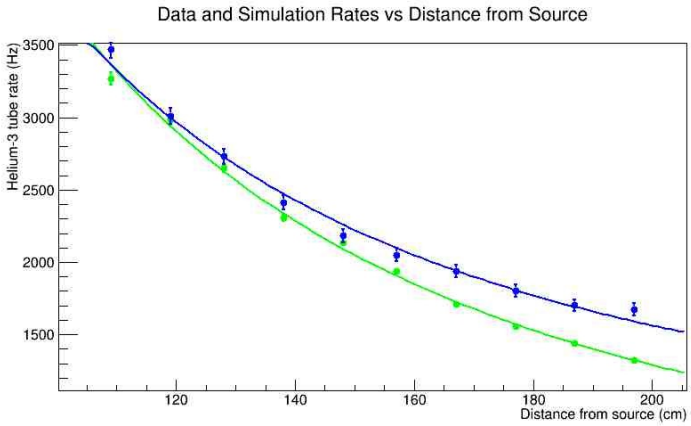

Figure 5.9: Comparison of simulated rates to measured. Simulation in blue, Data in green

5.11 Calibration

In order to finalize the calibration a comparison between the data and simulation is done. The way this is done is by assuming the neutron source behaves roughly as a point source. This means the measured rate at a distance r from the source is given by Equation 5.2 where $\mathcal{E}_t$ is an efficiency correction for a detector, A is the relative strength of the point source, r_0 is a displacement of the source from the assumed location, and B is an additional constant background rate caused by neutron reflections off the walls. The simulation is fit similarly, while constraining A,B, and r_0 to be constant between both data and simulation. As the simulation is lacking the large amount of random equipment scattered around the room an additional background term was added to the fit as seen in Equation 5.3 in an approach suggested by Sam de Jong [18].

$$\text{Rate} = \mathcal{E}_t \left(\frac{A}{(r - r_0)^2} + B \right) \tag{5.2}$$

$$\text{Rate} = \left(\frac{A}{(r - r_0)^2} + B \right) + C \tag{5.3}$$

The comparison between the simulation and the data collected from detector 4 can be seen in Figure 5.9. Only detector 4 was used as its preamplifier was the only one not displaying signs of the previously mentioned damage observed in the other preamplifiers. From detector 4 the fitted efficiency correction is 1.04±0.0003, This is applied to Table 5.4 to obtain the overall efficiency corrections for the other detectors. Table 5.5 shows the final calibrated efficiency corrections.

	$\mathcal{E}$
Detector 1	**0.99 ± 0.02**
Detector 2	**1.07 ± 0.01**
Detector 3	**1.06 ± 0.01**
Detector 4	**1.04 ± 0.0003**

Table 5.5: Detector efficiency corrections. The measured rate in each detector is multiplied by this factor.

5.12 Installation

On Oct.16 2017, the ^{3}He detectors were installed on the backward side of Belle II. The layout of the detectors as well as the other BEAST II detectors in the dockspace space can be seen in Figure 5.10. The position of the dockspaces and how they relate to the rest of Belle II can be seen in Figure 5.11. The calorimeter endcap was inserted and no conflicts with the detector cabling were found. However, during the cable installation from the dock spaces to the electronics racks, three kinks occurred in the data cables. These were not severe and did not have a noticeable effect. On Nov.29 2017, the other two detectors were installed in the forward dockspace, as seen in Figure 5.12. ARICH and the calorimeter endcap were successfully inserted and there were no issues encountered. With the detectors installed the detectors will be referred to by their installed location from here on. Detector 1 is installed on the forward face on the +X side and will be referred to as FWD O (forward and outside), Detector 2 is in the forward -X position so will be called FWD I (forward inner). Detector 3 and 4 are now BWD O and BWD I respectively using the same naming convention.

5.13 Phase 2 Operation

The BEAST II group starting monitoring beam conditions a few weeks before first beam and continued to monitor throughout the Phase 2. During this time period the ^{3}He neutron detectors encountered a few problems which required some modification to the DAQ system. The largest change was the inclusion of a monitoring program that restarted the DAQ in the event of a crash. Other changes were to the running of the DAQ to improve stability. As part of the routine running of the detector system data was grouped into daily summary files. These summary files accounted for the detector efficiencies so the resulting data files are ready for analysis.

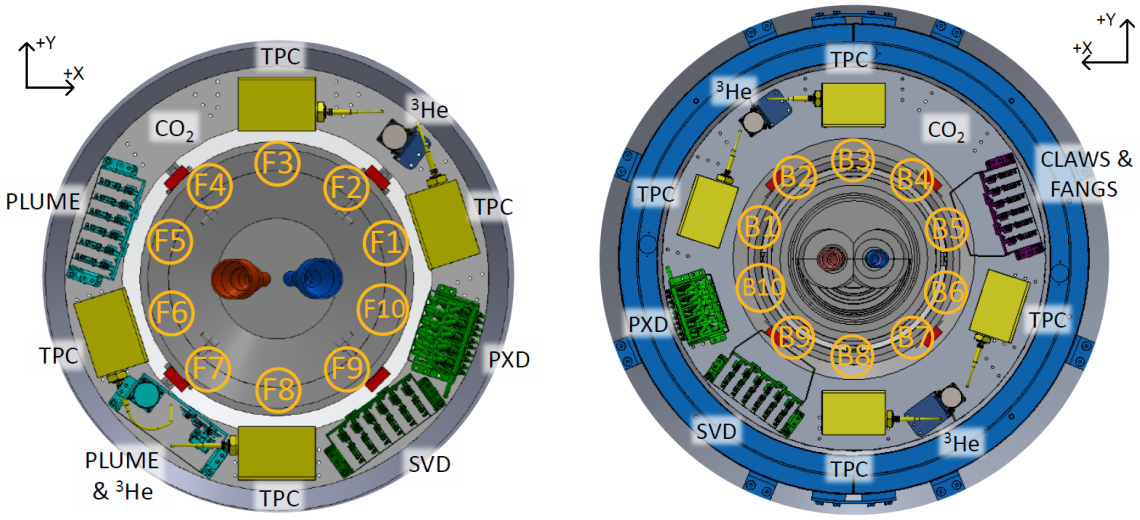

Figure 5.10: Forward (Left) and backward (Right) "dockspace" of Belle II

5.14 Phase 2 Data Analysis

In order to understand how well the Belle II simulations model the beam backgrounds the data collected by the BEAST II detectors were compared to the simulation. Aside from the total rate it is useful to know the production method of the backgrounds and how well each source is modelled by the simulation. In general the BEAST II group assumes the backgrounds are generated via two main sources. First electron-electron (and positron-positron) interactions within a beam bunch causes electrons to be kicked out of the main accelerating volume and lost. This type of background is known as Touschek scattering. Secondly if the beam collides with a gas molecule, bit of dust, or even scrapes the edge of the beampipe some amount of backgrounds can be produced. This is typically referred to as Beam Gas scattering. Equation 5.4 gives the relationship between these two sources and the expected neutron rate. The terms in this equation are I, the beam current; P, the residual pressure in the beamline; Z_{eff}, the average Z of the particles comprising the residual pressure; σ_y, the size of the beam in the y direction; and n_b, the number of electron bunches circulating in the ring. Finally the Touschek term (T) and the beam gas term (B) are condition-dependent scaling factors, these are fitted to give the relative size of the contribution to the total rate.

$$Rate = \frac{T}{\sigma_y n_b} I^2 + B Z_{eff}^2 P I \tag{5.4}$$

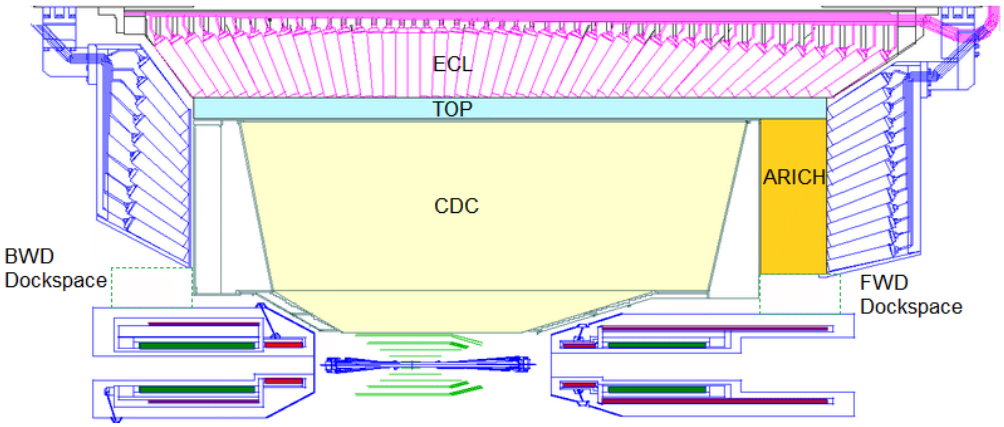

Figure 5.11: Cross-section of Belle II with dockspaces outlined in green dashed lines. KLM not shown[22]

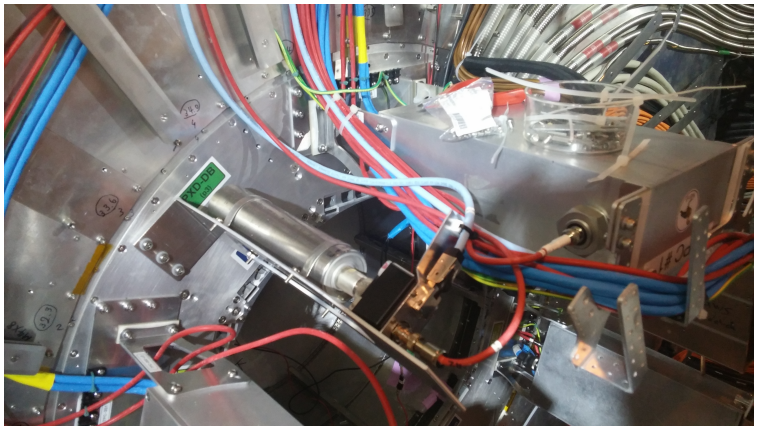

Figure 5.12: Installed ^{3}He Neutron Detector

In order to easily visualize how data collected under different run conditions differs, the BEAST II group employs a fitting method colloquially known as “heuristic". This involves dividing each of the terms in Equation 5.4 by $Z_{eff}^2 IP$ and then performing a linear fit. The resulting equation is shown in Equation 5.5, where T and B become the slope and intercept of the linear fit respectively.

$$\frac{Rate}{Z_{eff}^2 PI} = T\frac{I}{Z_{eff}^2 P\sigma_y n_b} + B \tag{5.5}$$

This method was applied to two different beam studies. The first study was done in June with a certain set of beam conditions known as the 2.1.3 beam optics, the second set was done in July with the 2.1.7 beam optics. During the 2.1.3 studies, the electron ring, also called the High Energy Ring (HER), beam was run at 3 different settings on the emittance control

knob (position 0,+1,and +2). The emittance control should have the effect of increasing the beam size. After the 3 runs the HER was then filled with 1576 bunches as opposed to the usual 789 and the same three runs were completed. For the positron ring, also called the Low Energy Ring (LER), beam the same set of 6 runs was completed. For the 2.1.7 study in July two runs were done with the HER, one at emittance knob position 0 and one at position +1. For the LER, 5 knob positions were tested, knob 0, +0.5, +1, -0.5, -1. Table 5.6 summarizes the runs in chronological order. The results of the heuristic fits are shown in Section 5.15, and follow a similar chronological ordering.

Figures 5.13a to 5.13d show the results for the June 11 data, while most of the data lies near the linear fit the slope results in a negative Touschek component which is non-physical. This is a known issue for other BEAST II detectors as well. Figures 5.14a to 5.14d show the fit for the case when only the knob 0 data is used. For the results reported in Section 5.17 only the knob 0 data was used. Examining the plots for June 12, Figures 5.15a to 5.15d, the fit is much better, but some of the populations are still off the fit. As a quick comparison, the two populations highest on the y axis are from the knob 0 data. Figures 5.16a and 5.16d are from the July 16 HER study and fit the linear model very well, however as there are only two populations this is entirely expected. The non model behaviour in these plots is the horizontal spread of the populations which currently is not well understood. Finally Figures 5.17a to 5.17d show the fits for the July 16 LER study. In the two FWD detectors, the knob 0 position is the uppermost population, while the other knob positions are on the fit line or below. For the BWD detectors the knob 0 positions are centred and extend horizontally. These plots show that the heuristic model is not capturing all of the parameters contributing to the backgrounds. Extensions to the model and a new fitting methodology are discussed in the Section on future work, Section 5.18.

Date	Beam Optics	Primary Beam	Knob	N_b
June 11	2.1.3	HER	0	789
			0	789
			+1	789
			-1	789
			+2	789
			+2	789
			0	1576
June 12	2.1.3	LER	0	789
			0	789
			0	789
			0	789
			+1	789
			-1	789
			+2	789
			+2	789
			0	1576
			+1	1576
			+2	1576
			-1	1576
			-2	1576
July 16	2.1.7	HER	0	789
			+1	789
July 16	2.1.7	LER	0	789
			0	789
			+1	789
			-1	789
			+0.5	789
			-0.5	789

Table 5.6: List of all background runs included in analysis.

5.15 Heuristic Fit Results

5.15.1 June 11 HER 2.1.3 Optics Study

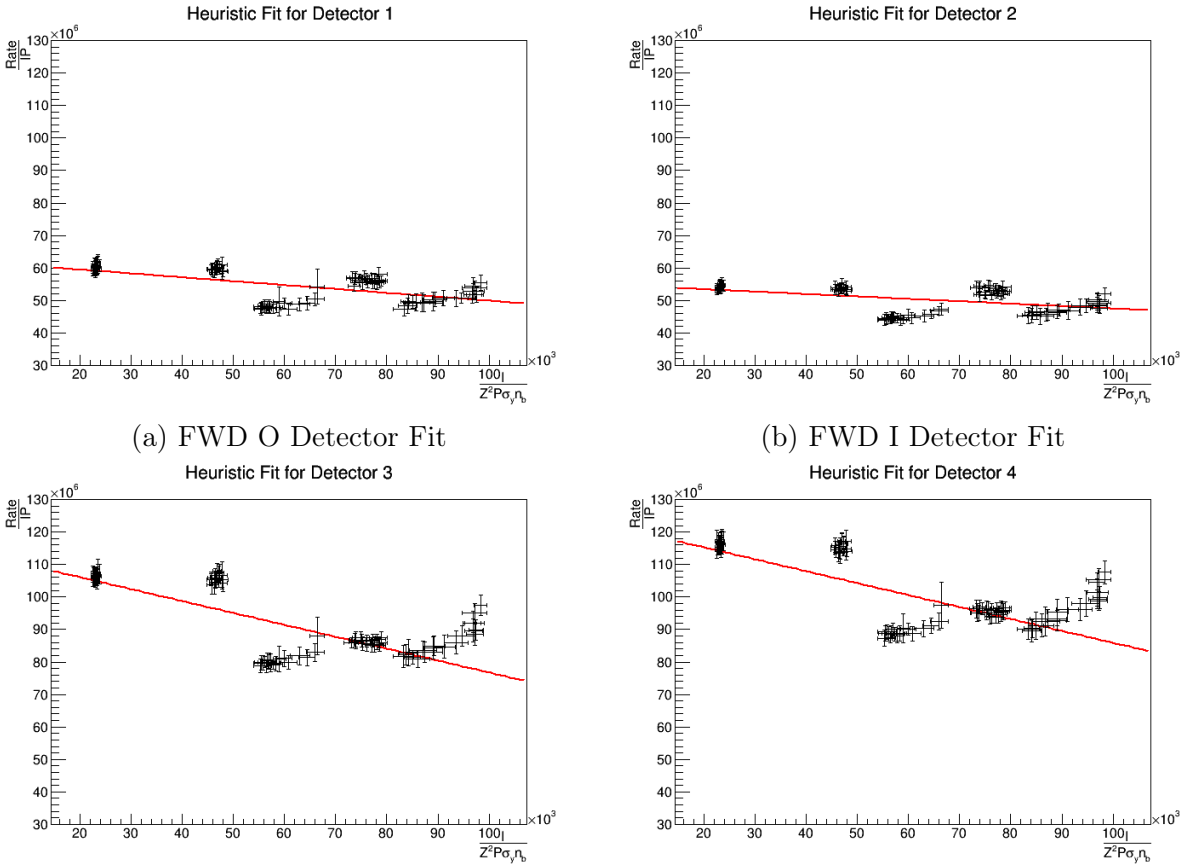

(a) FWD O Detector Fit

(b) FWD I Detector Fit

(c) BWD O Detector Fit

(d) BWD I Detector Fit

Figure 5.13: Heuristic fits for the June 11th HER beam studies.

5.15.2 June 11 HER 2.1.3 Optics Study, Knob 0 Only

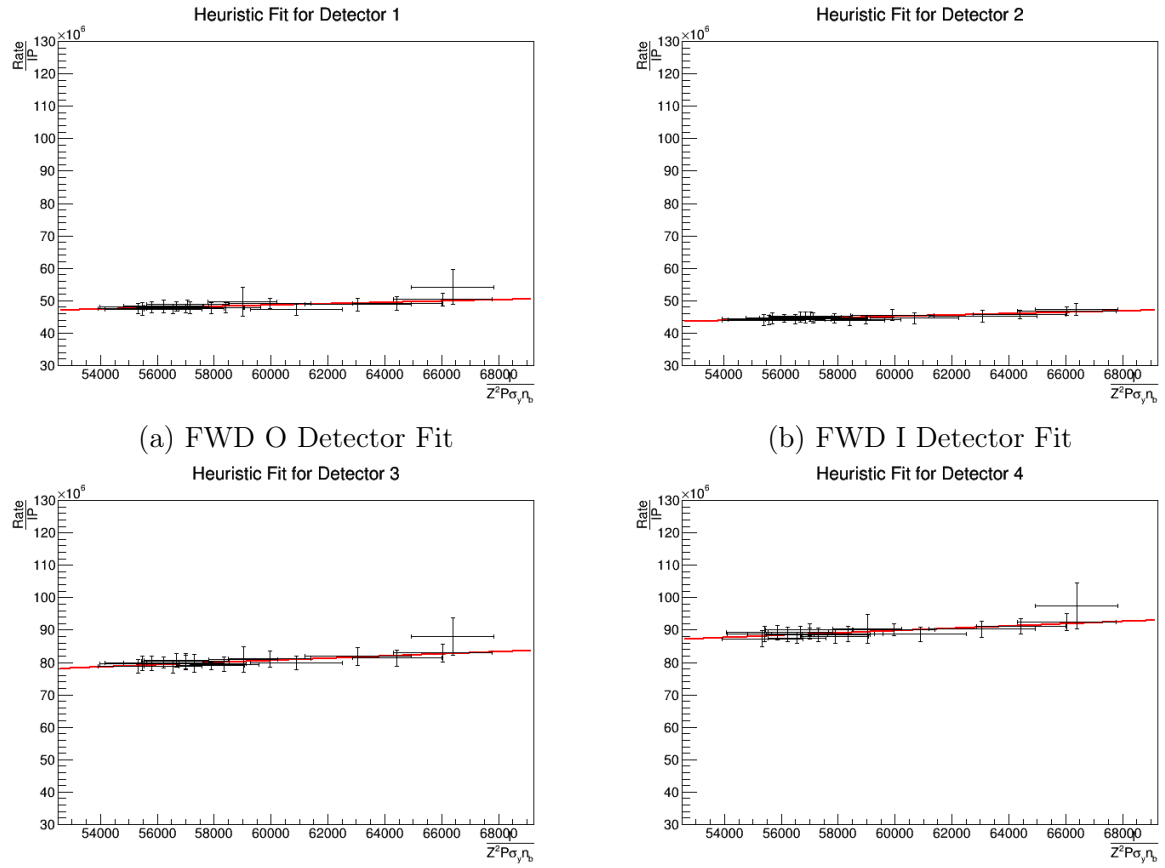

(a) FWD O Detector Fit

(b) FWD I Detector Fit

(c) BWD O Detector Fit

(d) BWD I Detector Fit

Figure 5.14: Heuristic fits for the June 11th HER knob 0 beam studies. The other knob setting cause the inverse slope seen in Figure 5.13.

5.15.3 June 12 LER 2.1.3 Optics Study

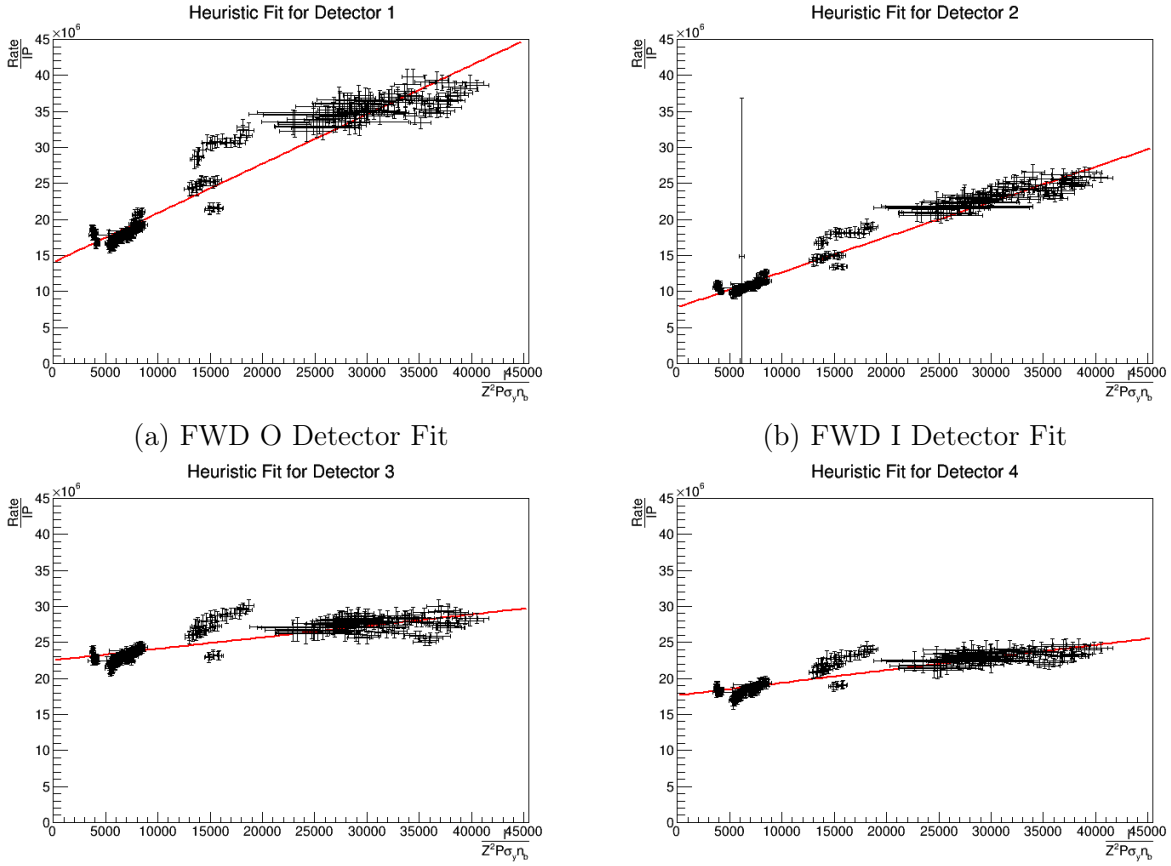

(a) FWD O Detector Fit

(b) FWD I Detector Fit

(c) BWD O Detector Fit

(d) BWD I Detector Fit

Figure 5.15: Heuristic fits for the June 12th LER beam studies.

5.15.4 July 16 HER 2.1.7 Optics Study

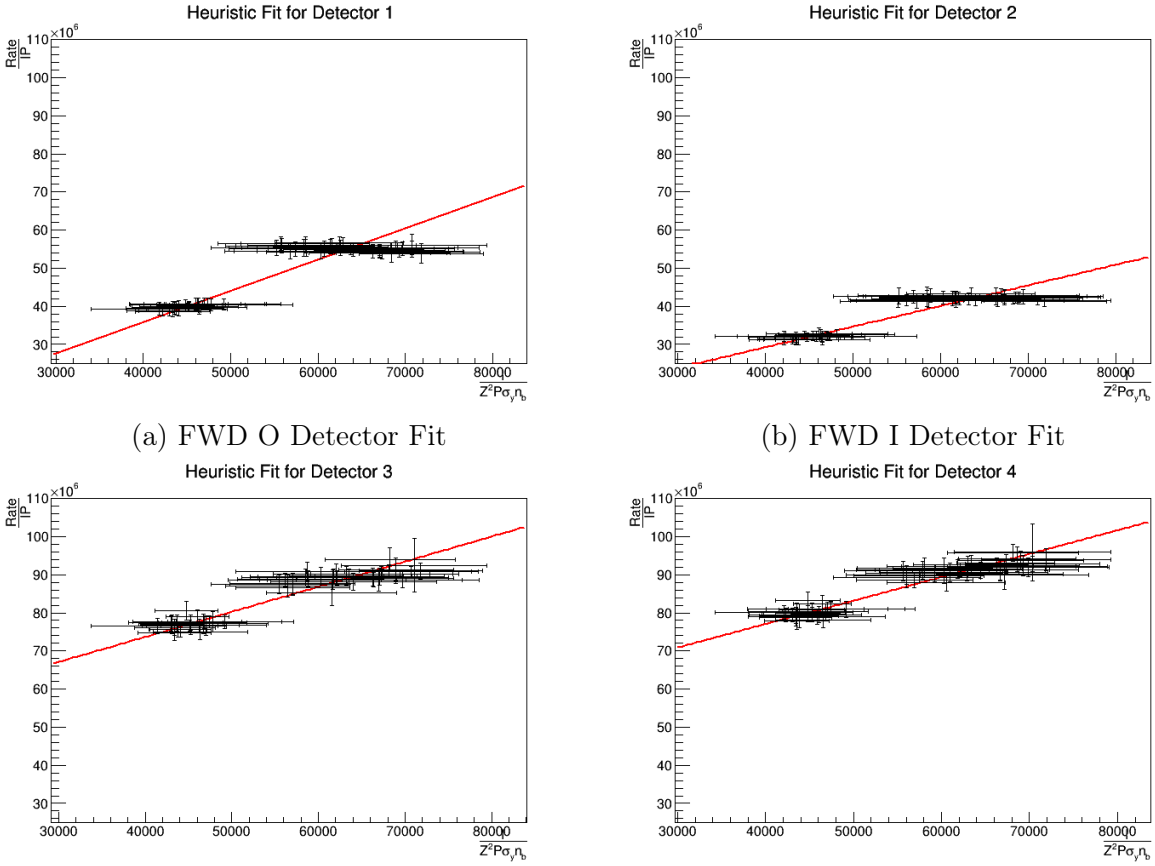

(a) FWD O Detector Fit

(b) FWD I Detector Fit

(c) BWD O Detector Fit

(d) BWD I Detector Fit

Figure 5.16: Heuristic fits for the July 16th HER beam studies.

5.15.5 July 16 LER 2.1.7 Optics Study

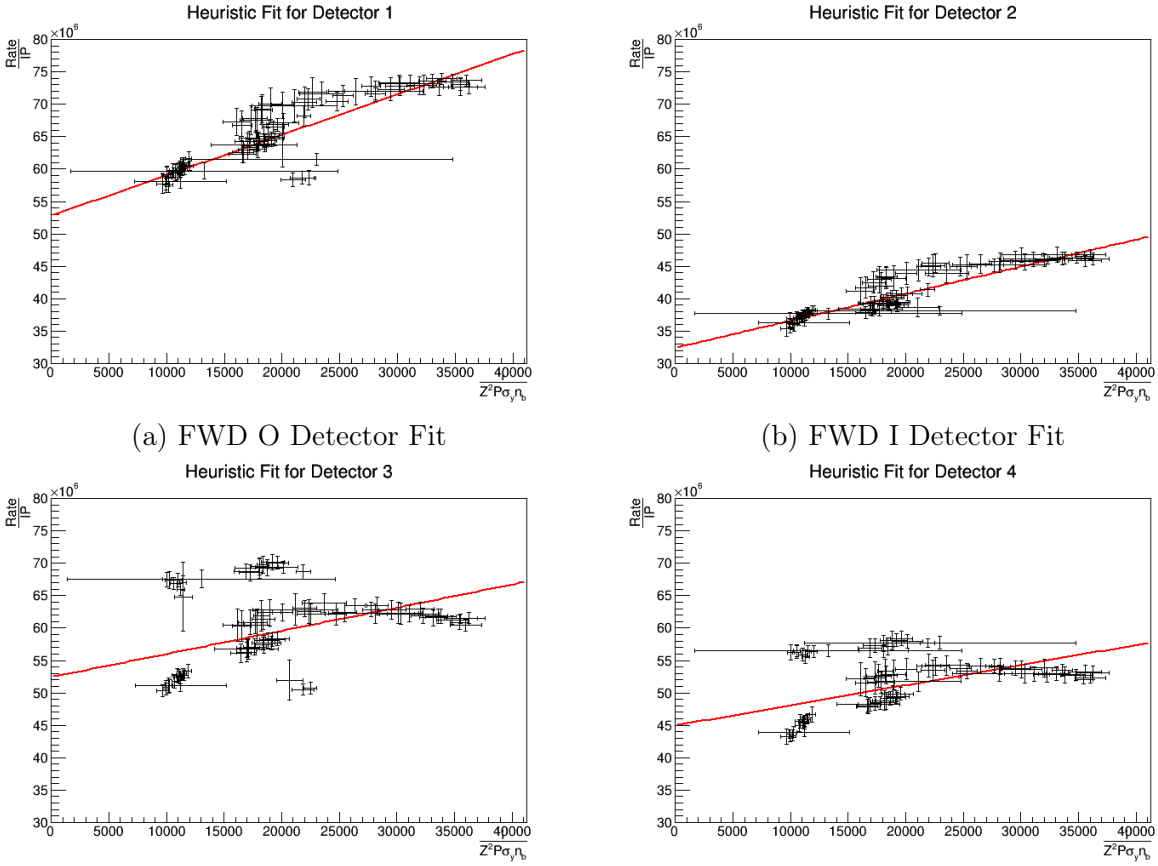

(a) FWD O Detector Fit

(b) FWD I Detector Fit

(c) BWD O Detector Fit

(d) BWD I Detector Fit

Figure 5.17: Heuristic fits for the July 16th LER beam studies.

5.16 Monte Carlo Simulation

The Monte Carlo (MC) simulation generated for the BEAST II analysis was produced in the form of 400 ms of running at one particular set of beam conditions. The MC is also generated in separate files for each of the background sources, i.e. there are separate files produced for backgrounds generated via Touschek scattering and beam gas scattering. This means if Equation 5.4 is assumed to be true, the T and B terms for MC can be directly calculated as shown in Equations 5.6 and 5.7.

$$T = \frac{N_{hits} I^2}{\sigma_y n_b t_{scale}} \tag{5.6}$$

$$B = \frac{N_{hits}}{Z_{eff}^2 I P t_{scale}} \tag{5.7}$$

Where N_{hits} is the number of hits seen by a detector in the MC, and t_{scale} gives the time scale necessary to convert N_{hits} to a neutron rate in Hz

5.17 Final Results

A comparison between the T and B scaling factors for data and MC gives insight into the validity of the MC and allows for predictions of the backgrounds to be made for future SuperKEKB conditions. These ratios, T_{data}/T_{MC} and B_{data}/B_{MC}, are calculated for each run and detector and shown in Tables 5.7 to 5.10. The ratios still vary significantly and is an indication that more work is needed to understand the backgrounds. This work is discussed in Section 5.18. The results from the Phase 2 studies have also been published in the Nuclear Instruments and Methods in Physics Research journal (NIM-A) [23].

2.1.3 HER	T/T_{MC}	B/B_{MC}
FWD O	1.33 ± 1.05	11.79 ± 3.62
FWD I	1.64 ± 0.97	11.06 ± 2.90
BWD O	1.16 ± 0.76	2.98 ± 0.67
BWD I	1.09 ± 0.64	2.66 ± 0.49

Table 5.7: Data over MC ratios from ^{3}He thermal neutron detectors for the June 2.1.3 HER study.

2.1.3 LER	T/T_{MC}	B/B_{MC}
FWD O	1.47 ± 0.09	3.55 ± 0.28
FWD I	0.72 ± 0.04	1.84 ± 0.14
BWD O	0.07 ± 0.00	0.34 ± 0.01
BWD I	0.09 ± 0.00	0.32 ± 0.01

Table 5.8: Data over MC ratios from ^{3}He thermal neutron detectors for the June 2.1.3 LER study

2.1.7 HER	T/T_{MC}	B/B_{MC}
FWD O	3.66 ± 0.60	5.90 ± 9.34
FWD I	2.58 ± 0.44	17.02 ± 10.25
BWD O	4.36 ± 0.81	23.42 ± 4.44
BWD I	3.96 ± 0.75	20.44 ± 3.42

Table 5.9: Data over MC ratios from ^{3}He thermal neutron detectors for the July 2.1.7 HER study

2.1.7 LER	T/T_{MC}	B/B_{MC}
FWD O	1.10 ± 0.09	7.79 ± 0.59
FWD I	0.53 ± 0.04	4.89 ± 0.38
BWD O	0.10 ± 0.01	0.36 ± 0.01
BWD I	0.10 ± 0.01	0.38 ± 0.01

Table 5.10: Data over MC ratios from ^{3}He thermal neutron detectors for the July 2.1.7 LER study

5.18 Improved Fitting Technique

Instead of finding T and B terms from separate runs the fit can be performed for both beams simultaneously. This simultaneous fit is then done by fitting the rate at each second as a function of all of the the parameters. T_{LR} and B_{LR} are then varied to minimize the chi-squared sum of the fit. This fitting method has been tested on the July 16 (2018) data-set as whole and the result can be seen in Figure 5.18. Examining the results shown in this figure allows for some interesting observations. First the beam gas contributions entirely dominate the Touschek contributions, which hints towards why it was difficult to align the data linearly in the heuristic model. Secondly the LER beam backgrounds are much larger than the HER and in the case of the July 16 studies the LER beam case contribution is the second leading background source during the HER study. Finally, while the fit follows the actual rates extremely well there is still some offset from the measured rates.

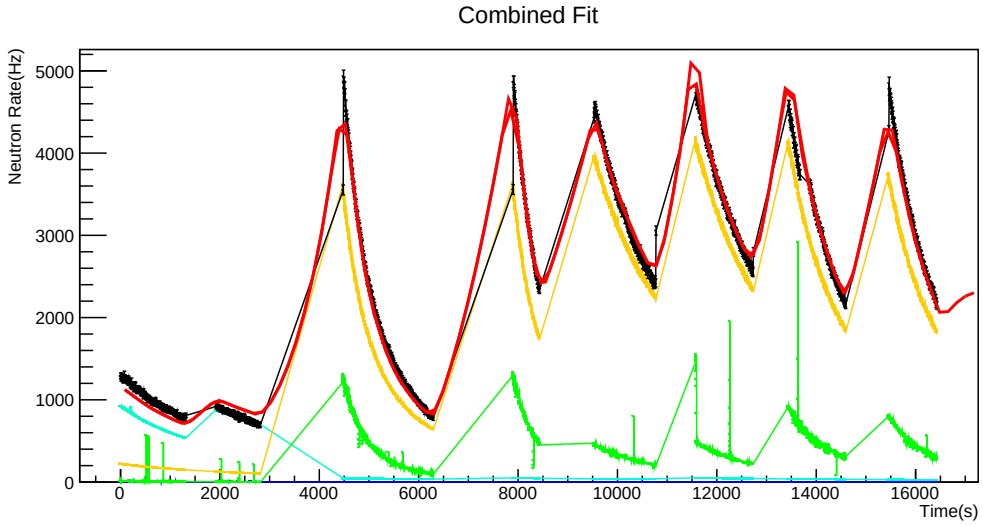

Figure 5.18: Neutron rate vs time from the July 16 beam background study. The two HER studies are on the left. Black is the data, while red is the fitted result. Cyan is the HER beam gas contribution, navy is the HER Touschek contribution, yellow is the LER beam gas contribution, and green is the LER Touschek contribution.

5.19 Phase 3

After the conclusion of Phase 2, the PXD and VXD was installed. These additional detectors required significant space for operation inside the dockspace and the detector and as such most BEAST II detectors were displaced. For Phase 3 ^{3}He detectors shifted to a monitoring

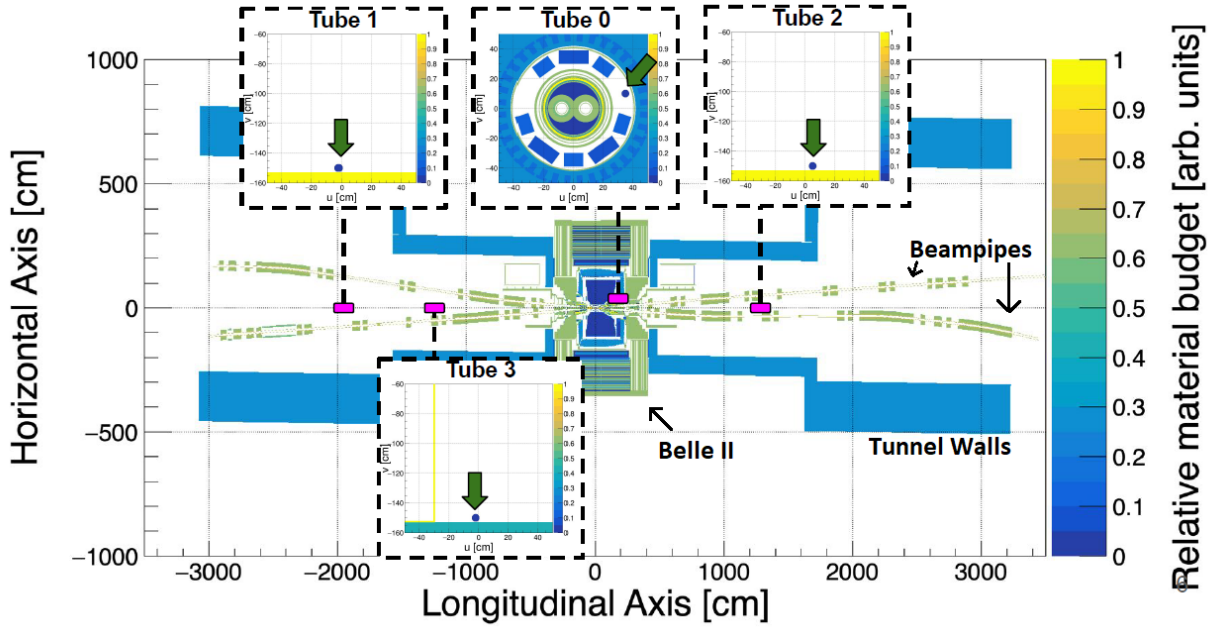

Figure 5.19: Position of ^{3}He detectors for Phase 3, courtesy of Andrii Natochii[24].

role. One detector remained in the dockspace while the other detectors were installed in the beam pipe as shown in Figure 5.19. The Phase 3 analysis of neutron rates has been carried out by the Belle II background group and the results contribute to the recent Phase 3 paper, currently in peer review[25].

5.20 Conclusions

The ^{3}He thermal neutron detectors continue to provide a valuable source of information on beam backgrounds around Belle II. The work in this dissertation has resulted in two publications including information collected by the detectors. The published figures displaying the data/MC agreement for the phase two detectors is shown in Figures 5.20 and 5.21. As Belle II continues to develop and upgrade the ^{3}He thermal neutron detectors will continue to be supported by UVic and provide Belle II with a valuable tool to monitor neutron radiation dosage and beam backgrounds.

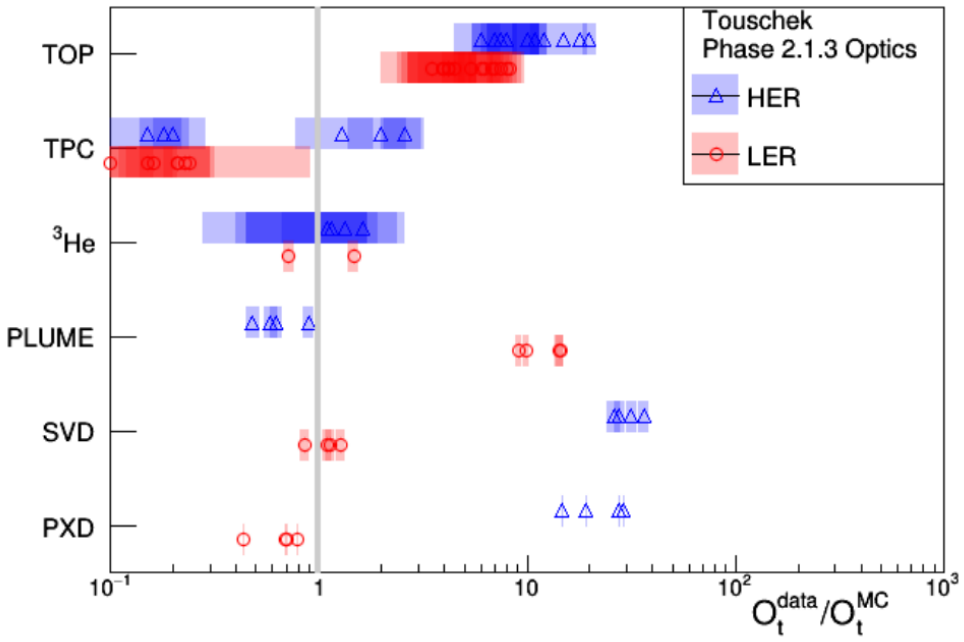

Figure 5.20: Agreement between data and MC in the Touschek parameter after simulation improvements resulting from the phase 2 studies[23].

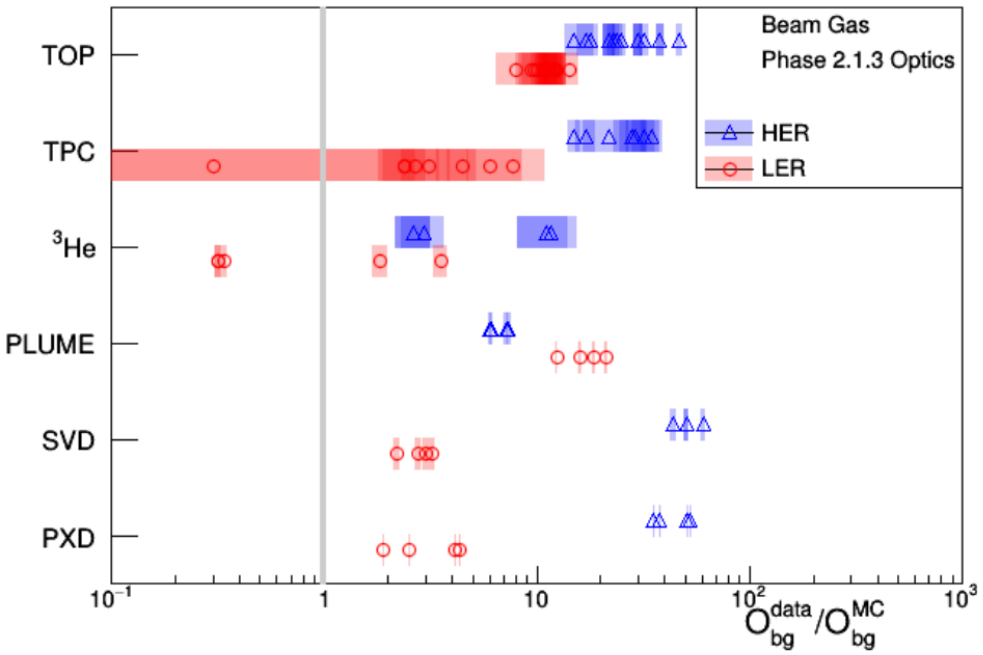

Figure 5.21: Agreement between data and MC in the beam-gas parameter after simulation improvements resulting from the phase 2 studies[23].

Chapter 6

Development of Tau Polarimetry Techniques at *BABAR*

6.1 Motivation

One of the highly active fields in modern physics is precise measurements of parameters of the Standard Model(SM). Deviations from the SM predicted values could be signs of new physics, which could significantly improve our ability to understand the universe. The Belle II experiment is currently operating in this "precision frontier" and the proposed Chiral Belle upgrade to polarize the electron beam of the accelerator would extend the physics reach. For many of these new measurements the precision is expected to be limited by how well the average beam polarization present in the collisions is known. This chapter will discuss the development of the concept of Tau Polarimetry, a technique for precisely measuring the beam polarization using the $e^+e^- \to \tau^+\tau^-$ process, and the initial proof of concept testing done with the unpolarized *BABAR* data. The longitudinal beam polarization in *BABAR* data is expected to be near zero due to the beam rings at PEP-II being unsuited to build up transverse polarization, with less than 0.8% transverse polarization expected. Even if a polarized beam were to be injected into the HER, it would depolarize in a time < 1.5 minutes[26]. If no transverse polarization exists in PEP-II, no longitudinal polarization is present either. In addition there was no effort to introduce polarized beams to PEP-II. This Chapter covers the initial efforts to understand and develop a selection of $\tau^\pm \to \pi^\pm \overline{\nu}_\tau$ decays to extract polarization from. The $\tau^\pm \to (\rho^\pm \to \pi^\pm\pi^0)\overline{\nu}_\tau$ decay is found to be the best tag for these decays and this Chapter further discusses the effort put into understanding the systematic uncertainties associated with the selection. In the end the selection was found to have an uncontrolled bias and the analysis shifted to a $\tau^\pm \to (\rho^\pm \to \pi^\pm\pi^0)\overline{\nu}_\tau$ signal selection which is the focus of Chapter 7.

6.2 Tau Polarimetry at 10.577 GeV

The core concept behind Tau Polarimetry is a coupling between the τ polarization and the kinematics of its decay products. Examining techniques developed by the LEP experiments to measure the τ polarization[27], and assuming the τ neutrino helicity is its SM predicted value of -1 (Only experimentally constrained to -0.985±0.030), the techniques can be extended to extract the beam polarization instead. For e^+e^- collisions at 10.577 GeV, the polarization of τ's produced can be expressed as[28]:

$$P_\tau = P_e \frac{\cos\theta}{1+\cos^2\theta} - \frac{8G_F s g_V^\tau}{4\sqrt{2}\pi\alpha}\left(g_A^\tau \frac{|\vec{p}|}{p^0} + 2g_A^e \frac{\cos\theta}{1+\cos^2\theta}\right) \tag{6.1}$$

Where P_ℓ is the polarization of the final state τ or initial state electron, G_F is the Fermi constant, s is the square of the centre-of-mass energy, α is the fine structure constant, $g_{V,A}^\ell$ are the neutral current vector and axial couplings respectively, $|\vec{p}|$ is the magnitude of the 3-momentum of the τ^- and p^0 is the energy of the τ^-, finally $\cos\theta$ is the angle between the e^- beam momentum direction and the momentum of the τ^-.
Coupling this with the kinematic dependence of τ decay products to the τ polarization state allows the average beam polarization to be extracted. The polarization-kinematic relationship can be mostly easily seen from the $\tau^\pm \to \pi^\pm \overline{\nu}_\tau$ decay, as the two body nature of the decay simplifies the process. Figure 6.1 shows the correlation between the spin of the τ and the momentum of the final state pion. Assuming a sample of 100% polarized

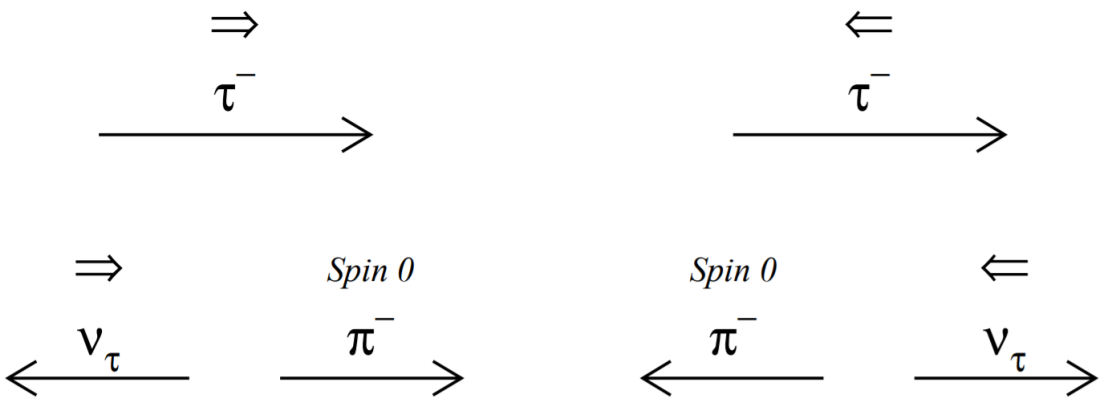

Figure 6.1: Relationship between τ helicity and pion momentum[29]. Momentum dependence reverses with spin as well as charge.

τ particles can be obtained, the momentum distributions for the final state pions is quite distinct, as shown in Figure 6.2. Of the possible fermion pairs, τ pairs are the best option

to extract beam polarization. This is due to the relatively low multiplicity decays and the short lifetimes allowing the kinematics of the decay products to be examined.

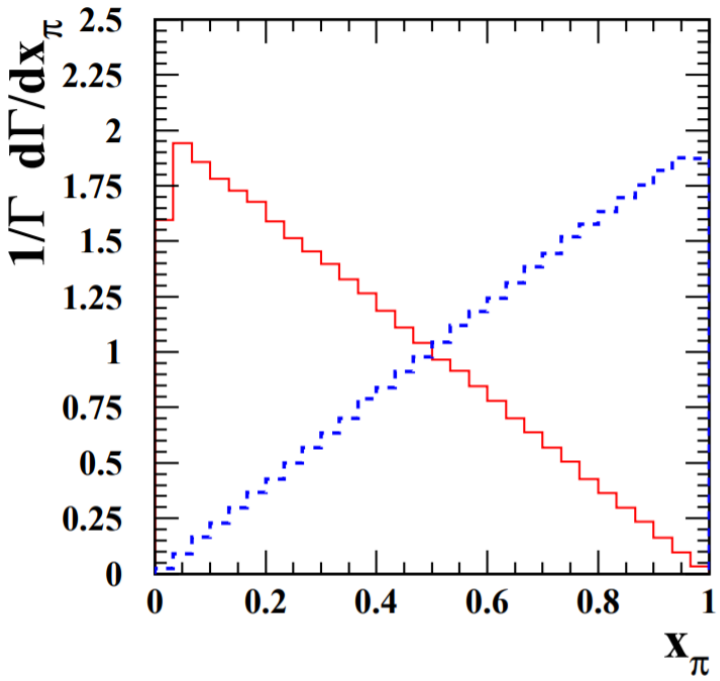

Figure 6.2: Scaled cross-section vs. x (p/E_{beam}) for producing a pion at each fraction of the available energy. The line in red represents lower momentum pions from either a left-handed τ^- or a right-handed τ^+. The blue line is for the right-handed τ^- or left-handed τ^+.[29]

6.2.1 Polarization Definition

The average τ polarization, $\langle P_\tau \rangle$, is given by Equation 6.2,

$$\langle P_\tau \rangle \equiv \frac{\sigma_+ - \sigma_-}{\sigma_+ + \sigma_-} \tag{6.2}$$

where σ_+ represents the cross-section for producing positive helicity τ^- leptons and σ_- those of negative helicity.

6.3 Tau Polarimetry via $\tau\tau \to \pi\nu\pi\nu$

The simplest τ decay to study beam polarization is through the $\tau^\pm \to \pi^\pm \overline{\nu}_\tau$ decay channel. This is primarily due to the two body nature of the decay. As the neutrino must carry off the spin information and only left handed neutrinos exist under the SM assumption, the

momentum of the pions is biased higher or lower depending on the τ polarization. The relationship between the τ polarization and the pion momentum is shown in Equation 6.3.

$$\frac{1}{\Gamma}\frac{d\Gamma}{dx_\pi} = 1 + \mathcal{P}_\tau(2x_\pi - 1) \tag{6.3}$$

The scenario where both τ particles decay to pions is a "golden" mode for the analysis. This is because of the correlation present between the two pions, if one pion is high momentum the other is significantly more likely to also be high momentum. This can be seen in Figures 6.3 and 6.4 which shows the momentum distribution of a pion when the other pion in the event is high or low energy. This correlation allows for the excellent tagging of τ helicity states and assuming a pure sample is obtained, a purely data-driven method for measuring the polarization.

6.3.1 $\tau\tau \to \pi\nu\pi\nu$ *BABAR* Monte Carlo study

In order to begin studying the polarization-kinematic relationships in the $\tau^\pm \to \pi^\pm\overline{\nu}_\tau$ decay mode the MC truth unpolarized *BABAR* $\tau^+\tau^-$ MC is studied. The *BABAR* MC contains two levels of information, the most precise level, "truth", gives the exact simulated event. The second level, "reconstructed", undergoes a detector simulation to model the *BABAR* detector response and attempts to be indistinguishable from real data. While the correlations are strong in MC truth, reconstructed MC must be studied to ensure the correlations survive real world conditions. The first step taken with the Monte Carlo analysis was to reproduce Figure 6.2 with the *BABAR* MC truth information. To do this the pions were split into energy bins of 1 GeV in size, and normalized by the beam energy (x$\equiv E_\pi/E_{\text{beam}}$). The normalized energy distribution of each pion was then plotted based on the energy of the other pion in the event (tag pion). When one of the pions is in the low energy bin the other pion has the energy distribution shown in Figure 6.3 and when the pion is in the high energy bin Figure 6.4 shows the other pions energy distribution. These distributions are highly linear and fitting the slopes produces the polarization shown in Table 6.1. In addition to the distributions formed with high and low energy tag pions, distributions at multiple intermediary tagging energies can also be made. The mean energy of the pions tagged by each slice in energy demonstrate a correlation between the pion energies. This correlation is shown in Figure 6.5 as well as the correlation between pions from different events. Since this results in a flat line the difference between the correlated and uncorrelated pions gives a method to determine how much sensitivity the data has to the polarization.

		$\mathcal{P}_\tau$
Negative Helicity Tau	π^+	-1.1±0.3
	π^-	-1.1±0.3
Positive Helicity Tau	π^+	0.9±0.2
	π^-	0.8±0.2

Table 6.1: Polarization extracted from the slopes of the pion distributions, as described by Eqn. 6.3.

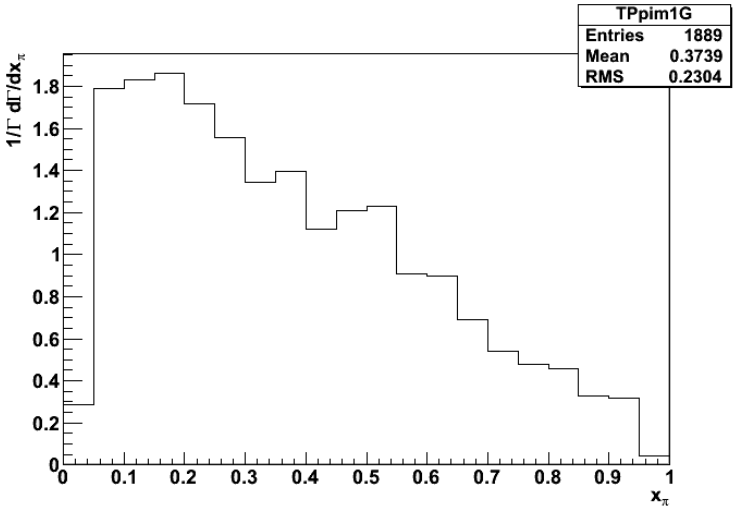

Figure 6.3: Energy distribution of the π^- for the opposing τ decay's π^+ having a low energy (< 1 GeV) from truth MC.

6.3.2 *BABAR* Reconstructed MC $\tau\tau \to \pi\nu\pi\nu$ Selection Criteria

With the expected behaviour verified with the truth MC a selection is defined for the reconstructed $\tau^+\tau^-$ MC to attempt to select only $\tau^\pm \to \pi^\pm\overline{\nu}_\tau$ decays from all $\tau^+\tau^-$ decay modes. To begin selecting τ-like events a list of charged particles from DCH tracks is generated. These tracks were required to be within 1.5cm of the beam spot in the XY plane and 2.5 cm on the Z axis, as determined by the *BABAR* tracking algorithms. τ-like events were then selected by requiring the τ background filter (BGFTAU) to trigger. *BABAR* tagged events with various filters designed to reduce backgrounds in B meson studies. The BGFTAU filter attempted to tag τ-like events by requiring a final state in which two charged particles were detected within the EMC acceptance (-0.74$<\cos\theta_{\rm Lab}<$0.92) and the particles have opposite charges. The two charged particles were then required to have less than 10 GeV of total momentum ($|\vec{p}_1^{\rm CM}|+|\vec{p}_2^{\rm CM}| < 10$ GeV. Next a cut of $(|\vec{p}_1^{\rm CM}|+|\vec{p}_2^{\rm CM}|)_\perp/(\sqrt{s}-|\vec{p}_1^{\rm CM}|-|\vec{p}_2^{\rm CM}|) > 0.02$ was imposed on the transverse momentum (momentum perpendicular to the beam axis). The

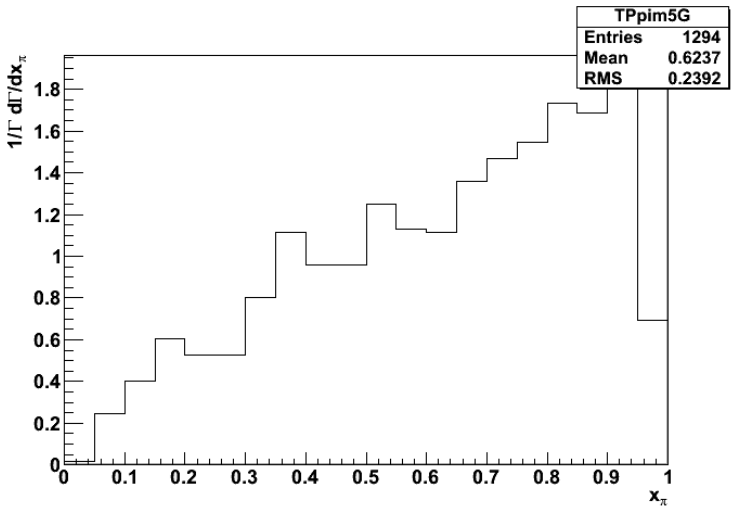

Figure 6.4: Energy distribution of the π^- for the opposing τ decay's π^+ having a high energy (> 4.43 GeV) from truth MC.

particles are further required to have an acollinearity (opening angle between tracks in CM frame) of at least 100 mrad and deposit 8.5 GeV of energy in the calorimeter. Finally the particles had further angular cuts based on the charge on the particle, namely: $\cos\theta_+^{\rm Lab} > 0$ and $\cos\theta_-^{\rm Lab} < 0.7$. More details of the BGFTAU distributions are available in the internal *BABAR* document BAD #1265[30]. With this definition of τ-like events selected, a list of neutral particles, primarily photons, was generated in order to study any neutral backgrounds/contamination. These neutral particles were required to deposit at least 30 MeV of energy in the calorimeter and have maximum lateral moment of 0.8 in order to be in the list. With these definitions in place for charged and neutral particles a selection criteria for $\tau^\pm \to \pi^\pm \overline{\nu}_\tau$ -like events was applied. First a geometric cut was applied requiring all charged particles to be in the barrel of the calorimeter. This can be seen in Figure 6.6. This cut could be loosened in the future but improved purity for this analysis. Next, the tracks must be separated by an angle of at least 90° in the CM frame. Each track must deposit at least 50 MeV of energy in the EMC. Finally a multi-step cut is placed on the neutral EMC clusters. If a neutral cluster had more than 200 MeV of energy the event is discarded. If a neutral cluster had less than 50 MeV of energy it is ignored. If a neutral cluster is between these energies a cut is placed on its distance from a charged track. If the neutral was within 40 cm of the charged track its energy was added to the charged particle's energy. If the neutral is greater than 40 cm from the track the event was also discarded. Finally, the *BABAR* particle identification systems were used to identify both tracks as pions and also identify them as not muons or electrons. *BABAR* has separate identification requirements for each kind of particle,

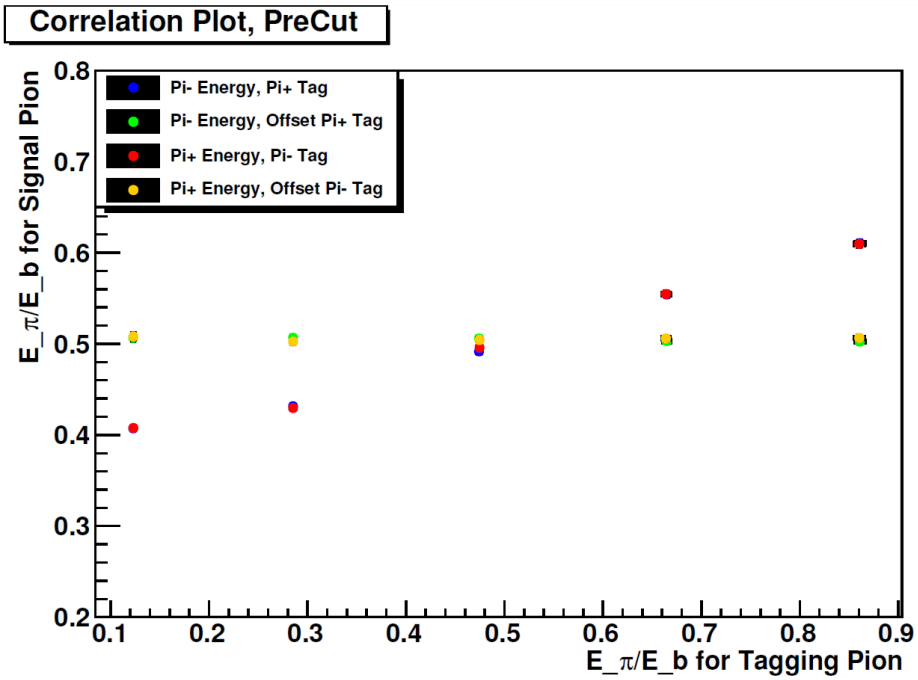

Figure 6.5: Energy correlation between truth MC pions from the same event or from an uncorrelated event, labeled 'offset'.

so it's possible for a track to be identified as both a pion and a muon. The efficiency of these selectors can be seen in Appendix A. With this initial selection a signal purity of 56% was achieved. The cuts are summarized in the following list:

1. From a MC sample of $e^+e^- \to \tau^+\tau^-$ the GoodTracksVeryLoose list is selected
2. The GoodPhotonLoose list is used for neutral clusters
3. The event is tagged by the BGFTAU filter
4. In the analysis the following requirements are made:
   (a) The event must have only two charged tracks
   (b) Both tracks must deposit at least 50 MeV in the EMC
   (c) Each charged track must be in the barrel of the detector(-0.76< $\cos\theta$ <0.80)
   (d) The two charged tracks must be at least 90° apart
   (e) If a neutral has less the 50 MeV in energy it is ignored
   (f) If a neutral has more than 200 MeV the event is discarded

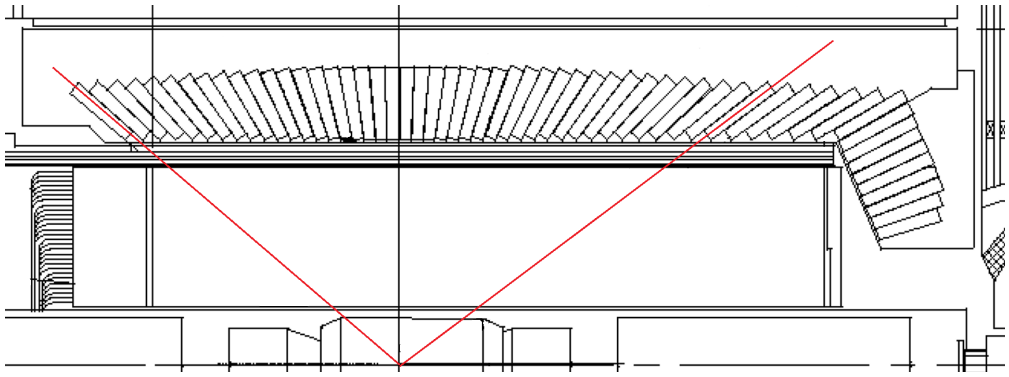

Figure 6.6: Angle of track acceptance for $\tau^{\pm} \to \pi^{\pm}\overline{\nu}_{\tau}$ study in the *BABAR* EMC.

(g) If a neutral is between 50 and 200 MeV:

- If the neutral is within 40cm of a charged EMC cluster the energy is added to the charged particle
- if the neutral is farther away than 40cm the event is discarded

(h) Each track must be identified as a pion and not a muon or electron by the BaBar PID selectors

- For Pions: VeryTightLHPionMicroSelection
- For Muons: BDTVeryLooseMuonSelectionFakeRate
- For Electrons: SuperLooseKMElectronMicro

6.3.3 Reconstructed MC Selection Analysis

Applying the selection criteria laid out in Section 6.3.1 reduces the number of pion pairs that can be plotted and introduces some slight biases to the distributions. This is seen in Figures 6.7 and 6.8, and the correlation plot Figure 6.9. The main reason to apply many of these cuts is to reduce a background which can be misidentified as an event with two pions. Table 6.2 shows the distribution of charged particle pairs selected from the $\tau^+\tau^-$ MC while Table 6.3 shows the overall fraction of which each charged particle appears in the selected $\tau^+\tau^-$ MC events. Adding in these backgrounds produced from other τ decay paths gives the results seen in Figures 6.10 and 6.11, while Figure 6.12 shows the surviving polarization correlation. The other major source of background is the $e^+e^- \to \mu^+\mu^-$ production mode. Muons are somewhat difficult to distinguish from pions and when treated to the same selection criteria as the τ backgrounds the surviving muons are biased towards the high energy regime. This can be seen in Figures 6.13 and 6.14.

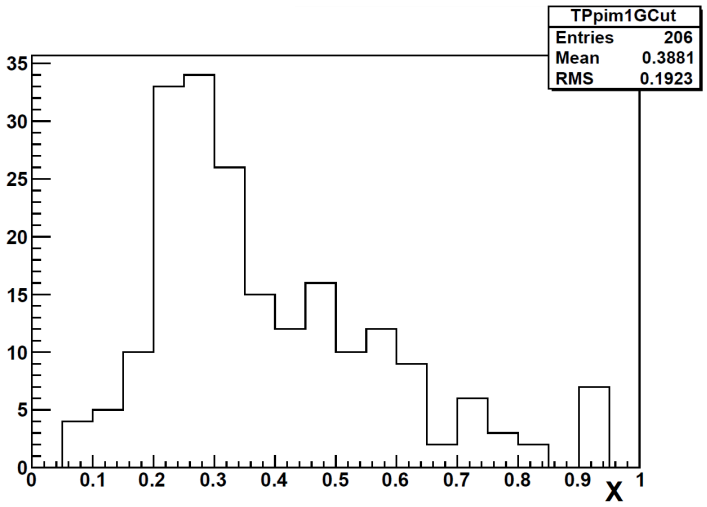

Figure 6.7: Energy distribution of the π^- for the opposing τ decay's π^+ having a low energy (< 1 GeV) from truth MC after $\tau^\pm \to \pi^\pm \overline{\nu}_\tau$ event selection.

τ decay	e	μ	π	ρ	a_1	other
e	233					
μ	621	520				
π	548	1325	889			
ρ	643	850	839	431		
a_1	108	125	64	82	14	
other	366	416	338	445	52	133

Table 6.2: Number of final states for each τ-pair decay mode selected by the $\pi - \pi$ selection.

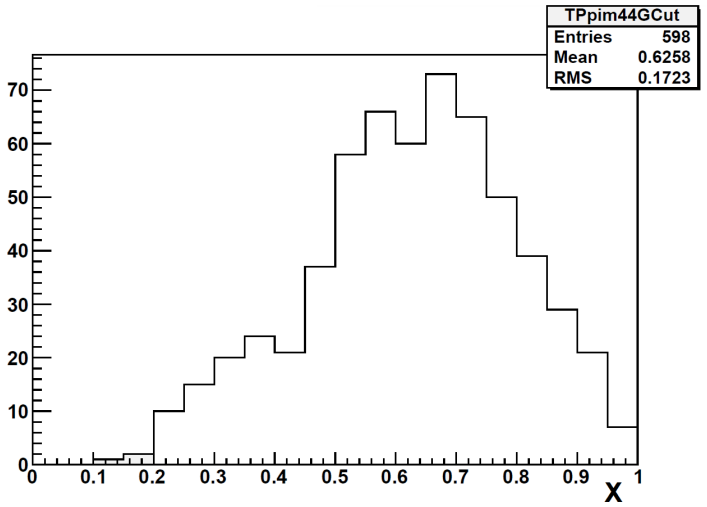

Figure 6.8: Energy distribution of the π^- for the opposing τ decay's π^+ having a high energy (> 4.43 GeV) from truth MC after $\tau^\pm \to \pi^\pm \overline{\nu}_\tau$ event selection.

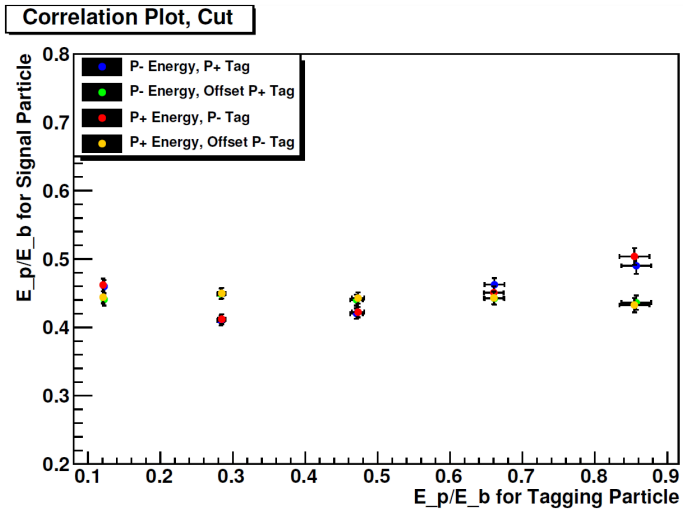

Figure 6.9: Energy correlation between pions from truth from the same event or from an uncorrelated event, labeled 'offset' after $\tau^{\pm} \to \pi^{\pm}\overline{\nu}_{\tau}$ selection.

τ decay	Fraction
e	27.89%
μ	42.71%
π	54.16%
ρ	36.43%
a_1	4.36%
other	19.26%

Table 6.3: Fraction of final states which include the given particle type.

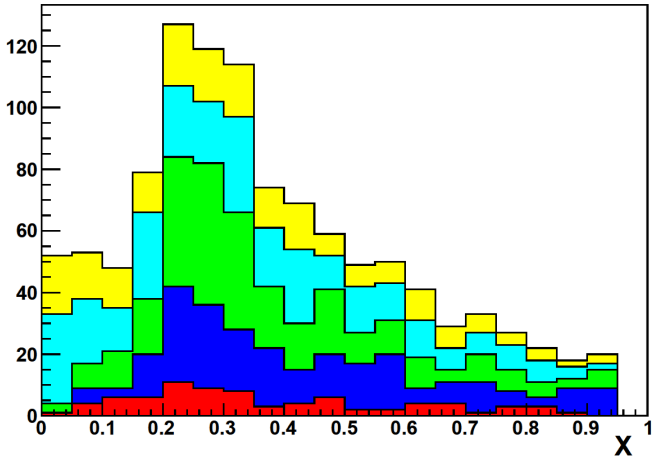

Figure 6.10: Energy distribution of selected π^- from $\tau^+\tau^-$ MC for low energy π^+ tag (< 1 GeV). Selection purity broken down by truth information resulting in the following colours. Red:$\tau^\pm \to e^\pm \nu_e \overline{\nu}_\tau$, blue:$\tau^\pm \to \mu^\pm \nu_\mu \overline{\nu}_\tau$, green:$\tau^\pm \to \pi^\pm \overline{\nu}_\tau$, cyan:$\tau^\pm \to (\rho^\pm \to \pi^\pm \pi^0)\overline{\nu}_\tau$, yellow:other.

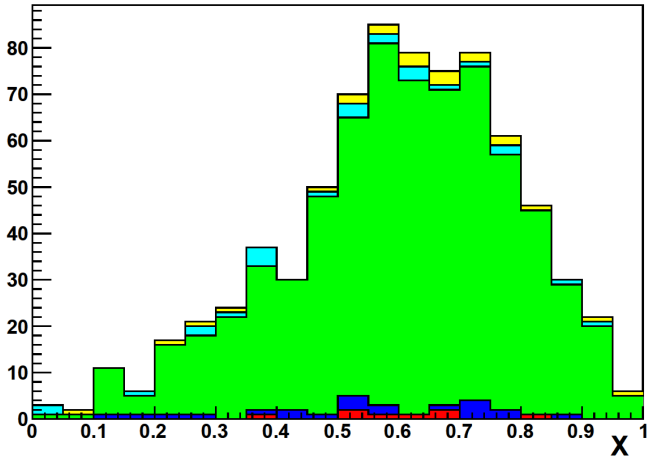

Figure 6.11: Energy distribution of selected π^- from $\tau^+\tau^-$ MC for high energy π^+ tag(> 4.43 GeV). Selection purity broken down by truth information resulting in the following colours. Red:$\tau^\pm \to e^\pm \nu_e \overline{\nu}_\tau$, blue:$\tau^\pm \to \mu^\pm \nu_\mu \overline{\nu}_\tau$, green:$\tau^\pm \to \pi^\pm \overline{\nu}_\tau$, cyan:$\tau^\pm \to (\rho^\pm \to \pi^\pm \pi^0)\overline{\nu}_\tau$, yellow:other.

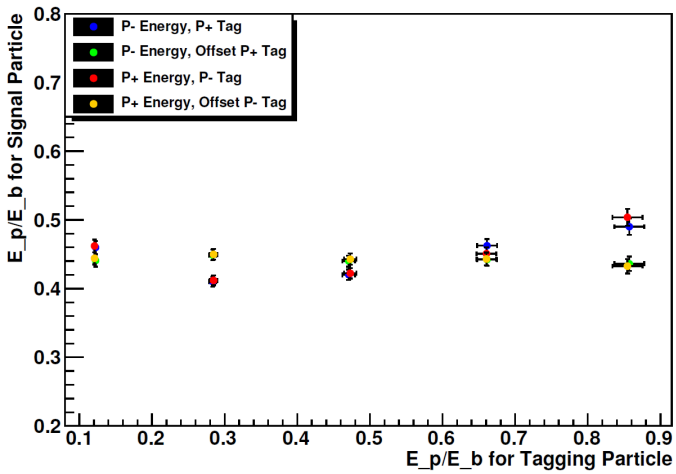

Figure 6.12: Energy correlation between 'pions' from the $\tau^{\pm} \to \pi^{\pm}\overline{\nu}_{\tau}$ selection criteria from the same event or from an uncorrelated event, labeled 'offset'. In the full $\tau^{+}\tau^{-}$ MC correlations barely survive selection.

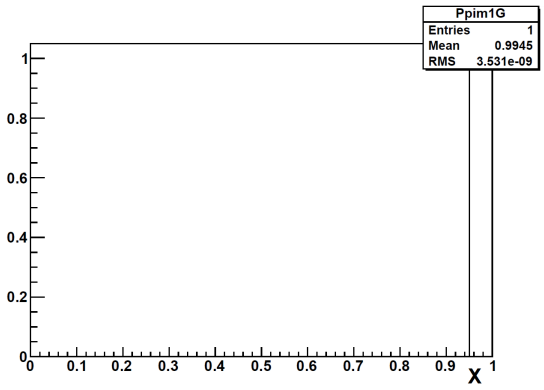

Figure 6.13: Muons from the $e^{+}e^{-} \to \mu^{+}\mu^{-}$ process selected by the $\tau^{\pm} \to \pi^{\pm}\overline{\nu}_{\tau}$ criteria. Energy distribution for a low energy tag 'pion' (< 1 GeV).

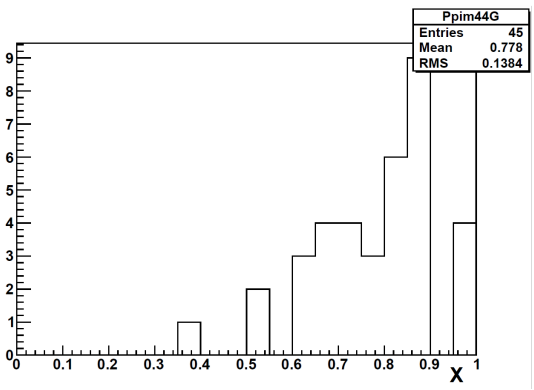

Figure 6.14: Muons from the $e^{+}e^{-} \to \mu^{+}\mu^{-}$ process selected by the $\tau^{\pm} \to \pi^{\pm}\overline{\nu}_{\tau}$ criteria. Energy distribution for a high energy tag 'pion' (> 4.43 GeV).

6.4 Machine Learning Tests

As the $\tau^+\tau^- \to \pi\nu\pi\nu$ events make up only 10% of the selection and the majority of backgrounds arise from muons, we investigated the use of machine learning to improve pion-muon separation. To implement this we made use of the TMVA package contained within ROOT. A subset of variables was chosen to give to the boosted decision tree (BDT) algorithm. From

BDT Training Variables	
EMC energy	Lateral Momentum
DOCA	SVT hits
DCH hits	IFR hits
Electron Micro PID Selector	Electron KM PID Selector
Muon BDT PID Selector	Muon NN PID Selector
Pion GLH PID Selector	Pion KM PID Selector
Invariant Mass of Hemisphere	Invariant Mass of Neutrals
Total EMC energy of Neutrals	π^0 likelihood

Table 6.4: List of variables used in TMVA BDT training.

these variables we train 3 separate BDTs. One for separating muons and pions, one for separating electrons and pions, and one for separating pions and other hadronic τ decays. The TMVA BDT implementation used required continuous variables to train correctly, while the PID selector's are binary. Within each selector included in the BDT there are four included binary variables. These sub-selectors are named VeryTight, Tight, Loose, and VeryLoose and refer to the strictness of their respective selections. To make a pseudo-continuous variable we assign each sub-selector a fractional value of 1/2, 1/4, 1/8, 1/16 respectively and sum the passed selectors to give each event a value between 0 and 1. This allows the BDT to vary the acceptance continuously. Figures 6.15 to 6.17 show the BDT separation as a function of BDT cut. After maximizing the event purity it was realized the BDT selection can significantly bias the momentum and angular distributions. The purity achieved was also found to be similar to the performance of the existing *BABAR* selectors. Rather than worry about systematic uncertainties in all the variables included in the BDT training it made more sense to continue using only the already defined PID selectors. As the $\pi - \pi$ selection is overwhelmed by backgrounds to the point where the momentum slope can no longer be extracted, a new approach is needed. The initial $\tau^\pm \to \pi^\pm \overline{\nu}_\tau$ analysis already discussed was performed on a small subset of MC, going forward the framework to use the full *BABAR* MC has been setup, and other τ decay modes can be investigated.

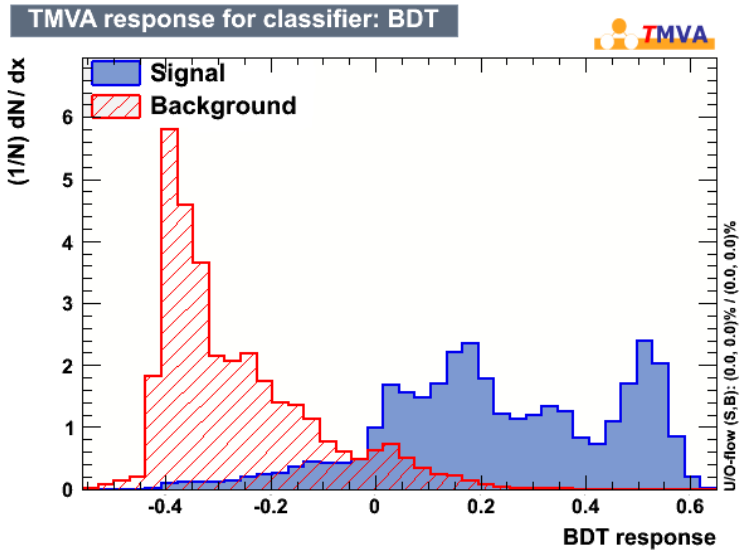

Figure 6.15: Separation of muons (Background) and pions (Signal) as a function of BDT cut value.

6.5 *BABAR* Data and MC definitions

In order to avoid introducing analyst bias a blind analysis approach is undertaken to develop Tau Polarimetry. The *BABAR* data are broken into chronological subsets known as Runs and the *BABAR* Run 3 data are used as a study sample to check the validity of the MC, develop the polarization fitting algorithm, and define the systematic uncertainty evaluation process. The absolute size of the *BABAR* data sets are summarized by run in Table 6.5. This analysis used

Run #	Date	$\mathcal{L}_{int}(\text{fb}^{-1})$
Run 1	Oct. 1999 - Oct. 2000	20.37±0.01±0.09
Run 2	Feb. 2001 - Jun. 2002	61.32±0.01±0.26
Run 3	Dec. 2002 - Jun. 2003	32.28±0.01±0.13
Run 4	Sep. 2003 - Jul. 2004	99.58±0.02±0.41
Run 5	Apr. 2005 - Aug. 2006	132.33±0.02±0.59
Run 6	Jan. 2007 - Sep. 2007	78.31±0.02±0.35

Table 6.5: Integrated luminosity collected by *BABAR* on the $\Upsilon(4S)$ resonance[31].

the *BABAR* software release 54 and MC skims from skim cycle 24. The specific Simulation Production (SP) modes called are listed in Table 6.6 and the production cross-sections shown in Table 6.7.

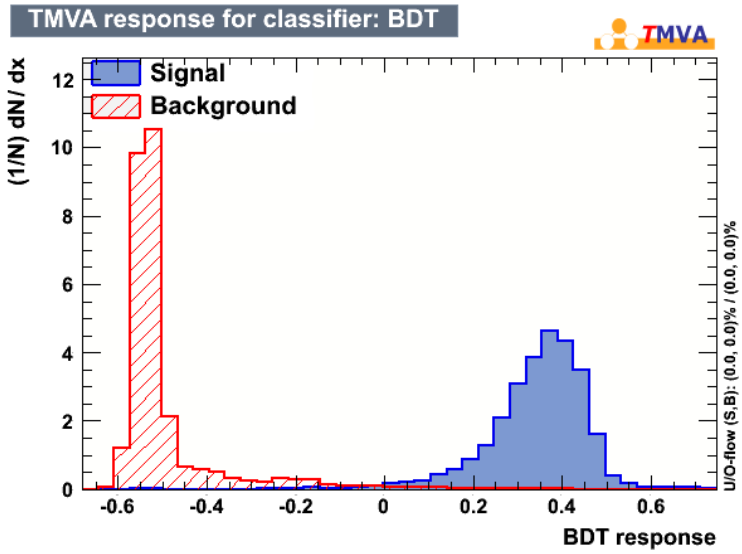

Figure 6.16: Separation of electrons (Background) and pions (Signal) as a function of BDT cut value.

Sample	Version
Data	AllEvents-R24-v10
$\tau^+\tau^-$	SP-3429-AllEventsSkim-R24h
$\mu^+\mu^-$	SP-3981-AllEventsSkim-R24h
uds	SP-998-AllEventsSkim-R24h
$c\bar{c}$	SP-1005-AllEventsSkim-R24h
e^+e^-	SP-2400-AllEventsSkim-R24h

Table 6.6: The SP/data modes used for each sample. Note that all the samples are Run dependent except for the Bhabha sample (SP-2400) which is Run independent. The AllEventsSkim is a predefined sub-set of data which contains all physics data.

6.6 Polarized MC Generation

The studies of the $\tau\tau \to \pi\nu\pi\nu$ selection have made clear that the samples are too contaminated by other τ decays and $e^+e^- \to \mu^+\mu^-$ events to reliably extract the τ helicity states from the slope of the momentum distributions. In order to understand the effects polarization has on the samples and develop new tools for extracting the beam polarization we use the KKMC [7] generator to produce polarized MC.

6.6.1 KKMC Generator

The KKMC generator does not allow for the production of MC from specific τ helicity states. This is due to how the spins of τ-pairs produced in e^+e^- collisions are subject to quantum

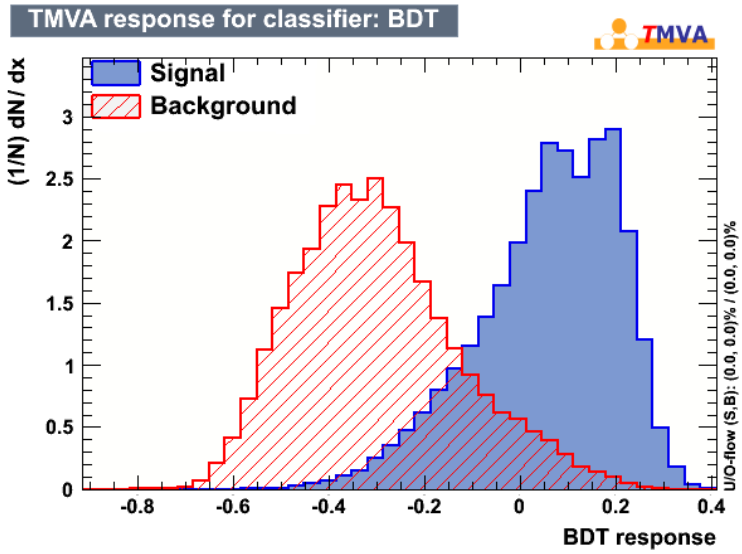

Figure 6.17: Separation of hadronic(excluding $\tau^{\pm} \to \pi^{\pm}\overline{\nu}_{\tau}$) τ decays (Background) and pions (Signal) as a function of BDT cut value.

MC	σ(nb)	Total Events	$\frac{\mathscr{L}_{MC}}{\mathscr{L}_{data}}$
$\tau^+\tau^-$	0.919	1615989000	3.423
$\mu^+\mu^-$	1.147	617278000	1.048
uds	2.1	3365048000	3.119
$c\bar{c}$	1.3	926820000	1.388
e^+e^-	25.52	2445000000	0.187

Table 6.7: Cross-section of MC assumed in this analysis, total MC events, and equivalent luminosity compared to data. Bhabha cross section is from ALIBABA MC Bhabha generator[32, 33] and assumes an acceptance of 15° to 165° in the CMS frame

entanglement[34]. Instead we polarize the e^+e^- beams and can use the distributions to bypass the τ helicity states in the measurement of beam polarization. Table 6.8 shows the generator calculated cross-sections for the $e^+e^- \to \tau\tau$ process for different longitudinal beam polarizations. As expected, polarizing only one beam does not effect the cross-section and polarizing both can double or nearly cancel out the cross-sections. Another test carried out to verify the generator performance is a calculation of the Born level (Electroweak interactions only) cross-section. The by-hand calculation predicts a value of $\sigma_{\text{ew}} = 776.712$ pb, and `KKMC` returns a value of 775.928 pb which is in good agreement within the certainty of the parameters used in the by-hand calculation.

e^-	e^+	σ(pb)
0	0	920.10±2.07
+1	0	920.99±2.13
-1	0	919.28±2.13
+1	+1	1832.11±5.99
+1	-1	4.19±0.07

Table 6.8: $e^+e^- \to \tau^+\tau^-$ production cross-sections for various longitudinal beam polarization states.

6.6.2 Polarized Distributions

By running the generator in a mode that only produces $\tau^\pm \to \pi^\pm \overline{\nu}_\tau$ events, we can easily see the effects of beam polarization on the kinematic distributions. Figure 6.18 shows the $\cos\theta$ distribution for the negatively charged pions with a left polarized e^- beam, an unpolarized beam, and a right polarized beam. Similarly Figures 6.19 to 6.21 show the momentum distributions for the same polarizations but for $\cos\theta > 0$, $\cos\theta$ unrestricted, and $\cos\theta < 0$.

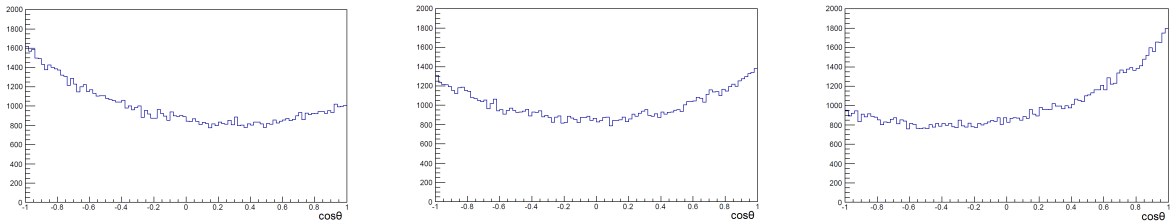

Figure 6.18: $\cos\theta$ distributions for negatively charged pions for a left polarized e^- beam (Left), an unpolarized beam (Middle), and a right polarized beam (Right).

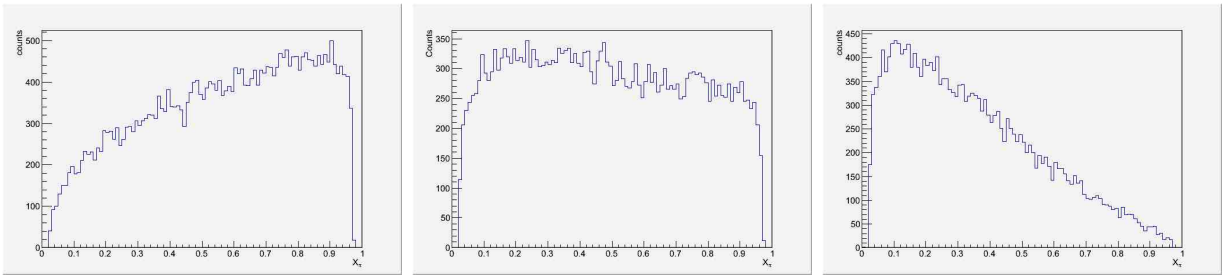

Figure 6.19: Momentum distributions for negatively charged pions, $\cos\theta < 0$ only, for a left polarized e^- beam (Left), an unpolarized beam (Middle), and a right polarized beam (Right).

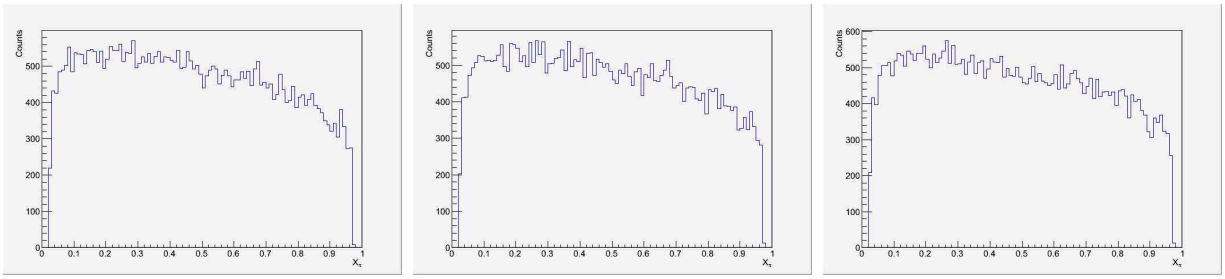

Figure 6.20: Momentum distributions for negatively charged pions, all $\cos\theta$, for a left polarized e^- beam (Left), an unpolarized beam (Middle), and a right polarized beam (Right).

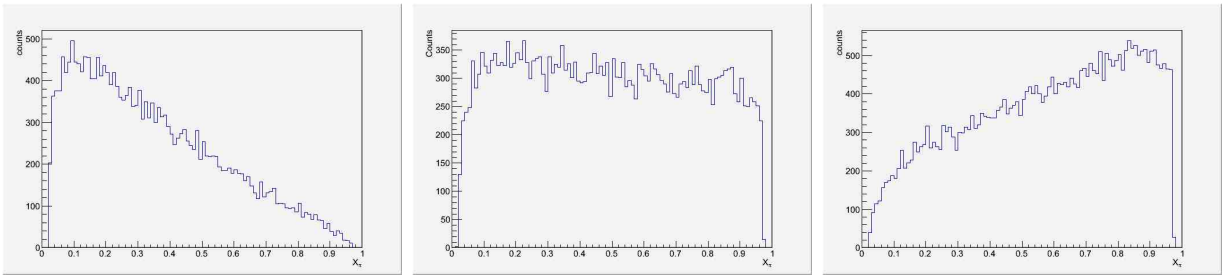

Figure 6.21: Momentum distributions for negatively charged pions, $\cos\theta > 0$ only, for a left polarized e^- beam (Left), an unpolarized beam (Middle), and a right polarized beam (Right).

6.6.3 Official *BABAR* MC Production

With the performance of KKMC verified, a large amount of offical MC is requested. The new simulation modes are listed in Table 6.9. The total number of events generated for each mode and run are summarized in Table 6.10. Also shown in Table 6.10 are the relative (compared to data luminosity) number of MC events produced. Additional MC was requested but was unable to be produced successfully before the SLAC shutdown of computing support for *BABAR*. Due to the shortage of MC, the later runs will be statistically limited, in the polarization measurement, by available MC rather than data.

Sample	Version
$\tau^+\tau^-$ (Left Polarized)	SP-11980-R24
$\tau^+\tau^-$ (Right Polarized)	SP-11981-R24

Table 6.9: Polarized $\tau^+\tau^-$ MC simulation modes.

	Left Polarized		Right Polarized	
	Events Generated	$\frac{\mathscr{L}_{MC}}{\mathscr{L}_{data}}$	Events Generated	$\frac{\mathscr{L}_{MC}}{\mathscr{L}_{data}}$
Run 1	42212000	2.25	42082000	2.25
Run 2	121840000	2.16	125163000	2.22
Run 3	57938000	1.95	65350000	2.20
Run 4	182149000	1.99	198732000	2.17
Run 5	255116000	2.10	152182000	1.25
Run 6	151513000	2.11	71970000	1.00

Table 6.10: Number of polarized events generated for each Run and SP-mode. The luminosity comparison is made using $\sigma_{\tau\tau} = 0.919$ nb to calculate the equivalent MC luminosity.

6.7 Tau Polarimetry Topology

With the full *BABAR* MC and polarized MC available to investigate the possible Tau Polarimetry approaches, a number of event topologies are investigated. The subset studied in this dissertation are summarized in Table 6.11.

Mode	Signal	Tag	Dominant τ Decay
$\pi^+\pi^-$	$\pi^\pm$	$\pi^\mp$	$\tau^+\tau^- \to \pi^+\overline{\nu}_\tau + \pi^-\nu_\tau$
π-e	$\pi^\pm$	$e^\mp$	$\tau^+\tau^- \to e^+\overline{\nu}_\tau\nu_e + \pi^-\nu_\tau$
3v1	$\pi^\pm$	$\pi^\pm\pi^\mp\pi^\mp$	$\tau^+\tau^- \to a_1^+\overline{\nu}_\tau(a_1^+ \to \pi^+\pi^+\pi^-) + \pi^-\nu_\tau$
π-ρ	$\pi^\pm$	$\pi^\mp\pi^0$	$\tau^+\tau^- \to \rho^+\overline{\nu}_\tau(\rho^+ \to \pi^+\pi^0) + \pi^-\nu_\tau$
ρ-e	$\pi^\pm\pi^0$	$e^\mp$	$\tau^+\tau^- \to \rho^+\overline{\nu}_\tau(\rho^+ \to \pi^+\pi^0) + e^-\overline{\nu}_e\nu_\tau$
ρ-ℓ	$\pi^\pm\pi^0$	$\ell^\mp$	$\tau^+\tau^- \to \rho^+\overline{\nu}_\tau(\rho^+ \to \pi^+\pi^0) + \ell^-\overline{\nu}_\ell\nu_\tau$

Table 6.11: τ-pair decay topologies investigated in this dissertation. ℓ refers to either an electron or a muon in the final state.

6.7.1 Polarization Sensitivity

All of the τ decays have some amount of kinematic-polarization sensitivity, however the more particles present in the final state, the more smeared out the effects are. Figures 6.22 to 6.25 shows how beam polarization influences the momentum of the pions or leptons in the τ final state as predicted by the *BABAR* detector simulations for the four most likely τ decays. As the $\tau^\pm \to \pi^\pm\overline{\nu}_\tau$ decay is the most sensitive to beam polarization we focused the development of Tau Polarimetry on this decay mode. In Chapter 7 this work is extended to the $\tau^\pm \to (\rho^\pm \to \pi^\pm\pi^0)\overline{\nu}_\tau$ decay mode and in the future other decay modes could be investigated. Table 6.12 shows the relevant τ decay branching fractions. In the case of the

ρ decay the momentum is not the most sensitive variable for measuring the polarization, instead an optimal variable can be constructed[35] which is discussed further in Chapter 7.

Decay Mode	Branching Fraction (%)
$\tau^- \to \pi^- \nu_\tau$	10.82±0.05
$\tau^- \to e^- \overline{\nu}_e \nu_\tau$	17.82±0.04
$\tau^- \to \mu^- \overline{\nu}_\mu \nu_\tau$	17.39±0.04
$\tau^- \to \rho^- \nu_\tau (\rho^- \to \pi^- \pi^0)$	25.49±0.09

Table 6.12: τ-decay branching fractions[10]. 85.24% of τ decays result in a single charged particle.

6.8 e-Tagged $\tau^\pm \to \pi^\pm \overline{\nu}_\tau$ analysis

A test of selecting $\tau^+\tau^- \to \pi^+ \overline{\nu}_\tau e^- \overline{\nu}_e \nu_\tau$ events found a significant amount of $e^+e^- \to e^+e^-$ contamination. Typical cuts to remove Bhabha-like events, such as acollinearity requirements had no effect. A possibility not investigated at the time is requiring the tagging electron to be below a momentum threshold, as most Bhabha electrons will have a momentum of 5.28 GeV ($\sqrt{s}/2$).

6.9 3 pion Tagged $\tau^\pm \to \pi^\pm \overline{\nu}_\tau$ analysis

Requiring a 3-prong τ decay, $\tau^+\tau^- \to \pi^+ \overline{\nu}_\tau \pi^- \pi^+ \pi^- \nu_\tau$, showed significant improvement over the previous analysis selections. The removal of leptonic decay modes eliminates any dilepton contamination at the cost of allowing in a small amount of $e^+e^- \to c\bar{c}$ events. The primary concern with this event selection is the overall branching fractions. Only 2% of all $\tau^+\tau^-$ events result in a 1v3 pion final state. Initial testing with a 2fb^{-1}equivalent MC sample suggests a 0.5% statistical uncertainty is achievable with 300fb^{-1}of data. This would need to be confirmed with a more statistically significant data-set.

6.10 ρ Tagged $\tau^\pm \to \pi^\pm \overline{\nu}_\tau$ analysis

As the 3 pion tagging showed strong results in selecting a relatively pure sample but with low statistics we examine tagging the $\tau^\pm \to \pi^\pm \overline{\nu}_\tau$ events with a $\tau^\pm \to (\rho^\pm \to \pi^\pm \pi^0) \overline{\nu}_\tau$ decay. The $\tau^\pm \to (\rho^\pm \to \pi^\pm \pi^0) \overline{\nu}_\tau$ decay mode is also purely hadronic and the ρ decay is 2.5$\times$ more prevalent than the 3-pion final final state.

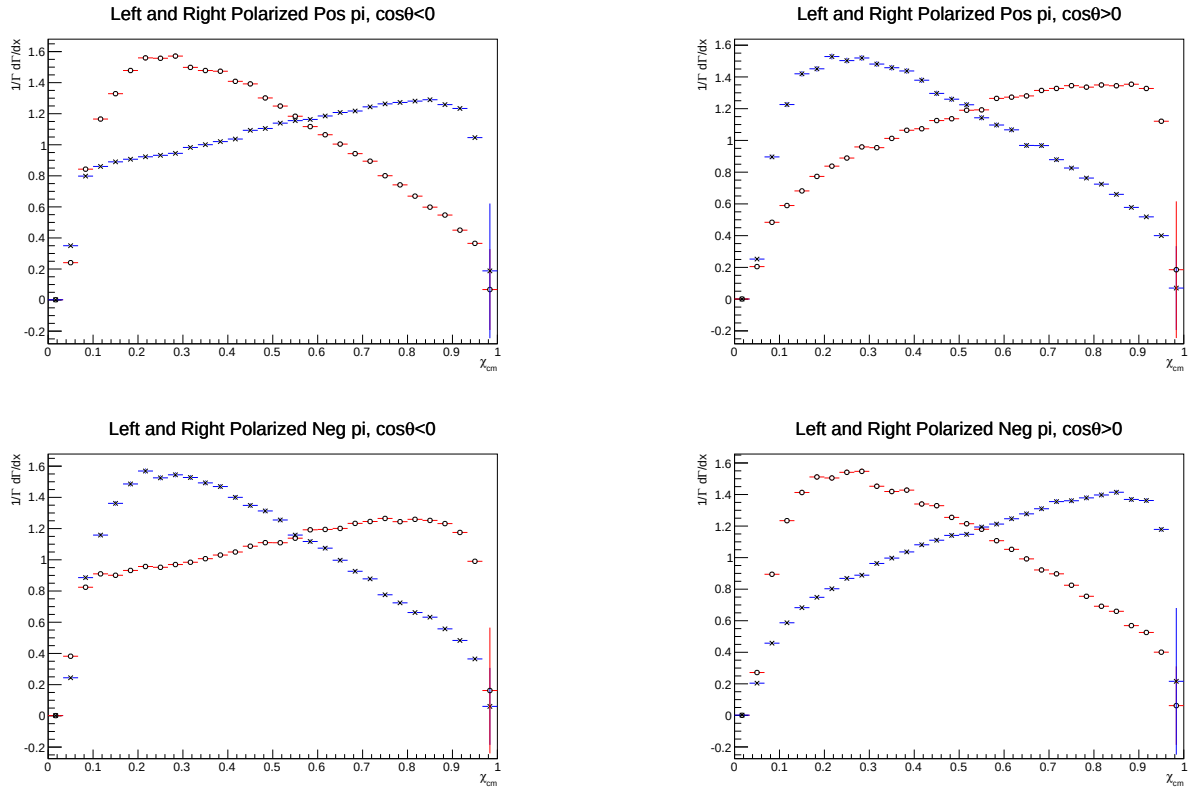

Figure 6.22: The momentum($\mathrm{X}_{cm} \equiv \frac{P_{cm}}{E}$) sensitivity to the beam polarization for the $\tau \to \pi\nu$ decay. The blue points are for a left handed electron beam, while the red points correspond to the right handed beam. The top plots correspond to a positively charged final state particle, while the bottom are negatively charged. The left plots correspond to the backward half of the detector, the right plots the forward.

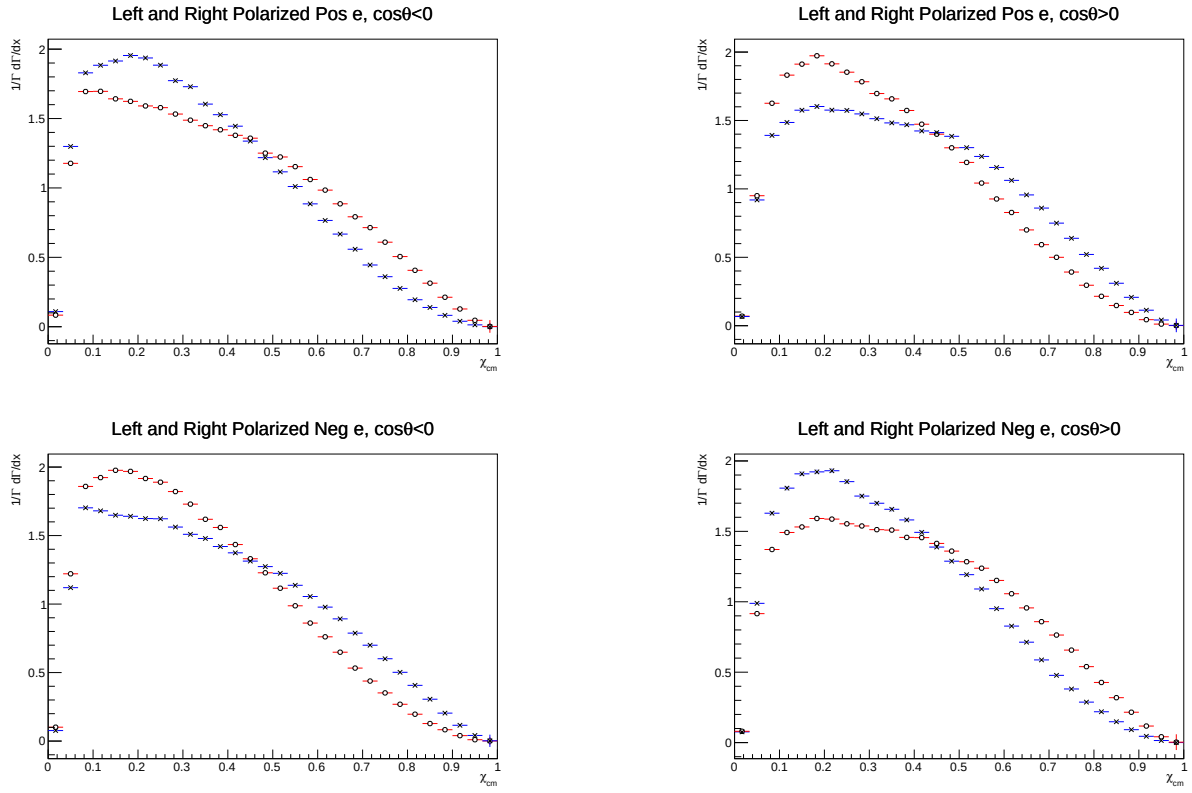

Figure 6.23: The momentum($X_{cm} \equiv \frac{P_{cm}}{E}$) sensitivity to the beam polarization for the $\tau \to e\nu\nu$ decay. The blue points are for a left handed electron beam, while the red points correspond to the right handed beam. The top plots correspond to a positively charged final state particle, while the bottom are negatively charged. The left plots correspond to the backward half of the detector, the right plots the forward.

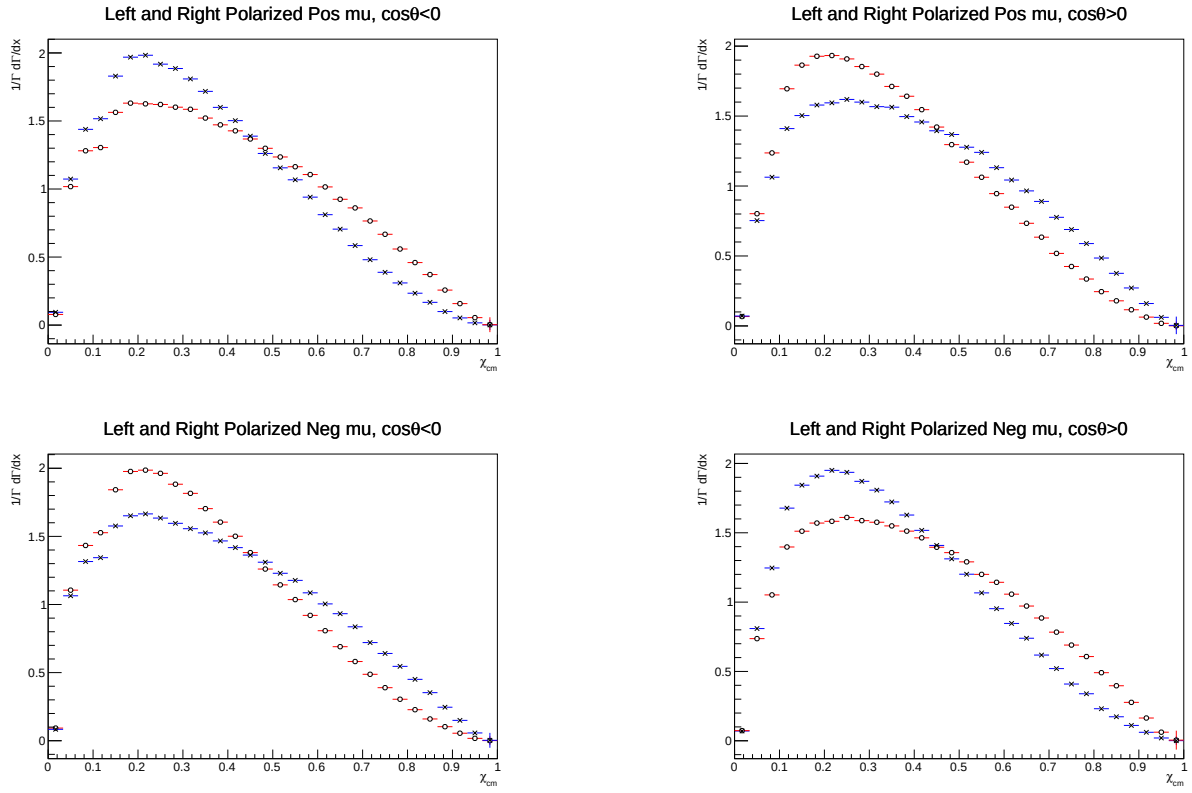

Figure 6.24: The momentum($X_{cm} \equiv \frac{P_{cm}}{E}$) sensitivity to the beam polarization for the $\tau \to \mu\nu\nu$ decay. The blue points are for a left handed electron beam, while the red points correspond to the right handed beam. The top plots correspond to a positively charged final state particle, while the bottom are negatively charged. The left plots correspond to the backward half of the detector, the right plots the forward.

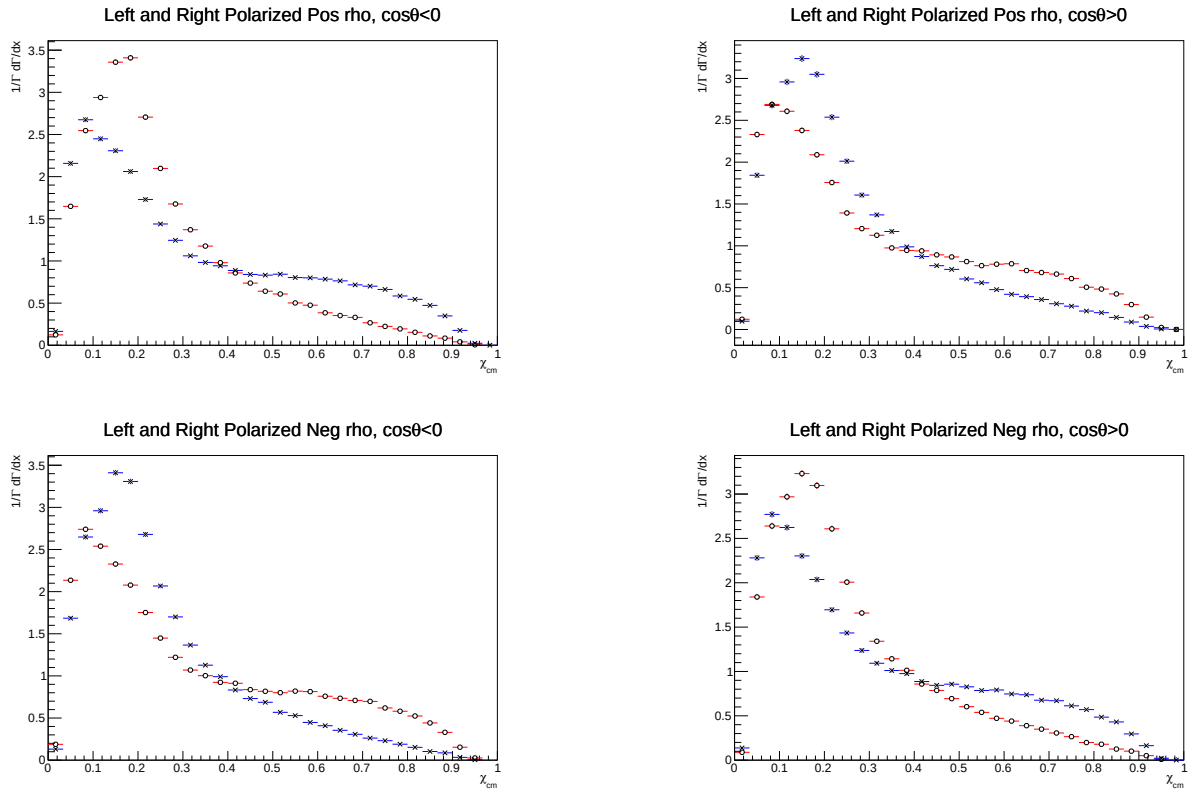

Figure 6.25: The momentum($X_{cm} \equiv \frac{P_{cm}}{E}$), of the charged pion from a ρ decay, sensitivity to the beam polarization for the $\tau \to \rho(\pi\pi^0)\nu$ decay. The blue points are for a left handed electron beam, while the red points correspond to the right handed beam. The top plots correspond to a positively charged final state particle, while the bottom are negatively charged. The left plots correspond to the backward half of the detector, the right plots the forward. It should also be noted momentum of the final state pion is not the optimal observable for the ρ mode

6.10.1 $\tau^{\pm} \to (\rho^{\pm} \to \pi^{\pm}\pi^0)\overline{\nu}_{\tau}$ Tagged Event Selection

In order to select $\tau^{\pm} \to (\rho^{\pm} \to \pi^{\pm}\pi^0)\overline{\nu}_{\tau}$ events, the following selection criteria was developed. The first step in this process is skimming the *BABAR* data into large analysis data sets. At this level two approaches were implemented. The first implementation required events pass the BGFTau and contain 1 or more charged tracks as defined by GoodTracksVeryLoose, the second implementation requires exactly two charged tracks as defined by GoodTracksVeryLoose. Both implementations have been run on all available data for runs 1-6. The ntuples produced via these implementations have been moved to the Digital Research Alliance of Canada (formally ComputeCanada) for further analysis and longterm storage. The reason for using both implementations was to allow for greater control of the BGFTau systematic uncertainties which were dominant for a portion of the analysis. From the skimmed ntuples further analysis cuts are then made. First the BGFTau, L3Trig (DCH or EMC trigger) and total charge requirements are applied. The analysis code then recalculates and adjusts the boost as is described in Section 6.12.2. An event topology check is then made, requiring that the tracks are in opposite thrust hemispheres[36, 37]. Additionally the tag and signal hemispheres are defined at this step with the signal hemisphere requiring no neutral clusters exceeding 50 MeV, and at least one neutral cluster exceeding 50 MeV within the tag hemisphere. This neutral requirement first merges clusters within 40 cm of the track cluster to minimize the analysis of the effects of hadronic split-offs. Next an angular fiducial requirement is placed on the charged tracks and a total event transverse momentum over 1.2 GeV is required. Finally the neutral clusters exceeding 100 MeV in the tag hemisphere are compared to a π^0 hypothesis and the signal track must pass PID cuts to remove τ to lepton decays.

Event P_T Requirement

The most significant cut to achieve agreement between data and MC is a cut on the total event transverse momentum. This is primarily targeted at removing two photon events, an example of which is shown in Figure 6.26, for which there is no MC and has the additional benefit of removing most dilepton events. The total event transverse momentum is calculated from the charged tracks and up to the 10 most energetic neutral clusters, excluding clusters with less than 50 MeV of energy. The requirement is that events must have a total P_T requirements of more then 1.2 GeV

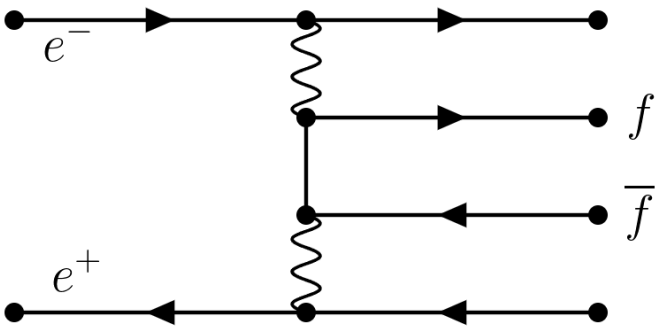

Figure 6.26: $e^+e^- \to f\overline{f}$ two-photon process. The final state particles will be lower energy than typical as the electron and positron are not annihilated.

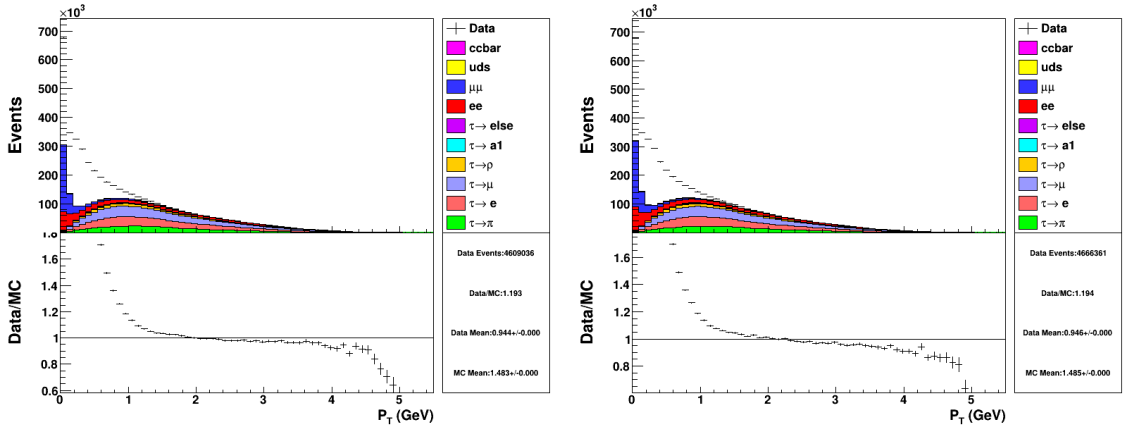

Figure 6.27: Event transverse momentum. Negatively charged candidates on left, positively charged on right. Colour scheme based on signal track.

6.10.2 Fiducial Angular Requirement

The angular requirement was added for two major reasons. The first reason was it was found that there was more Bhabha events in the backward region than predicted by MC. These events disappear once the full selection is required but is evidence the detector region may not be well modelled. Additionally there was disagreement between data and MC in the far forward and backward region of the detector when anomalous BGFTau events were being studied. The cut was placed at $0.430 < \theta_{lab} < 2.350$. $(0.909 > \cos\theta_{lab} > -0.703)(\sim 0.75 < \cos\theta_{CMS} <\sim -0.88)$

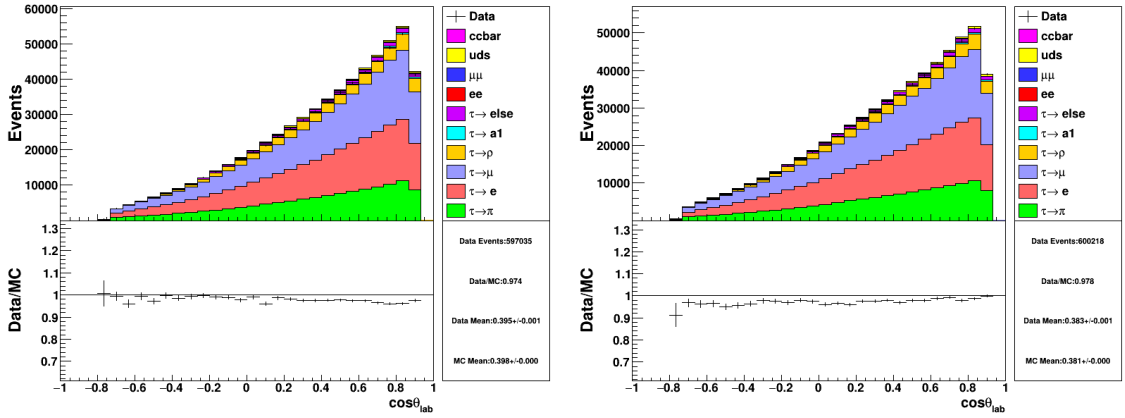

Figure 6.28: The $\cos\theta$ distribution of signal tracks in the lab frame. Angular cut not yet applied. Negatively charged candidates on left, positively charged on right.

π^0 Requirements

Neutral pions, π^0, are identified by two independent selection criteria. Both selections require neutral clusters less than 100 MeV in energy or within 40 cm of the tag track to be exempted from the selection. The remaining neutral clusters are checked for consistency with a "merged" π^0 hypothesis. This occurs when a π^0 decays and both photons emitted in the decay are detected in the same crystal or cluster of crystals. *BABAR* provides a likelihood variable that is assigned to each cluster. For this analysis merged π^0s with a likelihood larger than 20 are selected. If any π^0 s are identified through this method the number of π^0 s is returned and no further selection occurs. If no clusters meet the merged π^0 hypothesis the clusters are combined in combinatorial pairs and the invariant mass of each pair is calculated. The pair with a mass closest to 135 MeV is chosen as the candidate π^0 and if the invariant mass is between 115 and 155 GeV the event is selected. The π^0 requirement is an important cut to remove any dilepton events which pass the earlier cuts. Only a few rare lepton pair events have a neutral with any π^0 likelihood and even fewer reconstruct into the mass window.

Signal Track PID

The final step in the analysis to require the signal tracks fail a muon and electron selector to reduce the number of leptonic τ decays. For the muons we require the track fails the muBDTVeryLooseFakeRate selector and the VeryLooseKMElectronMicro for electrons.

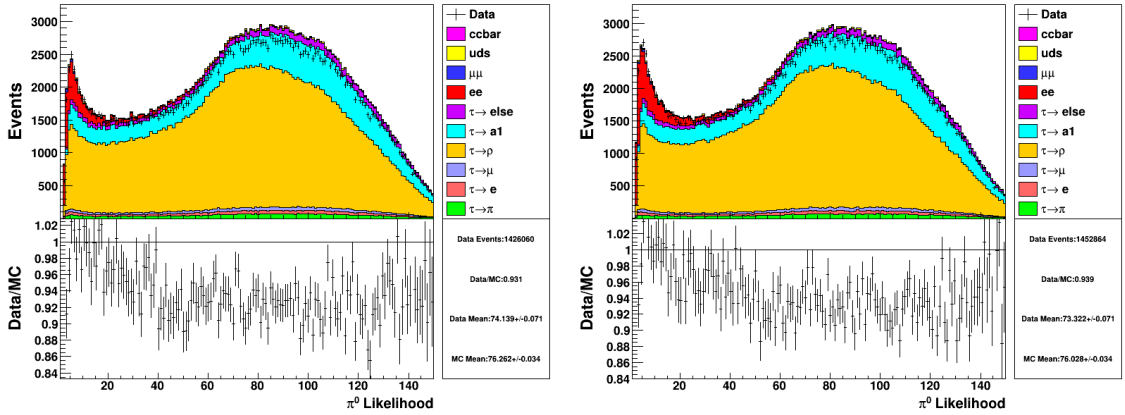

Figure 6.29: π^0 likelihood distribution. Colour scheme relates to the tag track. Negatively charged ρ tag on left, positively charged ρ tag on right.

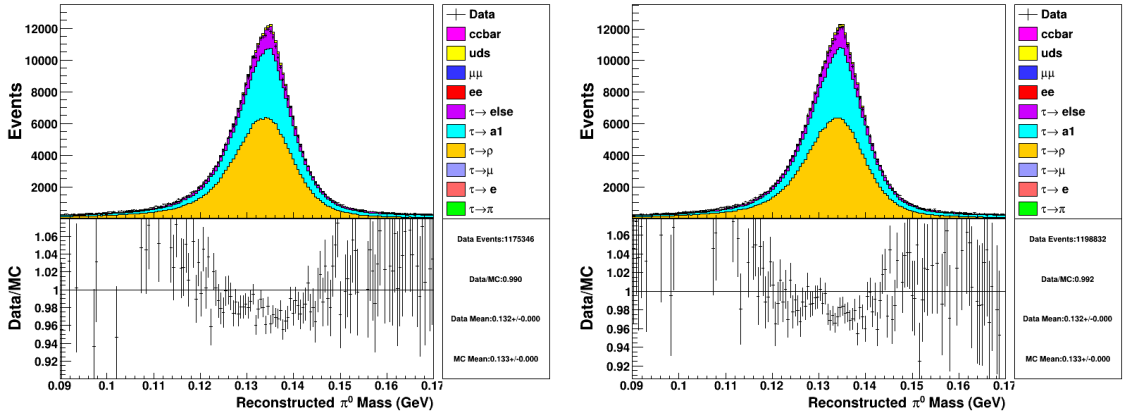

Figure 6.30: π^0 mass distribution. Colour scheme relates to the tag track. Negatively charged ρ tag on left, positively charged ρ tag on right.

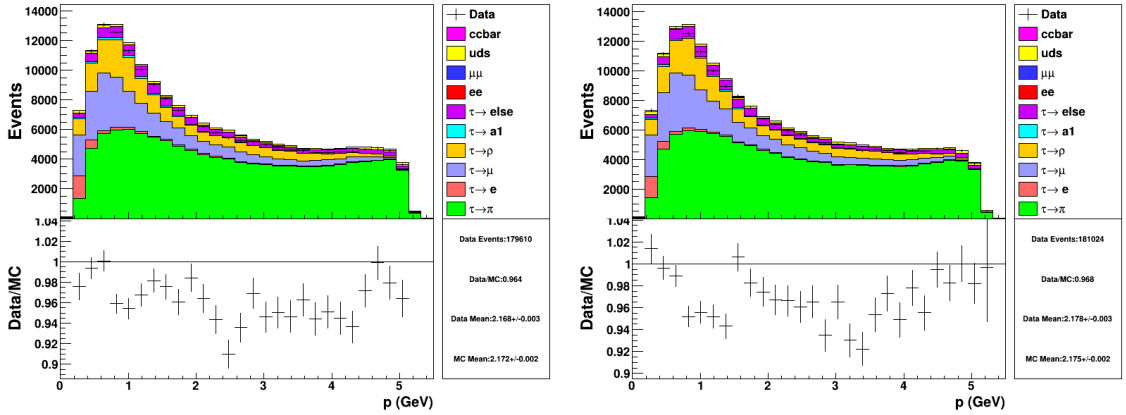

Figure 6.31: Momentum distributions of signal candidates after all cuts. Negatively charged candidates on left, positively charged on right.

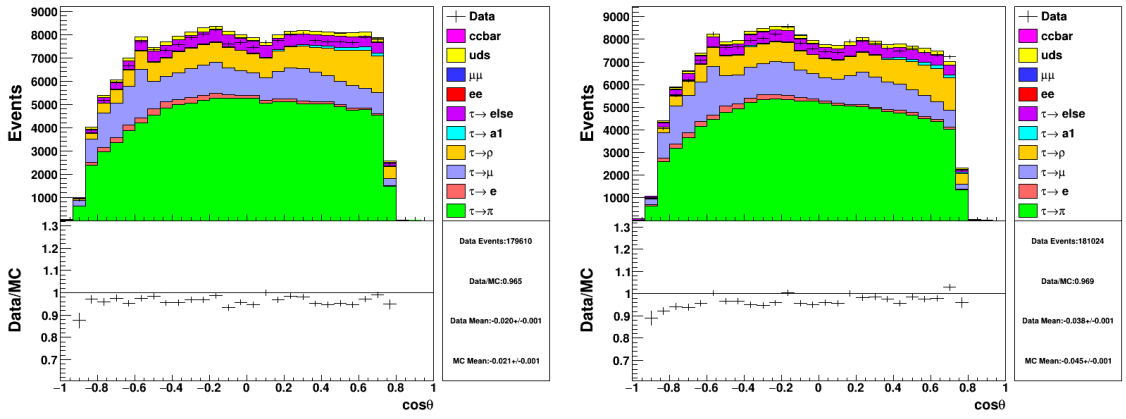

Figure 6.32: $\cos\theta$ distributions of signal candidates after all cuts. Negatively charged candidates on left, positively charged on right.

6.10.3 Corrections

In order to improve Data/MC agreement and efficiency a number of other cuts/corrections are made

Neutral-Track Association

It was found while investigating the spatial distribution of neutral clusters in relation to charged tracks that there is a difference in the neutrals near the tracks. We assume this is related to how hadronic split offs are modelled in *BABAR*. To reduce our dependence on this effect we remove neutral clusters within 40cm of the track, as measured on the EMC surface, from the event and add their deposited energy to that of the track. Figure 6.33 shows the disagreement between MC and data below 40 cm.

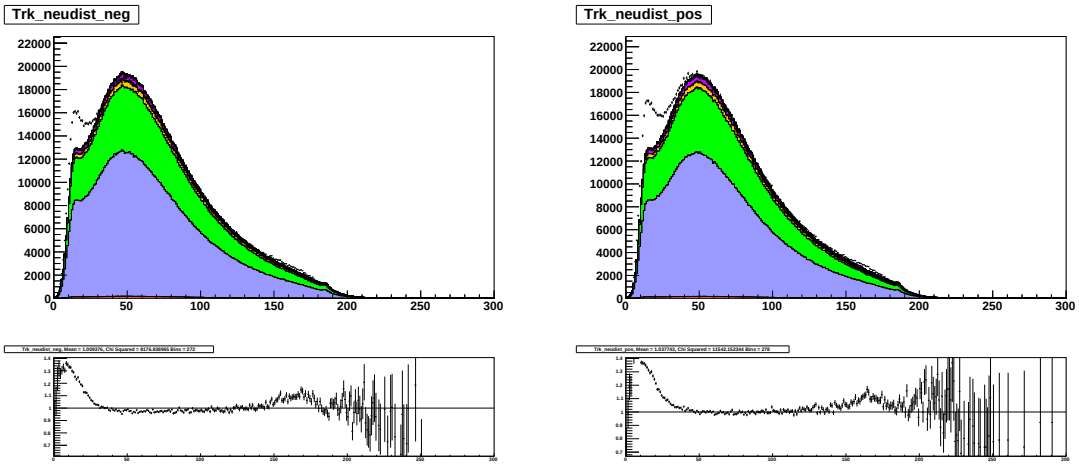

Figure 6.33: Distance between a neutral cluster and the nearest charged track

Track E/p Requirement

As a consequence of the neutral-track cluster association a large number of $\tau \to \rho\nu$ decays which remain as signal tracks can be removed. By combining the EMC energy within a radius of the track cluster, the additional EMC energy from the π^0 results in an E/p greater than 1. While the main body of E/p shows large Data/MC disagreements (We expect the disagreement is due to the lack of the Birks' correction in the *BABAR* MC[38]), the region above 1 shows good agreement so we remove all events with E/p$>$ 1. Figure 6.34 shows the main E/p distribution while Figure 6.35 shows an extended region with a zoom-in on the E/P$>$ 1 region

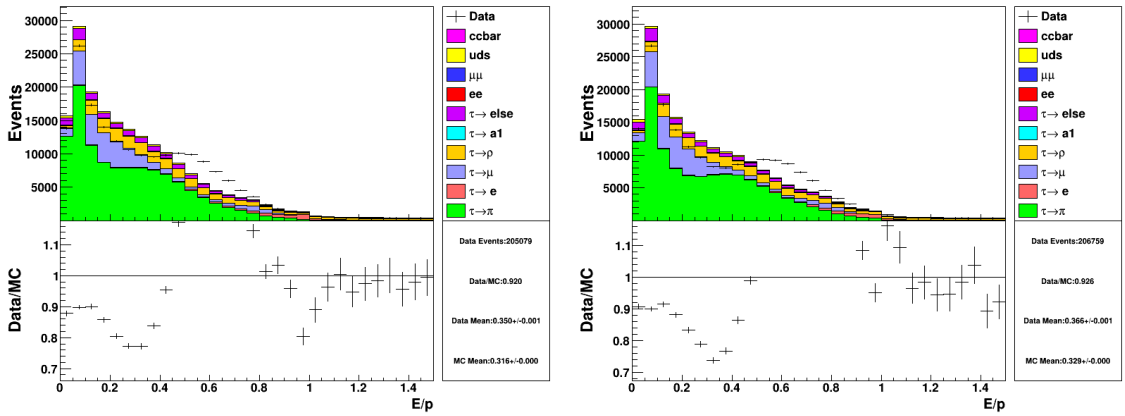

Figure 6.34: E/p distribution for the signal track, the shape of the data differs from MC specifically in the E/p=0.6 region. Negatively charged signal candidates on left, positively charged on right.

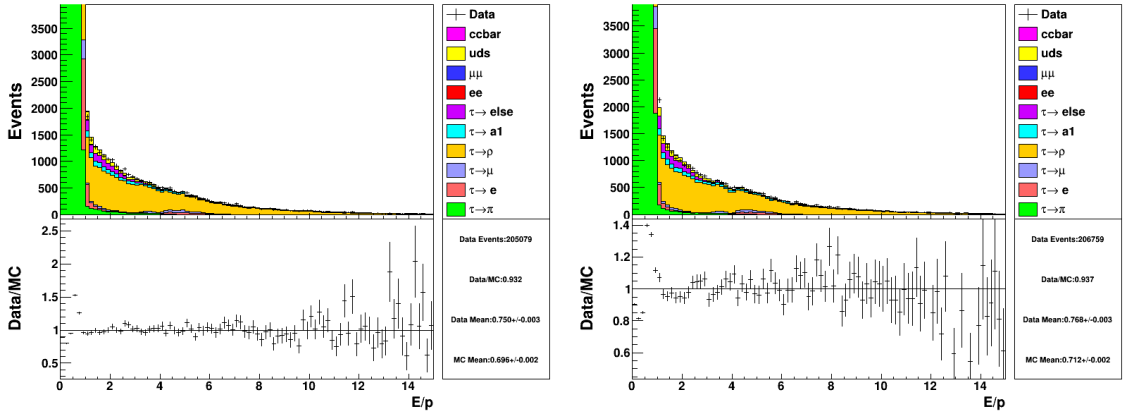

Figure 6.35: E/p distribution for the signal track. Zoom in on $E/p > 1$ region. Negatively charged signal candidates on left, positively charged on right.

Neutral Angular Requirement

For many of the variables studied to this point there was an excess of MC resulting in Data/MC≈0.92. With the disagreement spread uniformly across all distributions. After determining the luminosity weighting was not the culprit a few new variables were examined. It was noticed that in the angular distributions of the neutral clusters and the reconstructed π^0 s that there was larger disagreement near the edge of the detector. A cut was added requiring every neutral cluster be between 0.7< θ_{cm} <2.6. This resolved the discrepancy in the pi0's as well. After the cuts the data/MC agreement improves to to 0.94.

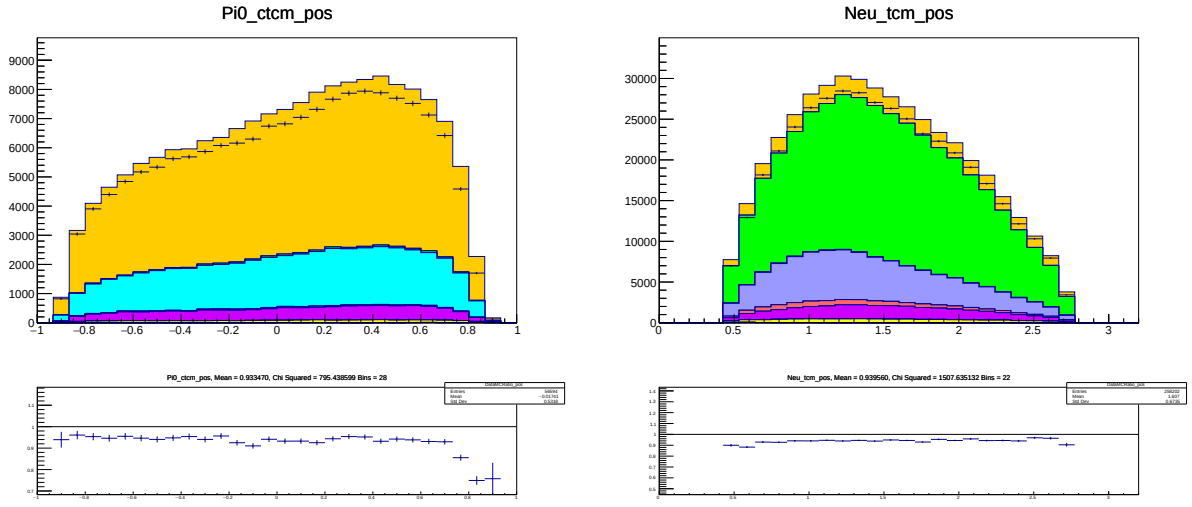

Figure 6.36: Angular distribution, $\cos\theta$, of the π^0 and all neutral clusters remaining in selection.

6.10.4 Cut Efficiency Summary

Table 6.13 shows the relative fraction of events surviving each cut applied sequentially. Table 6.14 shows the significance of each cut by removing only the specified cut from the selection. Table 6.15 shows the overall event purity achieved.

6.11 Polarization Fit

The beam polarization of a data set is extracted through a Barlow&Beeston template fit[39]. The concept behind this fit procedure is to fit the data with a combination of models/templates. A simple example of this would be trying to fit a population undergoing radioactive decay with an exponential curve and a linear background model. For this fit the MC distributions are used as the models and their relative contribution to the data is fitted for. This is done by using the event selection criteria as described in Section 6.7 on $\tau^+\tau^-$ MC with each beam polarization state to produce a template for the kinematics of left or right polarized electron beams. The MC is split based on the signal track charge and placed into two dimensional histograms, binned by momentum and cosθ. The Barlow&Beeston fit is fed the left and right polarized τ templates as well as templates for the non-tau MC modes. The non-tau MC modes ($e^+e^- \to e^+e^-$,$e^+e^- \to \mu^+\mu^-$,$e^+e^- \to (u\overline{u}$,$d\overline{d}$,$s\overline{s})$, and $e^+e^- \to c\overline{c}$), are scaled by luminosity and fixed in the fit. The weights of the left and right polarized templates are parameters of the fit and are expected to fit to roughly 0.5 and 0.5, for left and right respectively, when fitting an unpolarized sample. The fit also constrains the sum

	No Cuts	Event Topology	Event Quality	Signal Track
uds	1	0.0057	0.0034	7.23×10^{-4}
$c\bar{c}$	1	0.0015	0.0007	6.18×10^{-5}
ee	1	0.1501	0.027	0.0067
$\mu\mu$	1	0.6529	0.0787	0.0248
$\tau\tau$	1	0.3794	0.2927	0.133
$\tau \to e\nu\nu$	1	0.557	0.3375	0.187
$\tau \to \mu\nu\nu$	1	0.636	0.5711	0.3114
$\tau \to \pi\nu$	1	0.6149	0.5555	0.2965
$\tau \to \rho\nu$	1	0.2752	0.1986	0.0372
$\tau \to$ else	1	0.1155	0.0791	0.0141
continued	Angular Cut	Event P_T	Pi0 Cut	PID Cut
uds	6.27×10^{-4}	2.15×10^{-4}	1.07×10^{-4}	1.01×10^{-4}
$c\bar{c}$	4.72×10^{-5}	1.49×10^{-5}	8.80×10^{-6}	4.72×10^{-6}
ee	0.0059	0.0015	1.35×10^{-5}	1.89×10^{-6}
$\mu\mu$	0.0224	0.0011	8.29×10^{-6}	1.27×10^{-6}
$\tau\tau$	0.1282	0.0709	0.0337	0.0123
$\tau \to e\nu\nu$	0.1804	0.104	0.0516	0.0014
$\tau \to \mu\nu\nu$	0.3011	0.1649	0.0796	0.0118
$\tau \to \pi\nu$	0.2861	0.164	0.0761	0.0707
$\tau \to \rho\nu$	0.0349	0.016	0.0064	0.006
$\tau \to$ else	0.0133	0.0066	0.003	0.0029

Table 6.13: Fraction of unpolarized Run 3 MC events which remain after each cut is applied sequentially. Signal τ decays further broken down from the $\tau^+\tau^-$ component.

	Quality	Signal Track	$\cos\theta$ Cut	Event P_T	Pi0 Cut	PID Cut
uds	1.69	3.92	4.02	5.82	4.93	3.98
$c\bar{c}$	2.21	12.63	12.89	14.93	13.43	13.50
ee	4.30	1.18	1.30	14.06	116.17	7.34
$\mu\mu$	1.45	1.13	1.21	24.59	159.71	6.64
$\tau\tau$	1.19	1.83	1.86	2.59	3.02	3.57
$\tau \to e\nu\nu$	1.61	1.18	1.21	1.59	2.31	36.66
$\tau \to \mu\nu\nu$	1.12	1.08	1.11	1.68	2.15	6.81
$\tau \to \pi\nu$	1.03	1.12	1.15	1.87	2.27	1.19
$\tau \to \rho\nu$	1.94	5.37	7.54	8.51	9.01	7.56
$\tau \to$ else	1.35	3.98	14.09	14.95	15.26	14.10

Table 6.14: Ratio of unpolarized Run 3 MC events ($\epsilon_{N-1}/\epsilon_{ALL}$) which remain after all cuts have been applied, except for the one specified "(N-1)". Larger numbers mean the cut removes more of that event type. Signal τ decays further broken down from the $\tau^+\tau^-$ component.

	Luminosity Scaled Events	Ratio
uds	6850	0.0184
$c\bar{c}$	198	0.0005
ee	1555	0.0042
$\mu\mu$	47	0.0001
$\tau\tau$	364419	0.9768
$\tau \to e\nu\nu$	7462	0.0200
$\tau \to \mu\nu\nu$	60894	0.1632
$\tau \to \pi\nu$	226804	0.6079
$\tau \to \rho\nu$	45176	0.1211
$\tau \to$ else	24083	0.0646

Table 6.15: Unpolarized Run 3 MC remaining after all cuts. Luminosity scaling is applied to show predicted event number remaining in data. Fraction of total selection, i.e. purity, is also shown. Signal τ decays further broken down from the $\tau^+\tau^-$ component.

of all components to 1, leaving one free parameter in the fit. We define the free parameter to be the difference between the left and right polarized template contributions, which is the beam polarization. When the fit is performed there are five pieces of information extracted. The contribution from the left and right polarized templates (L and R), the errors on those numbers (σ_L and σ_R), and the covariance of the left and right components (ρ). The polarization is then measured as shown in Equation 6.4 and the error as shown in Equation 6.5. The fit is done separately for positively and negatively charged signal tracks, as the polarization sensitivity is reversed. The final measurement for a sample of data or MC is then found from the weighted average of the positively and negatively charged signal track fits.

To verify the fit performance and stability the unpolarized *BABAR* Tau MC is split into 3 independent samples each with roughly 1.2× the number of events as the *BABAR* data. Each sample is scaled to a data equivalent number of events, merged with non-tau backgrounds, and fit independently.

$$P = L - R \tag{6.4}$$

$$\sigma_P^2 = \sigma_L^2 + \sigma_R^2 - 2\rho\sigma_L\sigma_R \tag{6.5}$$

ρ is extracted from the symmetric ($\sigma_{01} = \sigma_{10}$) covariance matrix as shown in Equation 6.6.

$$V_{LR} = \begin{bmatrix} \sigma_{00} & \sigma_{01} \\ \sigma_{10} & \sigma_{11} \end{bmatrix} \Rightarrow \rho = \frac{\sigma_{01}}{\sigma_{00}} \tag{6.6}$$

Figure 6.37 shows an example of the templates for polarized and unpolarized τ MC with all

τ decay modes, while Figure 6.38 shows the templates for only the $\tau^{\pm} \to \pi^{\pm}\overline{\nu}_{\tau}$ decay mode.

	Positive Charge	Negative Charge	Combined Average
Sample 1	-0.0064±0.0156	0.0093±0.0158	0.0013±0.0111
Sample 2	-0.0018±0.0156	-0.0369±0.0158	-0.0191±0.0111
Sample 3	-0.0038±0.0155	0.0036±0.0157	-0.0002±0.0110
Data	0.0258±0.0164	-0.0027±0.0167	0.0118±0.0117

Table 6.16: Output of polarization fit for Run 3 MC samples and Run 3 data.

6.12 Systematic Studies

In order to assess the systematic uncertainty on the polarization measurement associated with each of the effects listed below, the following philosophy was applied. As a preliminary estimate of systematic uncertainty the variable associated with the effect was varied by an amount determined by how well the MC agrees with data for that variable. If this change results in a negligible change to the relative difference between MC and data polarization fits, ie. less than $\sim$0.001, then the relative shift is assigned as the systematic and no further investigation is done. Variables that produce a non-negligible shift in the fit are treated more carefully. The typical approach is to apply a correction to the MC and examine the effect on the data polarization fit. In the case that the correction results in a negligible shift in the data then only the shift is taken as the systematic uncertainty. After MC correction the variable can again be varied by an appropriate amount and the relative shift between MC and data polarization fits can be taken as the systematic uncertainty. All changes to variables in the following studies are applied after the TauBGF and two charged track only requirements but before any topology requirements or explicit cuts. A summary of all the systematic uncertainties is listed in Table 6.54. This section also only uses the Run 3 data as part of a blinded analysis approach.

6.12.1 Momentum

In order to understand the reconstruction of the momentum of charged tracks in the detector a sample of muon pairs was selected and the level of MC agreement with data in the momentum of this control sample used to evaluate how much to adjust the momentum in the systematic studies.

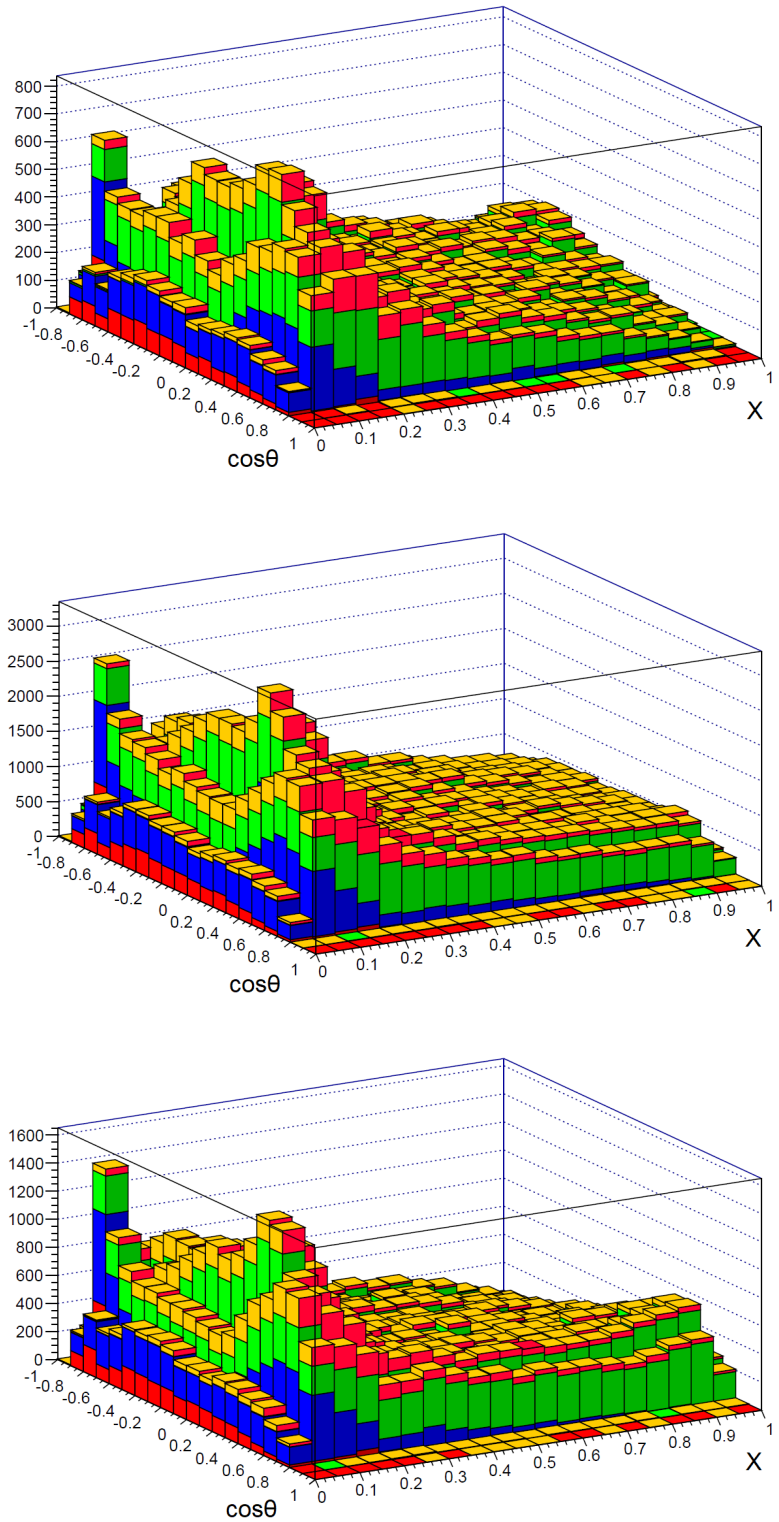

Figure 6.37: Top: Left polarized, Middle: Unpolarized, Bottom: Right polarized; Distribution of $\cos\theta$ and momentum for the signal side τ decay channels. The MC 'truth' is used to indicate the populations of the decays by colour. $\tau^{\pm} \to e^{\pm}\nu_e\overline{\nu}_\tau$ is red, $\tau^{\pm} \to \mu^{\pm}\nu_\mu\overline{\nu}_\tau$ is blue, $\tau^{\pm} \to \pi^{\pm}\overline{\nu}_\tau$ is green, and orange represents other τ decays.

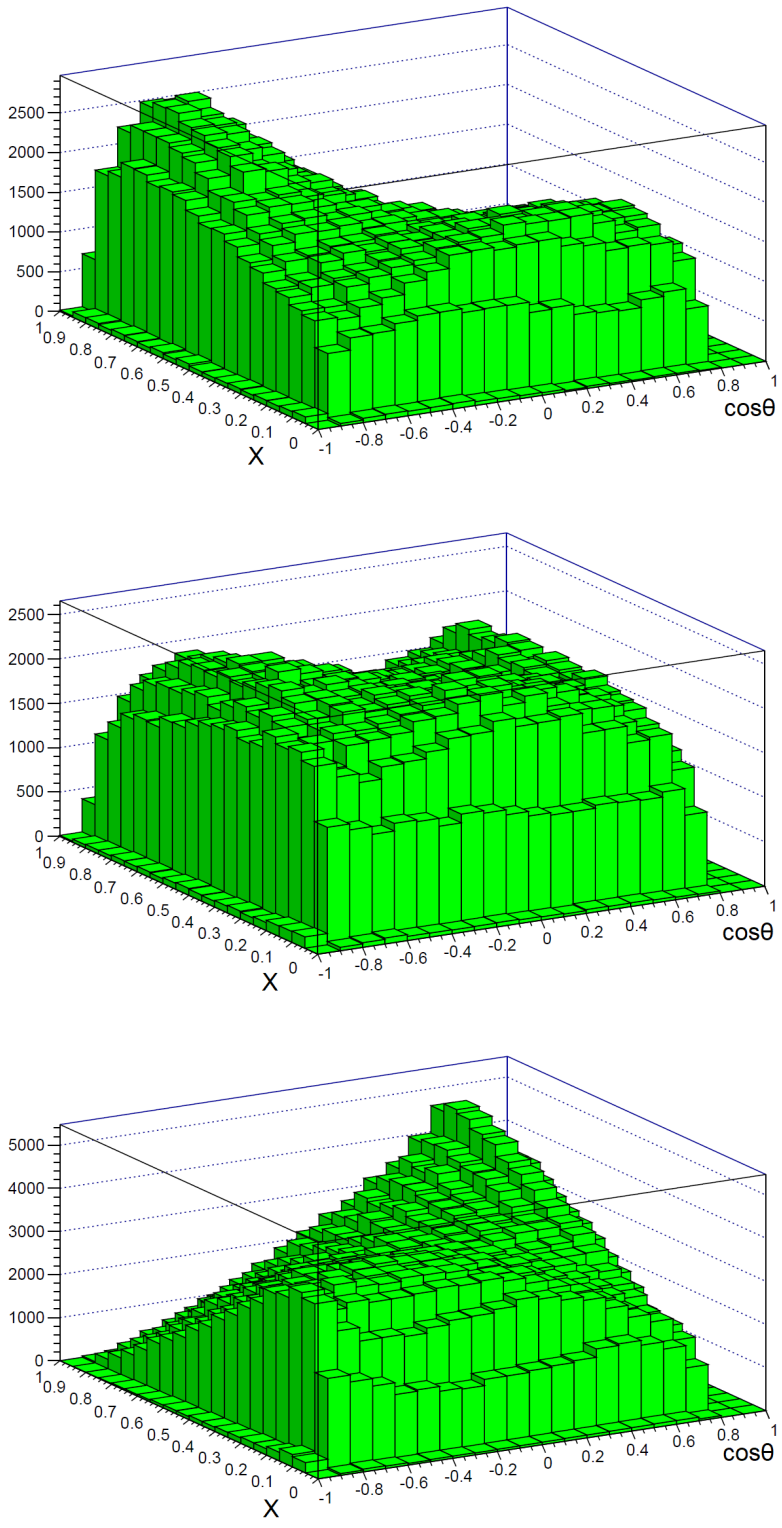

Figure 6.38: Top: Left polarized, Middle: Unpolarized, Bottom: Right polarized; Distribution of $\cos\theta$ and momentum for the $\tau^{\pm} \to \pi^{\pm}\overline{\nu}_{\tau}$ MC.

Muon Selection

Muon pairs were selected with the BGFMuMu tag and the following cuts were then applied.

- Two charged tracks with opposite sign
- The muons are within an angular acceptance
  - μ^- : $-0.801 < \cos\theta < 0.796$
  - μ^+ : $-0.836 < \cos\theta < 0.836$
- The event passes a L3 trigger
- The tracks are separated by at least 160°
- $0.8 < \frac{M_{\mu\mu}}{\sqrt{s}} < 1.1$
- One muon passes the muCombinedVeryLooseFakeRate selector[40]

With the muon pairs selected the magnitude of the muon momentum is compared between data and MC. This is done by first scaling the momentum by the beam constrained maximum muon momentum, $\frac{P_{CM}}{P_{CM}^{Max}}$ and comparing the results. Figures 6.39 to 6.40 shows the comparisons between data and MC for both charges. The data points peaking over the MC shows that the resolution of the reconstructed momenta for MC needs to be adjusted.

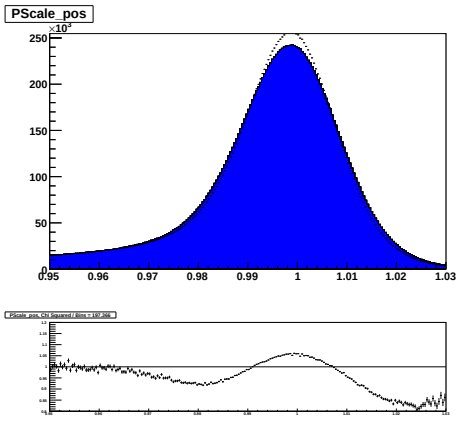

Figure 6.39: $\frac{P_{CM}}{P_{CM}^{Max}}$ for the positively charged muons. MC in color, data in points

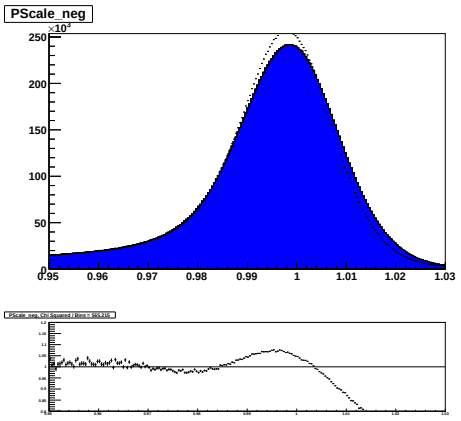

Figure 6.40: $\frac{P_{CM}}{P_{CM}^{Max}}$ for the negatively charged muons. MC in color, data in points

	Positive Track	Negative Track
R_P	0.93526±0.00099	0.91446±0.00092
S_P	1.000135±0.000006	0.999475±0.000006

Table 6.17: Momentum scaling and resolution factors

Momentum Scaling

In order to scale the momentum appropriately the momentum is corrected as shown in Equation 6.7. This method was used by Zinkoo Yun[41] to study momentum systematics in the past. In Equation 6.7 the P terms represent the reconstructed and truth momenta while R_P and S_P are scaling and resolution factors. S_P is defined as $\frac{\langle P\rangle_{Data}}{\langle P\rangle_{MC}}$, where $\langle P\rangle$ is the central value of a crystal ball fit performed on the P scale histograms (Figs 6.39-6.40). R_P is defined as $\frac{\sigma^P_{Data}}{\sigma^P_{MC}}$, where σ^P is the width of the crystal ball distribution. The results of the fits are shown in Table 6.17. After the corrections are applied the P scale plots are in much better agreement as seen in Figs 6.41-6.42

$$P^c_{Reco} = (P_{Truth} - R_P(P_{Truth} - P_{Reco}))S_P \tag{6.7}$$

The shifts in the polarization fit with and without the momentum corrections are shown

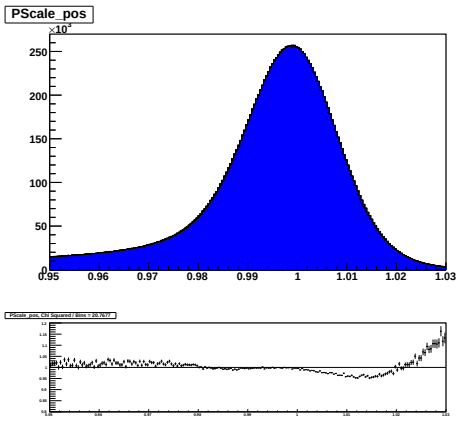

Figure 6.41: $\frac{P_{CM}}{P^{Max}_{CM}}$ for the positively charged muons after correction. MC in color, data in points

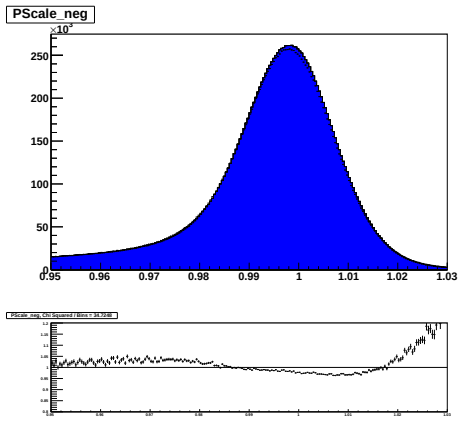

Figure 6.42: $\frac{P_{CM}}{P^{Max}_{CM}}$ for the negatively charged muons after correction. MC in color, data in points

in Table 6.18. The size of the shifts shows the importance of having the corrections as the systematic uncertainty would be dominating otherwise. Tables 6.19 to 6.26 show the shifts to the polarization fit when S_P and R_P are varied up and down by the uncertainties shown in Table 6.17. Taking the quadratic sum of the shifts in the data polarization fits as

	Positive	Negative	Average
Sample 1	0.0048	-0.0025	0.0010
Sample 2	0.0060	-0.0137	-0.0042
Sample 3	-0.0017	-0.0003	-0.0010
Data	-0.0019	-0.0286	-0.0157
Sample 1	0.1846σ	-0.0996σ	0.0556σ
Sample 2	0.2317σ	-0.5480σ	-0.2333σ
Sample 3	-0.0659σ	-0.0119σ	-0.0556σ
Data	-0.0667σ	-1.0400σ	-0.7929σ

Table 6.18: Run 3 shifts in the fit value with momentum tweaking applied

	Positive	Negative	Average
Sample 1	0.0000	0.0000	0.0001
Sample 2	0.0000	0.0000	0.0000
Sample 3	0.0001	0.0000	0.0001
Data	-0.0001	0.0000	-0.0001
Sample 1	0.0000 σ	0.0000 σ	0.0055 σ
Sample 2	0.0000 σ	0.0000 σ	0.0000 σ
Sample 3	0.0038 σ	0.0000 σ	0.0055 σ
Data	-0.0035 σ	0.0000 σ	-0.0050 σ

Table 6.19: Shift in polarization fit when S_P for the positively charged particles is increased by one sigma

	Positive	Negative	Average
Sample 1	0.0001	0.0000	0.0001
Sample 2	0.0001	0.0003	0.0002
Sample 3	-0.0002	0.0001	0.0000
Data	0.0000	0.0000	-0.0001
Sample 1	0.0038 σ	0.0000 σ	0.0055 σ
Sample 2	0.0038 σ	0.0119 σ	0.0109 σ
Sample 3	-0.0077 σ	0.0039 σ	0.0000 σ
Data	0.0000 σ	0.0000 σ	-0.0050 σ

Table 6.20: Shift in polarization fit when S_P for the positively charged particles is decreased by one sigma

	Positive	Negative	Average
Sample 1	0.0001	0.0000	0.0001
Sample 2	0.0001	0.0000	0.0000
Sample 3	0.0002	0.0002	0.0002
Data	0.0001	0.0000	0.0000
Sample 1	0.0038 σ	0.0000 σ	0.0055 σ
Sample 2	0.0038 σ	0.0000 σ	0.0000 σ
Sample 3	0.0077 σ	0.0078 σ	0.0109 σ
Data	0.0035 σ	0.0000 σ	0.0000 σ

Table 6.21: Shift in polarization fit when R_P for the positively charged particles is increased by one sigma

	Positive	Negative	Average
Sample 1	0.0000	0.0000	0.0001
Sample 2	0.0000	0.0003	0.0001
Sample 3	-0.0001	0.0000	0.0000
Data	0.0000	0.0000	0.0000
Sample 1	0.0000 σ	0.0000 σ	0.0055 σ
Sample 2	0.0000 σ	0.0119 σ	0.0055 σ
Sample 3	-0.0038 σ	0.0000 σ	0.0000 σ
Data	0.0000 σ	0.0000 σ	0.0000 σ

Table 6.22: Shift in polarization fit when R_P for the positively charged particles is decreased by one sigma

	Positive	Negative	Average
Sample 1	-0.0001	-0.0001	0.0000
Sample 2	0.0000	0.0003	0.0001
Sample 3	-0.0001	0.0000	0.0000
Data	0.0000	0.0000	-0.0001
Sample 1	-0.0038 σ	-0.0040 σ	0.0000 σ
Sample 2	0.0000 σ	0.0119 σ	0.0055 σ
Sample 3	-0.0038 σ	0.0000 σ	0.0000 σ
Data	0.0000 σ	0.0000 σ	-0.0050 σ

Table 6.23: Shift in polarization fit when S_P for the negatively charged particles is increased by one sigma

	Positive	Negative	Average
Sample 1	0.0000	-0.0001	0.0000
Sample 2	0.0000	0.0002	0.0001
Sample 3	0.0000	-0.0001	0.0000
Data	0.0000	0.0002	0.0001
Sample 1	0.0000 σ	-0.0040 σ	0.0000 σ
Sample 2	0.0000 σ	0.0079 σ	0.0055 σ
Sample 3	0.0000 σ	-0.0039 σ	0.0000 σ
Data	0.0000 σ	0.0072 σ	0.0050 σ

Table 6.24: Shift in polarization fit when S_P for the negatively charged particles is decreased by one sigma

	Positive	Negative	Average
Sample 1	0.0000	0.0000	0.0000
Sample 2	0.0000	0.0003	0.0001
Sample 3	0.0000	0.0000	0.0000
Data	-0.0001	0.0001	0.0000
Sample 1	0.0000 σ	0.0000 σ	0.0000 σ
Sample 2	0.0000 σ	0.0119 σ	0.0055 σ
Sample 3	0.0000 σ	0.0000 σ	0.0000 σ
Data	-0.0035 σ	0.0036 σ	0.0000 σ

Table 6.25: Shift in polarization fit when R_P for the negatively charged particles is increased by one sigma

	Positive	Negative	Average
Sample 1	-0.0001	-0.0002	-0.0001
Sample 2	0.0000	0.0000	0.0000
Sample 3	0.0003	-0.0001	0.0001
Data	-0.0001	0.0002	0.0000
Sample 1	-0.0038 σ	-0.0079 σ	-0.0055 σ
Sample 2	0.0000 σ	0.0000 σ	0.0000 σ
Sample 3	0.0115 σ	-0.0039 σ	0.0055 σ
Data	-0.0035 σ	0.0072 σ	0.0000 σ

Table 6.26: Shift in polarization fit when R_P for the negatively charged particles is decreased by one sigma

the systematic uncertainty gives σ_P^{sys}=0.0002. This may be too aggressive however as the χ^2 value of the ratio plots in Figures 6.41 and 6.42 are still large. In order to study the remaining discrepancy the centre of mass momentum of the muons was plotted. Figures 6.43 and 6.44 show the distribution after correction. Adjusting the MC momenta down by 2 MeV improves the fit significantly as seen in Figures 6.45 and 6.46. Taking this correction into account, Table 6.27 shows the shift in the polarization fit with and without this 2 MeV correction. Taking the shift in data as the systematic uncertainty and the standard deviation of spread in MC as the statistical uncertainty in the systematic results in σ_P^{sys}=0.0015±0.0004.

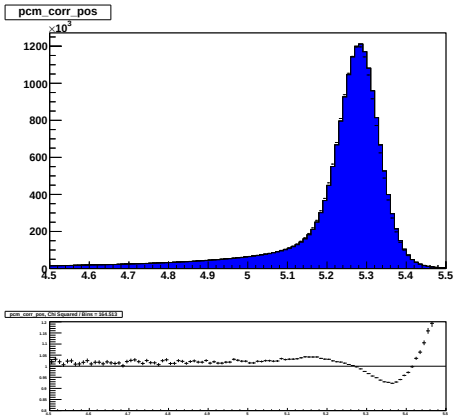

Figure 6.43: The momentum of the positive muons after correction

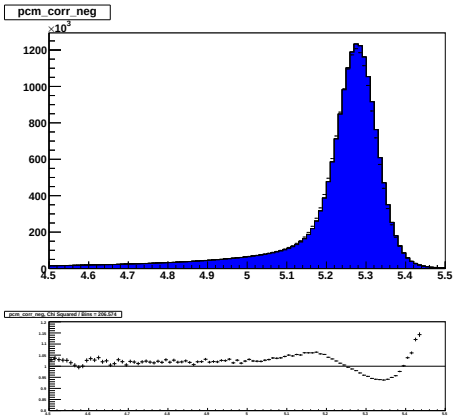

Figure 6.44: The momentum of the negative muons after correction

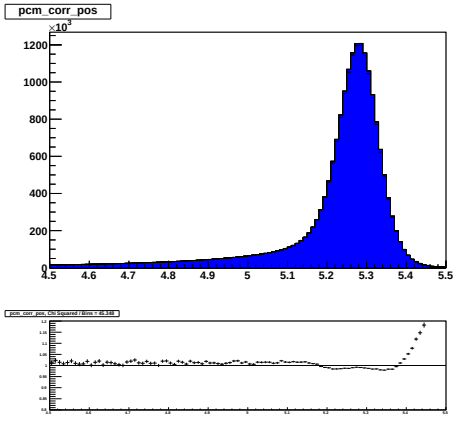

Figure 6.45: The momentum of the positive muons after correction, With a 2MeV shift on the MC

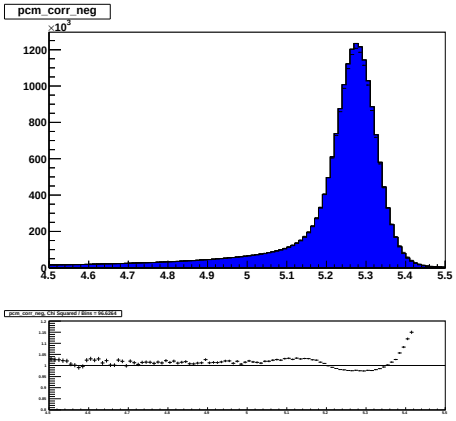

Figure 6.46: The momentum of the negative muons after correction, With a 2MeV shift on the MC

	Positive	Negative	Average
Sample 1	-0.0024	0.0016	-0.0004
Sample 2	-0.0025	0.0005	-0.0009
Sample 3	-0.0010	0.0007	-0.0002
Data	-0.0010	-0.0020	-0.0015
Sample 1	-0.0918 σ	0.0620 σ	-0.0197 σ
Sample 2	-0.0951 σ	0.0205 σ	-0.0504 σ
Sample 3	-0.0393 σ	0.0271 σ	-0.0082 σ
Data	-0.0349 σ	-0.0712 σ	-0.0730 σ

Table 6.27: Shift in polarization fit when the 2 MeV shift is applied.

6.12.2 Boost Vector

The boost vector was also checked with the muons pairs described earlier. The acollinearity of the muon pairs was plotted for both theta and phi as shown Figures 6.47 and 6.48. In order to correct the difference between and data and MC in the theta acollinearity the boost vector was increased by 4 MeV in the Z direction. Based on the minimal shifts in the fit we set the systematic uncertainty to be σ_{boost}=0.0005±0.0001

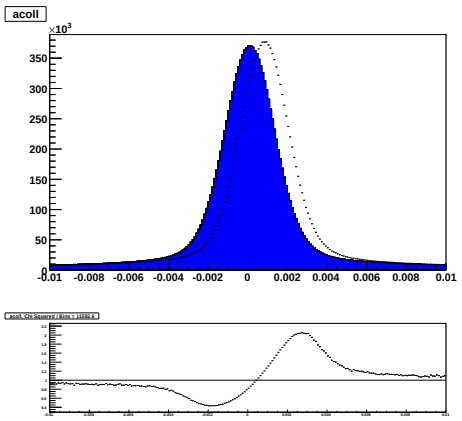

Figure 6.47: Acollinearity of muon pairs in theta

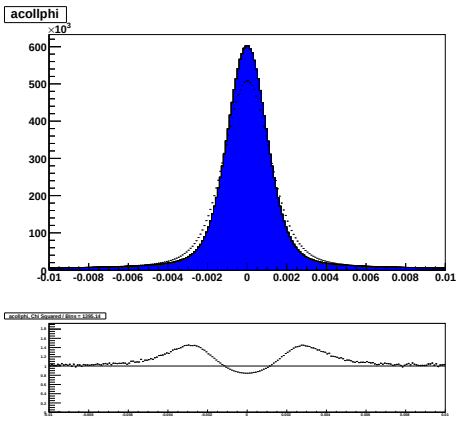

Figure 6.48: Acollinearity of muon pairs in phi

6.12.3 Theta

In order to test the polarization sensitivity to θ, the theta values of all charged tracks in the unpolarized MC is tweaked by 0.000897 ± 0.000005 radians[41]. This results in the shifts seen in Table 6.29 and 6.30. The shift down in theta results in the largest shifts, taking the average gives: $\sigma_{sys} = -0.0013 \pm 0.0016$.

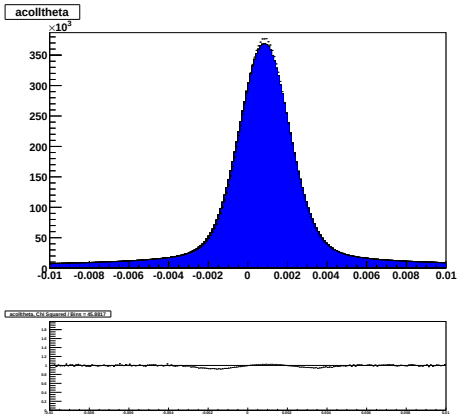

Figure 6.49: Acollinearity of muon pairs in theta, +4MeV Z boost

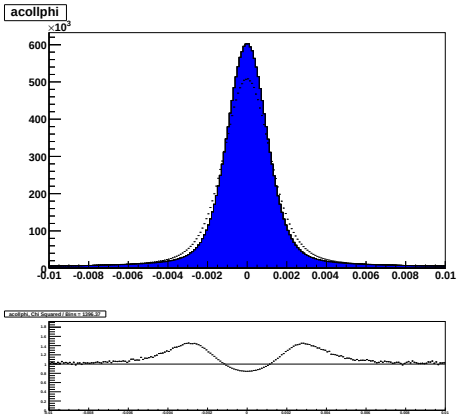

Figure 6.50: Acollinearity of muon pairs in phi, +4MeV Z boost

	Positive	Negative	Average
Sample 1	0.0005	-0.0005	0.0000
Sample 2	0.0003	-0.0002	0.0001
Sample 3	0.0010	-0.0008	0.0001
Data	-0.0044	0.0031	-0.0005
Sample 1	0.0189 σ	-0.0198 σ	0.0000 σ
Sample 2	0.0114 σ	-0.0079 σ	0.0055 σ
Sample 3	0.0382 σ	-0.0314 σ	0.0055 σ
Data	-0.1522 σ	0.1119 σ	-0.0250 σ

Table 6.28: Shifts in the polarization fits in Run 3 in response to the boost correction.

	Positive	Negative	Average
Sample 1	-0.0013	-0.0016	-0.0013
Sample 2	-0.0014	0.0029	0.0009
Sample 3	-0.0007	0.0003	-0.0001
Sample 1	-0.0544 σ	-0.0681 σ	-0.0778 σ
Sample 2	-0.0583 σ	0.1245 σ	0.0539 σ
Sample 3	-0.0293 σ	0.0128 σ	-0.0060 σ

Table 6.29: Shifts in the Run 3 polarization fits in response to theta increased by 1σ.

6.12.4 Phi

The phi angle of the charged tracks was studied similarly to theta. No notable effects were found so no systematic uncertainty is applied.

	Positive	Negative	Average
Sample 1	-0.0025	-0.0035	-0.0030
Sample 2	0.0000	-0.0021	-0.0011
Sample 3	0.0006	-0.0003	0.0002
Sample 1	-0.1050 σ	-0.1489 σ	-0.1796 σ
Sample 2	0.0000 σ	-0.0901 σ	-0.0659 σ
Sample 3	0.0251 σ	-0.0128 σ	0.0120 σ

Table 6.30: Shifts in the Run 3 polarization fits in response to theta decreased by 1σ.

6.12.5 Backgrounds

To test the sensitivity to non-τ backgrounds the number of background events was used to calculate a statistical uncertainty on the background contributions. This is a more realistic approach in comparison to using the uncertainty in the actual production cross-sections as the event numbers are small. Tables 6.31 and 6.32 show the shifts in the fit with the backgrounds added to the unpolarized τ MC varied up and down. Based on the results a total systematic uncertainty of $\sigma_{sys} = 0.0002 \pm 0.0001$. Since the sensitivity was small no further investigation was done.

	Positive	Negative	Average
Sample 1	-0.0001	0.0000	-0.0001
Sample 2	-0.0006	0.0000	-0.0003
Sample 3	-0.0001	-0.0002	-0.0002
Sample 1	-0.0032 σ	0.0000 σ	-0.0044 σ
Sample 2	-0.0191 σ	0.0000 σ	-0.0133 σ
Sample 3	-0.0032 σ	-0.0061 σ	-0.0088 σ

Table 6.31: Shifts in the Run 3 polarization fits in response to backgrounds being increased by 1σ.

	Positive	Negative	Average
Sample 1	0.0002	0.0000	0.0001
Sample 2	0.0007	0.0000	0.0004
Sample 3	0.0002	0.0001	0.0001
Sample 1	0.0063 σ	0.0000 σ	0.0044 σ
Sample 2	0.0223 σ	0.0000 σ	0.0177 σ
Sample 3	0.0063 σ	0.0031 σ	0.0044 σ

Table 6.32: Shifts in the Run 3 polarization fits in response to backgrounds being decreased by 1σ.

6.12.6 PID Studies

In order to evaluate the systematic uncertainties associated with the PID selectors a few approaches were studied. As *BABAR* has a number of options for PID a sub-set, consisting primarily of the most recent selectors, is studied. Table 6.33 lists all the PID selectors studied and the binary associated bits in the *BABAR* PID storage.

Particle	Selector	Map Bit
Electron	VeryLooseElectronMicroSelection	1
Electron	VeryLooseKMElectronMicro	7
Electron	LooseKMElectronMicro	8
Muon	BDTVeryLooseMuonSelection	16
Muon	BDTVeryLooseMuonSelectionFakeRate	20
Muon	BDTLooseMuonSelectionFakeRate	21

Table 6.33: List of selectors studied, bits 7,8,20,21 were chosen as the most recent selectors developed. 1 and 16 for comparison

Variation of Muon Selector

The default muon PID selector used in the analysis is the muBDTVeryLooseFakeRate selector which has a high muon acceptance rate as well as a more uniform pion acceptance rate compared to other selectors. In order to evaluate the systematic uncertainty we compare the VeryLoose version of the selector to the Loose version. This has small effect on the muon acceptance, a few percent, while decreasing pion efficiency by roughly 50%. This can be seen in Figures 6.51 and 6.52. Table 6.34 shows the shift in the fits as we switch between the selectors and we assign σ_{sys}=0.0030.

Variation of Electron Selector

The default electron selector for this analysis is VeryLooseKMElectronMicro. Similar to the muons the systematic uncertainty is evaluated by switching to the Loose version of the

Cut	Sample	Shift in Fit	Shift in Agreement
Loose PID	MC Data	-0.0065±0.0023 -0.0035	0.0030±0.0023

Table 6.34: Shift in fits caused by using Loose vs VeryLoose PID Selector

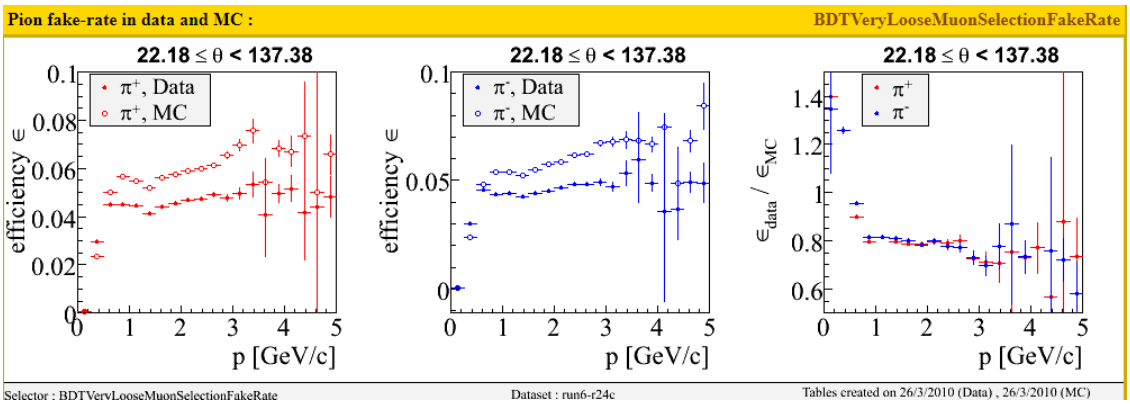

Figure 6.51: pion selection efficiency by VeryLoose muon PID[40].

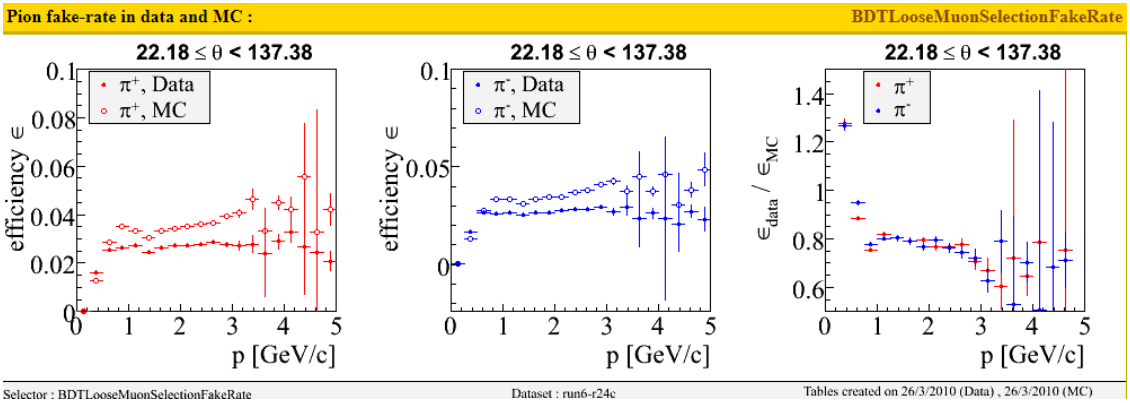

Figure 6.52: pion selection efficiency by Loose muon PID[40].

selector. The relative pion efficiencies are shown in Figures 6.53 and 6.54. Table 6.35 shows the effects of the switch and we assign $\sigma_{sys} = 0.0012 \pm 0.0007$ based on the shift.

6.12.7 Cross-checks of PID selection

As a cross-check of the PID variation tests a comprehensive test of all combinations of selectors was carried out. By defining electron selector '1' and muon selector '16' as default, the shift caused by the various PID selectors with respect to the default can by calculated. This was carried out in two ways, once using the full MC statistics and once splitting the

Cut	Sample	Shift in Fit	Shift in Agreement
Loose PID	MC	0.0010±0.0007	0.0012±0.0007
	Data	0.0022	

Table 6.35: Shift in fits caused by using Loose vs VeryLoose PID Selector

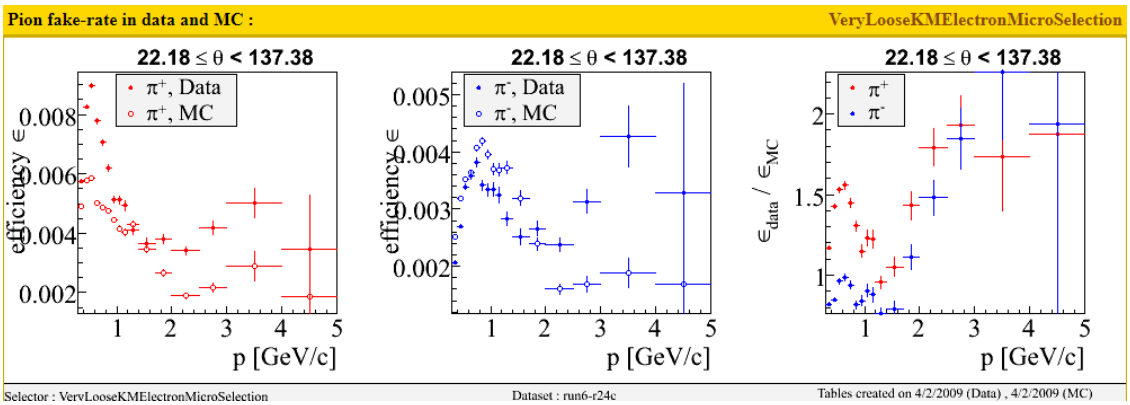

Figure 6.53: pion selection efficiency by VeryLoose electron PID[40].

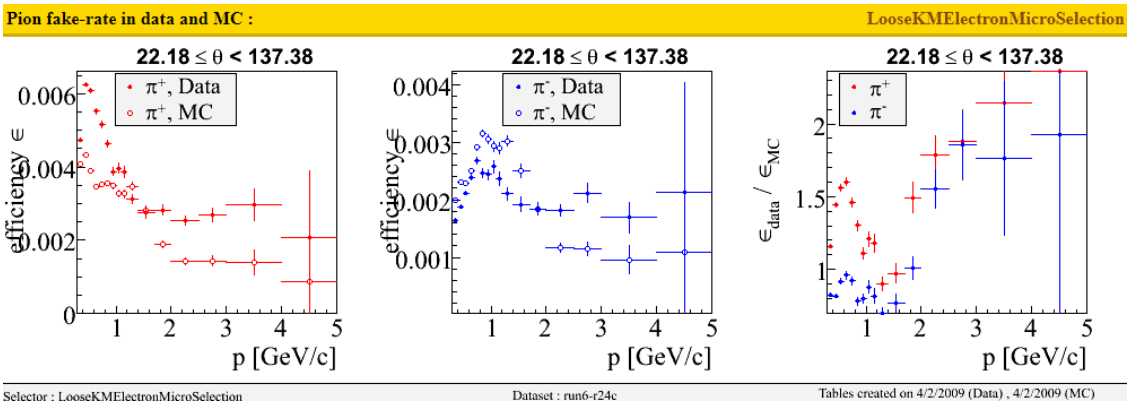

Figure 6.54: pion selection efficiency by Loose electron PID[40].

available MC into 3 samples as a way to evaluate the statistical uncertainty in the shifts. The results of both approaches are shown in Table 6.36 Examining Table 6.36 it can been seen that moving up or down a column (effectively changing electron selector) results in small shifts, while moving left or right along a row (changing muon selector) has a much larger effect. As a way to approximate a systematic uncertainty in the electron[muon] selector the average value and the standard deviation for each column[row] can be found. Taking the weighted average of the means across each column[row], using the standard deviation as the weight, provides a expected variation due to the change which can be interpreted as a systematic uncertainty. Applying this to Table 6.36 gives a systematic uncertainty of $\sigma_e^{PID} = 0.00021 \pm 0.00045$ and $\sigma_\mu^{PID} = 0.00328 \pm 0.0005$. These are in good agreement with the previously found numbers although the statistical uncertainties are small, suggesting this approach has underestimated the uncertainty.

Selectors	16	20	21
1	0.0000	-0.0065	-0.0039
7	0.0004	-0.0060	-0.0035
8	0.0006	-0.0059	-0.0034
E, M	16	20	21
1	0.0000 ± 0.0000	-0.0066 ± 0.0011	-0.0039 ± 0.0013
7	0.0002 ± 0.0002	-0.0062 ± 0.0011	-0.0037 ± 0.0014
8	0.0004 ± 0.0001	-0.0061 ± 0.0010	-0.0035 ± 0.0013

Table 6.36: Shifts in the central value of the fit caused by change in PID selector. Top half shows full MC statistics, bottom half shows average value when MC is split in order to approximate statistical uncertainty as the standard deviation in the shifts.

6.12.8 Branching Fraction Sensitivity

In order to determine the sensitivity to the τ decay branching fractions, the individual contributions of the different τ decay modes can be scaled by a multiplier derived from the world average uncertainty in the branching fractions [10] as shown in Table 6.12. In the case

Mode	Scale Down Factor	Scale Up Factor
e	0.99776	1.00224
μ	0.99770	1.00230
π	0.99538	1.00462
else	0.99860	1.00140

Table 6.37: BF scaling factors derived from the PDG uncertainties.

of the else branch, the branching fraction is taken to be $BF_{else} = 1 - BF_e - BF_\mu - BF\pi$ and $\sigma_{else} = \sqrt{\sigma_e^2 + \sigma_\mu^2 + \sigma_\pi^2}$. The scaling factor this produces are shown in Table 6.37. tables 6.38 to 6.45 show the results of varying the branching fractions. All shifts in the polarization measurement are very small and the systematic uncertainty associated with the branching fractions will be on the order of $\sigma_{sys} = 0.0001$. As was done with the non-tau backgrounds, the changes were only made to the unpolarized τ sample and since the resulting changes were insignificant no further investigation was done.

	Positive Diff	Negative Diff	Combined Diff
Sample 1	0.0007	-0.0009	-0.0001
Sample 2	0.0008	-0.0010	-0.0001
Sample 3	0.0009	-0.0010	-0.0001
Sample 1	0.0271 σ	-0.0357 σ	-0.0056 σ
Sample 2	0.0309 σ	-0.0398 σ	-0.0056 σ
Sample 3	0.0341 σ	-0.0395 σ	-0.0055 σ

Table 6.38: 1σ increase in the $\tau^{\pm} \to \pi^{\pm}\overline{\nu}_{\tau}$ branching fraction. Absolute shift in the fit(Top) and relative to statistical uncertainty(Bottom).

	Positive Diff	Negative Diff	Combined Diff
Sample 1	-0.0008	0.0010	0.0002
Sample 2	-0.0008	0.0009	0.0001
Sample 3	-0.0010	0.0010	0.0001
Sample 1	-0.0310 σ	0.0397 σ	0.0110 σ
Sample 2	-0.0308 σ	0.0357 σ	0.0055 σ
Sample 3	-0.0379 σ	0.0395 σ	0.0055 σ

Table 6.39: 1σ decrease in the $\tau^{\pm} \to \pi^{\pm}\overline{\nu}_{\tau}$ branching fraction. Absolute shift in the fit(Top) and relative to statistical uncertainty(Bottom).

	Positive Diff	Negative Diff	Combined Diff
Sample 1	0.0000	0.0000	0.0000
Sample 2	0.0000	0.0000	0.0000
Sample 3	0.0000	0.0000	0.0000
Sample 1	0.0000 σ	0.0000 σ	0.0000 σ
Sample 2	0.0000 σ	0.0000 σ	0.0000 σ
Sample 3	0.0000 σ	0.0000 σ	0.0000 σ

Table 6.40: 1σ increase in the $\tau^{\pm} \to e^{\pm}\nu_e\overline{\nu}_{\tau}$ branching fraction. Absolute shift in the fit(Top) and relative to statistical uncertainty(Bottom).

	Positive Diff	Negative Diff	Combined Diff
Sample 1	0.0000	0.0000	0.0000
Sample 2	0.0000	0.0000	-0.0001
Sample 3	-0.0001	0.0000	0.0000
Sample 1	0.0000 σ	0.0000 σ	0.0000 σ
Sample 2	0.0000 σ	0.0000 σ	-0.0055 σ
Sample 3	-0.0038 σ	0.0000 σ	0.0000 σ

Table 6.41: 1σ decrease in the $\tau^{\pm} \to e^{\pm}\nu_e\overline{\nu}_{\tau}$ branching fraction. Absolute shift in the fit(Top) and relative to statistical uncertainty(Bottom).

	Positive Diff	Negative Diff	Combined Diff
Sample 1	-0.0003	0.0004	0.0001
Sample 2	-0.0003	0.0004	0.0000
Sample 3	-0.0004	0.0004	0.0000
Sample 1	-0.0116 σ	0.0159 σ	0.0056 σ
Sample 2	-0.0116 σ	0.0159 σ	0.0000 σ
Sample 3	-0.0152 σ	0.0158 σ	0.0000 σ

Table 6.42: 1σ increase in the $\tau^{\pm} \to \mu^{\pm}\nu_{\mu}\overline{\nu}_{\tau}$ branching fraction. Absolute shift in the fit(Top) and relative to statistical uncertainty(Bottom).

	Positive Diff	Negative Diff	Combined Diff
Sample 1	0.0003	-0.0003	0.0000
Sample 2	0.0003	-0.0004	-0.0001
Sample 3	0.0003	-0.0004	-0.0001
Sample 1	0.0116 σ	-0.0119 σ	0.0000 σ
Sample 2	0.0116 σ	-0.0159 σ	-0.0055 σ
Sample 3	0.0114 σ	-0.0158 σ	-0.0055 σ

Table 6.43: 1σ decrease in the $\tau^{\pm} \to \mu^{\pm}\nu_{\mu}\overline{\nu}_{\tau}$ branching fraction. Absolute shift in the fit(Top) and relative to statistical uncertainty(Bottom).

	Positive Diff	Negative Diff	Combined Diff
Sample 1	0.0000	0.0001	0.0001
Sample 2	0.0000	0.0000	0.0000
Sample 3	-0.0001	0.0001	0.0000
Sample 1	0.0000 σ	0.0040 σ	0.0056 σ
Sample 2	0.0000 σ	0.0000 σ	0.0000 σ
Sample 3	-0.0038 σ	0.0040 σ	0.0000 σ

Table 6.44: 1σ increase in the $\tau \to$'else' branching fraction. Absolute shift in the fit(Top) and relative to statistical uncertainty(Bottom).

	Positive Diff	Negative Diff	Combined Diff
Sample 1	0.0000	0.0000	0.0000
Sample 2	0.0000	-0.0001	-0.0001
Sample 3	0.0000	0.0000	0.0000
Sample 1	0.0000 σ	0.0000 σ	0.0000 σ
Sample 2	0.0000 σ	-0.0040 σ	-0.0055 σ
Sample 3	0.0000 σ	0.0000 σ	0.0000 σ

Table 6.45: 1σ decrease in the $\tau \to$'else' branching fraction. Absolute shift in the fit(Top) and relative to statistical uncertainty(Bottom).

6.12.9 Neutral Clusters

The neutral clusters are handled in two different ways depending on the hemisphere they are in. Neutral clusters in the signal hemisphere must be below 50 MeV in energy. On the tag side of the event Neutrals below 100 MeV in energy are ignored and the remaining neutral clusters are used in the π^0 identification algorithms. In order to test the sensitivity to the minimum energy requirements for neutrals the cuts were shifted up and down by 1 MeV. This value was chosen as Figure 6.55 shows the comparison between data and MC and the agreement in the means of the distribution agree better than 1 MeV. Shifting the signal side minimum neutral energy requirement of 50 MeV by 1 MeV results in a relative shift between data and MC polarization fit results of $\sigma_{sys} = 0.0005 \pm 0.0001$. For the tag side requirement a similar cut shifting is done and results in a systematic uncertainty of $\sigma_{sys} = 0.0002 \pm 0.0009$.

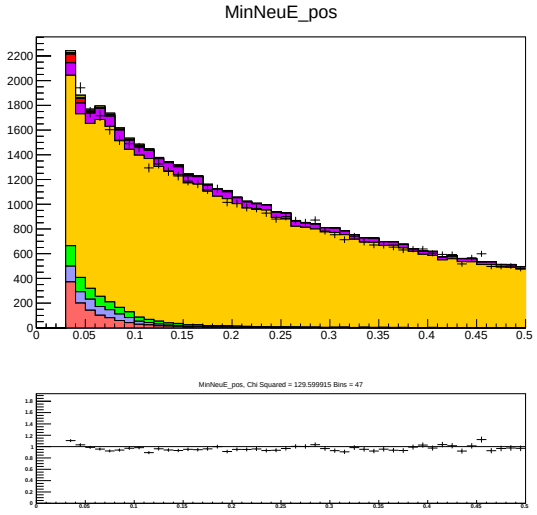

Figure 6.55: Neutral cluster energy of the lowest energy cluster in an event.

6.12.10 Charged Track List

The *BABAR* standard track list used in this analysis was GoodTracksVeryLoose. This is a minimal requirement on tracks. In order to test the efficiency of the selector I added the GoodTracksLoose requirements, ie. the track momenta must be less than 10 GeV and have a minimum Momentum of 50 MeV, to the analysis and looked at the shift in the fits. MC was not effected and the data fit shifted by 0.0003. So an uncertainty of σ_{sys}=0.0003 is assigned.

6.12.11 π^0 Requirements

As seen in Figure 6.56 the mass distributions for the reconstructed π^0 shows good agreement between data and MC. The average value of the histograms differs by 0.1 MeV. In order to quantify the level of agreement, the acceptance window for the π^0 mass was moved up and down by 1 MeV for both the high and low mass cut independently. The difference in the shift between the data and MC polarization fits is then used to estimate the systematic uncertainty. Taking the largest shift as the systematic uncertainty gives $\sigma_{sys}^{\pi^0 mass} = 0.0008$. For the π^0 likelihood variable, for a π^0 with both photons from its decay in the same EMC cluster (referred to as a "merged pi0"), a similar approach was taken. Finding a systematic uncertainty of $\sigma_{sys}^{\pi^0 lik} = 0.0003$

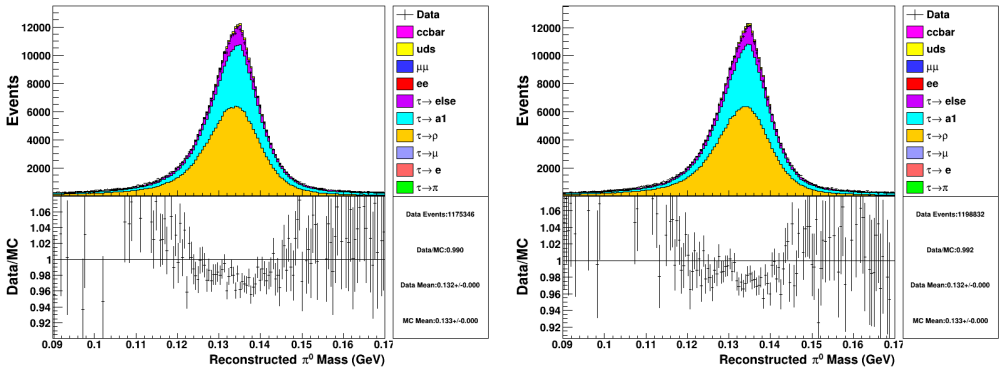

Figure 6.56: π^0 mass distributions.

	Variation	Shift
High Mass Cut	+1 Mev	0.0007
	-1 MeV	0.0008
Low Mass Cut	+1 Mev	0.0002
	-1 MeV	0.0004

Table 6.46: systematic shifts in the polarization fit between data and MC when the π^0 mass window is shifted by 1 MeV.

6.12.12 BGFTau

To evaluate the systematic effects associated with the BGFTAU flag, the analysis was skimmed without the flag. Turning the flag on and off caused only small shifts in the polarization fits, as only a small number of events pass the analysis and not the BGFTAU

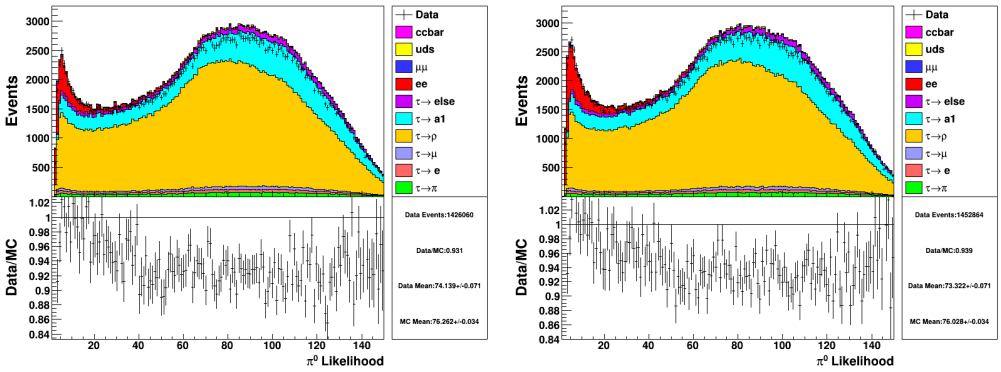

Figure 6.57: π^0 likelihood distributions.

Variation	Shift
+5 likelihood	-0.0003
-5 likelihood	0.0006

Table 6.47: systematic shifts in the polarization fit between data and MC when the likelihood cut is shifted

flag. Table 6.48 shows the shifts in the MC and Data shifts as the flag is turned off, and our assigned uncertainty of σ_{sys}=0.00086.

BGFTau Analysis

During the initial assessment of systematic uncertainties the inclusion/exclusion of the BGFTau flag was found to vary the fit results significantly. This was unexpected as the other analysis cuts were expected to place tighter restrictions than the BGFTau cut. However it was discovered that shifts on the order of 5% were occurring in the average polarization fit and up to 10% in the fits for the individual charges. Investigation into the BGFTau requirements revealed a few cuts that weren't explicitly required by the analysis. First an angular fiducial cut, requiring $\theta_{lab} \in [410, 2409]$mrad. Next a requirement that the total track momentum is less than 10 GeV. There is also a cut on the total track transverse momentum,

Cut	Sample	Shift in Fit	Shift in Agreement
BGFTau Off	MC	0.00097±0.00086	-0.00077±0.00086
	Data	0.0002	

Table 6.48: Shift in MC and Data when the BGFTau flag is turned off.

$\frac{\left(\vec{p}_{trk1}^{CM}+\vec{p}_{trk2}^{CM}\right)}{\sqrt{s}-|\vec{p}_{trk1}^{CM}|-|\vec{p}_{trk2}^{CM}|} > 0.02$. If any tracks have an $E/p > 0.8$ there are additional cuts. In order to reduce the effects on the BGFTau the following cuts were added/tightened in the analysis:

- $E/p < 0.75$ for both tracks
- $\theta_{lab} \in [430, 2350]$mrad
- $\frac{\left(\vec{p}_{trk1}^{CM}+\vec{p}_{trk2}^{CM}\right)}{\sqrt{s}-|\vec{p}_{trk1}^{CM}|-|\vec{p}_{trk2}^{CM}|} > 0.025$

The E/p cut is added to remove any dependence on that part of the BGF, the other two are set where they remove significant numbers of events which fail the BGFTau. Figure 6.58 shows the distributions of events in data for these variables. After applying these

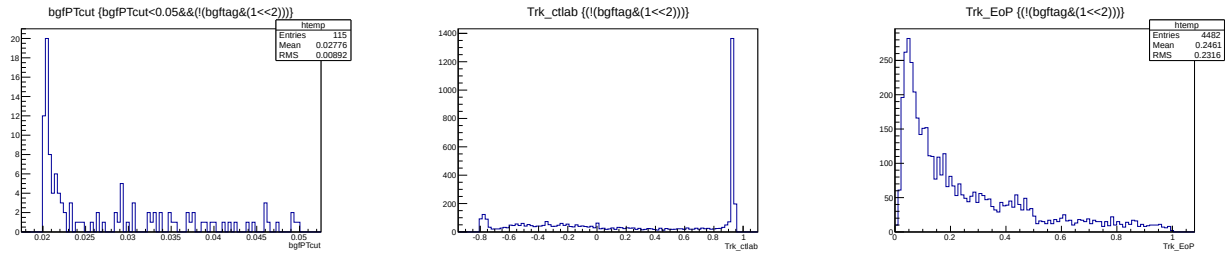

(a) Total track p_T (b) $\cos\theta$ in the lab frame (c) E/p for the Tracks

Figure 6.58: Events which fail the BGFTau but pass the analysis in Run 3 data. Cuts are set to remove the spikes in events in the first two plots. For the E/p plot the cut is placed arbitrarily with enough room to vary for systematic effects

cuts, switching between All-BGF and BGFTau still caused large shifts in the polarization fits. Investigating the τ decay mode in the τ MC of events that should fail the BGF but passed the analysis showed a large number of multitrack events which pass the analysis. This results from the inclusion of four track final states where only two of the four pass the GoodTracksVeryLoose requirement. In order to correct for this the requirement of two GoodTracksVeryLoose was changed to be teo charged tracks and two GoodTracksVeryLoose. This significantly improved the fit results and reduced the fluctuations to the order of 0.003. Examining the MC fits shows a statistical fluctuation on the order of 0.003. So full MC testing was carried out to determine the limit of the systematic uncertainty. Table 6.49 shows the shift in the MC and data polarization fits with and without the BGFTau.

6.12.13 Event P_T

There is excellent agreement between data and MC to the 1 MeV level in the total event P_T as seen in Fig. 6.59. To test for systematic sensitivities to this, the cut was varied up and

	Shift in Fit
MC	0.0031
Data	-0.0037

Table 6.49: Shifts in the MC and data fits when the BGFTau requirement is turned on and off

down by 5 MeV. The systematic uncertainty is assigned as 0.0003.

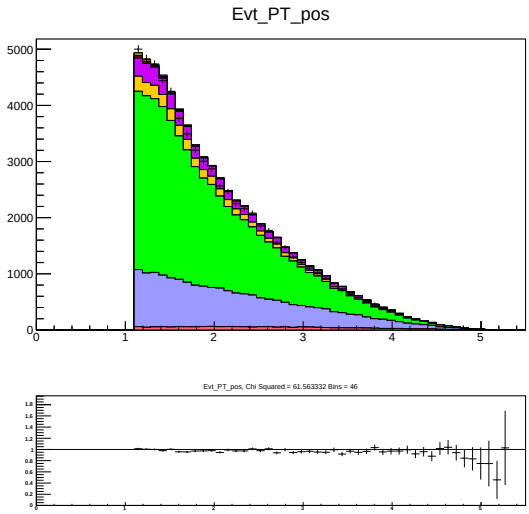

Figure 6.59: Event PT distribution after all cuts.

Cut Change	Sample	Shift	Difference
+5 MeV	MC	-0.00170	
	Data	-0.00169	0.00001
-5 MeV	MC	-0.00136	
	MC	-0.00166	-0.00030

Table 6.50: Shifts in polarization fits with changes to the total Event P_T requirement as described in the text.

6.12.14 E/p Systematics

An E/p cut was added as a replacement for the electron PID cut, but was eventually reverted back. It was initially experimented with as a way to stabilize the TauBGF and was subsequently found to have similar levels of separation with a simpler method. The cut was chosen to be at 0.75 and the systematic uncertainty measured by adjusting the cut and

Cut	Sample	Shift in Fit	Shift in Agreement
$E/p < 0.8$	MC	0.0003±0.002	-0.0002±0.002
	Data	0.0001	
$E/p < 0.7$	MC	-0.0008±0.002	0±0.002
	Data	-0.0008	
$E/p < 0.74$	MC	-0.0006±0.0015	0.0012±0.0015
	Data	0.0006	
$E/p < 0.76$	MC	0.0002±0.0011	-0.0007±0.0011
	Data	-0.0005	

Table 6.51: Shifts in agreement between Run 3 data and MC for the E/p systematic studies

looking at the shift in the agreement between data and MC. Table 6.51 shows the shift in data and MC for Run 3. The systematic is dominated by the fluctuations in the MC so we take the systematic to be σ_{sys}=0.0015. This systematic is no longer assigned as the E/p cut was found to bias the polarization fit and using Electron PID was found to be less biasing.

6.12.15 Luminosity Weighting

In the final version of the cuts there is a persistent 2% difference between data and MC that was not corrected until a source was discovered in Chapter 7. As the difference can be removed by changing the luminosity weighting we tested the effect of changing the MC luminosity by 5%. Table 6.52 shows the full fits for both setups. The Table shows no shifts in the central values of the fits and small shifts in the statistical uncertainties. As a precaution we assign a systematic uncertainty of σ_{sys}=0.0001 to account for the shift in the statistical uncertainty. However this shift is very small and provides a strong motive to not further pursue the weighting difference at this stage.

6.12.16 Neutral Veto Distance

In trying to understand the large effect the TauBGF variable was having on the analysis the distance between charged tracks and neutral clusters was investigated. It was discovered that there was a significant difference between data and MC for neutral clusters within ∼35cm of the charged tracks. We expect this is due to poor modelling of the hadronic split-offs, i.e. modelling of overlapping electromagnetic and hadronic interactions, from the tracks. In order to account for this a 40cm window around each track is defined. The neutral clusters within this region are combined with the track and removed from the event. To assign

Full MC			
Sample 1	-0.0010±0.0140	0.0034±0.0140	0.0012±0.0099
Sample 2	-0.0035±0.0140	-0.0339±0.0151	-0.0176±0.0103
Sample 3	-0.0074±0.0150	-0.0184±0.0151	-0.0128±0.0106
Data	0.0244±0.0146	0.0231±0.0157	0.0238±0.0107
0.95 Weighted MC			
Sample 1	-0.0010±0.0144	0.0034±0.0144	0.0012±0.0102
Sample 2	-0.0035±0.0144	-0.0339±0.0145	-0.0186±0.0102
Sample 3	-0.0074±0.0143	-0.0184±0.0143	-0.0129±0.0101
Data	0.0244±0.0148	0.0231±0.0158	0.0238±0.0108

Table 6.52: Polarization fits for MC and Data with correct luminosity weighting and a weighting shift of 5%.

Cut	Sample	Shift in Fit	Shift in Agreement
<39 cm	MC	-0.0001±0.0004	-0.0016±0.0004
	Data	-0.0017	
<41 cm	MC	0.0007±0.0008	-0.0008±0.0008
	Data	-0.0001	

Table 6.53: Shift in polarization fits due to shift in charged-neutral cluster recombination distance requirement.

an systematic uncertainty we vary the cut by 1 cm. Table 6.53 summarizes the shifts and suggests an uncertainty of σ_{sys}=0.0016.

6.12.17 Angular Separation between Charged and Neutral Tag Pions

While investigating the remaining discrepancies in the ρ mass peak and overall Data/MC weightings a deviation in the modelling of neutral pions which are nearly collinear with the charged pion was discovered. Figure 6.60 shows both of these discrepancies. A careful study of a variety of tag side variables revealed a discrepancy in the distributions of data and MC in the angular separation of the tag pions. There is already a correction in place to merge neutral clusters with charged EMC clusters that are within a 40cm radius. Figure 6.61 shows the distribution with the disagreement above 0.8. Figure 6.62 shows the improvement in the level of agreement in the previously shown ρ mass and signal track $\cos\theta$. Placing a cut at 0.8 for this separation requires 60% of the signal MC to be discarded. We also investigated the effect of a cut on the polarization fits and found shifts on the order of 0.3%. Since the signal and tag τ are spin correlated cutting on this variable could introduce a bias .

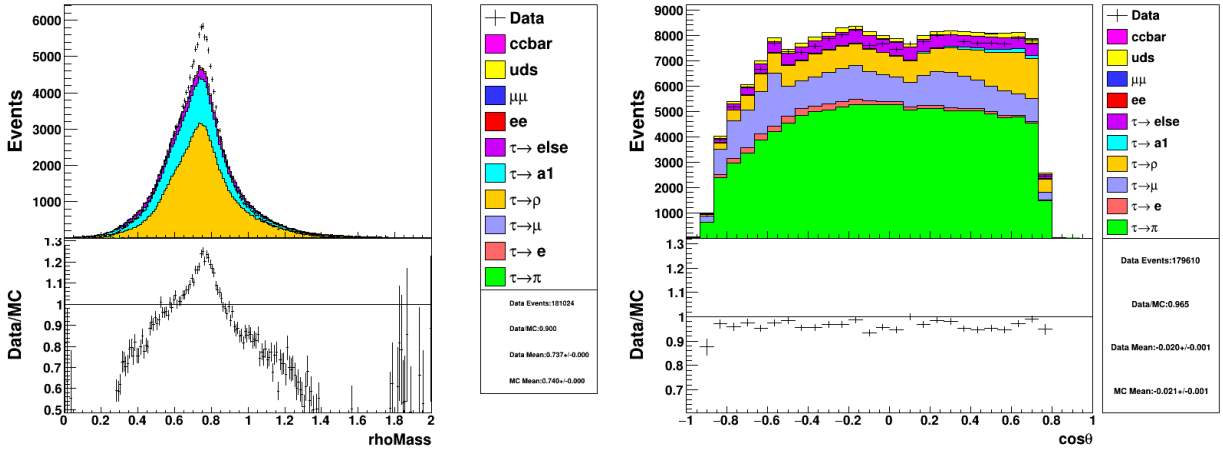

Figure 6.60: Reconstructed mass of the ρ meson in the tag hemisphere (left). There is a obvious difference between the shape of the data and MC. The right hand image shows the cosθ distribution for the negatively charged signal track, of note is the Data/MC ratio 0f 0.965.

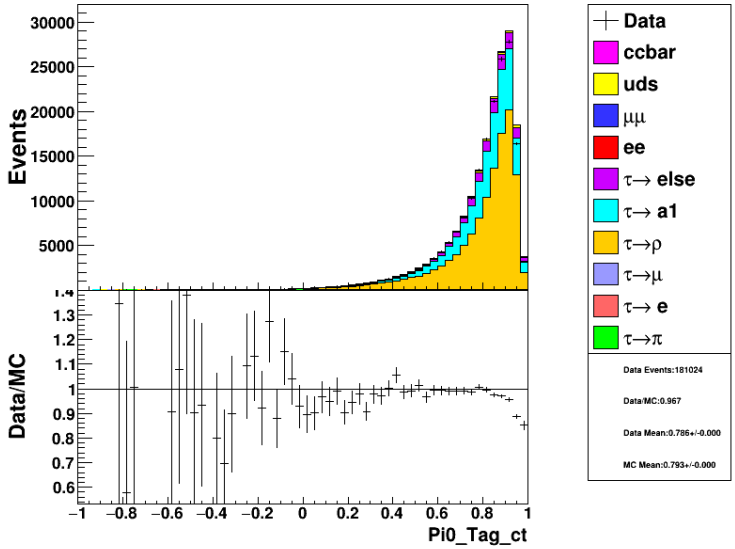

Figure 6.61: Angle between the momentum vectors of the charged tag pion and π^0.

Considering all of these effects we decided to not place any cut on the variable and since the effect is understood we don't apply a systematic uncertainty. A more complete discussion of this study is included below.

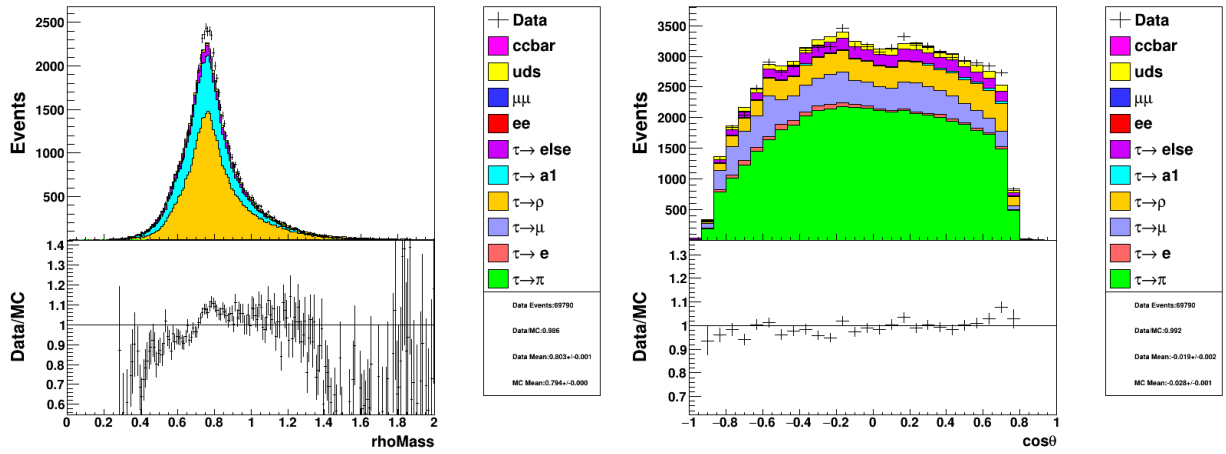

Figure 6.62: Reconstructed mass of the ρ meson in the tag hemisphere (left) and the $\cos\theta$ distribution of the signal track(right) after a cut of 0.8 is applied to the angle separating the tag pions.

Tag-pion angular separation bias study

Following the initial results in Section 6.12.17, The neutral pions on the tag side are accepted under one of two conditions. π^0's can be included in the event as either a single neutral cluster with a high pi0likelihood or as two neutral clusters with an invariant mass near the π^0 rest mass. As part of the study of the discrepancy in the tag side pions angular separation we looked at the distribution for each π^0 mode separately. Figure 6.63 shows the distributions of the angular separation for the two π^0 modes. The single neutral cluster seems to be better modelled however contributes to the Data/MC discrepancy below 0.8. The better agreement in the single neutral cluster is expected as neutral clusters nearby the charged cluster are already corrected for. The mass reconstructed π^0's show the majority of the shape disagreement in the angular separation. We studied cutting the distribution separately for the two π^0 modes but found no significant benefit to the final polarization fits as the loss of statistics outweighed any systematic shifts as these changes only affect the tag-side.

The systematic uncertainty associated with this discrepancy was evaluated by studying the effect on the polarization fit when the cut on the angular separation is stepped from 1 to 0.8. Figure 6.64 shows the shift in the agreement between the central values of the polarization fits for data and MC. ie. a negative value implies the data shifted more in the negative direction than the MC or the MC shifted more positive with respect to the data. The error bars capture the statistical fluctuations present in the MC, which is evaluated by

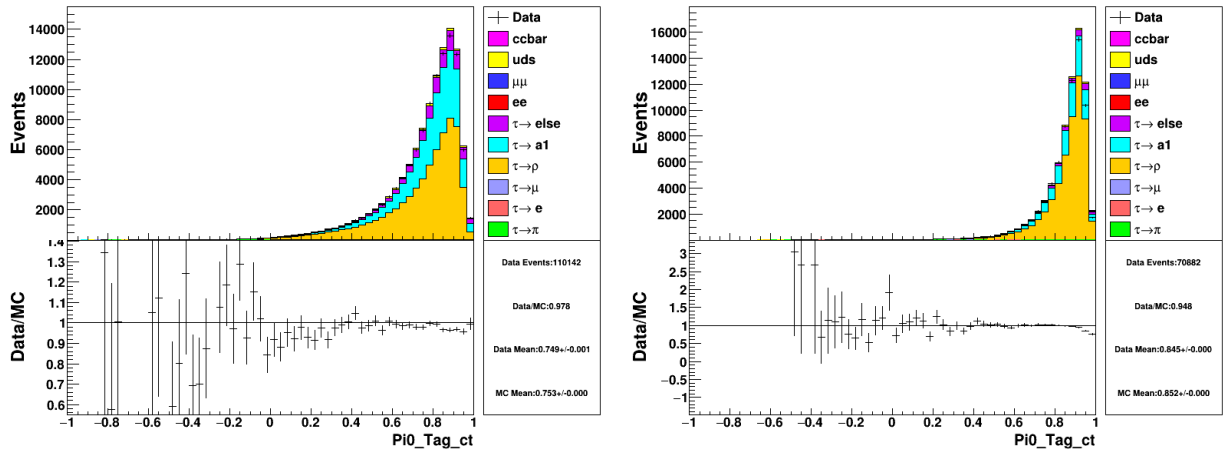

Figure 6.63: Angular separation between the tag-side charged and neutral pions. Left shows the distribution for pions from a single neutral cluster with a high likelihood. Right shows the distribution for π^0's reconstructed from the invariant mass of two clusters.

fitting the MC as three independent datasets. Figure 6.65 shows the shift in the central value of the polarization fit for the MC only. Comparing the two figures indicates the statistical uncertainties outweigh any underlying systematic effect. In order to reduce the statistical component all the available MC (Runs 1-6) was evaluated in the same manner. Figure 6.66 shows the MC only shifts once all runs are combined in a weighted average. The largest deviation is a 1.84% shift with a statistical uncertainty of 0.4%. As there appears to be no significant region for the cut which is results in a better fit result than having no cut in place, no cut on the angular separation is introduced.

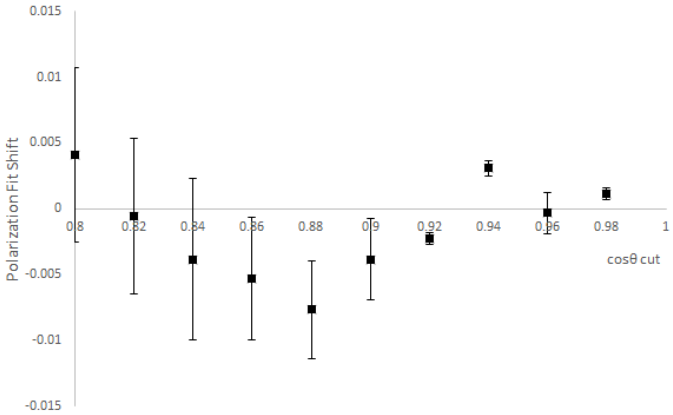

Figure 6.64: Shift in the agreement between data and MC polarization fits as the cut on the angular separation between the tag pions is stepped from 1(no cut) to 0.8(max cut).

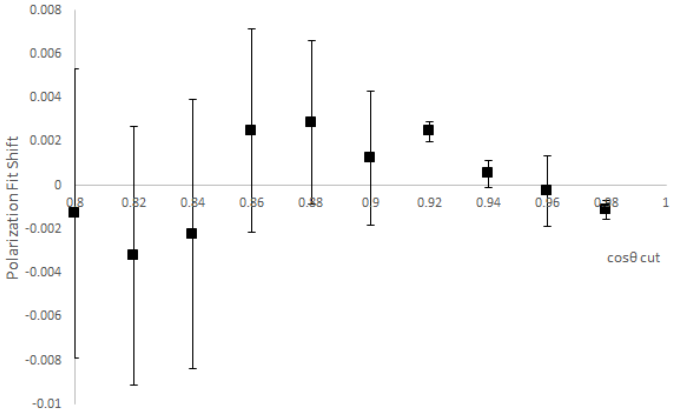

Figure 6.65: Shift in the MC polarization fits as the cut on the angular separation between the tag pions is stepped from 1(no cut) to 0.8(max cut).

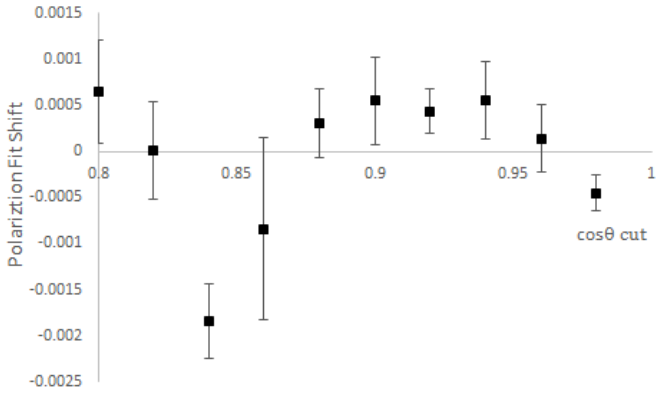

Figure 6.66: Weighted average shift in all runs MC polarization fits as the cut on the angular separation between the tag pions is stepped from 1(no cut) to 0.8(max cut).

6.12.18 Summary of Systematic Uncertainties

A summary of all the systematic uncertainties is listed in Table 6.54.

Study	Systematic
P	0.0015
Boost	0.0005
*θ	**0.0016**
ϕ	0
non-τ Backgrounds	0.0002
***PID$_\mu$**	**0.0030**
***PID$_e$**	**0.0012**
τ-BF	0.0001
E_γ^{signal}	0.0005
*E_γ^{tag}	**0.0009**
Charged List	0.0003
π^0 Mass	0.0008
π^0 Likelihood	0.0003
BGFTau	0.0009
Event P_T	0.0003
$\mathscr{L}$ Weight	0.0001
Neutral-Track Distance	0.0016
Total	0.0046

Table 6.54: Summary of systematic uncertainties associated with various requirements. Variables with a star are statistically dominated and may change with increased MC statistics.

6.13 Total Polarization Sensitivity

As the Tau Polarimetry method is being designed for use with a polarized electron beam, the method was tested at various total polarization states. In order to do this the available polarized τ MC was split into two samples. One sample for performing a polarization fit, and the other half for mixing various polarization states. Each section shows the fit results, a plot of the distribution of fits, a normalized plot of the fits, and a difference between the positive and negative charged fits. As the same sample measures each polarization state and there is a large overlap of data included in the fits there is a large correlation effect to be expected. This exhibits itself as a constant offset seen in all the measurements. Other effects such as a polarization dependence may hint towards a systematic effect. The Run 5 study is shown here and the other Runs are included as Appendix B.

Run 5 Sensitivity

The Run 5 results are seen in Table 6.55 and Figures 6.67 and 6.68.

Target	Positive Charge	Negative Charge	Combined Average	Deviation
-0.95	-0.9163 ± 0.0125	-0.9279 ± 0.0130	-0.9218 ± 0.0090	3.13 σ
-0.9	-0.8695 ± 0.0112	-0.8788 ± 0.0121	-0.8738 ± 0.0082	3.20 σ
-0.8	-0.7772 ± 0.0101	-0.7766 ± 0.0117	-0.7770 ± 0.0076	3.03 σ
-0.7	-0.6806 ± 0.0102	-0.6833 ± 0.0115	-0.6818 ± 0.0076	2.39 σ
-0.6	-0.5815 ± 0.0113	-0.5886 ± 0.0118	-0.5849 ± 0.0081	1.86 σ
-0.5	-0.4818 ± 0.0108	-0.4875 ± 0.0118	-0.4844 ± 0.0080	1.95 σ
-0.4	-0.3837 ± 0.0108	-0.3908 ± 0.0111	-0.3871 ± 0.0077	1.68 σ
-0.3	-0.2841 ± 0.0108	-0.2908 ± 0.0117	-0.2872 ± 0.0079	1.62 σ
-0.2	-0.1921 ± 0.0107	-0.1907 ± 0.0109	-0.1914 ± 0.0077	1.12 σ
-0.1	-0.0932 ± 0.0107	-0.0930 ± 0.0115	-0.0931 ± 0.0078	0.88 σ
0	0.0061 ± 0.0114	0.0040 ± 0.0107	0.0050 ± 0.0078	0.64 σ
0.1	0.1010 ± 0.0107	0.0998 ± 0.0114	0.1004 ± 0.0078	0.05 σ
0.2	0.1965 ± 0.0107	0.1965 ± 0.0106	0.1965 ± 0.0075	-0.47 σ
0.3	0.2973 ± 0.0107	0.2961 ± 0.0105	0.2967 ± 0.0075	-0.44 σ
0.4	0.3909 ± 0.0107	0.3959 ± 0.0105	0.3935 ± 0.0075	-0.87 σ
0.5	0.4840 ± 0.0108	0.4879 ± 0.0104	0.4860 ± 0.0075	-1.87 σ
0.6	0.5782 ± 0.0113	0.5851 ± 0.0104	0.5819 ± 0.0076	-2.38 σ
0.7	0.6753 ± 0.0108	0.6858 ± 0.0096	0.6812 ± 0.0072	-2.61 σ
0.8	0.7751 ± 0.0098	0.7821 ± 0.0108	0.7783 ± 0.0073	-2.97 σ
0.9	0.8719 ± 0.0098	0.8783 ± 0.0105	0.8749 ± 0.0072	-3.49 σ
0.95	0.9229 ± 0.0118	NAN	-	-

Table 6.55: Sensitivity to total polarization in Run 5 MC

6.14 Full *BABAR* MC Analysis

From the Run 3 studies an average beam polarization of $\langle P \rangle = 0.0118 \pm 0.0117_{\text{stat}} \pm 0.0046_{\text{sys}}$ was found for the $\tau^{\pm} \to \pi^{\pm}\overline{\nu}_{\tau}$ channel with a $\tau^{\pm} \to (\rho^{\pm} \to \pi^{\pm}\pi^{0})\overline{\nu}_{\tau}$ tag. In order to prepare for unblinding the analysis and fitting the data from all Runs a test run is performed on all the available MC. The results can be seen in Figure 6.69. Taking the average of the measurements gives 3 MC total measurements, these are shown in Table 6.56. With the Run 3 sample performing well and the MC test fits showing no issues, the Run 2 data-set was unblinded and fit for beam polarization.

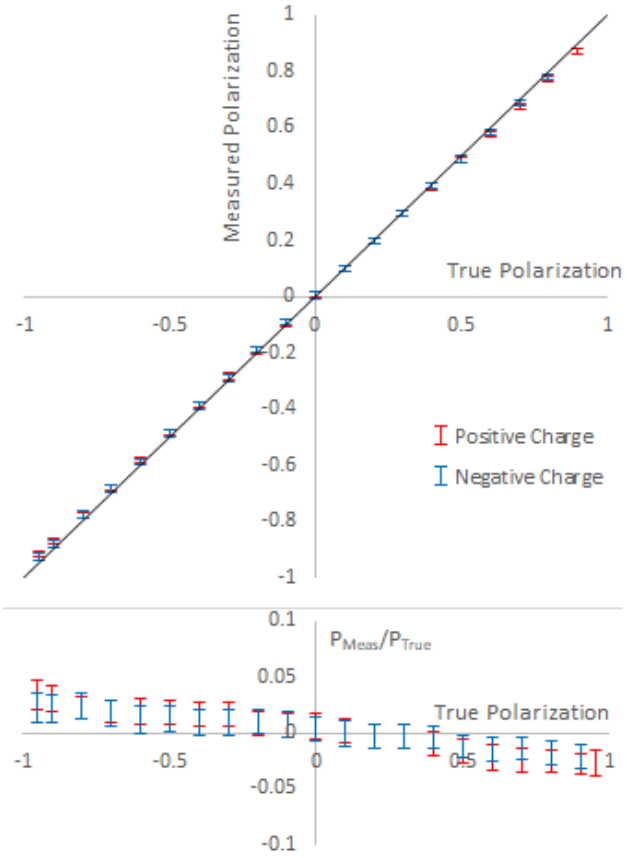

Figure 6.67: Results from Table 6.55 plotted. The line y=x also shown for reference. The lower plot shows the same points normalized by the true polarization.

Subset	Average Polarization
First MC Fits	0.0067±0.0030
Second MC Fits	0.0030±0.0030
Third MC Fits	0.0020±0.0030

Table 6.56: Weighted average of MC polarization fits shown in Figure 6.69. Points are combined as left most, middle, and right most from each run.

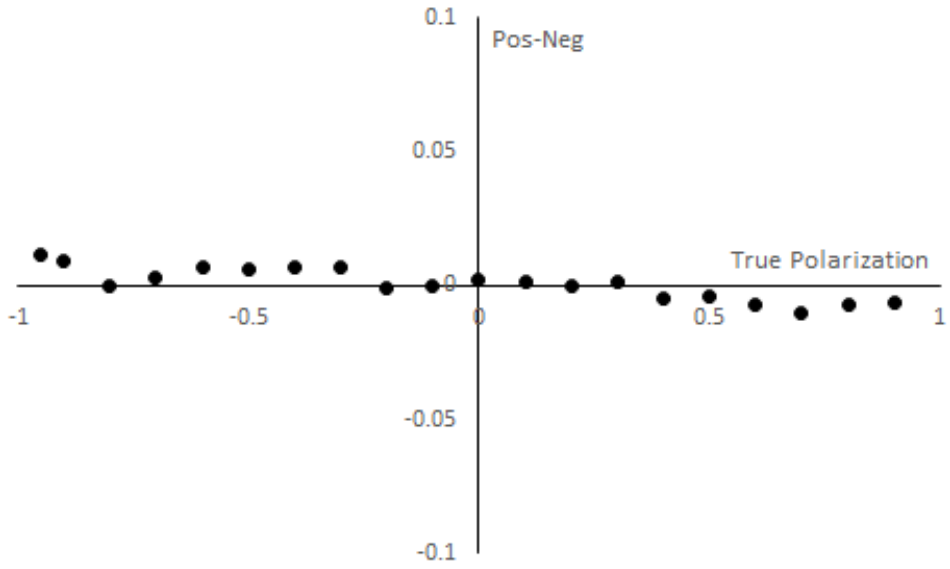

Figure 6.68: The difference between the positive and negative run 5 polarization measurements as a function of the true polarization.

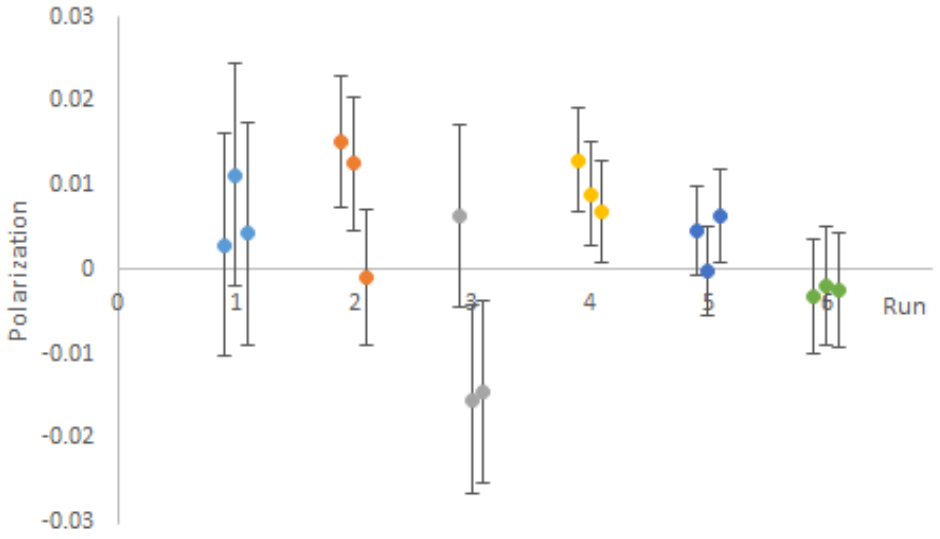

Figure 6.69: MC fits for all runs. MC is broken down into 3 samples by the usual method.

6.15 Initial Run 2 Polarization Measurement

The initial polarization fit of Run 2 showed nearly 8% polarization in the negative charged candidates. Table 6.57 shows the full Run 2 results, where only the negatively charged candidates in data deviate from zero. Given the 7σ tension with 0 observed in the Run 2 negative charge fit as seen in Table 6.58, we can strongly rule out the run 2 negative charge fit being solely a statistical fluctuation.

One could consider that a bias exists in either the Run 2 data or in the negative charge

	Positive Charge	Negative Charge	Combined Average
Sample 1	0.0103±0.0109	0.0212±0.0110	0.0157±0.0078
Sample 2	-0.0041±0.0110	0.0284±0.0110	0.0122±0.0078
Sample 3	-0.0069±0.0109	0.0113±0.0109	0.0022±0.0077
Data	0.0099±0.0111	0.0786±0.0112	0.0441±0.0079

Table 6.57: Run 2 default polarization fit

Run	Positive	Negative
2 Data	0.89σ	7.02σ
3 Data	0.97σ	0.16σ

Table 6.58: Level of agreement between fits and an assumption of no beam polarization.

Run	Positive	Negative	Agreement
2 Data	0.0099±0.0111	0.0786±0.0079	4.36σ
3 Data	0.0153±0.0158	0.0026±0.0158	0.57σ
Agreement	0.28σ	3.92σ	

Table 6.59: Level of agreement between charges (Horizontal) and Runs (Vertical). Results suggest 8% bias could either be a 4%(average) beam polarization effect in Run 2 with agreement requiring a 4σ tension, or a 4% selection bias in the negative charges with a 4σ tension existing between runs. (Under the assumption bias is only statistical effect)

event selection. Table 6.59 shows the level of consistency between the Run 2 and Run 3 fit results. The results suggest the bias could be interpreted as a 4σ statistical effect under one of two assumptions. The first assumption we consider is that there is a 4% beam polarization bias in the run 2 data-set and we observe two extreme measurements (near 0 in positive, near 8% in negative). The other possible interpretation is a 4% bias in the negative event selection criteria where we observe Run 3 being below the 4% average near 0% and Run 2 near 8%. Of these conclusions, the latter seems intuitively more likely however still requires

accepting a 4σ difference. To investigate potential sources of the polarization bias a number of possibilities for the source of the bias were investigated.

1. A different fit method, a bin-by-bin χ^2 minimization, was implemented
2. The muon PID was turned off and the fit performed with the combined final state muons and pions
3. Additional cuts which restrict the analysis to only use bins where the PID is modelled to better than 1%
4. Performing the fit on the tagging charged pion from the ρ instead, as another pion sample to test PID bias
5. All available muon PID selectors were tried
6. The electron PID was replaced with an E/p cut
7. The pi-zero requirements were loosened
8. The Event p_T and Track E/p requirements were loosened
9. The Fit results were visually verified
10. A new semi-independent event selection is developed

The results of all of these tests are discussed below but they all confirm the polarization in the negative charge is a real effect. It seems the only remaining possibility is a mismodelling of the detector behaviour for negatively charged pions in Run 2 that exhibits as polarization in this analysis.

Statistical Analysis

From all of these studies it seems that the polarization effect is caused by a real effect in the Data. There doesn't seem to any significant bias introduced by the event selection criteria.

6.15.1 Secondary Fit

In order to check that the fit is performing as expected a secondary fit was implemented. As a first step the χ^2 was calculated "by-hand" at arbitrary polarization states by looping over all the bins in the fit. The results of this cross-check are seen in Figure 6.70. As a followup a chi-squared minimization using the ROOT TF2 class was implemented. This minimization found similar results as seen in Table 6.60.

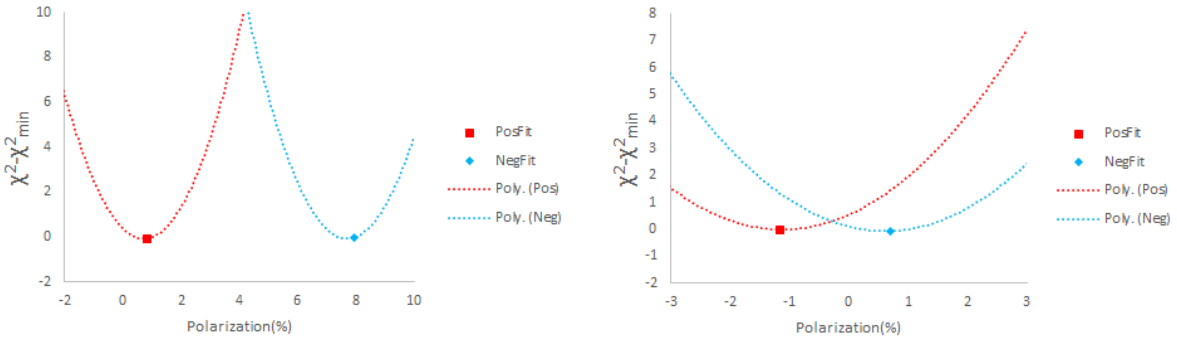

Figure 6.70: Fit Results for Run 2(left) and Run 3(right). The data point is the minimization from the TFractionFitter used in the analysis while the dashed line is the "by-hand" chi2 calculation at arbitrary polarization states.

Fit Type	Positive	Negative
Default	0.0099±0.0111	0.0786±0.0112
Chi2	0.0053±0.0098	0.0751±0.0098

Table 6.60: Fit results from the default TFractionFitter and the Chi2 minimization

6.15.2 Muon PID studies

High Statistics PID Corrections

While performing a cross-check that the left and right polarized τ MC behave the same as the unpolarized it was noticed that the right polarized MC has a statistically significant efficiency difference compared to left polarized MC when the PID cuts are applied. This can be seen in Table 6.61 and does not seem to be a generator or missing file issue as the discrepancy appears to be properly averaged in the unpolarized *BABAR* Tau MC. Moving

Sample	$\varepsilon_{\text{Positive}}$	$\varepsilon_{\text{Negative}}$	$\frac{\varepsilon_{\text{Positive}}}{\varepsilon_{\text{Negative}}}$
Left Tau MC	0.0719	0.0718	1.0010 ± 0.0016
Right Tau MC	0.0719	0.0703	1.0224 ± 0.0026
BABAR Tau MC	0.0720	0.0712	1.0108 ± 0.0011

Table 6.61: Selection efficiency for τ MC samples after the PID requirements are applied. The last column shows the ratio of the efficiencies for positive and negatively charged candidates.

forward with the assumption that this ∼2% efficiency difference could result in the observed polarization in data I investigated the muon PID tables and found a significant number of bins with low statistical significance. In order to test the hypothesis that the polarization was due to a statistical fluctuation in the muon PID I restricted the fit to only use regions

of the detector with enough statistics to “trust" the accuracy of the PID corrections. This was done by merging the phi bins in the PID tables to reduce down to momentum and theta bins only. Then a plot of all the bins which have better than 1% accuracy on the muon efficiency are plotted, as seen in Figure 6.71. From this plot two regions were selected to test the effects of the PID accuracy, a rectangular region between 2.4 and 3.2 GeV and a parallelogram moving towards lower degrees in theta as momentum increases.

```
if(p>2.4)
    if(p<3.2)
        if(theta>62 and theta<135) PASS
        else FAIL
    else
        if(theta<(-26*p+218) and theta>(-17*p+117)) PASS
        else FAIL
else FAIL
```

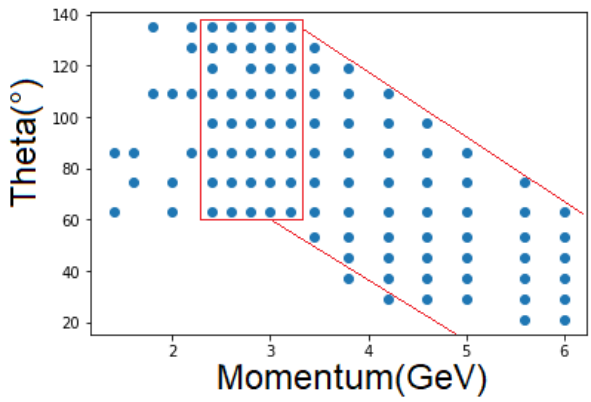

Figure 6.71: Bins in theta and momentum, lab frame, where the PID efficiency in data is known to better than 1%. Bins in phi have been averaged to produce the 2D representation. Red lines outline the acceptance region.

Applying these cuts reduces the centre of mass frame parameters significantly as seen in Figure 6.72. Fitting with this parameter region gives the results seen in Table 6.62. From these results we can conclude a bias in the bins of the PID with a small number of control samples is not the problem.

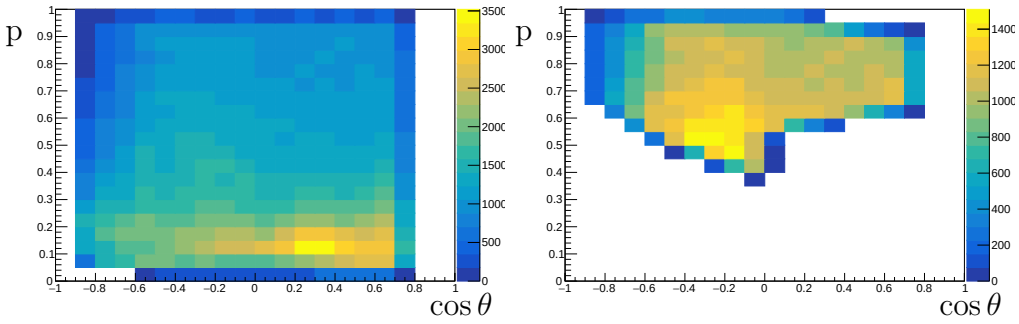

Figure 6.72: Distribution of events for default selection(Left), and only accepting bins with PID efficiency accuracy better than 1%(Right).

	Positive Charge	Negative Charge	Combined Average
Sample 1	-0.0233 ± 0.0132	0.0414 ± 0.0134	0.0087 ± 0.0094
Sample 2	-0.0237 ± 0.0133	0.0394 ± 0.0133	0.0077 ± 0.0094
Sample 3	-0.0390 ± 0.0132	0.0305 ± 0.0133	-0.0045 ± 0.0094
Data	-0.0215 ± 0.0134	0.0886 ± 0.0136	0.0329 ± 0.0095

Table 6.62: Run 2 polarization fit with only bins where the PID efficiency is known to better than 1%.

PID Bias on Tag Pion Test

As a final way to rule out the muon PID as the culprit for the bias, the fit is performed with the momentum of the tagging ρ decay pion. This effectively reverses the tag and signal side definitions, giving an independent source of pions to check for PID bias. Table 6.63 shows this tag side fit. In order to test the effect of PID on the tag side pions the electron and muon PID requirements are applied to the ρ decay pion and the tag side fit performed again. The results of this fit and the overall shift are shown in Table 6.64. The effect of adding PID to the tag side pions seems to have only a small effect on the fits, ranging from 0.0005 to 0.0080, which is not enough to account for the 8% bias observed in the signal side pions.

	Negative Charge	Positive Charge	Combined Average
Sample 1	-0.0007±0.0135	0.0133±0.0135	0.0063±0.0095
Sample 2	0.0021±0.0135	-0.0043±0.0152	-0.0007±0.0101
Sample 3	0.0068±0.0150	0.0332±0.0138	0.0212±0.0102
Data	-0.0377±0.0137	-0.0344±0.0154	-0.0362±0.0102

Table 6.63: Run 2 polarization ρ decay pion momentum fit using the momentum and cosθ of ρ decay pion. PID is only applied to the pion from the direct τ to pion decay and not on the ρ decay pion.

	Negative Charge	Positive Charge	Combined Average
Sample 1	0.0010±0.0139	0.0054±0.0156	0.0029±0.0104
Sample 2	0.0050±0.0139	-0.0073±0.0156	-0.0004±0.0103
Sample 3	0.0073±0.0155	0.0287±0.0139	0.0191±0.0103
Data	-0.0294±0.0157	-0.0316±0.0158	-0.0305±0.0112
Sample 1	-0.0079	0.0017	-0.0034
Sample 2	-0.0030	0.0029	0.0003
Sample 3	-0.0045	0.0005	-0.0021
Data	0.0028	0.0083	0.0057

Table 6.64: Run 2 polarization ρ decay pion momentum fit with PID requirements applied to both charged pions in the event. The shift in the fits compared to the PID only being applied to the $\tau^{\pm} \to \pi^{\pm}\overline{\nu}_{\tau}$ pion is also shown.

Muon PID Selector

The muon PID selector used in this analysis is BDTVeryLooseMuonSelectionFakeRate, and in order to rule out a bias associated with this selector two others were tested. First a neural net trained PID selector, and second a cut based selector, in both cases the VeryLoose versions were used. It was found that for both selectors only minimal changes are observed and the bias remains unexplained. From this and the previous muon PID studies we conclude that the muon PID is not the cause of the 8% bias.

6.15.3 Data Splitting

In order to determine if the bias is localized in the data the data is split in two ,$p/E_{beam} > 0.5$ and $p/E_{beam} < 0.5$, to test for bias in either set. This splitting was then repeated for $\cos\theta > 0$ and $\cos\theta < 0$. This is performed in both run 2 and run 3 to help identify anomalous results. Table 6.65 shows the results of this study, it was found that in all cases the MC would track with the changes in data and the run 2 bias persists.

6.15.4 Electron PID

In order to confirm the electron PID requirement is not responsible for the bias the electron PID is replaced with an E/p cut of less than 0.8. The fit result is shown in Table 6.66 and shows no sign of reducing the bias.

Run 2	Data		MC	
Cuts	Positive	Negative	Positive	Negative
Default	0.0085±0.0111	0.0801±0.0112	0.0002±0.0063	0.0199±0.0063
$p/E_{beam} > 0.5$	0.0008±0.0119	0.0676±0.0120	-0.0056±0.0068	0.0083±0.0068
$p/E_{beam} < 0.5$	-0.0023±0.0303	0.0622±0.0300	-0.0250±0.0168	0.0186±0.0168
$\cos\theta > 0$	0.0509±0.0177	0.0208±0.0168	0.0770±0.0101	-0.0452±0.0096
$\cos\theta < 0$	-0.0758±0.0166	0.0948±0.0175	-0.0663±0.0093	0.0919±0.0099
Run 3	Data		MC	
Cuts	Positive	Negative	Positive	Negative
Default	0.0125±0.0156	0.0024±0.0156	-0.0141±0.0088	-0.0013±0.0088
$p/E_{beam} > 0.5$	0.0181±0.0165	-0.0051±0.0167	-0.0156±0.0095	-0.0106±0.0094
$p/E_{beam} < 0.5$	-0.1170±0.0737	-0.1277±nan	-0.0055±0.0237	-0.0631±0.0235
$\cos\theta > 0$	0.0750±0.0238	-0.0325±0.0225	0.0690±0.0136	-0.0768±0.0132
$\cos\theta < 0$	-0.1029±0.0248	0.0243±0.0250	-0.0893±0.0139	0.0526±0.0143

Table 6.65: Data fit results when only 50% of parameter space is fit. In all cases the Run 2 Negative charge bias remains, expect in $\cos\theta > 0$. However MC fits predict the fit should return -5% so the positive bias is still present.

	Positive Charge	Negative Charge	Combined Average
Sample 1	0.0081±0.0109	0.0218±0.0117	0.0145±0.0080
Sample 2	-0.0045±0.0110	0.0281±0.0110	0.0119±0.0078
Sample 3	-0.0086±0.0109	0.0102±0.0109	0.0008±0.0077
Data	0.0153±0.0112	0.0759±0.0112	0.0456±0.0079

Table 6.66: Run 2 fit with E/p cut instead of electron PID selector

6.15.5 π^0, p_T, and E/p cuts

In order to test the effect of the other analysis cuts, they were significantly loosened to allow more events through. In all cases no significant effect on the 8% bias was observed. If the cuts are significantly tightened it is possible to reduce the statistics to a level where the statistical uncertainty can account for the shift at a 2σ level, however the central value never dips below 6% polarized.

6.15.6 New Event Selection

It was noticed after the ρ vs electron analysis that the Event p_T cut is not required to remove two photon events for that analysis. While the cut is still required in the pion vs ρ analysis an re-evaluation of the cut was done to see if the cut could be reduced. An initial evaluation of the variables suggested that some ρ variables may be able to replace the Event p_T cut

at least in part. Figure 6.73 shows the distribution for p_T without the cut, as well as the ρ mass reconstruction and the angular separation between the charged and neutral pions resulting from the τ decay. The two-photon contamination can be seen at the low values of p_T which necessitated the 1.2 GeV cut. It was noted that the majority of these two-photon

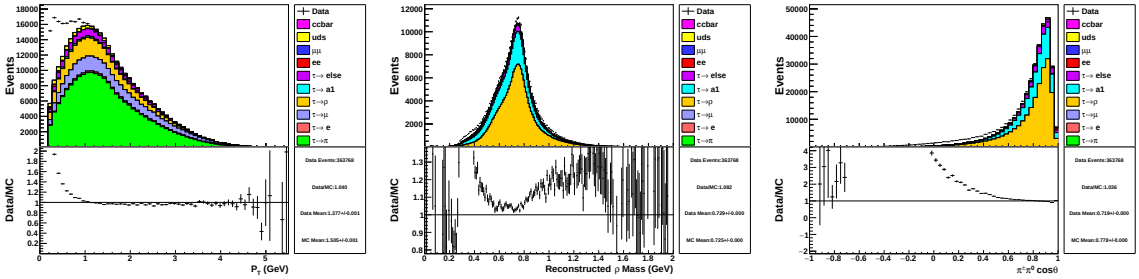

Figure 6.73: Distribution of transverse momentum, ρ mass, and angular separation of ρ decay pions for the pion vs ρ analysis with no cut on the transverse momentum.

events seem to be localized at large angular separation and low ρ mass. So in place of a cut on p_T two new cuts were evaluated. First the angular separation between the charged and neutral pions is required to be $\cos\theta > 0.6$, which still leaves the bump seen in the low ρ mass regime. So a second cut of ρ mass > 0.5 GeV is also added. The effects of these cuts are shown in Figure 6.74. After these two new cuts there is still a small amount of two photon

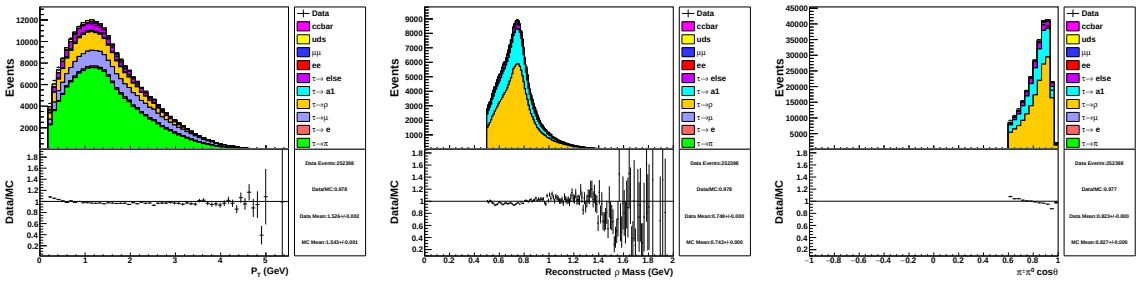

Figure 6.74: Distribution of transverse momentum, ρ mass, and angular separation of ρ decay pions for the pion vs ρ analysis with the following cuts: pion separation $\cos\theta > 0.6$, and ρ mass > 0.5 GeV.

events visible at low p_T, so a cut is reintroduced at 0.5 GeV. The final selection is shown in Figure 6.75. These new cuts improve the event selection efficiency significantly. With the number of run 2 events selected increasing from 184201 to 230380 which is a 25% increase in statistics. The effect on the data fit is shown in Table 6.67. The results show only an improvement in statistics but no significant shift in the bias.

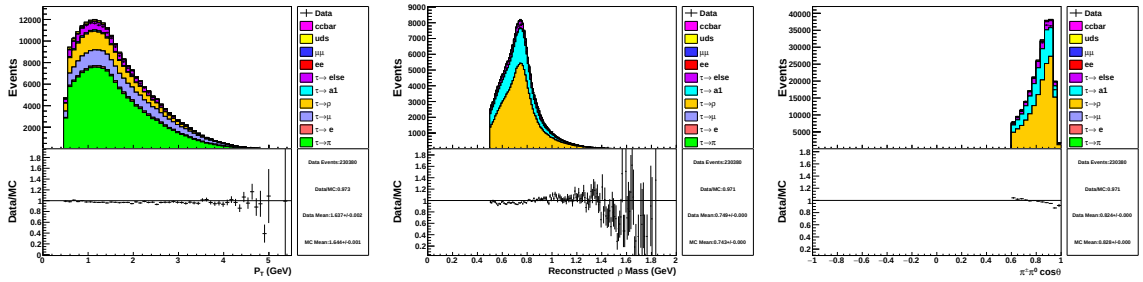

Figure 6.75: Distribution of transverse momentum, ρ mass, and angular separation of ρ decay pions for the pion vs ρ analysis with the following cuts: pion separation $\cos\theta > 0.6$, ρ mass > 0.5 GeV, and $p_T > 0.5$ GeV.

	Positive Charge	Negative Charge	Combined Average
Original Data Fit	0.0099±0.0111	0.0786±0.0112	0.0441±0.0079
New Data Fit	0.0110±0.0089	0.0795±0.0087	0.0460±0.0062

Table 6.67: Effect of new event selection strategy on the polarization fits in data. MC fits saw a similar lack of response.

6.15.7 Data Visualization

As the polarization fits are somewhat abstracted from direct view, due in part to the 2D nature of the fit as well as the use of templates rather than linear variables. It seemed plausible that some statistical bias in a small number of bins may bias the fit. In order to look for such effects, 1 Dimensional projections of the fit as well as 2D heatmaps were produced. Figures 6.76 and 6.77 show the 1D projections of fit for the $\cos\theta$ variable. The effect of the polarization is barely visible. To better visualize the Data polarization effect, a 2D heatmap is made. The heat map shows the ratio of the ratios of Data over MC for positive and negative charges. In equation form:

$$R_{\pm} = \frac{\text{Data}_{\pm}}{\text{MC}_{\pm}} \qquad \text{Plot} = \frac{R_{+}}{R_{-}} \tag{6.8}$$

The Run 2 and 3 heatmaps are shown in Figure 6.78. A forward-backward asymmetry is visible in the Run 2 which is not present in Run 3.

6.15.8 Run2 Bias Conclusions

At this stage it seems we're faced with only a few remaining possibilities:

- A 8% run dependent charge bias is introduced in the pre-analysis variables (Trigger,

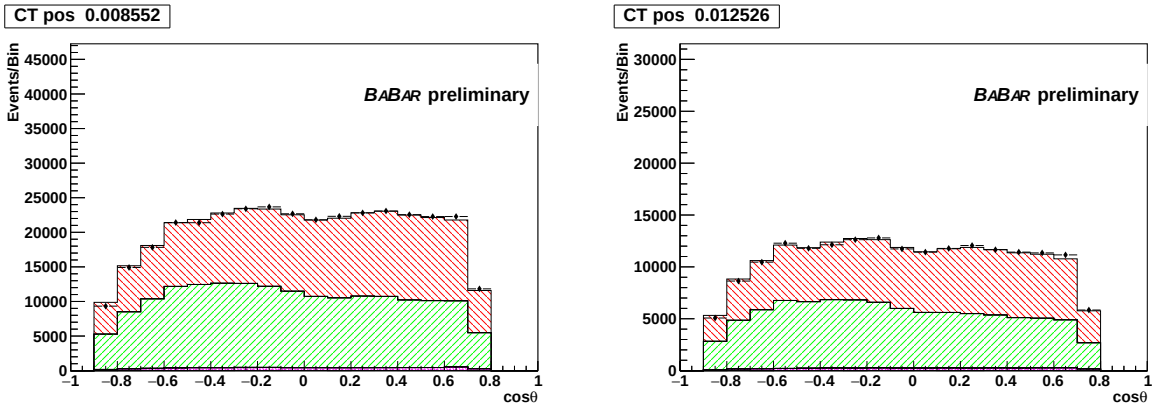

Figure 6.76: Positive Fits for Run 2(Left) and Run 3(Right). $\cos\theta$ Projection

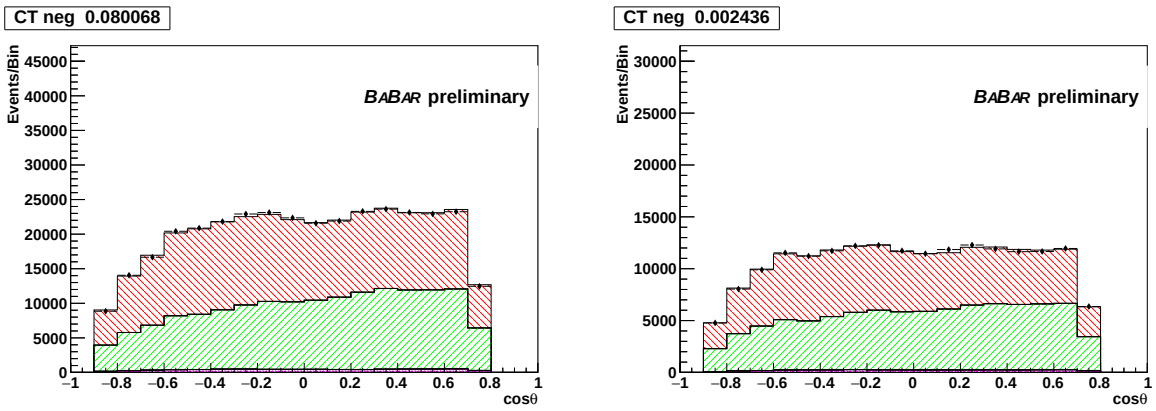

Figure 6.77: Negative Fits for Run 2(Left) and Run 3(Right). $\cos\theta$ Projection

TauBGF, TrackLists, etc..)

- A 4% selection bias in the negative charge with a 4σ tension between runs
- A 4% beam polarization bias in Run 2 with a 4σ tension between charges

All of these possibilities seem unlikely but no other solution seems to be readily available. In order to move the analysis forward another data-set will need to be unblinded to determine if this issue is unique to Run 2, or indicative of a larger issue with the analysis.

6.16 Conclusions

Through the development of Tau Polarimetry many useful insights were obtained. These include the degree to which muons contaminate the $\tau^{\pm} \to \pi^{\pm}\overline{\nu}_{\tau}$ samples from both $e^+e^- \to \mu^+\mu^-$ and $\tau^{\pm} \to \mu^{\pm}\nu_{\mu}\overline{\nu}_{\tau}$ events. This highlights the need for improved pion-muon separation,

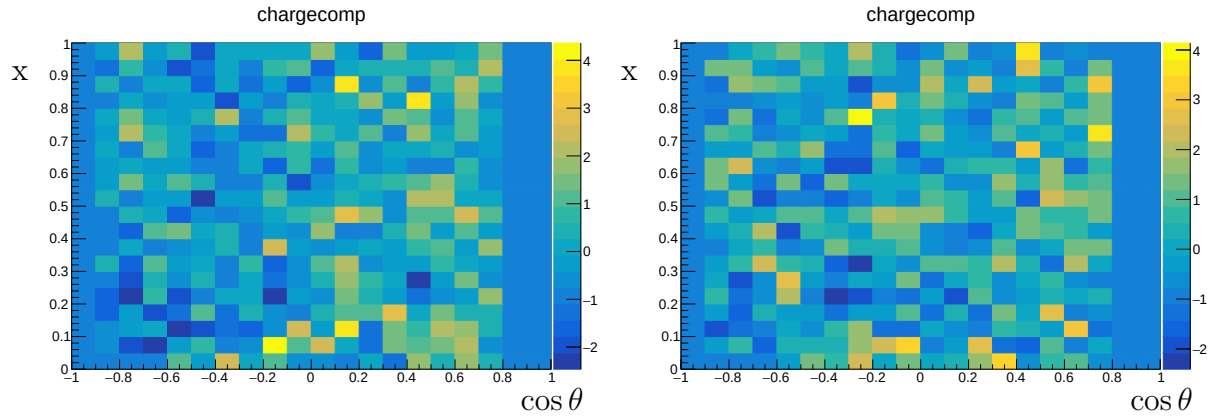

Figure 6.78: Heatmap of charge ratio of Data/MC ratio for Run 2(Left) and Run 3(Right). The Run 2 plot exhibits more of a forward-backward asymmetry than Run 3. While Run 3 exhibits a relatively uniform distribution, Run 2 has more blue-coloured bins in the left hand side of the plot.

though the possibility of recovering the pion vs. pion golden mode seems unlikely. Selecting $\tau^{\pm} \to \pi^{\pm}\overline{\nu}_{\tau}$ decays with a three pion decay mode showed some promise though contained fewer statistics. A detailed study of this topology may improve the selection and contribute meaningfully to a combined polarization measurement. The 1v1 decay topologies, pion tag, electron tag, and muon tag are all swamped by dilepton events. While acollinearity cuts were unable to remove them, a maximum momentum cut on the tagging particle may help reduce the backgrounds. For the pion tag this would significantly bias the polarization measurement due to the correlations, and the lepton modes would also have some bias but an order of magnitude less. All of these modes may contribute to a global polarization fit in the future. For the $\tau^{\pm} \to \pi^{\pm}\overline{\nu}_{\tau}$ vs $\tau^{\pm} \to (\rho^{\pm} \to \pi^{\pm}\pi^{0})\overline{\nu}_{\tau}$ analysis the bias seen in Run 2 was unable to be resolved. In order to have results with better controlled systematic uncertainties the analysis was transitioned to a measurement of the beam polarization from the $\tau^{\pm} \to (\rho^{\pm} \to \pi^{\pm}\pi^{0})\overline{\nu}_{\tau}$ decay with a electron tag. This mode may be recovered one day with the lessons learned in the $\tau^{\pm} \to (\rho^{\pm} \to \pi^{\pm}\pi^{0})\overline{\nu}_{\tau}$ analysis.

Chapter 7

Tau Polarimetry at *BABAR* with the $\tau \to \rho\nu_\tau$ decay

7.1 Motivation

During the study of the $\tau \to \pi\nu$ decay analysis a large bias was discovered in the negatively charged candidates in Run 2. In order to push forward a result with better controlled systematic uncertainties that could be shown at conferences, the analysis was switched to the $\tau^\pm \to (\rho^\pm \to \pi^\pm\pi^0)\overline{\nu}_\tau$ decay mode with a $\tau^\mp \to e^\mp\overline{\nu}_e\nu_\tau$ tag. The electron-tagged $\tau^\pm \to (\rho^\pm \to \pi^\pm\pi^0)\overline{\nu}_\tau$ results were approved by the *BABAR* collaboration as preliminary, and shown at a number of conferences[42, 43, 44, 45, 46, 47]. This mode appeared to be free of the biases observed in the $\tau^\pm \to \pi^\pm\overline{\nu}_\tau$ analysis, and this portion of the analysis was first implemented with only an electron tag with a similar set of cuts to the $\tau^\pm \to \pi^\pm\overline{\nu}_\tau$ analysis. This Chapter begins by describing the process of developing the electron-tagged analysis and the electron-tagged measurement. In order to improve statistics a muon tag was added to the analysis. During this process a small but statistically significant ($\sim 1\%$) bias was discovered. This led to an in-depth investigation of the selection criteria resulting in a much more robust selection which is in good agreement with the expected beam polarization of zero, as well as exhibiting good agreement between the independent charged fits. This Chapter discusses this process and concludes with the final result to be published, with the current paper draft included as Appendix D.

7.2 Introduction to $\tau^\pm \to (\rho^\pm \to \pi^\pm\pi^0)\overline{\nu}_\tau$ Polarimetry

The optimal observable for polarization in the ρ is not momentum but rather two variables relating to the energy of the ρ and the subsequent pion. The first, shown in Equation 7.1, represents the opening angle between the τ and the ρ in the τ restframe, where $z = E_\rho/E_{\text{beam}}$. The second, shown in Equation 7.2, represents the opening angle between the pion and the

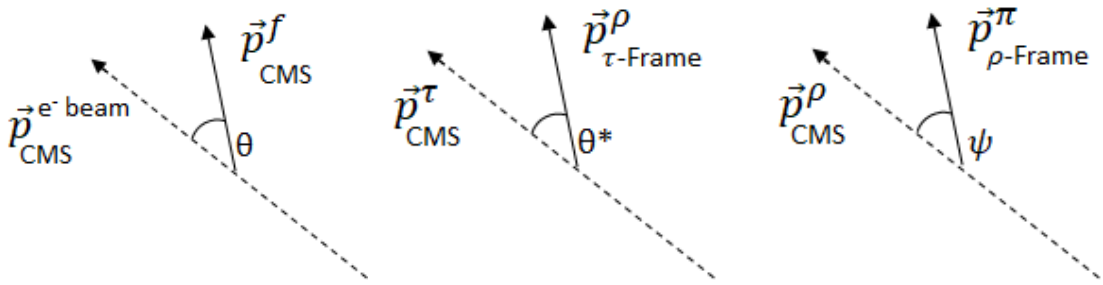

Figure 7.1: Illustrations of the definitions of $\cos\theta$ (left, f represents a final state particle), $\cos\theta^\star$ (centre), and $\cos\psi$ (right).

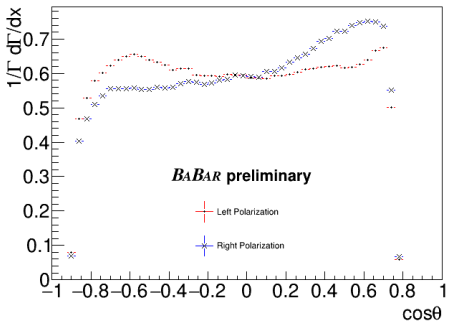

Figure 7.2: $\cos\theta$ distribution of the ρ decay pion in MC for a positively charged ρ decay.

ρ in the ρ rest frame[48], where $x = E_\pi/E_\rho$.

$$\cos\theta^* = \frac{2z - 1 - m_\rho^2/m_\tau^2}{1 - m_\rho^2/m_\tau^2} \tag{7.1}$$

$$\cos\psi = \frac{2x - 1}{\sqrt{1 - 4m_\pi^2/m_\rho^2}} \tag{7.2}$$

For the mass of the pion and the τ the PDG values are used[10], while for the mass of the ρ the event-by-event reconstructed $\pi\pi^0$ mass is used. $\cos\theta^\star$ is defined as the opening angle between the τ flight path in the centre-of-mass frame and ρ direction in the τ rest frame. Similarly $\cos\psi$ is the opening angle between the ρ flight direction in the centre-of-mass frame and the pion direction in the ρ rest frame[27]. Forward and backward regions are defined from the direction of the final state momentum with respect to the beam axis, $\cos\theta$, and the prior angular variables reverse their polarization behaviour switching between these regions. Figure 7.1 illustrates the angular definitions. The distributions of these variables are depicted in Figures 7.2, 7.3, and 7.4 for different values of the electron beam polarization.

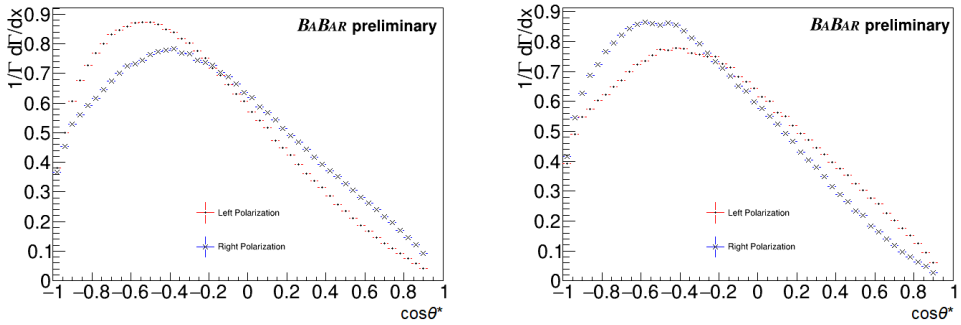

Figure 7.3: $\cos\theta^\star$ distribution in MC for positively charged ρ decay. For $\cos\theta < 0$ (left) and $\cos\theta > 0$ (right).

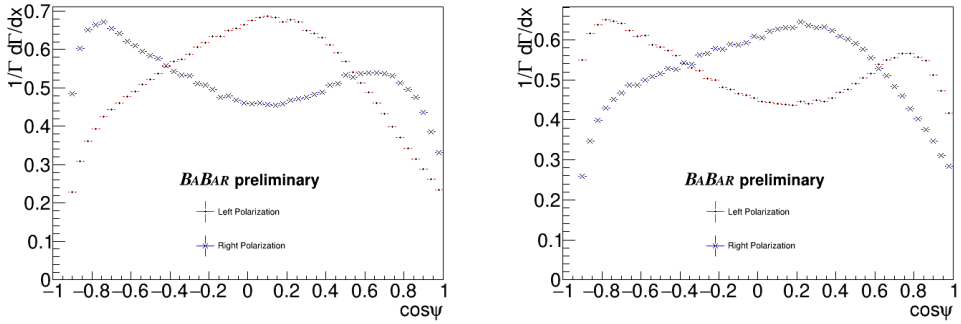

Figure 7.4: $\cos\psi$ distribution in MC for positively charged ρ decay. For $\cos\theta < 0$ (left) and $\cos\theta > 0$ (right).

7.3 Testing Tau Polarimetry via ρ Decay

7.3.1 $\tau^\pm \to (\rho^\pm \to \pi^\pm\pi^0)\overline{\nu}_\tau$ vs. $\tau^\mp \to e^\mp\overline{\nu}_e\nu_\tau$ Event Selection

The event selection was designed to select τ pair events where each of the τ particles decays into a single charged particle. Figure 7.5 shows the event topology for a signal event tagged with an electron. One τ lepton, labelled as the tag, was required to decay leptonically into an electron while the other τ, the signal, decays into a charged and a neutral pion. This requirement for a single charged hadron and a single charged lepton excluded nearly all Bhabha, $\mu\mu$, and $q\overline{q}$ events. The requirement of the neutral pion on the signal side of the event significantly reduced any remaining Bhabha events which contained one electron misidentified as a pion.

Charged tracks were first required to originate within 2.5 cm along the beam axis of the collision point, and within 1.5 cm in the transverse plane. From this track list the event was required to contain two and only two charged tracks. Neutral particles were identified as

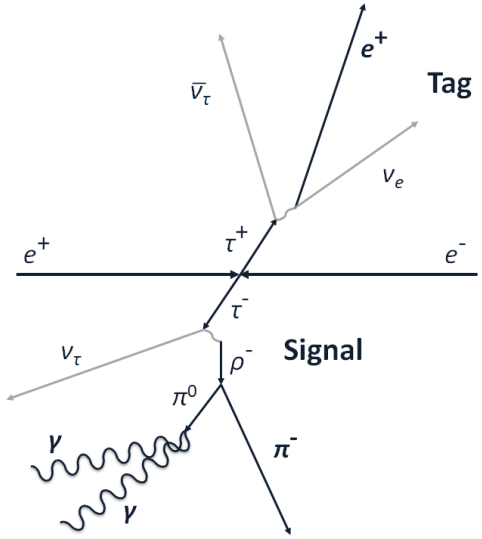

Figure 7.5: Example τ-pair signal event. Signal $\tau^\pm \to (\rho^\pm \to \pi^\pm\pi^0)\overline{\nu}_\tau$ decay tagged with a $\tau^\pm \to e^\pm\nu_e\overline{\nu}_\tau$ decay

energy clusters in the calorimeter with no associated charged track with energy exceeding 50 MeV. From the plane orthogonal to the thrust axis of the event two hemispheres were defined, the signal side and the tag side. On the tag side of the event a single charged track with no neutral clusters was required, while on the signal side a charged track with one or two neutral clusters (interpreted as photons from the π^0 decay) was required. The neutral particles were further required to exceed 100 MeV of energy and the surviving clusters were checked against a π^0 hypothesis. Each neutral cluster was first checked for the likelihood of being a 'merged' π^0, as previously defined. If no cluster meets this requirement, and two clusters remain the invariant mass is reconstructed and compared to a mass window of 115 MeV to 155 MeV. If a π^0 was selected via either method the ρ mass for the decay was reconstructed and required to be greater than 300 MeV to ensure $\cos\psi$ is real. $\tau^\pm \to e^\pm\nu_e\overline{\nu}_\tau$ decays were then selected on the tag side of the event with *BABAR* particle identification (PID) requirements applied to the charged track. This PID selector, VeryLooseKMElectronMicro, combines information from all *BABAR* sub-detectors to predict if a particle has a high likelihood of being an electron. The angular acceptance for charged tracks is slightly reduced such that each track was within the calorimeter acceptance, $0.430 < \theta_{\rm lab} < 2.350$. This angular requirement improves PID performance, improves data/MC agreement, and reduces the Bhabha contamination. In order to remove two photon events we apply a cut on total event transverse momentum, p_T, of at least 1.2 GeV. The remaining Bhabha events were further reduced by a factor of three by slightly trimming $\cos\theta^\star$, $-1 < \cos\theta^\star < 0.9$, and $\cos\psi$, $-0.9 < \cos\psi < 1$. These

MC source	Fraction
Bhabha	0.289%
$\mu^+\mu^-$	0.000%
$u\overline{u}$,$d\overline{d}$,$s\overline{s}$	0.005%
$c\overline{c}$	0.002%
$b\overline{b}$	0.000%
$\tau^+\tau^-$	99.704%

Tau Signal	Fraction
$\tau^\pm \to e^\pm \nu_e \overline{\nu}_\tau$	0.012%
$\tau^\pm \to \mu^\pm \nu_\mu \overline{\nu}_\tau$	0.018%
$\tau^\pm \to \pi^\pm \overline{\nu}_\tau$	0.033%
$\tau^\pm \to (\rho^\pm \to \pi^\pm \pi^0)\overline{\nu}_\tau$	89.994%
$\tau^\pm \to (a_1^\pm \to \pi^\pm \pi^0 \pi^0)\overline{\nu}_\tau$	8.028%
$\tau \to$ else	1.915%

Table 7.1: Fraction of event types in MC in the final event selection. The *tau*-pair events are further broken down to show the $\tau^\pm \to (\rho^\pm \to \pi^\pm \pi^0)\overline{\nu}_\tau$ selection.

Fit Type	Positive Charge	Negative Charge	Average
MC_1	-0.0226±0.0173	-0.0094±0.0174	-0.0160±0.0122
MC_2	-0.0098±0.0173	-0.0170±0.0175	-0.0134±0.0123
MC_3	0.0102±0.0175	0.0037±0.0174	0.0069±0.0123
Data	0.0277±0.0177	-0.0031±0.0177	0.0123±0.0125

Table 7.2: Run 3 ρ polarization fit, with ρ^+ and ρ^- signal decays shown separately.

requirements achieve a final τ selection which is 99.7% pure and with a 0.70% efficiency. The branching fraction for the tagging τ is 17.82% and 25.49% for the signal τ. Including these in our efficiency calculation, brings our efficiency to 15.40% for selecting $\tau^\pm\tau^\mp \to \rho^\pm\nu_\tau + e^\mp\nu_e\overline{\nu_\tau}$ events. The largest non-tau background is Bhabha events which make up 0.3% of the final sample. The final event selection break-down as predicted by MC is shown in Table 7.1.

7.3.2 Run 3 e-Tagged Fit Test

The Run 3 data is then used to test the new fit configuration and the fit result is shown in Table 7.2. The overall statistical sensitivity is slightly lower than observed in the pion fit from the same data, 0.0125 for the $\tau^\pm \to (\rho^\pm \to \pi^\pm\pi^0)\overline{\nu}_\tau$ fit vs. 0.0112 for the $\tau^\pm \to \pi^\pm\overline{\nu}_\tau$ fit. The electron tag has a τ decay branching fraction nearly double that of the pion decay, the event purity is also significantly improved, ∼90% for ρ selection and ∼60% for pions in the previous Chapter. The selection efficiency is also significantly improved in this analysis 15.4% compared to 7.07%. This corresponds to roughly a 5× improvement in statistics. The similar statistical sensitivity achieved in the end suggests the ρ polarization mode has a much lower sensitivity to polarization on an event-by-event basis. With the electron tagged $\tau^\pm \to (\rho^\pm \to \pi^\pm\pi^0)\overline{\nu}_\tau$ analysis Run 3 statistical uncertainty of 0.0125, the full *BABAR* statistical uncertainty extrapolates to 0.34%.

Hadronic Split-off Modelling	**0.0027**
π^0 Likelihood	0.0013
Minimum Neutral Energy	0.0013
$\cos\psi$	**0.0013**
π^0 Minimum Photon Energy	0.0011
π^0 High Mass cut	0.0011
Angular Resolution	**0.0010**
π^0 Low Mass cut	**0.0009**
Electron PID	**0.0006**
Background Modelling	0.0006
Event Transverse Momentum	**0.0006**
$\cos\theta^*$	0.0002
Boost	0.0002
Momentum Resolution	**0.0002**
Rho Mass	0.0002
Tau Branching Fraction	**0.0001**
Quadratic Sum	0.0042

Table 7.3: Systematic uncertainties for the ρ polarization measurement in Run 3. The bold numbers are systematic uncertainties where the associated statistical component of the systematic was larger than the central value. For these numbers the statistical component is reported in place of the central value.

7.3.3 Run 3 e-Tagged Systematic Uncertainties

Systematic uncertainties were calculated in a similar method as described in the pion analysis. These are listed in Table 7.3. Somewhat expectantly, due to the increased dependency on neutral modelling, the dominant systematic effect is the 40 cm cut that associates neutral clusters within that radius of a track as part of the track. Notably this systematic uncertainty is driven entirely by statistical fluctuations in the MC.

7.3.4 Extracted vs Input Beam Polarization Study

In order to ensure the polarimetry measurement is valid at beam polarization states other than 0, as expected for PEP-II runs, we used polarized τ MC to study the extracted polarization from this analysis of the ρ channel at multiple input beam polarization states. This was done by splitting each of the left and right polarized τ MC into two distinct samples, one reserved for fitting the beam polarization in MC "measurements" and the other for mixing beam polarization states. With the samples reserved for mixing, specific beam polarization states can be created, ie. 70% polarized is made with 85% left polarized MC and 15% right

polarized MC. Using this technique we tested polarization states from -1 to 1 in steps of 0.1, the results of which can been seen in Figure 7.6. The fit results to the MC are within good agreement of the input MC beam polarization states, which demonstrates the measurement technique will yield the correct polarization for any beam polarization.

7.3.5 e-Tagged Tau Polarimetry Fitting

To extract the average beam polarization we perform a binned likelihood fit as prescribed by the Barlow and Beeston method [39]. We fill three dimensional histograms of $\cos\theta^{\star}$, $\cos\psi$, and $\cos\theta$, for each of the data and MC modes. The 3D histogram for data is then fit as a combination of the MC histograms, where the weights of the non-tau MC is fixed based on the MC efficiency studies. This leaves only the left and right polarized contribution to vary in the fit, and with a constraint that the contributions sum to 1 leaves only one parameter in the fit. We define this fitted parameter as $\langle \mathrm{P} \rangle$=L-R, where L and R are the fitted fractions reported by the fit for the left and right polarized τ MC. As the polarization sign flips with electric charge we preform the fit separately for positively and negatively charged signal candidates, and extract the fit result, statistical uncertainty, the chi squared as defined by TFractionFitter, and the number of degrees of freedom (number of bins with at least one event subtract one fit parameter). A final fit result is then reported as the combined average of the two independent fits. In addition to the data fit we use unpolarized τ MC mixed with non-tau MC to produce three "data-size" samples for approximating the level of statistical uncertainty present in small perturbations to the fit. Figures 7.7, 7.8, and 7.9 show the 1D projections of the Run 3 fit, where the data points represent the data and the MC is stacked with relative proportions equal to the fit results. As the *BABAR* data sets are split into multiple data collection periods, Run numbers 1 to 6, and each set has its own unique beam conditions we treat each sample independently. As such we obtain 6 measurements of the beam polarization and corresponding statistical and systematic uncertainties. A final measurement of the beam polarization is then obtained from combining these measurements and accounting for correlations in the systematic uncertainties as is described below.

7.4 e-Tagged Tau Polarimetry Systematic Studies

The systematic uncertainties are largely evaluated in the same way as was presented in Section 6.12 with a few new considerations to account for the ρ decay mode in place of the pion. The Run 3 data is again used as a study sample to verify the size of systematic uncertainties, with the full systematic uncertainties listed in Table 7.9. The cuts applied to

Distribution	MC Mean	Data Mean	Difference
$\cos\theta^{\star+}$	-0.2695	-0.2716	0.0021
$\cos\theta^{\star-}$	-0.2690	-0.2694	0.0004
$\cos\psi^{+}$	0.0362	0.0262	0.0100
$\cos\psi^{-}$	0.0369	0.0283	0.0086

Table 7.4: Mean and difference in the mean of $\cos\theta^{\star}$ and $\cos\psi$ for MC and Data. The $\pm$ sign refers to the electric charge of the final state particle

$\cos\theta^{\star}$ and $\cos\psi$, as mentioned earlier, are shown in Figure 7.10. In order to evaluate the size of the modelling uncertainties in these variables first the level of agreement between data and MC is evaluated. This was done by comparing the average values of the distributions in data and MC and extracting the difference to use in systematic studies, as shown in Table 7.4. To be conservative the larger of the differences between positive and negative are taken as the fluctuation to be used in systematic studies. In the case of $\cos\psi$ the cut was varied from $\cos\psi > -0.9$ up and down to $\cos\psi > -0.91$ and $\cos\psi > -0.89$. This resulted in an overall shift in the level of agreement between data and MC in the polarization fit of -0.0007$\pm$0.0013. As the statistical component dominates, we list 0.0013 as the uncertainty seen in Table 7.9. To evaluate the uncertainties arising from our treatment of neutral clusters we vary the thresholds for the related cutoffs. In the case of the hadronic split-off modelling the relevant variable is the distance within which the neutral clusters are recombined with charged tracks, 40 cm by default. While there is significant data vs. MC disagreement in this variable, shown in Figure C.19, there is good agreement above $\sim$35 cm. the MC suggests the resolution for the distance between a track and a neutral cluster is better than 1cm. By varying the acceptance cut by 1 cm a systematic uncertainty of 0.27% was estimated. Note that the final uncertainty could be significantly different as this value is statistically dominated. For the minimum neutral energy, 50 MeV, as well as the photon energy cutoff for π^0 reconstruction, 100 MeV, we vary the acceptance by $\pm$1 MeV, as dictated by the level of agreement between MC and data. Both of these variables resulted in small systematic uncertainties of 0.13% and 0.11% respectively. The systematic uncertainty is evaluated by scaling the momentum up or down based on its resolution and results in a 0.02% systematic uncertainty in the polarization fit. Similarly for $\cos\theta$ the angle is varied by it's resolution and results in a 0.10% systematic uncertainty. The π^0 identification systematic uncertainty was evaluated by varying the mass window for the reconstructed π^0's by 1 MeV or by varying the π^0 likelihood acceptance from 20 by $\pm$5 (the uncut distributions are shown in Figure C.25), as determined by the selection criteria selecting a particular π^0. The combined systematic

uncertainty for the π^0 identification is 0.19%. In addition to already mentioned variables, similar studies were performed on the τ trigger decision, the boost calculation, the charged track definition, the total event transverse momentum, uncertainties within the τ branching fraction, the weights of non-τ backgrounds, the luminosity weighting of the MC, the effects of re-binning in the fit, the electron PID requirements, and the cuts on $\cos\psi$ and $\cos\theta^\star$. None of these exhibited any notable effects, and the full details of how these are assessed is described in Chapter 6. The final systematic uncertainties found in Run 3 are shown in Table 7.5.

Systematic Source	Uncertainty
π^0 Likelihood	0.0013
Hadronic Split-off Modelling	0.0027
Minimum Neutral Energy	0.0013
π^0 Mass	0.0011
$\cos\psi$	0.0013
Angular Resolution	0.0010
Electron PID	0.0006
$\cos\theta^\star$	0.0002
Event Transverse Momentum	0.0006
Momentum Resolution	0.0002
π^0 Minimum Photon Energy	0.0011
Tau Branching Fraction	0.0001
Rho Mass	0.0002
Boost	0.0002
Background Modelling	0.0006
Total	0.0041

Table 7.5: Run 3 Systematic Uncertainties

7.5 Correlation of Systematic Uncertainties

As the systematic uncertainties can be correlated between Runs, a method more sophisticated than finding the average or weighted mean is required. This requires an approach where systematic uncertainties dominated by statistical fluctuations can pull the fit in either direction while systematic uncertainties with small statistical sensitivity only pull the fit in one direction. To achieve this the first step in the process is to assign a left polarizing and right polarizing bias to each systematic uncertainty. For systematic uncertainties with small statistical sensitivity the statistical uncertainty is still assigned as the opposing bias to be conservative. An example of this step, including the quadratic combination of bias to

assign an overall left(or right) systematic uncertainty, is shown in Table 7.6. Once each run

Variable	Systematic	Left Systematic	Right Systematic
π^0 Likelihood	-0.0013±0.0006	0.0006	0.0013
$\cos\psi$	-0.0007±0.0013	0.0013	0.0013
Quad Sum	-	0.0014	0.0018

Table 7.6: Example of how systematic uncertainties are split into left and right polarization contributions, and summed. The larger final sum, right polarized in this example, is taken as the systematic uncertainty for the run.

and systematic uncertainty is split in this way the systematic uncertainties can be combined through a weighted mean, where the weight of each run is taken as the statistical variance from the data polarization fits, as shown in Equation 7.3. An example of this step is also shown in Table 7.7.

$$\sigma^{sys}_{1-6} = \sqrt{\frac{\sum_{i=1-6}\left(\frac{\sigma_i^{sys}}{\sigma_i^{\text{data stat}}}\right)^2}{\sum_{i=1-6}\left(\frac{1}{\sigma_i^{\text{data stat}}}\right)^2}} \tag{7.3}$$

Finally once all the systematic uncertainties are combined by run the systematic uncer-

Run	Systematic	Left Bias	Right Bias	Data σ_{stat}	Weight
1	-0.0032±0.0014	0.0014	-0.0032	0.0157	4100
2	-0.0002±0.0012	0.0012	-0.0012	0.0090	12000
3	-0.0013±0.0002	0.0002	-0.0013	0.0125	6400
4	-0.0009±0.0006	0.0006	-0.0009	0.0071	20000
5	-0.0010±0.0007	0.0007	-0.0010	0.0063	25000
6	-0.0020±0.0003	0.0003	-0.0020	0.0082	15000
Weighted Mean		0.0005	-0.0014		

Table 7.7: Example of how a systematic is split into left and right bias and then weighted for an average

tainties can be summed in quadrature to get a final left bias systematic and a right bias systematic, as shown in Table 7.8. To arrive at the final reported systematic uncertainty the larger of the left and right biasing systematic uncertainties shown in Table 7.8 is taken. Table 7.9 shows the final table of systematic uncertainties.

7.6 $\tau^\pm \to (\rho^\pm \to \pi^\pm\pi^0)\overline{\nu}_\tau$ v.s. $\tau^\mp \to e^\mp\overline{\nu}_e\nu_\tau$ Full Results

The fit results for all of the *BABAR* data sets are shown in Table 7.10. Taking the weighted mean of these fit results gives the average beam polarization of PEP-II runs to be $\langle P\rangle =$

Systematic	Left Bias	Right Bias
Hadronic Split-off Modelling	0.0013	0.0012
π^0 Likelihood	0.0005	0.0014
Minimum Neutral Energy	0.0005	0.0011
$\cos\psi$	0.0007	0.0009
π^0 Minimum Photon Energy	0.0008	0.0004
π^0 Mass	0.0006	0.0009
Angular Resolution	0.0007	0.0007
Electron PID	0.0009	0.0007
Background Modelling	0.0006	0.0002
Event Transverse Momentum	0.0004	0.0004
$\cos\theta^\star$	0.0006	0.0006
Boost	0.0003	0.0002
Momentum Resolution	0.0004	0.0004
Rho Mass	0.0003	0.0003
Tau Branching Fraction	0.0005	0.0004
Total	0.0025	0.0029

Table 7.8: Breakdown of all systematic uncertainties by left and right bias

$0.0001 \pm 0.0035_{\text{stat}} \pm 0.0029_{\text{sys}}$. This measurement demonstrates that a 0.5% systematic uncertainty in the beam polarization can be achieved in e^+e^- colliders, and strongly motivates the addition of beam polarization to SuperKEKB for precision electroweak measurements. In addition we can estimate that 56 fb^{-1} of data is needed to achieve a total uncertainty of 1% in measurement, with the statistical uncertainty scaling with $1/\sqrt{N_{\text{Events}}}$ as expected. A number of additional fit projections and analysis variable plots were prepared as part of the approval of presenting these preliminary results at conferences. These figures are included in Appendix C.

7.7 Tau Polarimetry with $\tau^\pm \to (\rho^\pm \to \pi^\pm\pi^0)\overline{\nu}_\tau$ vs. $\tau^\mp \to \ell^\mp\overline{\nu}_\ell\nu_\tau$

After completing the $\tau^\pm \to (\rho^\pm \to \pi^\pm\pi^0)\overline{\nu}_\tau$ vs. $\tau^\mp \to e^\mp\overline{\nu}_e\nu_\tau$ the idea of adding the $\tau^\pm \to \mu^\pm\nu_\mu\overline{\nu}_\tau$ events as an additional tag was requested by the *BABAR* collaboration. This roughly doubles the amount of statistics, which could also improve the systematic uncertainties. At a high level this addition is fairly simple as the only required change is the PID selection to change from VeryLooseKMElectronMicroSelection to VeryLooseKMElectronMicroSelection or BDTVeryLooseMuonSelectionFakeRate. It was also discovered during the wrapping up of the electron-tagged analysis that the transverse momentum requirements are much stricter than necessary. This was a cut introduced in the pion analysis which was not re-evaluated

Source	Run 1	Run 2	Run 4	Run 5	Run 6	Combined
π^0 Likelihood	0.0032	0.0012	0.0009	0.0010	0.0020	**0.0015**
Hadronic Split-off Modelling	0.0035	0.0012	0.0015	0.0011	0.0005	**0.0011**
$\cos\psi$	0.0022	0.0012	0.0006	0.0008	0.0010	**0.0010**
Angular Resolution	0.0010	0.0015	0.0012	0.0002	0.0007	**0.0009**
Minimum Neutral Energy	0.0006	0.0009	0.0005	0.0006	0.0016	**0.0009**
π^0 Mass	0.0018	0.0005	0.0009	0.0006	0.0014	**0.0009**
$\cos\theta^\star$	0.0012	0.0007	0.0012	0.0009	0.0007	**0.0008**
Electron PID	0.0022	0.0008	0.0007	0.0014	0.0010	**0.0007**
Tau Branching Fraction	0.0007	0.0006	0.0010	0.0006	0.0005	**0.0006**
Event Transverse Momentum	0.0013	0.0006	0.0006	0.0002	0.0005	**0.0005**
Momentum Resolution	0.0005	0.0008	0.0004	0.0003	0.0006	**0.0005**
π^0 Minimum Photon Energy	0.0008	0.0008	0.0009	0.0003	0.0010	**0.0004**
Rho Mass	0.0007	0.0002	0.0002	0.0004	0.0005	**0.0003**
Background Modelling	0.0027	0.0002	0.0002	0.0007	0.0009	**0.0003**
Boost	0.0000	0.0002	0.0001	0.0005	0.0004	**0.0002**
Total	0.0070	0.0033	0.0032	0.0027	0.0038	**0.0030**

Table 7.9: Summary of systematic uncertainties associated with polarization measurement. Run 3 excluded from the sum as expected with a blinded approach.

during the quick transition to the ρ analysis. Figure 7.11 shows the transverse momentum distributions for the pion and ρ analyses and it can be easily seen why the 1.2 GeV cut is required in the pion analysis but not in the ρ analysis. For this electron or muon tagged ρ analysis the event p_T cut has been lowered from 1.2 GeV to 250 MeV to significantly improve statistics while retaining the signal purity. The rest of this Chapter describes the implementation of these new selection criteria, the results of the fit, and the swath of new effects discovered in the process.

7.8 Muon Tag Only Testing

In order to ensure the introduction of the muon tag doesn't introduce a bias to the analysis a number of tests are performed using only the muon tag first before the combined tag is performed.

7.8.1 Muon Tag Event Purity

With the event selection changes described above, Table 7.11 shows the 90.8% signal purity achieved. This is very similar compared to the 90.7% purity of the electron tag only analysis.

Data Set	Positive Charge	Negative Charge	Average Polarization
Run 1	-0.0018±0.0222	0.0143±0.0224	0.0062±0.0157
χ^2/NDF	934/881	1022/882	
Run 2	-0.0064±0.0127	0.0056±0.0128	-0.0004±0.0090
χ^2/NDF	785/884	819/877	
Run 4	0.0054±0.0101	-0.0280±0.0100	-0.0114±0.0071
χ^2/NDF	890/888	832/883	
Run 5	0.0053±0.0092	-0.0124±0.0087	-0.0040±0.0063
χ^2/NDF	914/886	993/886	
Run 6	0.0256±0.0117	0.0060±0.0116	0.0157±0.0082
χ^2/NDF	939/881	1022/882	
Total	0.0070±0.0052	-0.0087±0.0051	-0.0010±0.0036

Table 7.10: Average beam polarization measured in each data set. The average for each run is found from the weighted mean of the positive and negative fit results.

7.8.2 Run 3 Muon Fit Test

The Run 3 fit result is shown in Table 7.12. The overall statistical sensitivity is significantly improved due to the larger transverse momentum acceptance. With just the muon tag the full *BABAR* statistical uncertainty extrapolates to 0.27%.

7.8.3 Run 3 Systematic Uncertainty Test

There were no surprises in the systematic uncertainties with the largest uncertainty being the muon PID, which was expected from the pion studies. The uncertainties are listed in Table 7.13.

7.9 $\tau^{\pm} \to (\rho^{\pm} \to \pi^{\pm}\pi^0)\overline{\nu}_{\tau}$ vs. $\tau^{\mp} \to \ell^{\mp}\overline{\nu}_{\ell}\nu_{\tau}$ Event Selection

The event selection is very similar to the $\tau^{\mp} \to e^{\mp}\overline{\nu}_e\nu_{\tau}$ tag, however the full event selection is included again here for completeness. Charged tracks are first required that they originate within 2.5 cm along the beam axis of the collision point, and within 1.5 cm in the transverse plane. From this track list we require the event contains two and only two charged tracks. Neutral particles are identified as energy clusters in the calorimeter with no associated charged track with energy exceeding 50 MeV of energy. From the thrust axis of the event we split the event into two hemispheres, the signal side and the tag side. On the tag side of the event we require a single charged track with no neutral clusters, while on the signal side a charged track with one or two neutral clusters is required. From the two

MC Type	Events Selected	Luminosity Scaled	Fraction
Bhabha	7	14	4×10^{-5}
$\mu\mu$	1031	511	0.0014
uds	836	205	0.0006
$c\bar{c}$	42	20	6×10^{-5}
$\tau\tau$	1422065	358438	0.9979
$\tau \to e$	319	80	0.0002
$\tau \to \mu$	407	103	0.0003
$\tau \to \pi$	568	143	0.0004
$\tau \to \rho$	1251077	315340	0.8779
$\tau \to a_1$	135937	34264	0.0954
$\tau \to$else	33757	8509	0.0237

Table 7.11: Number of events of each MC type left after selection. τ specific decays are for the signal side of the event.

	Positive Charge	Negative Charge	Combined Average
Sample 1	0.0257±0.0137	0.0095±0.0139	0.0176±0.0098
Sample 2	0.0078±0.0137	-0.0124±0.0138	-0.0022±0.0097
Sample 3	0.0042±0.0137	-0.0144±0.0138	-0.0050±0.0097
Data	0.0299±0.0139	-0.0048±0.0140	0.0127±0.0098

Table 7.12: Run 3 $\tau^{\pm} \to (\rho^{\pm} \to \pi^{\pm}\pi^0)\overline{\nu}_{\tau}$ polarization fit with muon tag

neutral clusters we look for a neutral pion as follows. First each neutral cluster over 100 MeV in energy is considered a π^0 candidate. Next, each π^0 candidate is checked for consistency with a merged π^0 hypothesis as defined by *BABAR* π^0 likelihood algorithms. If no π^0's are identified this way we reconstruct the invariant mass of each pair of candidates and check if the invariant mass is within a mass window of 115 MeV to 155 MeV. The identified π^0 is then used to reconstruct the ρ mass for the decay, which is required to be greater than 300 MeV to ensure $\cos\psi$ is real. $\tau^{\pm} \to e^{\pm}\nu_e\overline{\nu}_{\tau}$ tagged events are then selected on the tag side of the event with *BABAR* particle identification (PID), VeryLooseKMElectronMicro. $\tau^{\pm} \to \mu^{\pm}\nu_{\mu}\overline{\nu}_{\tau}$ tagged events are similarly selected with the BDTVeryLooseMuonSelectionFakeRate PID selector. The angular acceptance for charged tracks is slightly reduced such that each track is within the calorimeter acceptance, $0.430 < \theta_{\rm lab} < 2.350$. This angular requirement improves PID performance, improves data/MC agreement, and reduces the Bhabha contamination. In order to remove two photon events we apply a cut on total event transverse momentum, p_T, of at least 250 MeV. The remaining Bhabha events are further reduced by a factor of three by trimming $\cos\theta^{\star}$ and $\cos\psi$ by $-1 < \cos\theta^{\star} < 0.9$, and $-0.9 < \cos\psi < 1$. These requirements achieve a final τ selection which is 99.7% pure and with a 2.4% efficiency. The branching

Source	Muon Tag	Electron Tag
muon PID	0.0031	-
Trk-Neu Association	**0.0028**	**0.0027**
Pi0 likelihood	**0.0014**	0.0013
Neu, 50 MeV cut	0.0011	0.0013
Pi0 Mass 155 MeV cut	0.0011	0.0011
m_ρ	0.0010	0.0002
Pi0 Mass 115 MeV cut	0.0010	**0.0009**
P	0.0009	0.0002
Neu,100 MeV cut	0.0008	0.0011
Backgrounds	0.0008	0.0006
$\cos\theta^*$	0.0007	0.0002
Angular	0.0006	**0.0010**
Branching Fraction	0.0006	0.0001
e PID	-	0.0006
Boost	0.0004	0.0002
Event p_T	0.0003	0.0006
$\cos\psi$	0.0003	**0.0013**
Quadratic Sum	0.0053	0.0042

Table 7.13: Systematic uncertainties for the ρ polarization measurement in Run 3 with the new muon tag and the previous electron tag for comparison. The bold numbers are systematic uncertainties where the associated statistical component of the systematic was larger than the central value. For these numbers the statistical component is reported in place of the central value.

fraction for the tag τ is 35.21% and 25.49% for the signal τ. Including these in our efficiency calculation, brings our efficiency to 27.11% for selecting $\tau^\pm\tau^\mp \to \rho^\pm\nu_\tau + \ell^\mp\nu_\ell\overline{\nu_\tau}$ $(\ell = e, \mu)$ events. Our largest non-tau background is Bhabha events which make up 0.2% of the final sample. The final event selection break-down as predicted by MC is shown in Table 7.14.

7.9.1 p_T Cut Change

The change from a minimum p_T of 1.2 GeV to 250 MeV is the most significant improvement in the analysis which was a hold over from the original pion polarization analysis. In the pion analysis there is a significant number of unmodelled two photon events present at low p_T which is not present with the lepton tag. Figure 7.12 shows the presence of unmodelled two-photon events at low p_T for the pion analysis as well as the lepton tags. From these plots it's evident that the p_T cut can be lowered to 250 MeV.

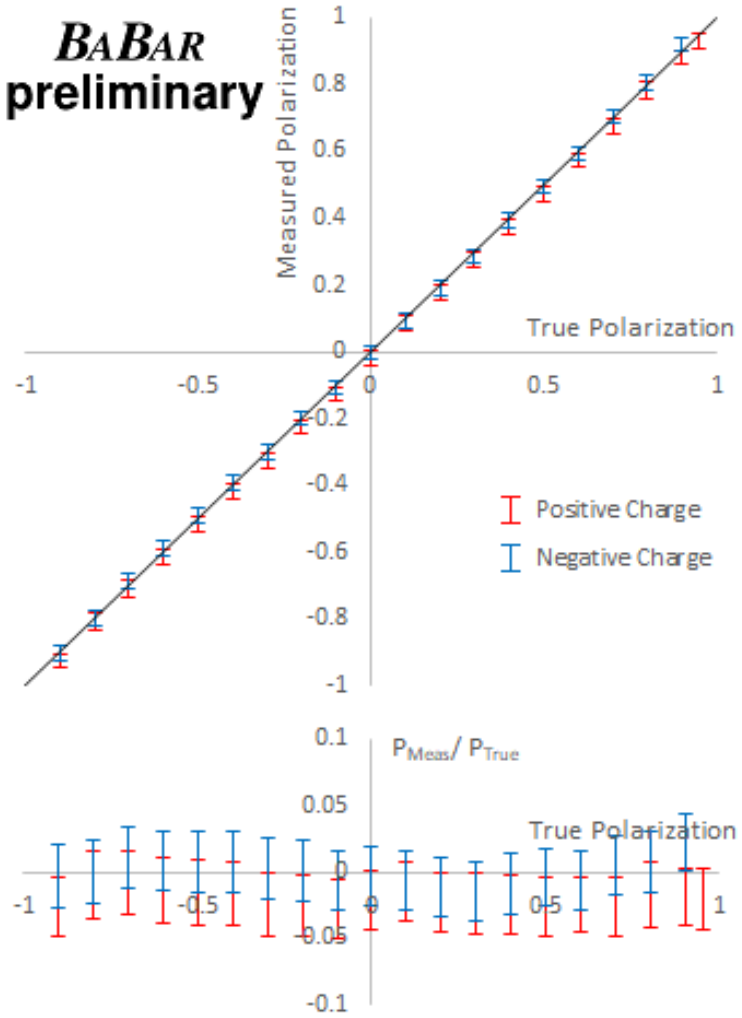

Figure 7.6: Measured beam polarization for a given input polarization mixed from polarized τ MC. The red points correspond to the measurements for positively charged signal candidates while the blue points correspond to the negatively charged candidates.

MC source	Fraction
Bhabha	0.215%
$\mu^+\mu^-$	0.067%
$u\bar{u}$,$d\bar{d}$,$s\bar{s}$	0.031%
$c\bar{c}$	0.005%
$b\bar{b}$	0.000%
$\tau^+\tau^-$	99.681%

Tau Signal	Fraction
$\tau^\pm \to e^\pm \nu_e \overline{\nu}_\tau$	0.017%
$\tau^\pm \to \mu^\pm \nu_\mu \overline{\nu}_\tau$	0.024%
$\tau^\pm \to \pi^\pm \overline{\nu}_\tau$	0.035%
$\tau^\pm \to (\rho^\pm \to \pi^\pm \pi^0) \overline{\nu}_\tau$	87.667%
$\tau^\pm \to (a_1^\pm \to \pi^\pm \pi^0 \pi^0) \overline{\nu}_\tau$	9.561%
$\tau \to$ else	2.377%

Table 7.14: Fraction of event types in MC in the final event selection. The τ-pair events are further broken down to show the $\tau^\pm \to (\rho^\pm \to \pi^\pm \pi^0) \overline{\nu}_\tau$ selection.

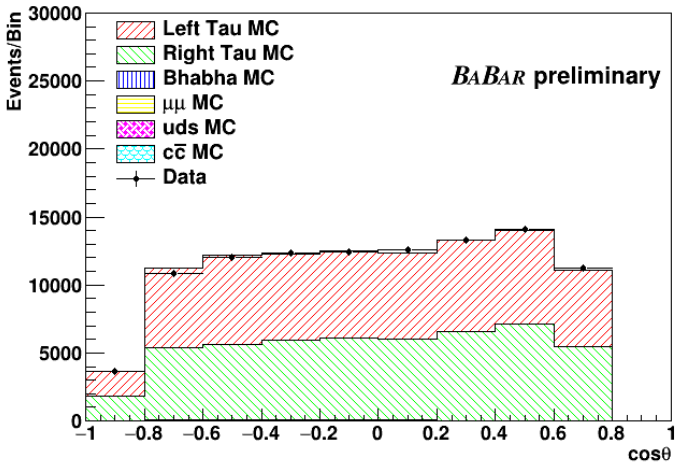

Figure 7.7: One dimensional projection of the fit result for $\cos\theta$ in positively charged candidates in Run 3.

7.10 Lepton Tag Overall Polarization Sensitivity

In order to ensure the polarimetry measurement is valid at beam polarization states other than 0, as expected for PEP-II runs, we used polarized τ MC to study the extracted polarization from this analysis of the ρ channel at multiple input beam polarization states. This was done by splitting each of the left and right polarized τ MC into two distinct samples, one reserved for fitting the beam polarization in MC "measurements" and the other for mixing beam polarization states. With the samples reserved for mixing beam polarization states specific beam polarization states can be created, ie. 70% polarized is made with 85% left polarized MC and 15% right polarized MC. Using this technique we tested polarization states from -1 to 1 in steps of 0.1, the results of which can been seen in Figure 7.13. The fit results to the MC are within good agreement of the input MC beam polarization states, which demonstrates the measurement technique will yield the correct polarization for any beam polarization.

7.11 Lepton Tag Fitting

The fit procedure is identical to what was performed in the electron-tagged analysis (Section 7.3.5). The only difference is the fits were performed on electron-tag, muon-tag, and combined tag consecutively in order to track any polarization biases. For the combined fits, Figures 7.14, 7.15, and 7.16 show the 1D projections of the Run 3 fit, where the data points represent the data and the MC is stacked with relative proportions equal to the fit results.

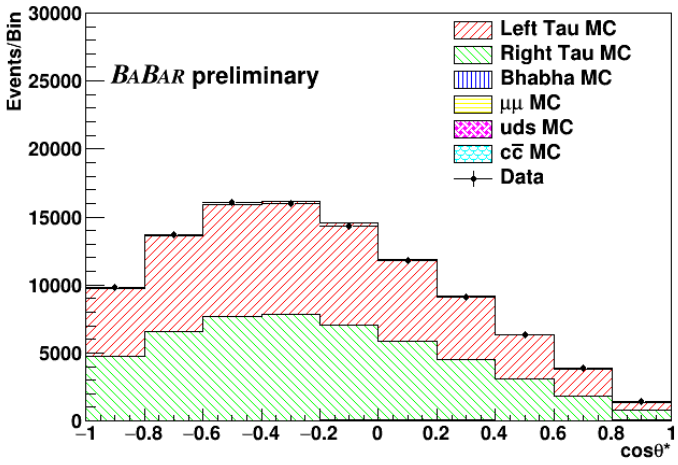

Figure 7.8: One dimensional projection of the fit result for $\cos\theta^{\star}$ in positively charged candidates in Run 3.

As the *BABAR* data sets are split into multiple data collection periods, run numbers 1 to 6, and each set has it's own unique beam conditions we treat each sample independently. As such we obtain 6 measurements of the beam polarization and corresponding statistical and systematic uncertainties. A final measurement of the beam polarization is then obtained from combining these measurements and accounting for correlations in the systematic uncertainties as is described below.

Data Set	Positive Charge	χ^2/NDF	Negative Charge	χ^2/NDF	Average Polarization
Run 3	0.0145±0.0100	850/885	-0.0071±0.0105	854/882	0.0042±0.0073

Table 7.15: Average beam polarization in the Run 3 study sample for the electron or muon tagging.

7.12 Systematic Studies

Systematic uncertainties are evaluated as described in Section 6.12. The final systematic uncertainties found in Run 3 are shown in Table 7.16.

7.13 Initial Lepton Tagged Results

The fit results for all of the *BABAR* data sets are shown in Table 7.18. Taking the weighted mean of these fit results gives the average beam polarization of PEP-II runs to be $\langle P \rangle =$

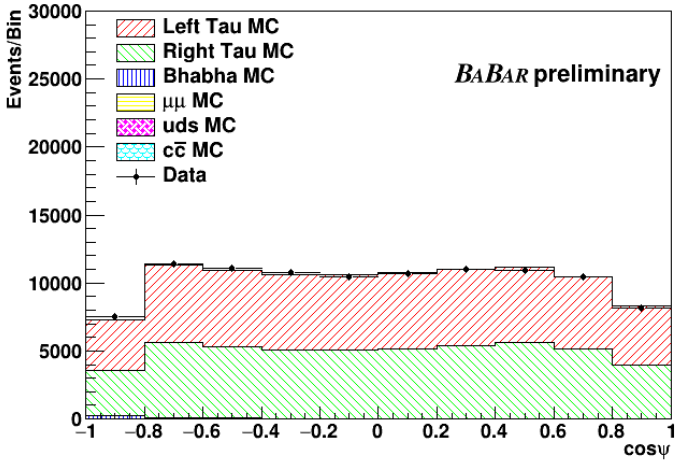

Figure 7.9: One dimensional projection of the fit result for $\cos\psi$ in positively charged candidates in Run 3.

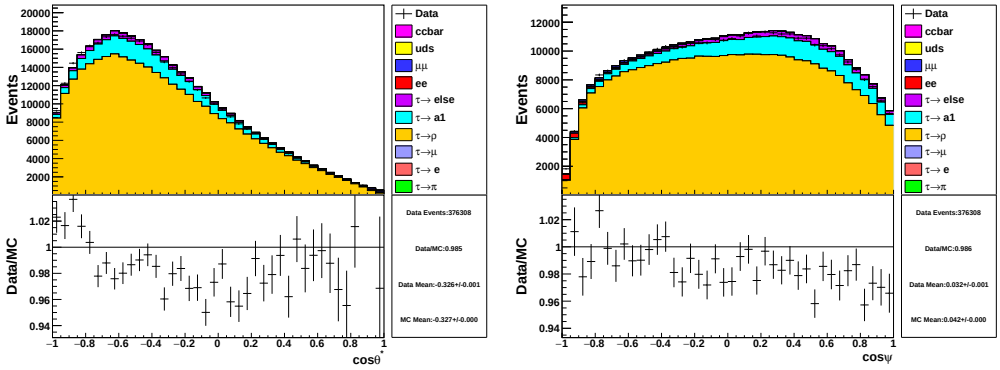

Figure 7.10: $\cos\theta^{\star}$ (Left) and $\cos\psi$ (Right), before other analysis cuts.

$-0.0133 \pm 0.0021_{\text{stat}} \pm 0.0023_{\text{sys}}$. This result is in significant tension with zero polarization and so a number of further investigations are carried out to understand if any sources of bias have been missed.

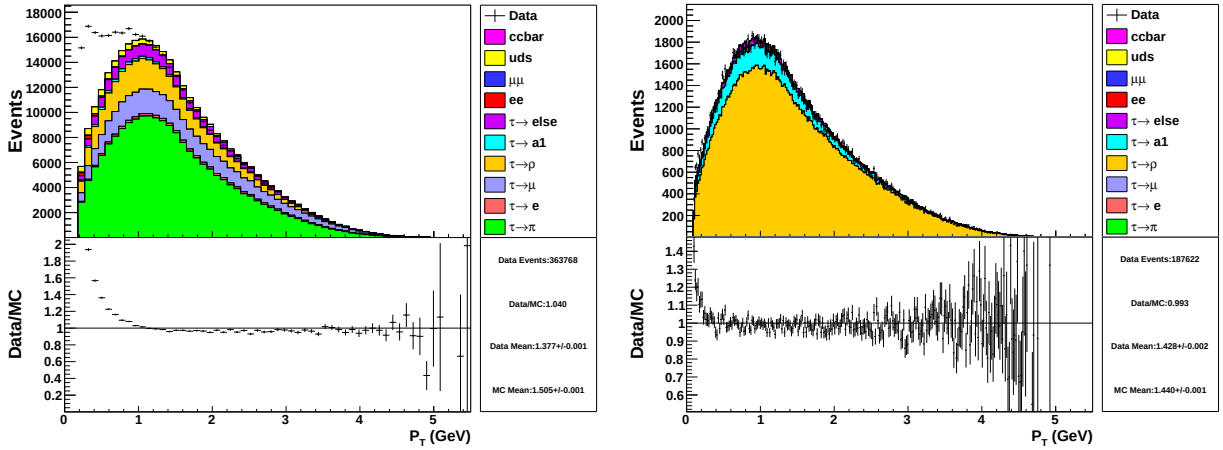

Figure 7.11: Event p_T for pion analysis (left) and ρ analysis (right). All cuts applied except the p_T cut.

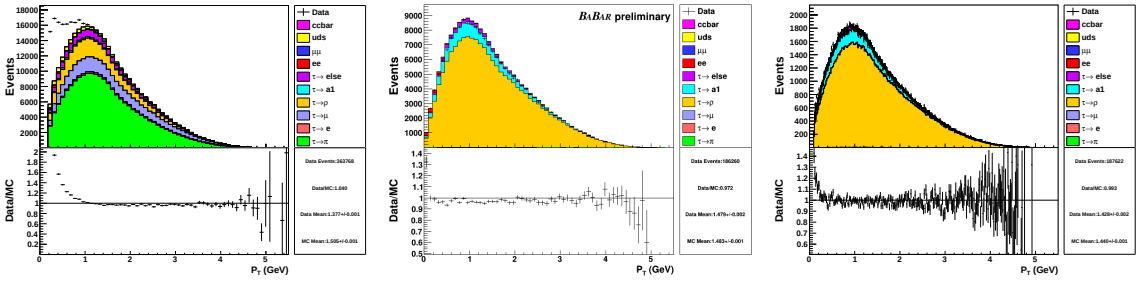

Figure 7.12: Distribution of p_T for the pion analysis(Left), e tagged ρ analysis(Centre), and μ tagged ρ analysis (Right).

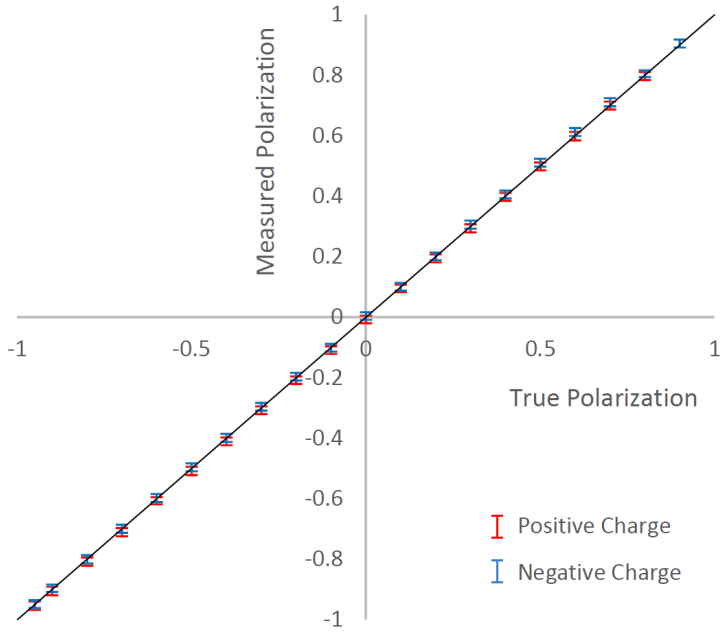

Figure 7.13: Measured beam polarization for a given input polarization mixed from $\tau^{\pm} \to (\rho^{\pm} \to \pi^{\pm}\pi^0)\overline{\nu}_\tau$ signal with $\tau^{\mp} \to \ell^{\mp}\overline{\nu}_\ell\nu_\tau$ tagging. The red points correspond to the measurements for positively charged signal candidates while the blue points correspond to the negatively charged candidates.

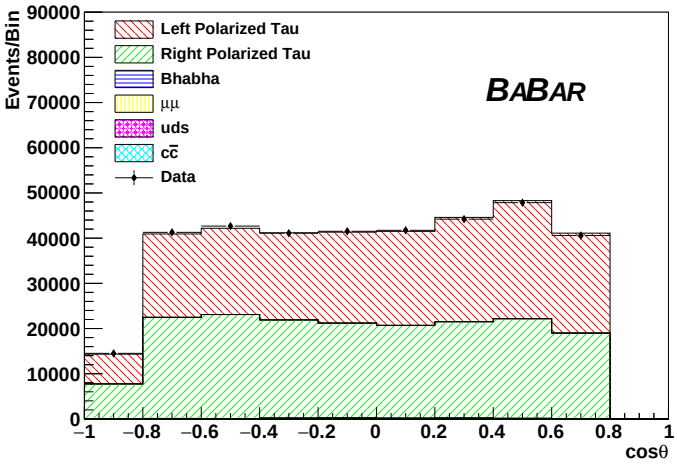

Figure 7.14: One dimensional projection of the fit result for $\cos\theta$ in positively charged candidates in Run 3. $\tau^{\pm} \to (\rho^{\pm} \to \pi^{\pm}\pi^0)\overline{\nu}_\tau$ signal, $\tau^{\mp} \to \ell^{\mp}\overline{\nu}_\ell\nu_\tau$ tagged.

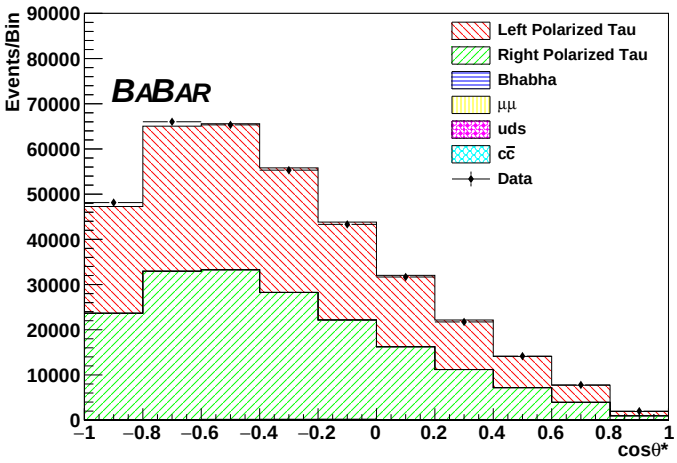

Figure 7.15: One dimensional projection of the fit result for $\cos\theta^\star$ in positively charged candidates in Run 3. $\tau^\pm \to (\rho^\pm \to \pi^\pm\pi^0)\overline{\nu}_\tau$ signal, $\tau^\mp \to \ell^\mp\overline{\nu}_\ell\nu_\tau$ tagged.

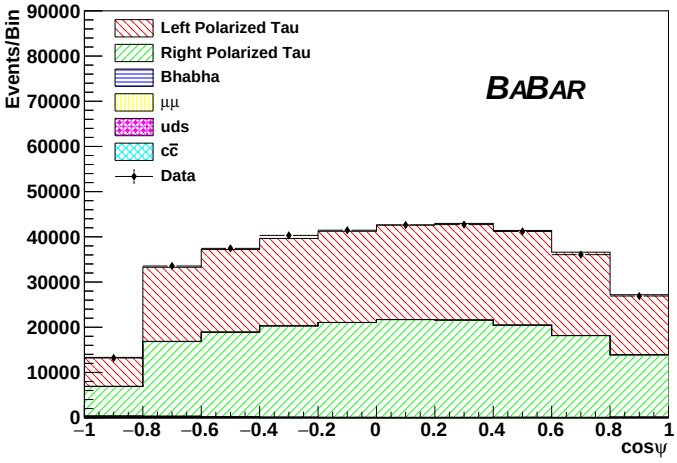

Figure 7.16: One dimensional projection of the fit result for $\cos\psi$ in positively charged candidates in Run 3. $\tau^\pm \to (\rho^\pm \to \pi^\pm\pi^0)\overline{\nu}_\tau$ signal, $\tau^\mp \to \ell^\mp\overline{\nu}_\ell\nu_\tau$ tagged.

Systematic Source	Uncertainty
Muon PID	0.0020
π^0 Likelihood	0.0008
Hadronic Split-off Modelling	0.0013
Minimum Neutral Energy	0.0009
π^0 Mass	0.0017
$\cos\psi$	0.0008
Angular Resolution	0.0008
Electron PID	0.0009
$\cos\theta^\star$	0.0002
Event Transverse Momentum	0.0011
Momentum Resolution	0.0011
π^0 Minimum Photon Energy	0.0008
Tau Branching Fraction	0.0007
Rho Mass	0.0004
Boost	0.0004
Background Modelling	0.0008
Total	0.0041

Table 7.16: Run 3 Systematic Uncertainties.

Source	Run 1	Run 2	Run 4	Run 5	Run 6	Final
Muon PID	0.0016	0.0012	0.0014	0.0008	0.0009	**0.0008**
π^0 Mass	0.0019	0.0008	0.0007	0.0007	0.0008	**0.0006**
Hadronic Split-off Modelling	0.0016	0.0006	0.0011	0.0012	0.0011	**0.0009**
Momentum Resolution	0.0007	0.0005	0.0005	0.0002	0.0008	**0.0004**
Event Transverse Momentum	0.0003	0.0002	0.0003	0.0004	0.0010	**0.0004**
Electron PID	0.0010	0.0010	0.0008	0.0002	0.0003	**0.0005**
Minimum Neutral Energy	0.0008	0.0006	0.0005	0.0004	0.0011	**0.0005**
π^0 Likelihood	0.0026	0.0008	0.0008	0.0008	0.0006	**0.0006**
π^0 Minimum Photon Energy	0.0013	0.0004	0.0006	0.0005	0.0012	**0.0006**
$\cos\psi$	0.0011	0.0008	0.0009	0.0006	0.0010	**0.0007**
Angular Resolution	0.0004	0.0006	0.0007	0.0007	0.0006	**0.0005**
Background Modelling	0.0009	0.0004	0.0012	0.0013	0.0002	**0.0006**
Tau Branching Fraction	0.0007	0.0007	0.0005	0.0005	0.0004	**0.0004**
Boost	0.0012	0.0001	0.0003	0.0010	0.0001	**0.0003**
Rho Mass	0.0005	0.0006	0.0004	0.0004	0.0007	**0.0004**
$\cos\theta^\star$	0.0007	0.0006	0.0005	0.0005	0.0007	**0.0005**
Total	0.0049	0.0026	0.0031	0.0028	0.0031	**0.0023**

Table 7.17: Summary of systematic uncertainties associated with polarization measurement. Run 3 excluded from the sum as expected with a blinded approach.

Data Set	Positive Charge	Negative Charge	Average Polarization
Run 1	-0.0324 ± 0.0124	-0.0073 ± 0.0126	-0.0201 ± 0.0088
χ^2/NDF	776/880	847/879	
Run 2	-0.0051 ± 0.0075	-0.0175 ± 0.0079	-0.0110 ± 0.0055
χ^2/NDF	1017/888	1008/890	
Run 4	-0.0103 ± 0.0057	-0.0213 ± 0.0061	-0.0155 ± 0.0042
χ^2/NDF	1116/891	1087/887	
Run 5	-0.0038 ± 0.0050	-0.0160 ± 0.0053	-0.0096 ± 0.0037
χ^2/NDF	1250/890	1233/892	
Run 6	0.0066 ± 0.0068	-0.0105 ± 0.0066	-0.0023 ± 0.0047
χ^2/NDF	1121/888	1153/887	
Total	-0.0086 ± 0.0028	-0.0183 ± 0.0030	-0.0133 ± 0.0021

Table 7.18: Average beam polarization measured in each data set. The average for each run is found from the weighted mean of the positive and negative fit results.

7.14 Post-Fit Analysis

After unblinding the final result was found to be in 4.3σ tension with a no polarization hypothesis. As the initial measurement with the p_T cut at 1.2 GeV was in good agreement with zero we expect an unknown source of bias has been introduced. In order to diagnose the source the measurement was performed on the electron and muon tag individually in addition to the combined tag. All four measurements are summarized in Table 7.19. While

Measurement	Fit
This Fit (e or μ-tag)	$-0.0133 \pm 0.0021_{\text{stat}} \pm 0.0023_{\text{sys}}$
μ-tag only	$-0.0062 \pm 0.0030_{\text{stat}} \pm 0.0036_{\text{sys}}$
e-tag only	$-0.0148 \pm 0.0030_{\text{stat}} \pm 0.0022_{\text{sys}}$
e-tag $p_T < 1.2$ GeV	$-0.0010 \pm 0.0036_{\text{stat}} \pm 0.0030_{\text{sys}}$

Table 7.19: Fit results for this analysis, both lepton tags individually, and the original preliminary fit.

all these measurements are in agreement at the 2σ level, the largest discrepancy is between the original e-tagged fit ($p_T > 1.2$ GeV) and the current e-tagged only fit. This suggests the change of p_T has introduced an unaccounted for bias in the analysis. At first glance this suggests that the additional Bhabhas introduced by the lowered p_T cut are responsible for the bias. Figure 7.17 shows this distribution and the exponential behaviour at low values of p_T. However since the Data/MC is in good agreement the bias would have to be caused by a

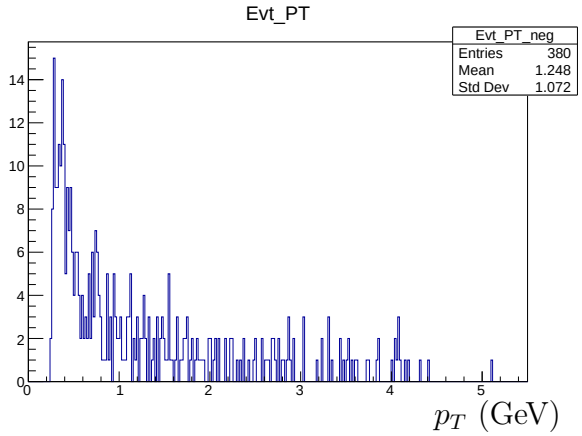

Figure 7.17: p_T distribution of Bhabhas in analysis.

significant shape difference in real Bhabhas compared to MC, as it's clear for the background systematic studies that the number of events has a negligible effect. Figure 7.18 shows that the Bhabha bias hypothesis can be simply tested by requiring $\cos\psi > 0$. Table 7.20 shows

the effect of such a cut, and that the negative bias increases with the cut. Which eliminates Bhabhas as the most likely source of the negative bias.

The second avenue of investigation was an angular restriction to have the tracks be in the

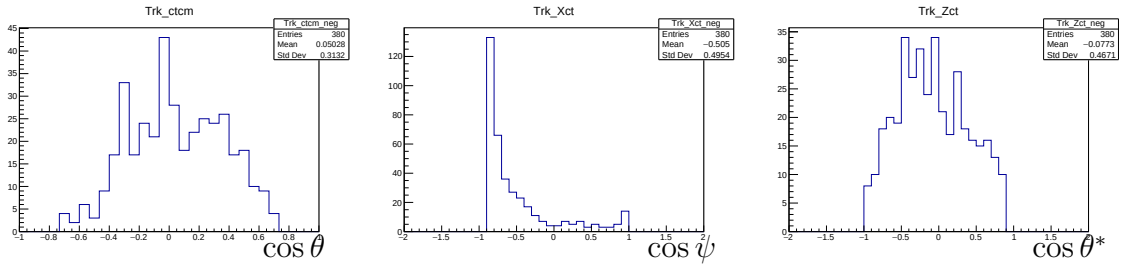

Figure 7.18: Signal variables for MC Bhabhas. $\cos\theta$ (Left), $\cos\psi$ (Middle), $\cos\theta^{\star}$ (Right).

Sample	Positive	Negative	Average
Run 4 Default	-0.0103±0.0061	-0.0213±0.0061	-0.0158±0.0043
Run 4 $\cos\psi > 0$	-0.0180±0.0073	-0.0277±0.0073	-0.0228±0.0052

Table 7.20: Effect of cuts on $\cos\psi$ on Run 4 fit.

barrel. This was done by first restricting the angular cuts from $-0.9 < \cos\theta < 0.8$ to a symmetric $-0.8 < \cos\theta < 0.8$, before finally restricting it to $-0.7 < \cos\theta < 0.7$. Table 7.21

Sample	Positive	Negative	Average
Run 4, $-0.9 < \cos\theta < 0.8$	-0.0090±0.0062	-0.0213±0.0058	-0.0155±0.0042
Run 4, $-0.8 < \cos\theta < 0.8$	-0.0058±0.0063	-0.0199±0.0062	-0.0129±0.0044
Run 4, $-0.7 < \cos\theta < 0.7$	-0.0082±0.0077	-0.0123±0.0080	-0.0102±0.0055
Run 5, $-0.9 < \cos\theta < 0.8$	-0.0025±0.0054	-0.0141±0.0054	-0.0083±0.0038
Run 5, $-0.8 < \cos\theta < 0.8$	-0.0000±0.0060	-0.0115±0.0059	-0.0058±0.0042
Run 5, $-0.7 < \cos\theta < 0.7$	-0.0004±0.0066	-0.0063±0.0066	-0.0033±0.0047

Table 7.21: Run 4 and 5 fits for various angular cuts.

shows the fits for the various $\cos\theta$ cuts and the trend towards zero with increasing cut. As Bhabha contamination seems to not be the source of the bias another source that would correspond to large values of $\cos\theta$ is needed. Checking all signal and tag variables for a hint of bias for tracks in the calorimeter endcaps reveals no source for the bias.

Since the larger p_T acceptance seems to have introduced the bias the p_T selection is varied to determine the behaviour of the bias. To confirm the bias is arising from the events with p_T <1.2 GeV the fit is performed on only these events and the results are shown in Table 7.22.

Sample	Positive	Negative	Average
Run 4, $p_T > 0.25$ GeV	-0.0103±0.0057	-0.0213±0.0061	-0.0155±0.0042
Run 4, $p_T < 1.2$ GeV	-0.0472±0.0100	-0.0363±0.0094	-0.0414±0.0069

Table 7.22: Comparison of polarization fits in full, and isolated to low p_T events.

This shows that the bias towards negative polarization is dominated by the low p_T events, by stepping this cut between 0.25 and 1.2 GeV any threshold effects can be searched for. This is done in two different ways, first by fitting the events above a specific p_T threshold, and secondly by only fitting events below the specified p_T threshold. While this effectively accomplishes the same thing twice it provides two unique perspectives on the bias. This is shown in Figures 7.19 and 7.20 for Runs 4 and 5 respectively. The error bars on these plots represent the statistical error only the difference in the statistical uncertainty. i.e. error bars $= \sqrt{|\sigma^2_{\text{original}} - \sigma^2_{\text{new}}|}$. The p_T study shows that the negative bias appears in a relatively

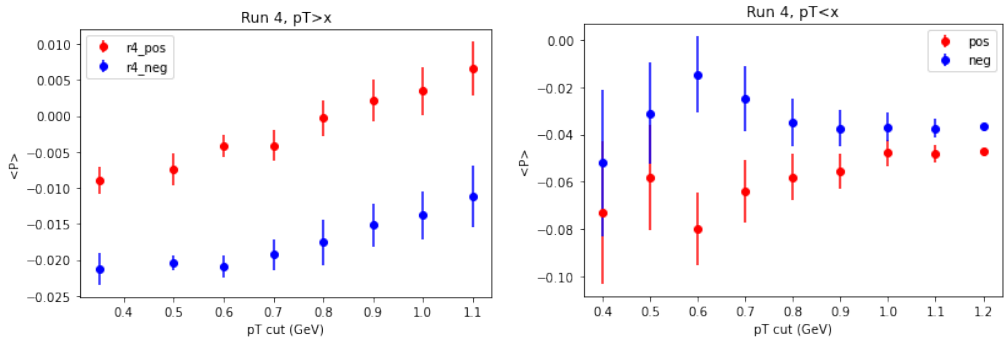

Figure 7.19: Distributions of the polarization fit as a function of p_T cut for the Run 4 data. Fitting with p_T greater than the cut (Left), less than the cut (Right). Error bars represent uncorrelated statistical error.

linear fashion as the p_T cut is loosened, exhibiting definite threshold effect. However, the drifts seem to only begin to occur once the cut moves 100-200 MeV away from the nominal cut value demonstrating a local stability. This suggest no need to assign a large systematic uncertainty to the cut if the overall shift can be understood. Fitting all data with a variety of p_T and $\cos\theta$ cuts is shown in Tables 7.23 to 7.25. From this it seems the most unbiased result occurs at a p_T cut of 1.2 GeV, however the best fit location occurs separately for electrons and muons. With the most unbiased result from electrons at a 1.2 GeV cut and a 800 MeV cut for muons. Table 7.26 shows the deviation from zero polarization for when both leptons are fitted simultaneously. In either case the $\cos\theta$ cut gives little or no improvement to the analysis at the cost of statistics. As such it seems that if no other source of the bias can be determined an intermediate cut of 1.0 GeV may be required.

	$-0.9 < \cos\theta < 0.8$	$-0.8 < \cos\theta < 0.8$	$-0.7 < \cos\theta < 0.7$
$p_T > 0.25$ GeV	-0.0093±0.0020	-0.0092±0.0022	-0.0071±0.0027
$p_T > 0.35$ GeV	-0.0087±0.0021	-0.0080±0.0022	-0.0062±0.0027
$p_T > 0.8$ GeV	-0.0046±0.0022	-0.0039±0.0023	-0.0041±0.0029
$p_T > 1.2$ GeV	0.0033±0.0025	0.0036±0.0027	0.0042±0.0032
$p_T > 0.25$ GeV	4.56σ	4.21σ	2.61σ
$p_T > 0.35$ GeV	4.24σ	3.63σ	2.32σ
$p_T > 0.8$ GeV	2.08σ	1.66σ	1.43σ
$p_T > 1.2$ GeV	1.34σ	1.34σ	1.30σ

Table 7.23: Combined fits for all data with e or μ-tag for various angular requirements. The fit results and the tension with zero are both presented.

	$-0.9 < \cos\theta < 0.8$	$-0.8 < \cos\theta < 0.8$	$-0.7 < \cos\theta < 0.7$
$p_T > 0.25$ GeV	-0.0139±0.0029	-0.0131±0.0030	-0.0083±0.0038
$p_T > 0.35$ GeV	-0.0128±0.0029	-0.0112±0.0031	-0.0071±0.0038
$p_T > 0.8$ GeV	-0.0075±0.0031	-0.0061±0.0033	-0.0047±0.0040
$p_T > 1.2$ GeV	0.0007±0.0035	0.0006±0.0038	0.0037±0.0046
$p_T > 0.25$ GeV	4.85σ	4.31σ	2.18σ
$p_T > 0.35$ GeV	4.41σ	3.62σ	1.87σ
$p_T > 0.8$ GeV	2.45σ	1.84σ	1.17σ
$p_T > 1.2$ GeV	0.21σ	0.15σ	0.81σ

Table 7.24: Combined fits for all data with e-tag for various angular requirements. The fit results and the tension with zero are both presented.

	$-0.9 < \cos\theta < 0.8$	$-0.8 < \cos\theta < 0.8$	$-0.7 < \cos\theta < 0.7$
$p_T > 0.25$ GeV	-0.0049±0.0029	-0.0056±0.0030	-0.0057±0.0037
$p_T > 0.35$ GeV	-0.0049±0.0029	-0.0047±0.0030	-0.0049±0.0037
$p_T > 0.8$ GeV	-0.0026±0.0031	-0.0027±0.0033	-0.0035±0.0040
$p_T > 1.2$ GeV	0.0062±0.0036	0.0059±0.0038	0.0057±0.0045
$p_T > 0.25$ GeV	1.73σ	1.88σ	1.56σ
$p_T > 0.35$ GeV	1.72σ	1.57σ	1.31σ
$p_T > 0.8$ GeV	0.84σ	0.82σ	0.86σ
$p_T > 1.2$ GeV	1.74σ	1.58σ	1.25σ

Table 7.25: Combined fits for all data with μ-tag for various angular requirements. The fit results and the tension with zero are both presented.

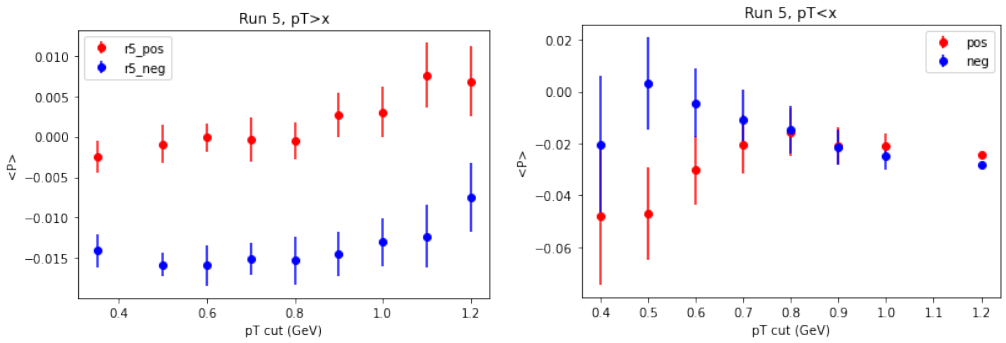

Figure 7.20: Distributions of the polarization fit as a function of p_T cut for the Run 5 data. Fitting with p_T greater than the cut (Left), less than the cut (Right). Error bars represent uncorrelated statistical error.

p_T Cut	$\langle P \rangle$	
1.2 GeV	0.0033±0.0025	1.34σ
1.1 GeV	0.0011±0.0024	0.46σ
1.0 GeV	-0.0007±0.0023	0.33σ
0.9 GeV	-0.0023±0.0022	1.00σ

Table 7.26: Full data fits at various p_T cuts, the fit results and the tension with zero are both presented.

Charge Asymmetry

It was also noted that the unblinded full measurement exhibits a significant charge asymmetry, -0.0086±0.0028 for the positive charges, and -0.0183±0.030 for the negative charges. This represents a 2.4σ tension between charges, and this tension persists regardless of p_T cut. The nature of the polarization sensitivity in the analysis has the dependence flip with both $\cos\theta$ and charge. As such non-polarization dependent biases in the fit will pull the charged fits in opposing directions. This leads to large cancellations of the bias in the average. In order to demonstrate this effect a ±2% slope bias is introduced to $\cos\theta$ in the fit. Importantly this bias is only applied to the fitted sample and not to the templates and acts as a polarization insensitive bias. Tables 7.27 and 7.28 show the effects and absolute shift

Default	Positive	Negative	Average
Sample 1	0.0151±0.0099	0.0045±0.0100	0.0098±0.0070
Sample 2	-0.0022±0.0105	-0.0046±0.0100	-0.0034±0.0072
Sample 3	0.0071±0.0099	-0.0073±0.0099	-0.0001±0.0070
Data	0.0145±0.0106	-0.0071±0.0105	0.0036±0.0075
+2%	Positive	Negative	Average
Sample 1	-0.0027±0.0100	0.0231±0.0106	0.0094±0.0072
Sample 2	-0.0195±0.0100	0.0116±0.0100	-0.0040±0.0071
Sample 3	-0.0113±0.0100	0.0120±0.0100	0.0003±0.0071
Data	-0.0037±0.0101	0.0101±0.0101	0.0032±0.0072
+1%	Positive	Negative	Average
Sample 1	0.0062±0.0104	0.0129±0.0100	0.0097±0.0072
Sample 2	-0.0097±0.0099	0.0029±0.0100	-0.0034±0.0070
Sample 3	-0.0008±0.0105	0.0019±0.0100	0.0006±0.0072
Data	0.0038±0.0101	0.0018±0.0101	0.0028±0.0071
-1%	Positive	Negative	Average
Sample 1	0.0235±0.0099	-0.0041±0.0100	0.0098±0.0070
Sample 2	0.0067±0.0099	-0.0142±0.0100	-0.0036±0.0070
Sample 3	0.0165±0.0105	-0.0146±0.0105	0.0010±0.0074
Data	0.0226±0.0106	-0.0158±0.0101	0.0024±0.0073
-2%	Positive	Negative	Average
Sample 1	0.0317±0.0105	-0.0137±0.0100	0.0080±0.0073
Sample 2	0.0143±0.0105	-0.0227±0.0100	-0.0050±0.0072
Sample 3	0.0234±0.0100	-0.0248±0.0106	0.0007±0.0072
Data	0.0329±0.0101	-0.0244±0.0101	0.0044±0.0071

Table 7.27: Run 3 fits for the default fit and ±2% and ±1% slope biases introduced to the fitted sample.

+2%	Positive	Negative	Average
Sample 1	-0.0178	0.0186	-0.0001
Sample 2	-0.0173	0.0162	-0.0006
Sample 3	-0.0184	0.0193	0.0004
Data	-0.0182	0.0172	-0.0010
+1%	Positive	Negative	Average
Sample 1	-0.0089	0.0084	-0.0001
Sample 2	-0.0075	0.0075	0.0000
Sample 3	-0.0079	0.0092	0.0007
Data	-0.0107	0.0089	-0.0008
-1%	Positive	Negative	Average
Sample 1	0.0084	-0.0086	0.0000
Sample 2	0.0089	-0.0096	-0.0002
Sample 3	0.0094	-0.0073	0.0011
Data	0.0081	-0.0087	-0.0012
-2%	Positive	Negative	Average
Sample 1	0.0166	-0.0182	-0.0015
Sample 2	0.0165	-0.0181	-0.0016
Sample 3	0.0163	-0.0175	0.0008
Data	0.0184	-0.0173	0.0002

Table 7.28: Overall shift from the default fit for each of the introduced slope biases with respect to the default. Central values presented in Table 7.27

.

in the fits the introduction of a 1% bias has. The charge fits show an average shift of 0.0086 in either direction, while the combined fits show an average shift of 0.0001. Looking at the Data fits alone, the 1% bias brings the charge asymmetry to near zero. This suggests the source of the bias may be entirely a linear effect that is canceled out when combining data from the two charge states. Such a cancellation might be advantageous to future polarimetry measurements as a way to remove unmodelled detector biases.

$\cos\theta$ Definition

Further investigation revealed the $\cos\theta$ definition used in the fit may not be optimal. The relationship between the beam polarization and the τ polarization, as shown in Equation 6.1, defines $\cos\theta$ as the angle of the τ^- particle. As the τ direction is impossible to know at the experimental level, the angle of the charged track/pion is used in the fit as a proxy. Investigating different definitions that can be used in the fit as a better proxy for the τ direction is investigated. First the difference between three different $\cos\theta$ definitions and

truth is investigated, as seen in Figure 7.21. These definitions are the previously used charged pion direction, the reconstructed ρ direction, and the angle of the thrust vector (which uses information from both τ decays to determine the directional axis). In order

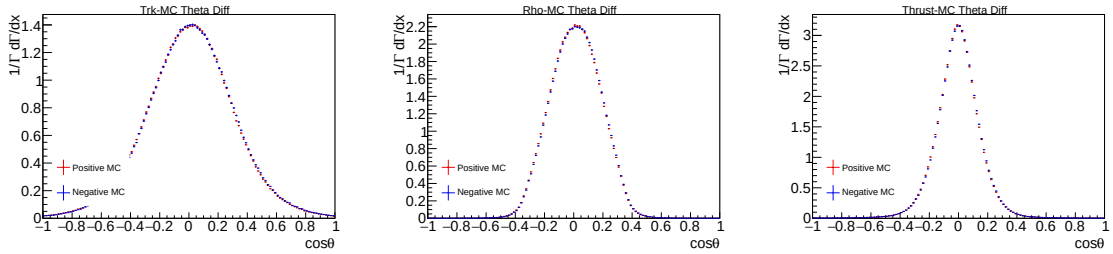

Figure 7.21: Difference in angle (radians) between Track (left), ρ angle (middle), Thrust vector(right) and the τ true direction. From these plots we can see the Thrust definition appears to provide the best representation of the true direction.

to test the effect of the different angular definitions the Run 3 fits were tested. While the MC fits stay relatively consistent throughout, the data fits shift significantly. Tables 7.29 and 7.32 shows these fits under the three definitions and a fourth definition where only the negative charge direction is used(i.e. positive charges use an angle inverted by 180°).

The distribution of events under these $\cos\theta$ definitions is shown in Figure 7.22. The

Source	Positive	Negative	Average
Sample 1	0.0151±0.0104	0.0045±0.0100	0.0096±0.0072
Sample 2	-0.0022±0.0099	-0.0046±0.0100	-0.0034±0.0070
Sample 3	0.0071±0.0099	-0.0073±0.0099	-0.0001±0.0070
Data	0.0145±0.0100	-0.0071±0.0105	0.0042±0.0073

Table 7.29: Run 3 fits for final state charged pion direction as $\cos\theta$ definition. "Default" setup.

Source	Positive	Negative	Average
Sample 1	0.0125±0.0096	0.0071±0.0091	0.0097±0.0066
Sample 2	-0.0025±0.0087	-0.0074±0.0090	-0.0048±0.0062
Sample 3	0.0063±0.0090	-0.0050±0.0087	0.0004±0.0063
Data	0.0363±0.0088	0.0005±0.0088	0.0185±0.0062

Table 7.30: Run 3 fits for reconstructed ρ direction as $\cos\theta$ definition.

non-symmetric shape observed in the thrust definition suggests a bias being introduced from the tag side τ. Judging from these distributions and the improved truth resolution shown earlier the ρ direction definition seems to be the best proxy for the true τ direction.

Source	Positive	Negative	Average
Sample 1	0.0171±0.0083	0.0068±0.0084	0.0120±0.0059
Sample 2	0.0008±0.0083	-0.0142±0.0087	-0.0064±0.0060
Sample 3	0.0044±0.0087	-0.0066±0.0087	-0.0011±0.0061
Data	0.0269±0.0084	-0.0074±0.0087	0.0104±0.0061

Table 7.31: Run 3 fits for thrust direction as $\cos\theta$ definition.

Source	Positive	Negative	Average
Sample 1	0.0170±0.0083	0.0068±0.0084	0.0119±0.0059
Sample 2	0.0009±0.0083	-0.0142±0.0087	-0.0063±0.0060
Sample 3	0.0046±0.0083	-0.0066±0.0087	-0.0008±0.0060
Data	0.0271±0.0084	-0.0074±0.0087	0.0105±0.0061

Table 7.32: Run 3 fits for thrust direction of τ^- only as $\cos\theta$ definition.

Asymmetry of Selection

In order to ensure the forward-backward charge asymmetry remaining in the $\rho\cos\theta$ definition is consistent with expectations, the effect is compared to truth MC as shown in Table 7.33.

$\cos\theta\rho$	Backward	Forward
Positive	771035	663052
Negative	725378	703465
$\frac{N-P}{N+P}$	-0.03	0.03
$\cos\theta\tau$ Truth	Backward	Forward
Positive	23890454	23330485
Negative	23663347	23557592
$\frac{N-P}{N+P}$	-0.005	0.005

Table 7.33: Charge asymmetry present in selection and in truth before selection using the ρ momentum direction as the $\cos\theta$ definition. Importantly the sign of the asymmetry remains the same in the data and truth.

p_T Selection on the Charged Tracks

While a total event p_T cut has already been used to reduce two-photon and Bhabha backgrounds there has been no cut on the individual track p_T's. This is a cut used in other *BABAR* τ analyzes so its addition to this analysis to further improve the selection purity is investigated. Table 7.34 shows the expected number of events effected by such a cut for Runs 3 and 5. Figure 7.23 shows the level of agreement between data and MC for the track

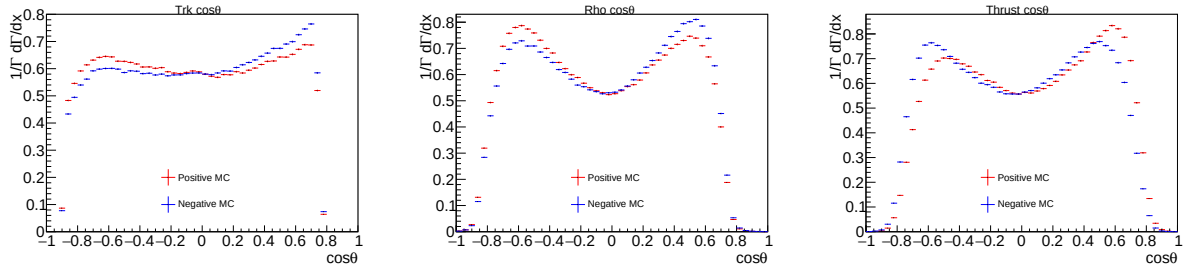

Figure 7.22: Distribution of angles for charged tracks (Left), reconstructed ρ (Middle), and thrust direction (Right).

Run	Total Events	(Trk$_1$|| Trk$_2$) <250 MeV	(Trk$_1$&& Trk$_2$) <250 MeV
3	710908	24527 (3.4%)	2 (0.0003%)
5	2862930	97212 (3.4%)	15 (0.0005%)

Table 7.34: Number of events potentially effected by a minimum p_T requirement.

p_T. While a 250 MeV cut removes the shoulder observed in the distribution the data/MC agreement is poor below 350 MeV. As such both cut thresholds are investigated. Tables 7.35 to 7.37 show the fit results in data for no cut, a 250 MeV cut, and a 350 MeV cut. From these tables the 350 MeV cut shows the best agreement with 0.

Run	Positive	Negative	Average
Run 1	-0.0207 ± 0.0136	-0.0033 ± 0.0139	-0.0122 ± 0.0097
Run 2	0.0124 ± 0.0080	-0.0008 ± 0.0080	0.0058 ± 0.0056
Run 3	0.0301 ± 0.0115	0.0052 ± 0.0110	0.0171 ± 0.0080
Run 4	-0.004 ± 0.0063	0.0020 ± 0.0063	-0.0010 ± 0.0045
Run 5	0.0148 ± 0.0059	0.0112 ± 0.0057	0.0130 ± 0.0041
Run 6	0.0083 ± 0.0075	0.0056 ± 0.0075	0.0069 ± 0.0053
Combined	0.0078 ± 0.0032	0.0049 ± 0.0031	0.0064 ± 0.0022

Table 7.35: All data fits with no track p_T requirement.

Minimum Calorimeter Deposition

Similarly to the track p_T requirement a minimum calorimeter deposition on the charged tracks is a typical analysis requirement. Figure 7.24 shows the distribution and the data/MC agreement. Typically a requirement of 50 MeV is used, however the data/MC comparison shows this response is poorly modelled and a cut will have a minimal effect.

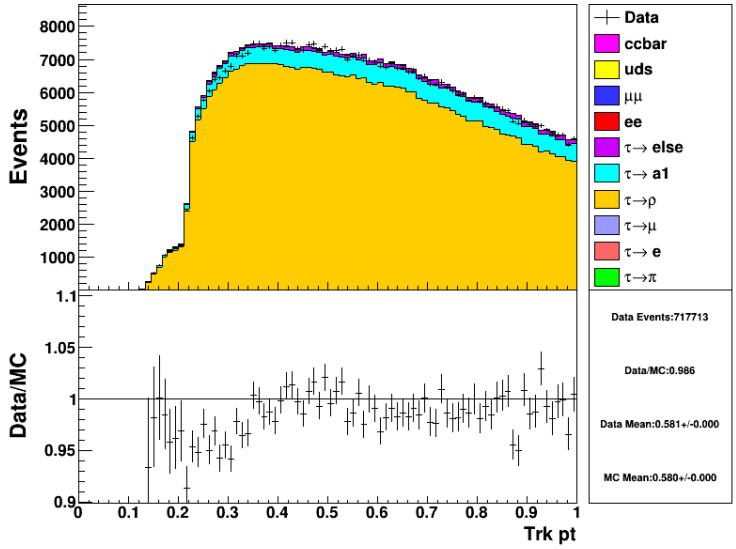

Figure 7.23: Distribution of transverse momentum for the charged signal tracks.

Run	Positive	Negative	Average
Run 1	-0.0168 ± 0.0149	-0.0020 ± 0.0145	-0.0092 ± 0.0104
Run 2	0.0113 ± 0.0087	-0.0040 ± 0.0083	0.0033 ± 0.0060
Run 3	0.0288 ± 0.0120	0.0065 ± 0.0115	0.0172 ± 0.0083
Run 4	-0.0095 ± 0.0069	-0.0017 ± 0.0066	-0.0054 ± 0.0048
Run 5	0.0125 ± 0.0058	0.0137 ± 0.0058	0.0131 ± 0.0041
Run 6	0.0087 ± 0.0075	0.0023 ± 0.0075	0.0055 ± 0.0053
Combined	0.0064 ± 0.0033	0.0040 ± 0.0032	0.0052 ± 0.0023

Table 7.36: All data fits with a track p_T requirement of $p_T > 250$ MeV.

Combination of aforementioned cuts

Applying the cuts one at a time, we observe the track p_T cut has the largest effect in removing the apparent bias to the polarization fit, and reducing the charge asymmetry.

Run	Positive	Negative	Average
Run 1	-0.0176 ± 0.0157	0.0009 ± 0.0160	-0.0085 ± 0.0112
Run 2	0.0075 ± 0.0092	-0.0086 ± 0.0097	-0.0001 ± 0.0067
Run 3	0.0069 ± 0.0126	-0.0018 ± 0.0127	0.0026 ± 0.0090
Run 4	-0.0072 ± 0.0076	-0.0120 ± 0.0073	-0.0097 ± 0.0052
Run 5	0.0072 ± 0.0066	0.0085 ± 0.0067	0.0078 ± 0.0047
Run 6	0.0065 ± 0.0087	-0.0060 ± 0.0083	-0.0001 ± 0.0060
Combined	0.0025 ± 0.0036	-0.0029 ± 0.0036	-0.0003 ± 0.0026

Table 7.37: All data fits with a track p_T requirement of $p_T > 350$ MeV.

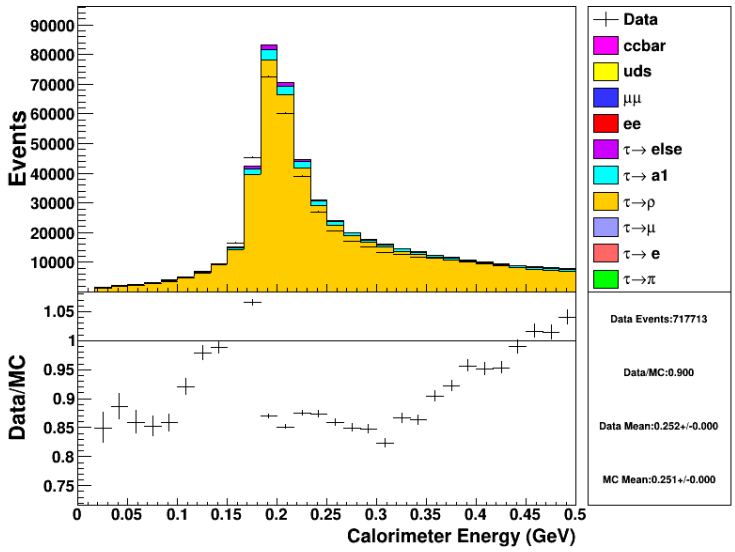

Figure 7.24: Distribution of calorimeter response to charged tracks in data and MC.

Default	Positive	Negative	Average
Sample 1	0.0093±0.0052	-0.0031±0.0052	0.0031±0.0037
Sample 2	0.0033±0.0052	0.0064±0.0050	0.0049±0.0036
Sample 3	0.0042±0.0052	0.0009±0.0054	0.0026±0.0037
Data	0.0155±0.0053	-0.0043±0.0053	0.0057±0.0037
(1)			
Sample 1	0.0090±0.0053	-0.0006±0.0055	0.0044±0.0038
Sample 2	0.0035±0.0053	0.0055±0.0056	0.0045±0.0039
Sample 3	0.0048±0.0055	0.0019±0.0056	0.0034±0.0039
Data	0.0097±0.0054	-0.0078±0.0054	0.0010±0.0038
(2)			
Sample 1	0.0083±0.0057	0.0016±0.0055	0.0048±0.0039
Sample 2	0.0041±0.0054	0.0061±0.0058	0.0051±0.0040
Sample 3	0.0045±0.0056	0.0026±0.0055	0.0036±0.0039
Data	0.0114±0.0055	-0.0069±0.0058	0.0027±0.0040
(3)			
Sample 1	0.0079±0.0057	0.0016±0.0055	0.0046±0.0040
Sample 2	0.0038±0.0055	0.0069±0.0059	0.0053±0.0040
Sample 3	0.0054±0.0057	0.0031±0.0056	0.0042±0.0040
Data	0.0126±0.0055	-0.0066±0.0060	0.0037±0.0041

Table 7.38: Change in central value of fits in response to new cuts. (1) Track p_T >0.250 GeV, (2) previous and minimum track calorimeter energy of 50 MeV, (3) previous and Event $p_T > 0.350$ GeV.

$\pi^{\pm} - \pi^{0}$ Angular Separation

In the past the angular separation between the charged and neutral pion from the ρ was investigated as a source of Data/MC discrepancy. However this angular variable has not been investigated as a source of charge asymmetry before. As matter and anti-matter is known to interact differently within a detector made of matter the poor modelling suggests a charge dependent effect could exist. Figure 7.25 shows the distribution and the level of disagreement appearing above $\cos\theta = 0.9$. Table 7.39 shows all the data fits without a cut on this variable and the tension between charges. Table 7.40 shows the fits and charge asymmetry with the 0.9-1.0 region cut out. This shows a significant improvement in the agreement between charges due to the cut, suggesting a bias is removed by applying the restriction to this variable. To study the systematic effects associated with the cut,

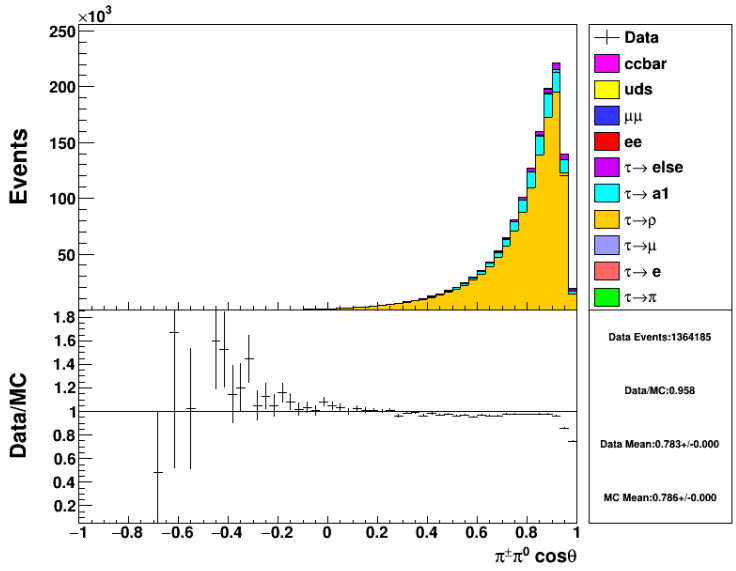

Figure 7.25: Angular separation between charged and neutral pions produced from the ρ decay.

the cut value was varied to a number of values and the shift in the central value of the fit and systematic uncertainties associated with each fit are shown in Figure 7.26. This figure demonstrates a threshold effect occurring at $\cos\theta = 0.9$ suggesting the cut value should remain in the relatively stable region above 0.9. In order to evaluate the level of systematic uncertainty in this variable the uncertainty from the ρ mass of 2 MeV is used. The relationship between fluctuations in the ρ mass and the angular separation of the decay products is given by $\Delta\cos\theta \approx m_{\rho}\Delta m_{\rho}/(E_{\pi}E_{\pi^0}) \approx 0.001$.

Source	Positive	Negative	Average	Asymmetry
Run 1	-0.0097±0.0115	0.0090±0.0122	-0.0009±0.0084	-1.12σ
Run 2	0.0159±0.0071	-0.0055±0.0068	0.0049±0.0049	2.18σ
Run 3	0.0378±0.0093	-0.0041±0.0094	0.0170±0.0066	3.17σ
Run 4	0.0148±0.0057	-0.0061±0.0056	0.0042±0.0040	2.62σ
Run 5	0.0261±0.0047	-0.0033±0.0047	0.0115±0.0033	4.42σ
Run 6	0.0300±0.0064	0.0009±0.0062	0.0150±0.0044	3.27σ
Average	0.0219±0.0027	-0.0030±0.0026	0.0094±0.0019	6.60σ

Table 7.39: Fits with all previous changes implemented and the tension between the charged fits.

Source	Positive	Negative	Average	Asymmetry
Run 1	-0.0180±0.0146	-0.0055±0.0149	-0.0118±0.0104	-0.60σ
Run 2	0.0136±0.0085	-0.0037±0.0086	0.0050±0.0061	1.43σ
Run 3	0.0321±0.0117	0.0023±0.0118	0.0174±0.0083	1.79σ
Run 4	-0.0048±0.0068	-0.0021±0.0068	-0.0035±0.0048	-0.28σ
Run 5	0.0138±0.0062	0.0136±0.0062	0.0137±0.0044	0.02σ
Run 6	0.0106±0.0077	0.0040±0.0078	0.0073±0.0055	0.60σ
Average	0.0085±0.0033	0.0035±0.0033	0.0060±0.0024	1.06σ

Table 7.40: Fits with all previous changes implemented and an angular separation of $\cos\theta < 0.9$ between the final state charged and neutral pion. Charge asymmetries show a significant reduction and the averages are in better agreement with zero.

$\cos\theta^*$ and $\cos\psi$ range

As the $\cos\theta^*$ and $\cos\psi$ are constructed angles rather than true angular measurements, they can extend beyond the -1 to 1 range due to resolution effects. This is shown in Figures 7.27 and 7.28. The fit results with the extended regions is shown in Table 7.41, and while the fits exhibit similar charge asymmetry and agreement with zero, the statistical uncertainty has remained the same. This suggests that the extension of the range actually loses sensitivity at the same rate the statistics improve. For the *BABAR* measurement this gives us no incentive to implement this change.

Total Calorimeter Energy

In order to reduce residual Bhabha backgrounds a cut is placed on the total calorimeter energy in the event. Requiring the total energy to be below 10 GeV removes half the remaining Bhabha backgrounds with only a small amount of signal lost. The distribution of energy deposited in the calorimeter is shown in Figure 7.29 for τ and Bhabha events. At 10

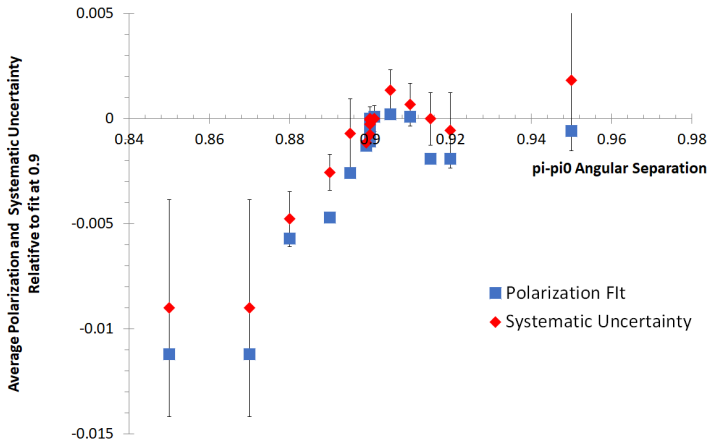

Figure 7.26: Distribution of central values of the polarization fits with respect to the cut on pi-pi0 angular separation. Statistical uncertainty not shown. Systematic uncertainties and corresponding MC statistical uncertainty also included.

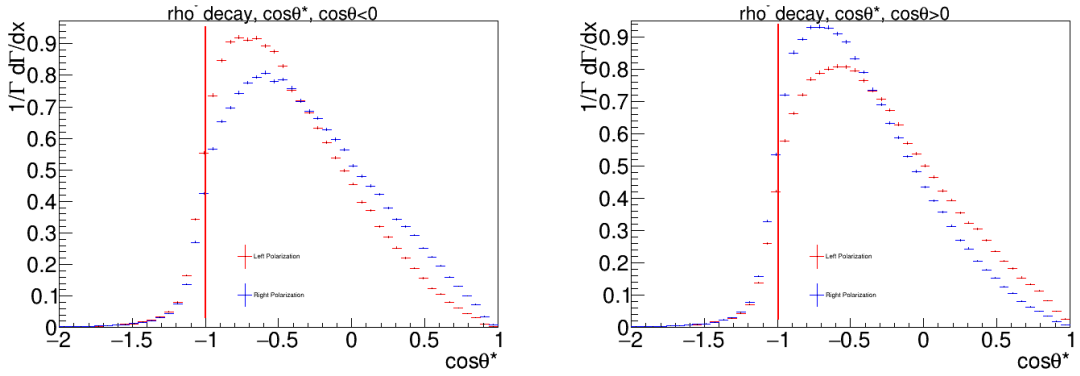

Figure 7.27: Polarization Sensitivity in the backward (Left) and forward (Right) region for $\cos\theta^*$

GeV, 119 out of 226 Bhabha events are cut, a 53% reduction. While 521 τ events are cut, a 0.028% reduction in signal. The effect on the fits is minimal, with the Data fit shifting by $\sim$0.0015, as shown ion Table 7.42.

Event Selection and Purity

All of the post-fit variables which were investigated above were determined before the investigation began to avoid as much bias as possible. After the investigation the following changes were made:

1. $\cos\theta$ definition changed from pion direction to ρ direction

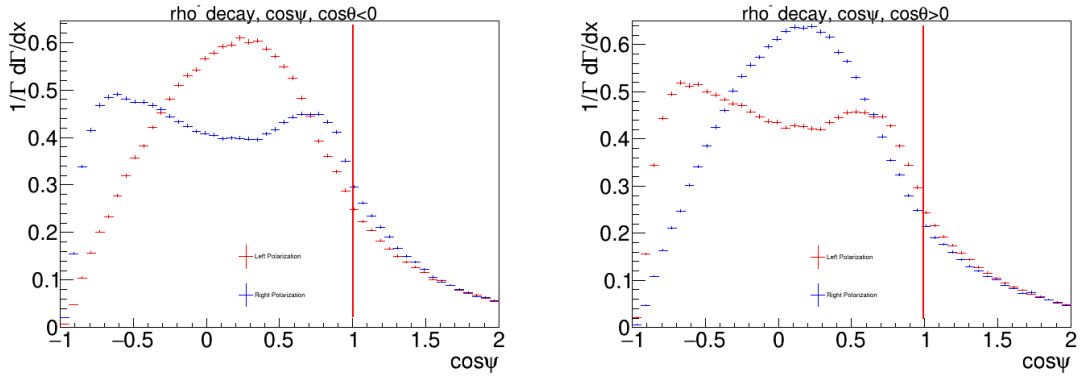

Figure 7.28: Polarization Sensitivity in the backward (Left) and forward (Right) region for $\cos\psi$

Source	Positive	Negative	Average	Asymmetry
Run 1	-0.0185±0.0146	-0.0058±0.0149	-0.0123±0.0104	-0.61σ
Run 2	0.0165±0.0086	-0.0062±0.0087	0.0053±0.0061	1.86σ
Run 3	0.0275±0.0111	0.0112±0.0118	0.0199±0.0081	1.01σ
Run 4	-0.0038±0.0068	-0.0019±0.0069	-0.0029±0.0048	-0.20σ
Run 5	0.0095±0.0064	0.0130±0.0060	0.0114±0.0044	-0.40σ
Run 6	0.0066±0.0077	0.0028±0.0078	0.0047±0.0055	0.35σ
Average	0.0070±0.0033	0.0038±0.0033	0.0053±0.0024	0.67σ

Table 7.41: Fits with $\cos\theta^*$ extended to 1.5 and $\cos\psi$ extended to -1.5.

2. p_T requirement of 350 MeV added to charged tracks
3. $\pi - \pi^0$ separation of $\cos\theta < 0.9$ required
4. Total event calorimeter energy is less than 10 GeV

With these new cuts the total event purity has improved as shown in Table 7.43.

Data/MC check

With all new cuts in place the Data/MC ratio improves for all runs as well but a 1% efficiency difference remains as shown in Table 7.44.

7.15 Corrected Fit Results

With all of the corrections implemented the fits are significantly improved as shown in Table 7.45. Evaluating all the systematic uncertainties with this new selection gives the results shown in Table 7.46, Run 3 is no longer excluded due to the unblinded nature of the post-fit

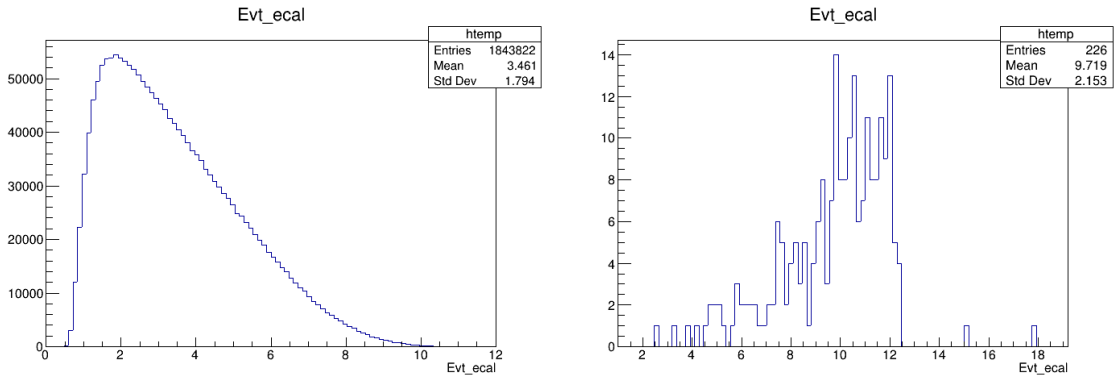

Figure 7.29: Total calorimeter energy for τ events (Left) and Bhabha events (Right).

No E cut	Positive	Negative	Average
Sample 1	0.0113±0.0122	0.0024±0.0119	0.0068±0.0085
Sample 2	-0.0067±0.0117	-0.0207±0.0125	-0.0132±0.0085
Sample 3	0.0086±0.0117	-0.0153±0.0119	-0.0031±0.0083
Data	0.0298±0.0117	0.0033±0.0119	0.0168±0.0083
E< 10 GeV	Positive	Negative	Average
Sample 1	0.0107±0.0116	0.0021±0.0119	0.0065±0.0083
Sample 2	-0.0065±0.0117	-0.0206±0.0119	-0.0134±0.0083
Sample 3	0.0082±0.0122	-0.0158±0.0126	-0.0034±0.0088
Data	0.0283±0.0122	0.0026±0.0119	0.0151±0.0085

Table 7.42: Fits of Run 3 MC and Data for no cut on calorimeter energy and requiring it to be less than 10 GeV

analysis. While the central value of the fit is in good agreement with the expectation of zero, the overall χ^2 of the fits is poor, particularly runs 4,5,6. The next sections will describe the investigations into the fits to see if the source of the poor χ^2 values can be identified.

7.16 Fit χ^2 Studies

In order to evaluate the appropriate size of the fit χ^2 values and whether the previously achieved χ^2 indicate an issue, a variety of tests are performed. This includes: an independent technique to evaluate the χ^2 values, whether background mis-modelling is an issue, a check to see if the poor χ^2 values arise from merged or reconstructed neutral pions, the effect of low statistics bins in the fit, whether the tag side is contributing to the χ^2 values, and the effect of the π^0 efficiency as contributes to the remaining data/MC discrepancy.

MC	Old %	New %
uds	0.031	0.030
cc	0.005	0.006
ee	0.215	0.046
$\mu\mu$	0.067	0.046
$\tau\tau$	99.681	99.871
$\tau \to e$	0.017	0.018
$\tau \to \mu$	0.024	0.031
$\tau \to \pi$	0.035	0.035
$\tau \to \rho$	87.667	87.858
$\tau \to a_1$	9.561	9.785
$\tau \to$else	2.377	2.145

Table 7.43: Purity of event selection before and after new selection criteria.

Run	Positive	Negative
Run 1	0.979	0.981
Run 2	0.989	0.993
Run 3	0.999	1.002
Run 4	0.986	0.988
Run 5	0.978	0.979
Run 6	0.982	0.984

Table 7.44: Data/MC ratios for all runs

7.16.1 Validation of χ^2 Values

In order to ensure the χ^2 values are correct we perform our own calculation from the fit results to see if they are in agreement. The χ^2 values and degrees of freedom shown in Table 7.45 are reported by the fit, whereas for thisr calculation a bin-by-bin summation is done.

$$\chi^2 = \sum_{bins} \frac{(N_D - (N_L + N_R + N_{ee} + N_{\mu\mu} + N_{uds} + N_{c\bar{c}}))^2}{N_D + N_L + N_R + N_{ee} + N_{\mu\mu} + N_{uds} + N_{c\bar{c}}} \tag{7.4}$$

Where D refers to the data, and the other subscripts to their respective MC sources. The non-data numbers are also scaled based on the contribution to the fit. Using this method the χ^2's found are shown in Table 7.47. From these results it can be seen that the poor χ^2 results are inherent to the data-set and not just a product of the method used to determine it.

Data Set	Positive Charge	Negative Charge	Average Polarization
Run 1	-0.0199±0.0157	0.0040±0.0160	-0.0081±0.0112
χ^2/NDF	689/833	729/835	
Run 2	0.0056±0.0092	-0.0071±0.0092	-0.0007±0.0065
χ^2/NDF	826/875	847/867	
Run 3	0.0051±0.0126	0.0007±0.0127	0.0029±0.0090
χ^2/NDF	803/850	845/841	
Run 4	-0.0090±0.0076	-0.0098±0.0073	-0.0094±0.0053
χ^2/NDF	1166/878	1048/877	
Run 5	0.0053±0.0064	0.0104±0.0063	0.0079±0.0045
χ^2/NDF	1619/881	1476/889	
Run 6	0.0051±0.0088	-0.0040±0.0082	-0.0002±0.0060
χ^2/NDF	1431/886	1319/877	
Total	0.0007±0.0036	-0.0006±0.0035	0.0001±0.0025

Table 7.45: Average beam polarization measured in each data set after the post-analysis corrections are added. The average for each run is found from the weighted mean of the positive and negative fit results.

7.16.2 Background Fixed Contributions

As the background contributions in the fit are fixed based on the MC efficiencies a slightly different selection in the data would lead to a higher χ^2 evaluation. Using the Run 4 data and allowing the background contributions to fluctuate, i.e. no longer fixed, by up to a factor of 20 from their nominal values gave the following results. Allowing the backgrounds to float in the fit significantly improves the χ^2 scores with small changes to the central values. The fit itself performs notably worse however as the backgrounds contributions all hit the limit of the fluctuation allowed suggesting the distributions do not differ significantly enough for the fit to weight them correctly. The fit also partially fails on the negatively charged fit resulting in the statistical uncertainty not being able to be extracted. Due to these issues the background contributions are not changed.

7.16.3 Merged vs. Reconstructed π^0 Modes

In order to check if the poor χ^2 values are primarily from merged or reconstructed π^0's the fit is performed using only merged, and then only reconstructed events, as shown in Table 7.48. From these fit results it can be seen that a large amount of charge sensitive bias enters while only seeing significant improvement to the χ^2 in the reconstructed π^0 portion of the fit. This suggests both samples are needed in the fit to get a good result, and there may be some sensitivity to the respective efficiencies in their selection.

	Run 1	Run 2	Run 3	Run 4	Run 5	Run 6	Combined
Muon PID	0.0018	0.0018	0.0029	0.0011	0.0006	0.0016	**0.0012**
Hadronic Split-off Modelling	0.0015	0.0017	0.0016	0.0006	0.0016	0.0020	**0.0011**
π^0 Mass	0.0018	0.0028	0.0010	0.0005	0.0004	0.0004	**0.0008**
$\pi - \pi^0$ Angular Separation	0.0015	0.0009	0.0016	0.0007	0.0005	0.0005	**0.0007**
π^0 Likelihood	0.0015	0.0009	0.0015	0.0006	0.0003	0.0010	**0.0006**
π^0 Minimum Photon Energy	0.0018	0.0006	0.0005	0.0012	0.0003	0.0004	**0.0005**
Electron PID	0.0011	0.0020	0.0008	0.0006	0.0005	0.0001	**0.0005**
Minimum Neutral Energy	0.0005	0.0007	0.0008	0.0003	0.0004	0.0005	**0.0004**
Particle Transverse Momentum	0.0012	0.0007	0.0009	0.0002	0.0003	0.0006	**0.0004**
Boost	0.0004	0.0019	0.0003	0.0004	0.0004	0.0004	**0.0004**
Momentum Resolution	0.0001	0.0014	0.0005	0.0002	0.0001	0.0005	**0.0004**
Max Calorimeter Response	0.0001	0.0011	0.0008	0.0001	0.0002	0.0005	**0.0003**
τ Direction Definition	0.0003	0.0007	0.0008	0.0003	0.0001	0.0004	**0.0003**
Angular Resolution	0.0003	0.0008	0.0003	0.0003	0.0002	0.0003	**0.0003**
Background Modelling	0.0005	0.0006	0.0010	0.0002	0.0003	0.0003	**0.0003**
Event Transverse Momentum	0.0001	0.0013	0.0005	0.0002	0.0002	0.0004	**0.0003**
Rho Mass	0.0000	0.0011	0.0003	0.0001	0.0002	0.0005	**0.0003**
Tau Branching Fraction	0.0001	0.0007	0.0004	0.0002	0.0002	0.0002	**0.0002**
$\cos\theta^\star$	0.0002	0.0006	0.0004	0.0001	0.0001	0.0004	**0.0002**
$\cos\psi$	0.0002	0.0003	0.0002	0.0002	0.0002	0.0003	**0.0002**
Total	0.0045	0.0057	0.0047	0.0023	0.0021	0.0032	**0.0025**

Table 7.46: Systematic uncertainties from all Runs after the post-fit analysis corrections. Run 3 not excluded as the nature of the post-fit analysis was unblinded so excluding Run 3 does not remove the introduced potential analyst bias.

χ^2/NDF	Positive Charge	Negative Charge
From Fit	1319/886	1312/877
This Calculation	1362/909	1317/903

Table 7.47: Comparison of goodness of fit between internal fit calculation and comparative validation.

7.16.4 Excluding Bins in Fit due to Low Statistics

Bins with 0 events are excluded from the fit to avoid any biases arising from low statistics bins, this is the root source of the fits containing different numbers of degrees of freedom. To test the sensitivity to this requirement, the requirement was raised from more than 0 events to more than 100 events. The effect of this change is shown in Table 7.49. While the central values of the fits remain largely the same, the χ^2 values and NDF shift significantly. Converting these to P-values as shown in Table 7.50 shows a decrease in likelihood although both remain effectively zero. This indicates no bias arising from the low statistics bins, and therefore no reason to exclude them.

	Positive Charge	Negative Charge	Combined Average
Run 6	0.0051±0.0088	-0.0040±0.0082	0.0002±0.0060
χ^2/NDF	1431/886	1319/877	
merged	0.1345±0.0126	-0.0938±0.0126	0.0210±0.0089
χ^2/NDF	1368/804	1296/794	
reconstructed	-0.0485±0.0103	0.0307±0.0102	-0.0087±0.0073
χ^2/NDF	947/853	972/853	

Table 7.48: Sensitivity of the fit to the separate π^0 modes. Large charge asymmetries result in the separate modes.

	Positive Charge	Negative Charge	Combined Average
>0 events	0.0066±0.0087	-0.0060±0.0087	0.0003±0.0062
χ^2/NDF	1390/886	1312/877	
>100 events	0.0062±0.0087	-0.0078±0.0085	-0.0010±0.0061
χ^2/NDF	953/530	941/531	

Table 7.49: Effect on polarization fits due to requiring a minimum number of events in each bin.

	χ^2/NDF	P-Value
>0 events	1390/886 & 1312/877	10^{-19} & 10^{-24}
>100 events	953/530 & 941/531	10^{-25} & 10^{-26}

Table 7.50: Comparison of probability for excluding more bins. Probability decreases with more excluded bins.

7.16.5 Tag-Side Bias from 40 cm Cut

The 40 cm re-association of neutral particles with the charged tracks is not well modelled in the MC, given the correlations between the τs on either side of the event it's feasible the tag–side τ introduces a bias. By removing the 40 cm re-association for the lepton tags the overall efficiency drops due to more events failing the no neutrals on the tag-side requirement. The shifts in the fit are shown in Table 7.51 and two effects are notable, the improvement in the χ^2 values and the increase in statistical uncertainty. Ignoring the shifts in the central value of the fit for the moment, the increase in statistical uncertainty alone would be expected to reduce the χ^2 values as the error bars across all bins are larger. The statistical uncertainty should scale as $1/\sqrt{N}$ which means the new fit has only 48.7% of the number of events compared to the original. This should also correspond to the same drop in the χ^2 values. Suggesting if the central value remained the same a χ^2 as low as 650-700 could be explained by just the change is statistics. As the χ^2 values remain much larger than this it is concluded

that a significant underlying bias is still present.

	Positive Charge	Negative Charge	Combined Average
Run 6	0.0051±0.0088	-0.0040±0.0082	0.0002±0.0060
χ^2/NDF	1431/886	1319/877	
no 40cm on leptons	-0.0126±0.0117	0.0201±0.0115	0.0040±0.0082
χ^2/NDF	1198/858	1052/849	

Table 7.51: Effect of removing the 40 cm re-association on the tag-side leptons on the polarization fit. Significant reduction in statistics fully accounts for shift in χ^2 values.

7.16.6 Run-by-Run Comparisons

As Runs 4,5,6 appear to behave differently than Runs 1,2,3 a comparison on the consistency between runs is carried out. This is done by normalizing the 3D data histogram by it's integral and calculating the χ^2 difference between runs in the same bin-by-bin calculation used to validate the χ^2 values before. This is shown as a χ^2/NDF in Tables 7.52 and 7.53 and as an order of magnitude of the P-Value in Tables 7.54 and 7.55. From these tables it is observed that the adjoining runs tend to be the most compatible, this suggests the detector is changing with time which is expected, and no particular run stands out as problematic.

7.16.7 π^0 Efficiency

Much of the data/MC efficiency discrepancies are rooted in the π^0 selection efficiencies, which is a known feature from internal *BABAR* notes. Observing the lab frame π^0 momentum and angular data/MC distributions, shown in Figure 7.30 highlights the modelling issues. In addition to these ratios being a few percent less than 1, there is a clear shape discrepancy in the momentum plot. As the distribution of these events is polarization sensitive a correction

χ^2/NDF	Run1	Run2	Run3	Run4	Run5	Run6
Run1	X					
Run2	752/696	X				
Run3	831/691	820/695	X			
Run4	938/699	818/700	766/699	X		
Run5	959/701	879/700	793/700	671/704	X	
Run6	902/699	838/701	849/700	956/704	815/705	X

Table 7.52: Difference between runs calculated bin-by-bin as a χ^2 for the negative charged selection.

χ^2/NDF	Run1	Run2	Run3	Run4	Run5	Run6
Run1	X					
Run2	753/700	X				
Run3	775/693	735/703	X			
Run4	851/696	799/704	757/699	X		
Run5	980/697	937/702	795/700	749/701	X	
Run6	854/700	818/704	821/700	884/703	866/702	X

Table 7.53: Difference between runs calculated bin-by-bin as a χ^2 for the positive charged selection.

prob O(x)	Run1	Run2	Run3	Run4	Run5	Run6
Run1	X					
Run2	-2	X				
Run3	-4	-4	X			
Run4	-9	-3	-2	X		
Run5	-10	-6	-3	-1	X	
Run6	-7	-4	-5	-10	-3	X

Table 7.54: Order of magnitude of probability of statistical compatibility between runs for the negative charged selection. Calculated from χ^2 values in above tables. e.g. probability of $10^{-5} \rightarrow -5$.

to them is an important step missed in the analysis to this point.

As a way to improve the agreement in both of the distributions simultaneously and potentially improve the polarization fit χ^2's a correction is designed for the two-dimensional momentum vs. $\cos\theta$ distributions. The data/MC ratios for the unpolarized MC are binned in a 20x20 2D histogram shown in Figure 7.31. The polarized MC is then corrected bin-by-bin with these ratios to result in a corrected distribution. This corrected histogram is also shown in Figure 7.31. The one dimensional projections of this corrections are shown in Figure 7.32. The corrected distributions are notably in better agreement with 1 and exhibit flat distributions. Table 7.56 shows the fit results after the corrections are applied.

7.16.8 Update to the Weighting Method

Prior to this point, the histograms in the fit have been pre-weighted to account for any luminosity or efficiency differences in the MC. It was pointed out that this approach risks the statistical uncertainties being incorrect as the fitting algorithm calculates its own errors rather than using the ones provided in the histograms. To correct for this, a weighting histogram was created which can be generated for each type of MC and be passed to the

prob O(x)	Run1	Run2	Run3	Run4	Run5	Run6
Run1	X					
Run2	-2	X				
Run3	-2	-1	X			
Run4	-5	-3	-2	X		
Run5	-12	-9	-3	-1	X	
Run6	-5	-3	-3	-6	-5	X

Table 7.55: Order of magnitude of probability of statistical compatibility between runs for the positive charged selection. Calculated from χ^2 values in above tables. e.g. probability of $10^{-5} \rightarrow -5$.

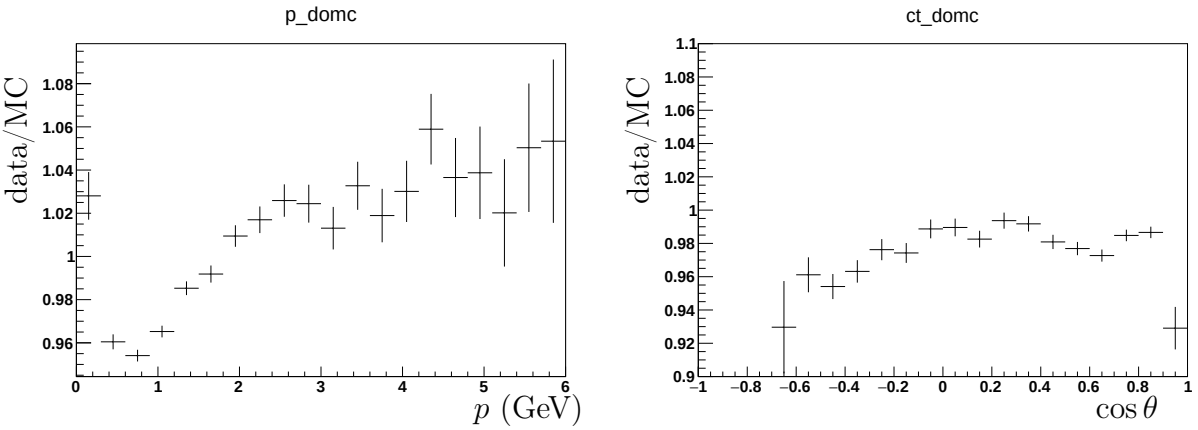

Figure 7.30: Data over MC ratios for momentum (Left) and $\cos\theta$ (Right). Uncorrected distributions.

fitting algorithm. This weighting histogram functionally does the same as the pre-scaling but is usable by the fit. This has the added benefit of being able to apply luminosity and efficiency corrections to the weighting histograms which are easier to verify than scaling the template histograms. Table 7.57 shows the re-weighted fit results under the same selection criteria shown in Table 7.45, i.e. before the π^0 efficiency correction. Table 7.58 shows the fits with the π^0 efficiency correction applied which demonstrates slight improvements to the statistical uncertainties and more significant improvements in the reported χ^2 values .

7.16.9 π^0 Efficiency Systematic Uncertainty

In order to assign a systematic uncertainty to the π^0 correction a number of options are investigated. The first option investigated is the most conservative method which is to compare the central values of the uncorrected and corrected fits and assign an uncertainty of half the total shift. Next, a novel approach is tested. This approach assumes the systematic

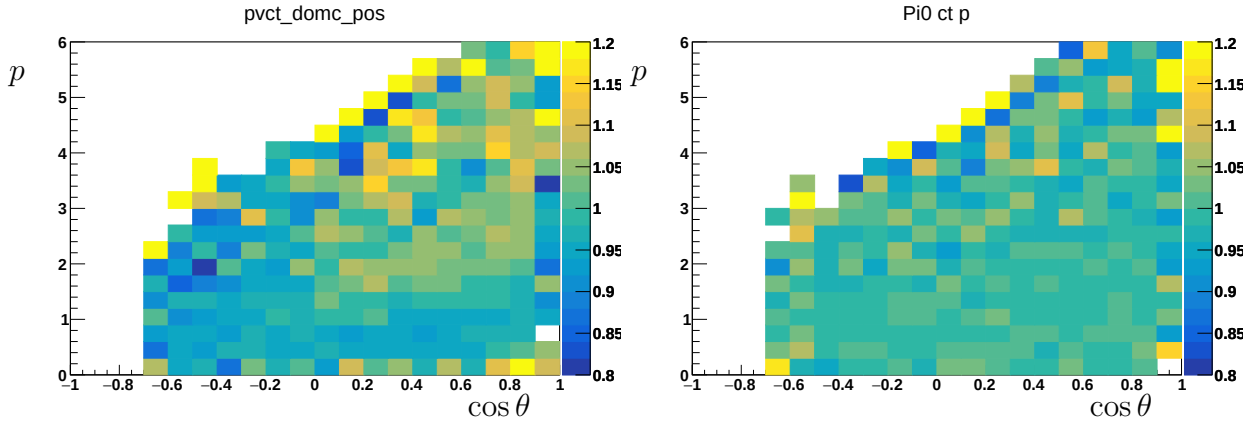

Figure 7.31: Data over MC 2D distributions. Uncorrected (Left) and bin-by-bin corrected (Right).

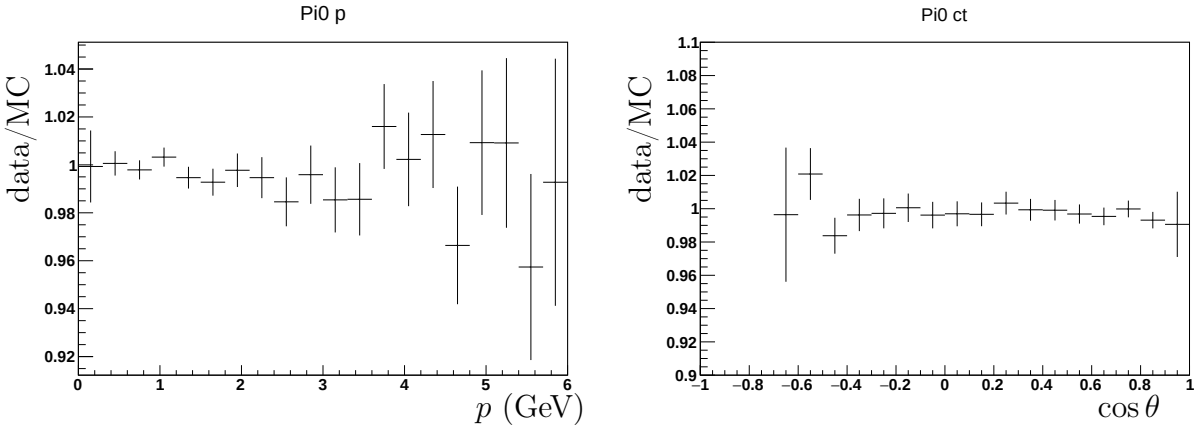

Figure 7.32: Data over MC ratios for momentum (Left) and $\cos\theta$ (Right). Bin-by-bin corrected distributions.

effect is independent of statistics or other systematic uncertainties and assigns an uncertainty based on the change in the fit reported χ^2 values. Under this assumption the final χ^2 value can be expressed as:

$$\chi^2_f = \frac{\chi^2_i}{1 + \frac{\sigma^2_{\text{sys}}}{\sigma^2_{\text{stat}}}} \tag{7.5}$$

Which rearranged gives:

$$\sigma^2_{\text{sys}} = \sigma^2_{\text{stat}} \left(\frac{\chi^2_i}{\chi^2_f} - 1 \right) \tag{7.6}$$

This approach is designed to give a quick approximation of the systematic uncertainties and if the results are insignificant, no further analysis is required. The final approach is the more typical approach, which varies the correction values up or down by 1 σ based on the

	Positive Charge	Negative Charge	Combined Average
Run 1	0.0013±0.0203	-0.0063±0.0207	-0.0024±0.0145
χ^2/NDF	395/833	426/835	
Run 2	0.0076±0.0119	0.0005±0.0119	0.0040±0.0084
χ^2/NDF	435/875	463/867	
Run 3	0.0162±0.0164	-0.0060±0.0166	0.0052±0.0117
χ^2/NDF	430/850	466/841	
Run 4	-0.0030±0.0093	0.0014±0.0100	-0.0010±0.0068
χ^2/NDF	549/878	530/877	
Run 5	-0.0004±0.0088	0.0172±0.0087	0.0084±0.0062
χ^2/NDF	791/881	720/889	
Run 6	0.0015±0.0083	0.0122±0.0083	0.0069±0.0058
χ^2/NDF	1231/886	1123/877	
Average	**0.0019±0.0044**	**0.0076±0.0044**	**0.0047±0.0031**

Table 7.56: Fit results for all runs after the 2D efficiency corrections are applied.

bin-by-bin statistical uncertainties. The results of all these approaches are summarized in Table 7.59. For this analysis the final column, the statistical variation of bins, is used as it is inline with the rest of the analysis methodology and the standard approach. However the run-by-run consistency of the χ^2 evaluation method suggests it may be a robust method for estimating systematic uncertainties, although the results will be more conservative. This method would be a quick way to evaluate systematic uncertainties and identify sources that require a more detailed approach. Running the last column results, the $\pm\sigma$ numbers, through the same correlation sensitive method as the rest of the systematic uncertainties results in a overall systematic uncertainty of 0.0013 being assigned to the efficiency correction.

7.17 Conclusions

With all of the post-fit analysis completed the average beam polarization measured at *BABAR* has been found to be $\langle P \rangle = 0.0035 \pm 0.0024_{\text{stat}} \pm 0.0029_{\text{sys}}$. Table 7.58 shows the final fit results and Table 7.60 shows the full list of systematic uncertainties.

A huge number of lessons have been learned in the development of the $\tau^{\pm} \to (\rho^{\pm} \to \pi^{\pm}\pi^0)\overline{\nu}_{\tau}$ v.s. $\tau^{\mp} \to \ell^{\mp}\overline{\nu}_{\ell}\nu_{\tau}$ analysis and those insights will go a long way in the implementation of Tau Polarimetry at Belle II and potentially at other future colliders. The primary achievement of this analysis has been to identify the modelling of neutral particles in the *BABAR* detector as the primary source of systematic uncertainties, as this gives Belle II a clear goal for where it needs to do much better to surpass the *BABAR* accuracy.

Data Set	Positive Charge	Negative Charge	Average Polarization
Run 1	-0.0157±0.0142	0.0023±0.0144	-0.0068±0.0101
χ^2/NDF	808/833	871/835	
Run 2	0.0067±0.0086	-0.0078±0.0088	-0.0003±0.0061
χ^2/NDF	981/875	1025/867	
Run 3	0.0077±0.0120	-0.0007±0.0116	0.0033±0.0083
χ^2/NDF	988/850	1010/841	
Run 4	-0.0081±0.0069	-0.0105±0.0071	-0.0093±0.0049
χ^2/NDF	1314/878	1295/877	
Run 5	0.0036±0.0064	0.0069±0.0060	0.0054±0.0044
χ^2/NDF	1692/881	1667/889	
Run 6	0.0075±0.0085	-0.0052±0.0088	0.0014±0.0061
χ^2/NDF	1361/886	1246/877	
Total	0.0010±0.0034	-0.0021±0.0034	-0.0006±0.0024

Table 7.57: All data fits with weighted histograms passed to the fitter rather than pre-scaling. π^0 efficiency corrections not applied.

	Positive Charge	Negative Charge	Combined Average
Run 1	0.0018±0.0142	-0.0047±0.0144	-0.0014±0.0101
χ^2/NDF	756/833	819/835	
Run 2	0.0075±0.0083	0.0007±0.0083	0.0041±0.0059
χ^2/NDF	830/875	887/867	
Run 3	0.0151±0.0120	-0.0047±0.0116	0.0048±0.0083
χ^2/NDF	840/850	905/841	
Run 4	-0.0035±0.0072	0.0010±0.0067	-0.0011±0.0049
χ^2/NDF	1033/878	987/877	
Run 5	-0.0028±0.0062	0.0136±0.0064	0.0052±0.0045
χ^2/NDF	1367/881	1276/889	
Run 6	0.0036±0.0089	0.0133±0.0088	0.0084±0.0062
χ^2/NDF	1150/886	1065/877	
Average	**0.0015±0.0034**	**0.0055±0.0034**	**0.0035±0.0024**

Table 7.58: All data fits with weighted histograms passed to the fitter rather than pre-scaling. π^0 efficiency corrections applied.

Run	$\Delta\langle P\rangle/2$	χ^2	$\pm\sigma$
Run 1	0.0088	0.0037	0.0025
Run 2	0.0042	0.0036	0.0016
Run 3	0.0037	0.0045	0.0013
Run 4	0.0058	0.0038	0.0018
Run 5	0.0034	0.0032	0.0006
Run 6	0.0092	0.0036	0.0017

Table 7.59: Systematic uncertainties in the polarization fit due to the π^0 efficiency correction for all Runs evaluated under different methods. Half the overall shift in the polarization fits (Left), Change in fit χ^2 in response to the correction (Middle), Systematic variation of the correction (Right).

Source	Run 1	Run 2	Run 3	Run 4	Run 5	Run 6	Combined
π^0 Efficiency	0.0025	0.0016	0.0013	0.0018	0.0006	0.0017	**0.0013**
Muon PID	0.0018	0.0018	0.0029	0.0011	0.0006	0.0016	**0.0012**
Photon Split-off Modelling	0.0015	0.0017	0.0016	0.0006	0.0016	0.0020	**0.0011**
Neutral Energy Scale	0.0027	0.0012	0.0023	0.0009	0.0014	0.0008	**0.0010**
π^0 Mass	0.0018	0.0028	0.0010	0.0005	0.0004	0.0004	**0.0008**
$\pi - \pi^0$ Angular Separation	0.0015	0.0009	0.0016	0.0007	0.0005	0.0005	**0.0007**
π^0 Likelihood	0.0015	0.0009	0.0015	0.0006	0.0003	0.0010	**0.0006**
Electron PID	0.0011	0.0020	0.0008	0.0006	0.0005	0.0001	**0.0005**
Particle Transverse Momentum	0.0012	0.0007	0.0009	0.0002	0.0003	0.0006	**0.0004**
Boost Modelling	0.0004	0.0019	0.0003	0.0004	0.0004	0.0004	**0.0004**
Momentum Scale	0.0001	0.0014	0.0005	0.0002	0.0001	0.0003	**0.0004**
Max EMC Acceptance	0.0001	0.0011	0.0008	0.0001	0.0002	0.0005	**0.0003**
τ Direction Definition	0.0003	0.0007	0.0008	0.0003	0.0001	0.0004	**0.0003**
Angular Resolution	0.0003	0.0008	0.0003	0.0003	0.0002	0.0003	**0.0003**
Background Modelling	0.0005	0.0006	0.0010	0.0002	0.0003	0.0003	**0.0003**
Event Transverse Momentum	0.0001	0.0013	0.0005	0.0002	0.0002	0.0004	**0.0003**
Momentum Resolution	0.0001	0.0012	0.0004	0.0002	0.0001	0.0005	**0.0003**
Rho Mass Acceptance	0.0000	0.0011	0.0003	0.0001	0.0002	0.0005	**0.0003**
Tau Branching Fraction	0.0001	0.0007	0.0004	0.0002	0.0002	0.0002	**0.0002**
$\cos\theta^\star$ Acceptance	0.0002	0.0006	0.0004	0.0001	0.0001	0.0004	**0.0002**
$\cos\psi$ Acceptance	0.0002	0.0003	0.0002	0.0002	0.0002	0.0003	**0.0002**
Quadratic Sum	0.0058	0.0062	0.0054	0.0030	0.0026	0.0038	**0.0029**

Table 7.60: Summary of systematic uncertainties associated with the Tau Polarimetry polarization measurement.

Chapter 8

Conclusions

This dissertation has covered a range of topics from hardware calibration with thermal neutron detectors, to a novel data analysis, to validation of theoretical calculations. The work has been focused on developing Belle II and preparing for the presence of a polarized e^- beam. The dissertation is started with a comparison between pairs of theory calculations from Ref. [6, 4] and the KKMC[7] and ReneSANCe[8] simulations of electroweak parameters. These comparisons show good agreement between the two theory approaches suggesting the A_{LR} measurements are sufficiently well understood to be able to correctly interpret the future precision measurements performed by Chiral Belle. This work also provided the opportunity to work with and suggest features for the ReneSANCe MC generator which will likely become a standard MC generator for colliders with polarized beams.

As part of the effort to commission Belle II and begin bringing it to a state where it can perform high quality measurements, thermal neutron detectors were deployed to measure the beam backgrounds arising from the SuperKEKB rings. These measurements were used to determine the accuracy of the beam modelling which in turn is used to determine the level of improvement needed in beam operation and background reduction. The ^{3}He thermal neutron detectors performed well at this task, showing the neutron modelling agreed within an order of magnitude, which demonstrated the best agreement between the models of the accelerator background and data collected with the phase 2 detectors[23]. The detectors have since proven to be quite robust, continuously monitoring neutron backgrounds around the Belle II detector.

The primary focus of this dissertation work was on the development of the Tau Polarimetry technique. The work on the technique began as a simple approach in extracting the polarization from the slope of the pion momentum distribution and eventually developed into a 3-dimensional template fit of ρ decay parameters. This shift in approach was driven by the limitations of the modelling of the charged particle identification and resulted in a much

more comprehensive body of work than suspected when the dissertation began. The final result is very robust and has established the systematic effects limiting the uncertainties on the beam polarization measurement the SuperKEKB collider, operating at $\sqrt{s} = 10.58$ GeV should expect. It has also opened the field of Tau Polarimetry to a number of additional questions and areas of study. For the actual measurement, Tau Polarimetry has been used at *BABAR* to measure the PEP-II beam polarization to $\langle P \rangle = 0.0035 \pm 0.0024_{\text{stat}} \pm 0.0029_{\text{sys}}$ demonstrating a level of precision exceeding the original expectations. The dissertation has left open the question of whether the $\tau^{\pm} \to \pi^{\pm}\overline{\nu}_{\tau}$ decay can be used to successfully extract the beam polarization at a useful level of precision and hopefully this can be answered in the near future. Additional questions include but are not limited to:

- Can the lepton decay kinematics be used for polarimetry?
- Can the correlation between the τ decays be exploited to improve precision?
- Can the $\tau^{\pm} \to \pi^{\pm}\overline{\nu}_{\tau}$ decays be cleanly selected with lepton tags?
- Can Tau Polarimetry be implemented at other energy regimes?

If Belle II goes ahead with the planned polarization upgrade, the experiment will have a number of advantages in demonstrating the capability and reliability of Tau Polarimetry. First Belle II is expected to have a detector which performs better overall compared to *BABAR*, and will have a larger unpolarized data-set with which to benchmark the technique. The Chiral Belle upgrade proposes to vary the beam polarization between left and right polarized bunches to enable the A_{LR} measurements. This approach will provide Belle II with a number of options to test the validity of the Tau Polarimetry technique, as the measurement can be performed on each polarized data-set as well as arbitrary mixes of the polarization data-sets to measure any partial beam polarizations between the maximum polarization achieved for each handedness.

Overall the research described this dissertation provided an opportunity to work on a variety of different areas, network with many incredible researchers, and develop the Tau Polarimetry technique which will hopefully be useful for years to come and inspire future research on the topic.

Bibliography

[1] D. M. Asner *et al.*, "Snowmass 2021 White Paper on Upgrading SuperKEKB with a Polarized Electron Beam: Discovery Potential and Proposed Implementation," in *2022 Snowmass Summer Study*, 5 2022.

[2] Cush, "Standard model of elementary particles.svg — wikimedia commons," 2019.

[3] S. Collaboration, "SuperB Technical Design Report," 2013. arxiv:1306.5655.

[4] A. G. Aleksejevs, S. G. Barkanova, Y. M. Bystritskiy, and V. A. Zykunov, "Electroweak Corrections with Allowance for Hard Bremsstrahlung in Polarized Bhabha Scattering," *Physics of Atomic Nuclei*, vol. 83, pp. 463–479, Sept. 2020.

[5] H. Davoudiasl, H.-S. Lee, and W. J. Marciano, "Low Q^2 weak mixing angle measurements and rare higgs decays," *Phys. Rev. D*, vol. 92, p. 055005, Sep 2015.

[6] A. Aleksejevs, S. Barkanova, C. Miller, J. M. Roney, and V. Zykunov, "NLO radiative corrections for forward-backward and left-right asymmetries at a *b*-factory," *Phys. Rev. D*, vol. 101, p. 053003, Mar 2020.

[7] S. Jadach, B. Ward, and Z. Wąs, "The precision monte carlo event generator kk for two-fermion final states in e+e- collisions," *Computer Physics Communications*, vol. 130, no. 3, pp. 260–325, 2000.

[8] R. Sadykov and V. Yermolchyk, "Polarized NLO EW e+e- cross section calculations with ReneSANCe-v1.0.0," *Computer Physics Communications*, vol. 256, p. 107445, 2020.

[9] R. Sadykov and V. Yermolchyk. personal communication.

[10] M. Tanabashi, K. Hagiwara, K. Hikasa, K. Nakamura, Y. Sumino, F. Takahashi, J. Tanaka, *et al.*, "Review of particle physics," *Phys. Rev. D*, vol. 98, Aug 2018.

[11] F. Abudinén *et al.* vol. 44, p. 021001, feb 2020.

[12] "UVic B-Physics webpage." https://www.uvic.ca/science/physics/vispa/research/projects/bphysics/index.php.

[13] D. Boutigny *et al.*, *The BABAR physics book: Physics at an asymmetric B factory*. 10 1998.

[14] T. Abe *et al.*, "Belle II Technical Design Report," 2010.

[15] B. Aubert *et al.*, "The BaBar detector," *Nucl. Instrum. Meth. A*, vol. 479, pp. 1–116, 2002.

[16] S. Longo *et al.*, "CsI(Tl) pulse shape discrimination with the Belle II electromagnetic calorimeter as a novel method to improve particle identification at electron–positron colliders," *Nucl. Instrum. Meth. A*, vol. 982, p. 164562, 2020.

[17] P. M. Lewis *et al.*, "First Measurements of Beam Backgrounds at SuperKEKB," *Nucl. Instrum. Meth.*, vol. A914, pp. 69–144, 2019.

[18] S. R. de Jong, *Study of Thermal Neutron Flux from SuperKEKB in the Belle II Commissioning Detector*. PhD thesis, Victoria U., 2017.

[19] "Voltage monitor online manual." https://www.dataq.com/products/di-2108-p/.

[20] S. Agostinelli *et al.*, "Geant4—a simulation toolkit," *Nuclear Instruments and Methods in Physics Research Section A: Accelerators, Spectrometers, Detectors and Associated Equipment*, vol. 506, no. 3, pp. 250–303, 2003.

[21] J. Allison, K. Amako, J. Apostolakis, H. Araujo, P. Arce Dubois, *et al.*, "Geant4 developments and applications," *IEEE Transactions on Nuclear Science*, vol. 53, no. 1, pp. 270–278, 2006.

[22] S. Sandilya, "Particle Identification at Belle II," *J. Phys. Conf. Ser.*, vol. 770, no. 1, p. 012045, 2016. Editted with permission.

[23] Z. J. Liptak *et al.*, "Measurements of beam backgrounds in SuperKEKB Phase 2," *Nucl. Instrum. Meth. A*, vol. 1040, p. 167168, 2022.

[24] A. Natochii. personal communication.

[25] A. Natochii *et al.*, "Measured and projected beam backgrounds in the Belle II experiment at the SuperKEKB collider," 2 2023.

[26] Y. Nosochkov, M. Minty, and A. Chao, "Expected polarization in the present pep-2 design," 1996. https://www.osti.gov/biblio/486213.

[27] The ALEPH, DELPHI, L3, OPAL, SLD Collaborations, the LEP Electroweak Working Group, the SLD Electroweak and Heavy Flavour Groups, "Precision electroweak measurements on the Z resonance," *Physics Reports*, vol. 427, pp. 257–454, May 2006.

[28] O. Vives, "Electroweak Observables at SuperB," in *XVII SuperB Workshop, Elba*, 2011.

[29] D. Decamp *et al.*, "Measurement of the polarization of tau leptons produced in Z decays," *Phys. Lett. B*, vol. 265, pp. 430–444, 1991.

[30] "BGFTAU Filter." `https://inspirehep.net/literature/1594313`.

[31] J. P. Lees *et al.*, "Time-Integrated Luminosity Recorded by the BABAR Detector at the PEP-II e^+e^- Collider," *Nucl. Instrum. Meth. A*, vol. 726, pp. 203–213, 2013.

[32] W. Beenakker, F. A. Berends, and S. C. van der Marck, "Small angle Bhabha scattering," *Nucl. Phys. B*, vol. 355, pp. 281–294, 1991.

[33] W. Beenakker, F. A. Berends, and S. C. van der Marck, "Large angle Bhabha scattering," *Nucl. Phys. B*, vol. 349, pp. 323–368, 1991.

[34] Z. Wąs. personal communication.

[35] M. Davier, L. Duflot, F. Le Diberder, and A. Rouge, "The Optimal method for the measurement of tau polarization," *Phys. Lett. B*, vol. 306, pp. 411–417, 1993.

[36] S. Brandt, C. Peyrou, R. Sosnowski, and A. Wroblewski, "The Principal axis of jets. An Attempt to analyze high-energy collisions as two-body processes," *Phys. Lett.*, vol. 12, pp. 57–61, 1964.

[37] E. Farhi, "A QCD Test for Jets," *Phys. Rev. Lett.*, vol. 39, pp. 1587–1588, 1977.

[38] J. Birks, *The theory and practice of scintillation counting*. Macmillan&Pergamon, 1964.

[39] R. J. Barlow and C. Beeston, "Fitting using finite Monte Carlo samples," *Comput. Phys. Commun.*, vol. 77, pp. 219–228, 1993.

[40] "Particle ID Selectors in BABAR." `https://babar.heprc.uvic.ca/BFROOT/www/Physics/Tools/Pid/Selectors/r24c/selectors.html`.

[41] Z. Yun, "A Study of $e^+e^- \to \mu^+\mu - (\gamma)$ events at BaBar," Master's thesis, University of Victoria, 2005.

[42] C. Miller, "Measurement of PEP-II Beam Polarization with Tau Polarimetry," 2022. Lake Louise Winter Institute.

[43] C. Miller, "Measurement of Beam Polarization at an e^+e^- B-Factory with New Tau Polarimetry Technique," in *20th Conference on Flavor Physics and CP Violation* , 7 2022.

[44] C. Miller, "Chiral Belle," 2022. IPP 50th Anniversary Symposium.

[45] C. Miller, "Measurement of Beam Polarization at an e^+e^- B-Factory with New Tau Polarimetry Technique," 2022. CAP Congress.

[46] C. Miller, "Measurement of Beam Polarization at an e^+e^- B-Factory with New Tau Polarimetry Technique," 2022. BEACH2022.

[47] C. Miller, "Measurement of Beam Polarization at an e^+e^- B-Factory with New Tau Polarimetry Technique," *PoS*, vol. ICHEP2022, p. 872, 2022.

[48] K. Hagiwara, A. D. Martin, and D. Zeppenfeld, "Tau Polarization Measurements at LEP and SLC," *Phys. Lett. B*, vol. 235, pp. 198–202, 1990.

Appendix A

Efficiency of *BABAR* PID Selectors

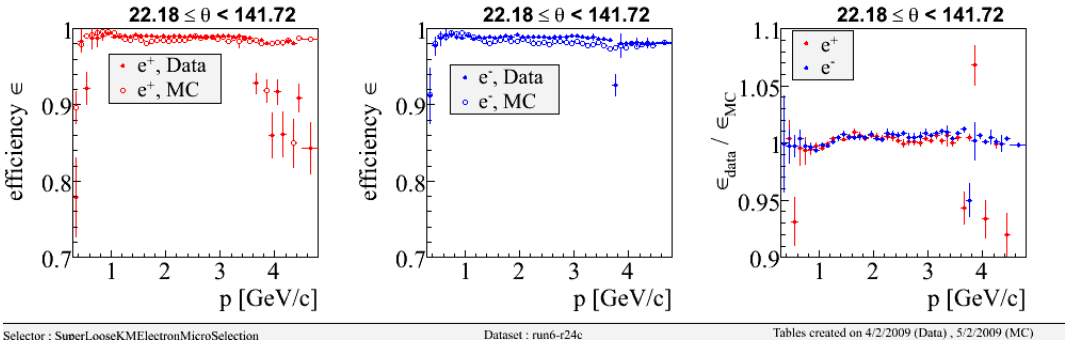

Figure A.1: Efficiency for finding electrons with SuperLooseKMElectronMicro[40].

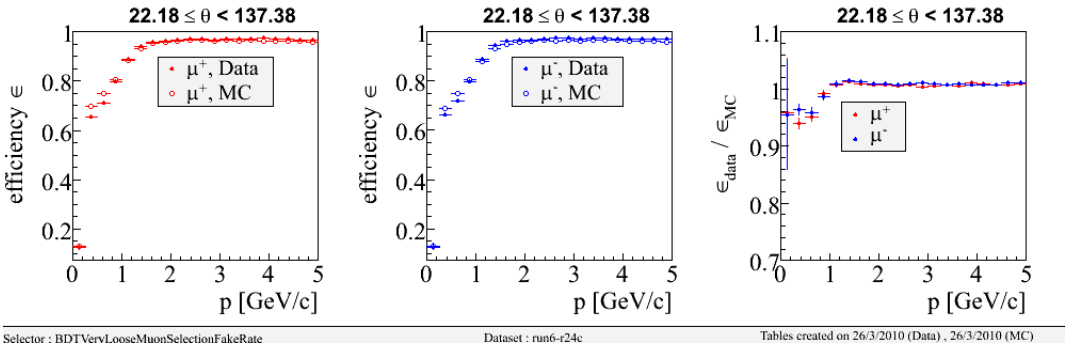

Figure A.2: Efficiency for finding muons with BDTVeryLooseMuonSelectionFakeRate[40].

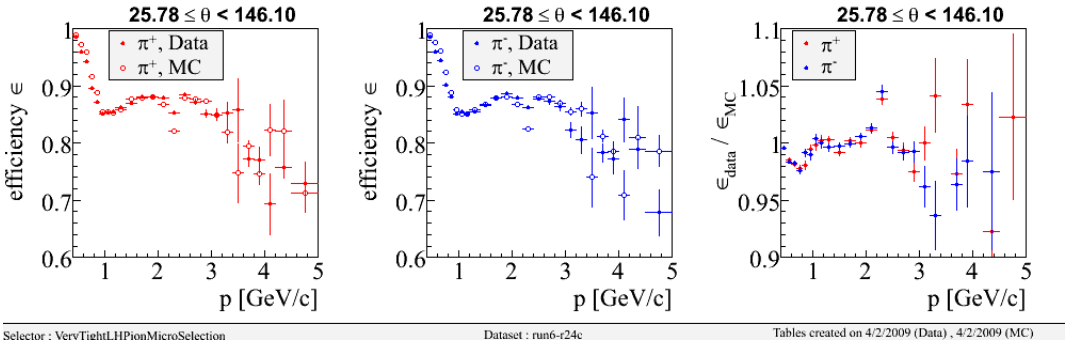

Figure A.3: Efficiency for finding pions with VeryTightLHPionMicroSelection[40].

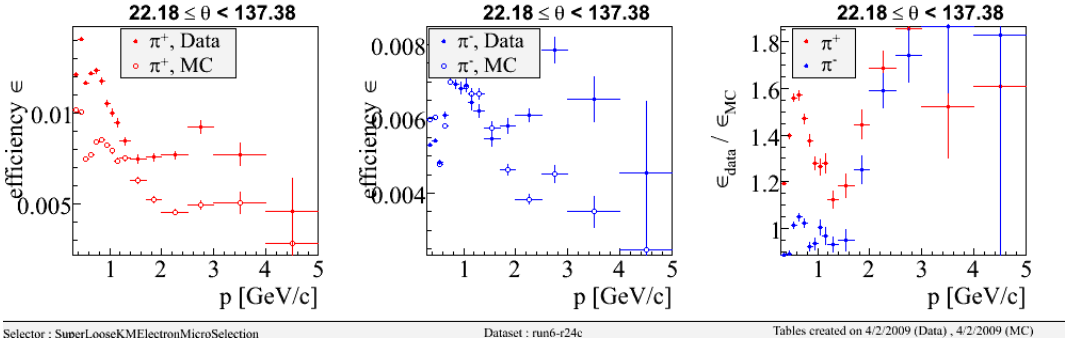

Figure A.4: Probability of a pion being identified as an electron with SuperLooseKMElectronMicro[40].

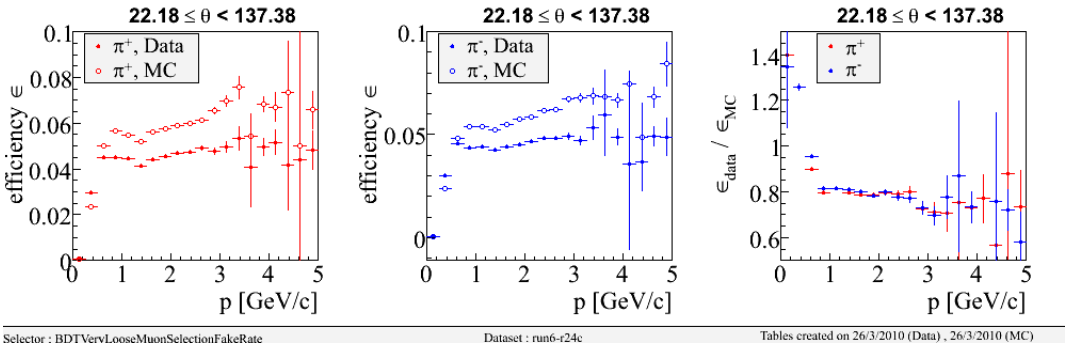

Figure A.5: Probability of a pion being identified as a muon with BDTVeryLooseMuonSelectionFakeRate[40].

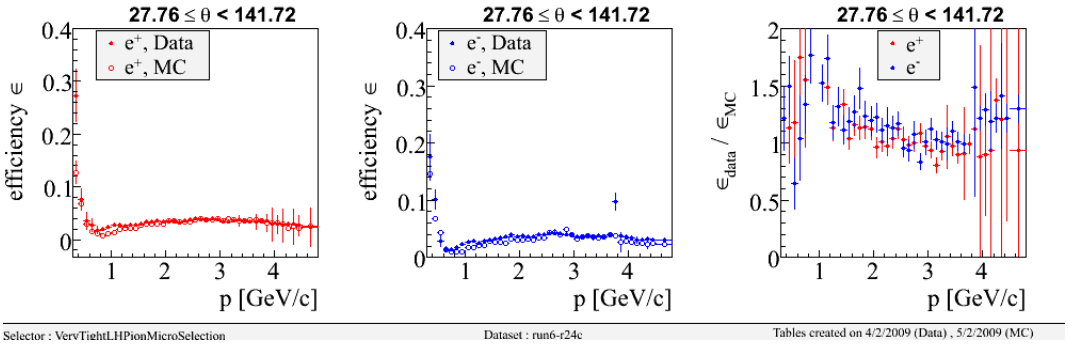

Figure A.6: Probability of an electron being identified as a pion with VeryTightLHPionMicroSelection[40].

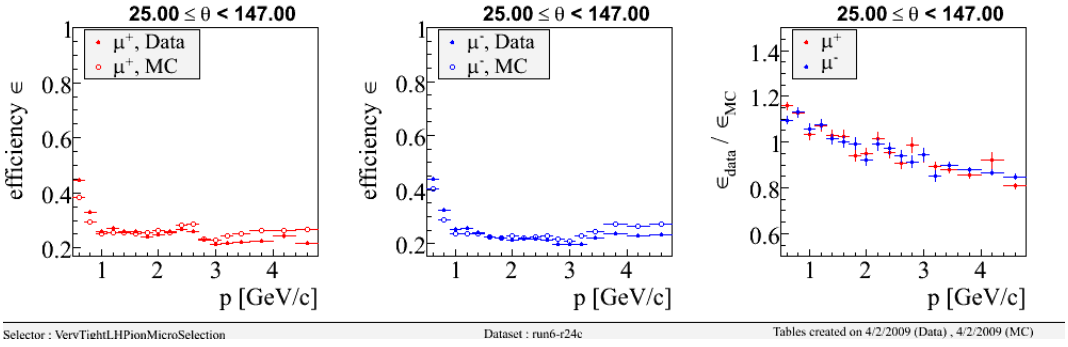

Figure A.7: Probability of a muon being identified as a pion with VeryTightLHPionMicroSelection[40].

Appendix B

Total Polarization Sensitivity in $\tau^{\pm} \to \pi^{\pm}\overline{\nu}_{\tau}$ Selection

Run 1 Sensitivity

The run 1 results are see in Table B.1 and Figures B.1 and B.2.

Target	Positive Charge	Negative Charge	Combined Average	Deviation
-0.95	NAN	NAN	-	-
-0.9	-0.9100 ± 0.0244	-0.8796 ± 0.025	-0.8952 ± 0.0174	0.28 σ
-0.8	-0.8159 ± 0.0252	-0.7769 ± 0.0233	-0.7949 ± 0.0171	0.30 σ
-0.7	-0.7104 ± 0.0253	-0.6705 ± 0.0241	-0.6895 ± 0.0175	0.60 σ
-0.6	-0.6116 ± 0.0245	-0.5772 ± 0.0207	-0.5915 ± 0.0158	0.54 σ
-0.5	-0.5162 ± 0.0251	-0.4738 ± 0.0229	-0.4931 ± 0.0169	0.41 σ
-0.4	-0.4194 ± 0.0223	-0.3798 ± 0.0243	-0.4013 ± 0.0165	-0.08 σ
-0.3	-0.3224 ± 0.0250	-0.2834 ± 0.0245	-0.3025 ± 0.0175	-0.14 σ
-0.2	-0.2196 ± 0.0237	-0.1857 ± 0.0232	-0.2023 ± 0.0166	-0.14 σ
-0.1	-0.1263 ± 0.0237	-0.0948 ± 0.0231	-0.1102 ± 0.0165	-0.62 σ
0	-0.0281 ± 0.0235	0.0054 ± 0.0231	-0.0110 ± 0.0165	-0.67 σ
0.1	0.0710 ± 0.0234	0.1118 ± 0.0230	0.0917 ± 0.0164	-0.51 σ
0.2	0.1664 ± 0.0233	0.2140 ± 0.0230	0.1906 ± 0.0164	-0.57 σ
0.3	0.2643 ± 0.0233	0.3160 ± 0.0229	0.2906 ± 0.0163	-0.58 σ
0.4	0.3689 ± 0.0233	0.4185 ± 0.0240	0.3930 ± 0.0167	-0.42 σ
0.5	0.4671 ± 0.0243	0.5177 ± 0.0239	0.4928 ± 0.0170	-0.42 σ
0.6	0.5585 ± 0.0242	0.6160 ± 0.0238	0.5877 ± 0.0170	-0.72 σ
0.7	0.6610 ± 0.0241	0.7157 ± 0.0213	0.6917 ± 0.0160	-0.52 σ
0.8	0.7668 ± 0.0220	0.8038 ± 0.0232	0.7843 ± 0.0160	-0.98 σ
0.9	0.8663 ± 0.0215	0.8982 ± 0.0220	0.8819 ± 0.0154	-1.18 σ
0.95	0.9098 ± 0.0214	0.9499 ± 0.0252	0.9266 ± 0.0163	-1.44 σ

Table B.1: Sensitivity to total polarization in Run 1 MC

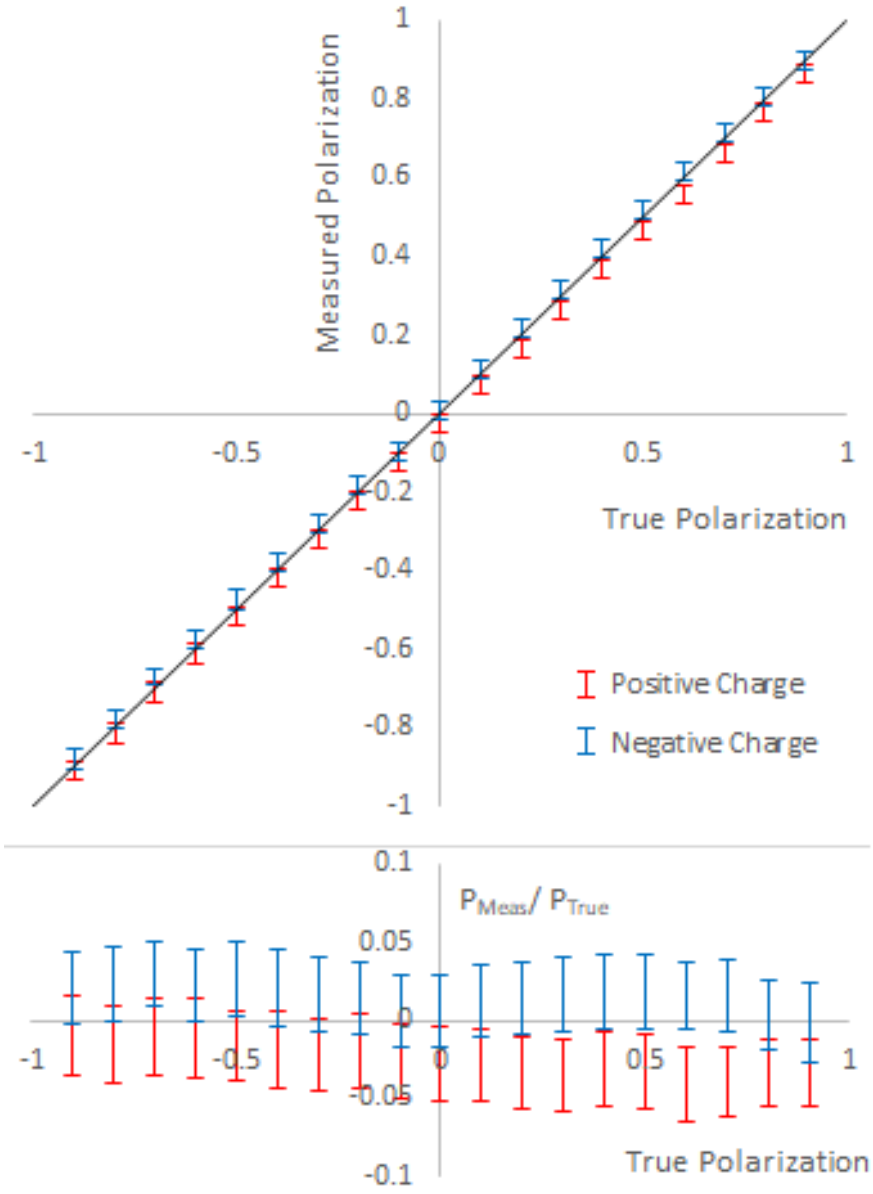

Figure B.1: Results from Table B.1 plotted. The line y=x also shown for reference. The lower plot shows the same points normalized by the true polarization.

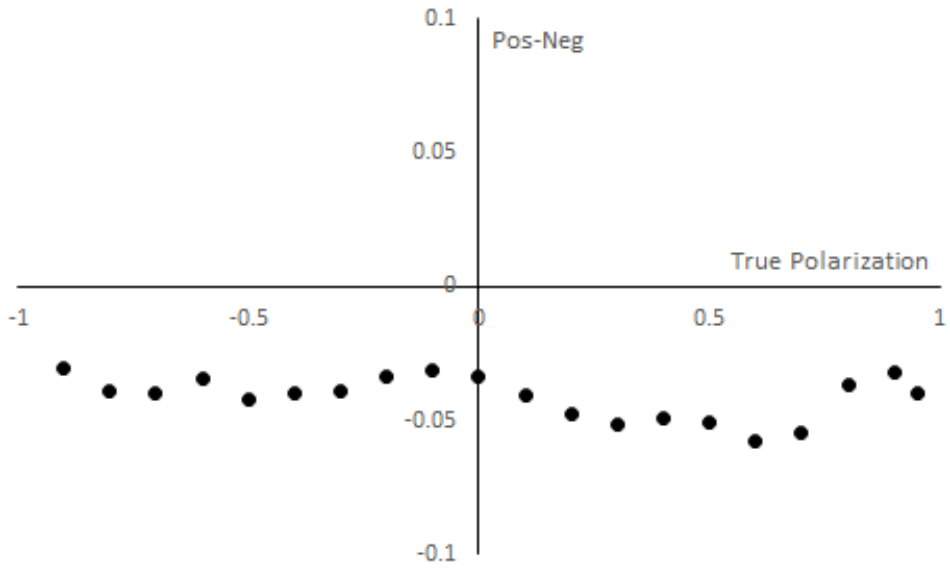

Figure B.2: The difference between the positive and negative run 1 polarization measurements as a function of the true polarization.

Run 2 Sensitivity

The run 2 results are see in Table B.2 and Figures B.3 and B.4.

Target	Positive Charge	Negative Charge	Combined Average	Deviation
-0.95	-0.9259 ± 0.0151	-0.9207 ± 0.0153	-0.9233 ± 0.0108	2.47 σ
-0.9	-0.8798 ± 0.0155	-0.8680 ± 0.0152	-0.8737 ± 0.0108	2.44 σ
-0.8	-0.7770 ± 0.0128	-0.7665 ± 0.0146	-0.7724 ± 0.0096	2.88 σ
-0.7	-0.6868 ± 0.0129	-0.6649 ± 0.0144	-0.6770 ± 0.0096	2.40 σ
-0.6	-0.5903 ± 0.0141	-0.5677 ± 0.0151	-0.5797 ± 0.0103	1.97 σ
-0.5	-0.4891 ± 0.0146	-0.4717 ± 0.0149	-0.4806 ± 0.0104	1.87 σ
-0.4	-0.3853 ± 0.0139	-0.3706 ± 0.0147	-0.3783 ± 0.0101	2.15 σ
-0.3	-0.2863 ± 0.0138	-0.2669 ± 0.0149	-0.2773 ± 0.0101	2.25 σ
-0.2	-0.1871 ± 0.0138	-0.1749 ± 0.0139	-0.1811 ± 0.0098	1.93 σ
-0.1	-0.0869 ± 0.0146	-0.0741 ± 0.0139	-0.0802 ± 0.0101	1.96 σ
0	0.0076 ± 0.0137	0.0235 ± 0.0138	0.0155 ± 0.0097	1.60 σ
0.1	0.1093 ± 0.0145	0.1228 ± 0.0138	0.1164 ± 0.0100	1.64 σ
0.2	0.2121 ± 0.0136	0.2242 ± 0.0146	0.2178 ± 0.0100	1.78 σ
0.3	0.3070 ± 0.0137	0.3255 ± 0.0144	0.3157 ± 0.0099	1.59 σ
0.4	0.4030 ± 0.0142	0.4258 ± 0.0137	0.4148 ± 0.0099	1.49 σ
0.5	0.5038 ± 0.0144	0.5311 ± 0.0144	0.5175 ± 0.0102	1.72 σ
0.6	0.6003 ± 0.0138	0.6278 ± 0.0138	0.6140 ± 0.0097	1.44 σ
0.7	0.6966 ± 0.0123	0.7210 ± 0.0138	0.7074 ± 0.0092	0.80 σ
0.8	0.7960 ± 0.014	0.8191 ± 0.0139	0.8076 ± 0.0099	0.77 σ
0.9	0.8959 ± 0.0133	0.9150 ± 0.0143	0.9048 ± 0.0098	0.49 σ
0.95	NAN	NAN	-	-

Table B.2: Sensitivity to total polarization in Run 2 MC

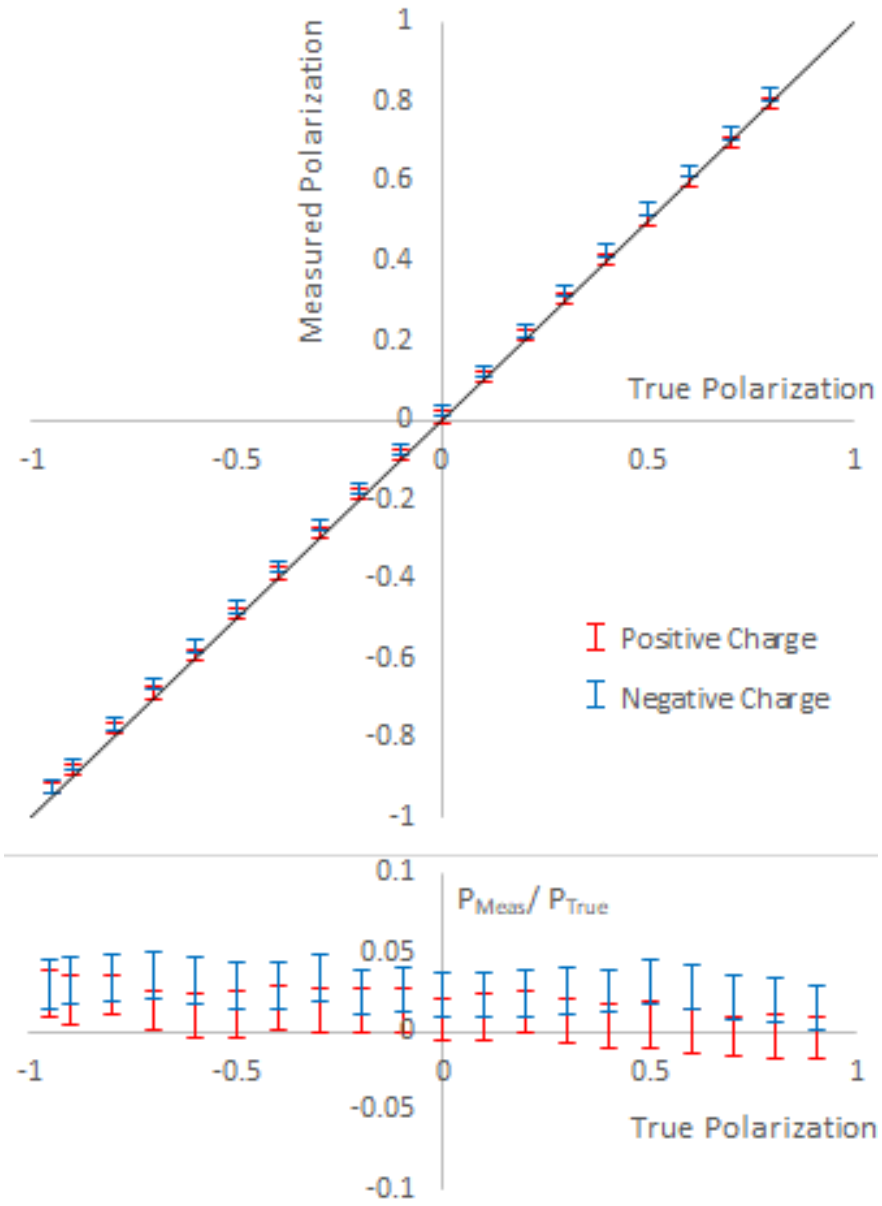

Figure B.3: Results from Table B.2 plotted. The line y=x also shown for reference. The lower plot shows the same points normalized by the true polarization.

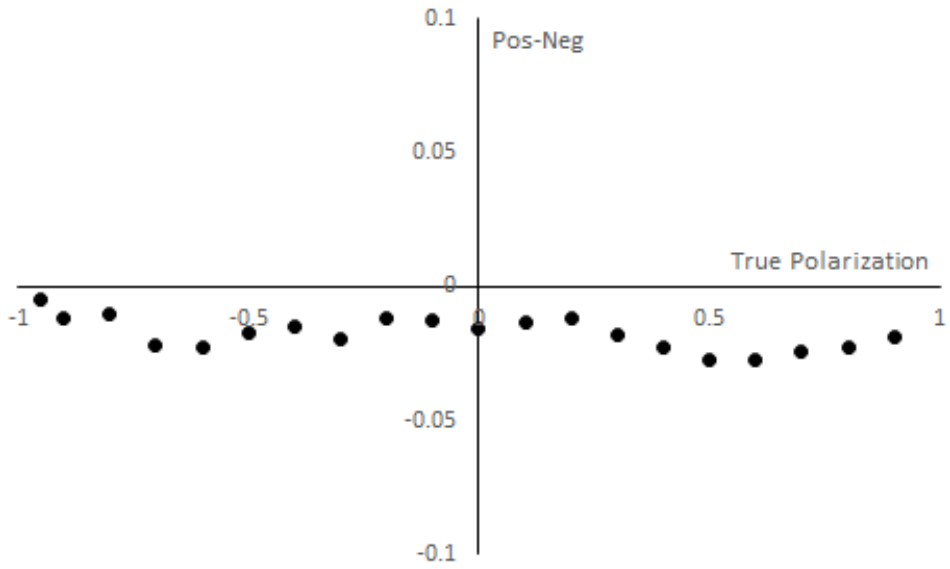

Figure B.4: The difference between the positive and negative run 2 polarization measurements as a function of the true polarization.

Run 3 Sensitivity

The run 3 results are see in Table B.3 and Figures B.5 and B.6.

Target	Positive Charge	Negative Charge	Combined Average	Deviation
-0.95	-0.9485 ± 0.0218	-0.9419 ± 0.0228	-0.9453 ± 0.0157	0.30 σ
-0.9	-0.8997 ± 0.0204	-0.8983 ± 0.0200	-0.8990 ± 0.0143	0.07 σ
-0.8	-0.7987 ± 0.0200	-0.8004 ± 0.0209	-0.7995 ± 0.0145	0.03 σ
-0.7	-0.6983 ± 0.0176	-0.7121 ± 0.0217	-0.7038 ± 0.0137	-0.28 σ
-0.6	-0.6007 ± 0.0205	-0.6081 ± 0.0214	-0.6042 ± 0.0148	-0.28 σ
-0.5	-0.4943 ± 0.0204	-0.5064 ± 0.0211	-0.5001 ± 0.0147	-0.01 σ
-0.4	-0.4028 ± 0.0200	-0.4084 ± 0.0207	-0.4055 ± 0.0144	-0.38 σ
-0.3	-0.3032 ± 0.0207	-0.3134 ± 0.0206	-0.3083 ± 0.0146	-0.57 σ
-0.2	-0.2020 ± 0.0195	-0.2098 ± 0.0196	-0.2059 ± 0.0138	-0.43 σ
-0.1	-0.0974 ± 0.0195	-0.1084 ± 0.0195	-0.1029 ± 0.0138	-0.21 σ
0	-0.0061 ± 0.0195	-0.0131 ± 0.0193	-0.0096 ± 0.0137	-0.70 σ
0.1	0.0916 ± 0.0195	0.0870 ± 0.0192	0.0893 ± 0.0137	-0.78 σ
0.2	0.1899 ± 0.0195	0.1849 ± 0.0191	0.1873 ± 0.0136	-0.93 σ
0.3	0.2842 ± 0.0204	0.2775 ± 0.0187	0.2806 ± 0.0138	-1.41 σ
0.4	0.3897 ± 0.0205	0.3753 ± 0.0186	0.3818 ± 0.0138	-1.32 σ
0.5	0.4931 ± 0.0208	0.4823 ± 0.0197	0.4874 ± 0.0143	-0.88 σ
0.6	0.5848 ± 0.0207	0.5810 ± 0.0194	0.5828 ± 0.0142	-1.21 σ
0.7	0.6819 ± 0.0215	0.6772 ± 0.0192	0.6793 ± 0.0143	-1.45 σ
0.8	0.7829 ± 0.0204	0.7714 ± 0.0191	0.7768 ± 0.0139	-1.67 σ
0.9	0.8828 ± 0.0198	0.8723 ± 0.0175	0.8769 ± 0.0131	-1.76 σ
0.95	0.9651 ± 0.0187	0.9463 ± 0.0197	0.9562 ± 0.0136	0.46 σ

Table B.3: Sensitivity to total polarization in Run 3 MC

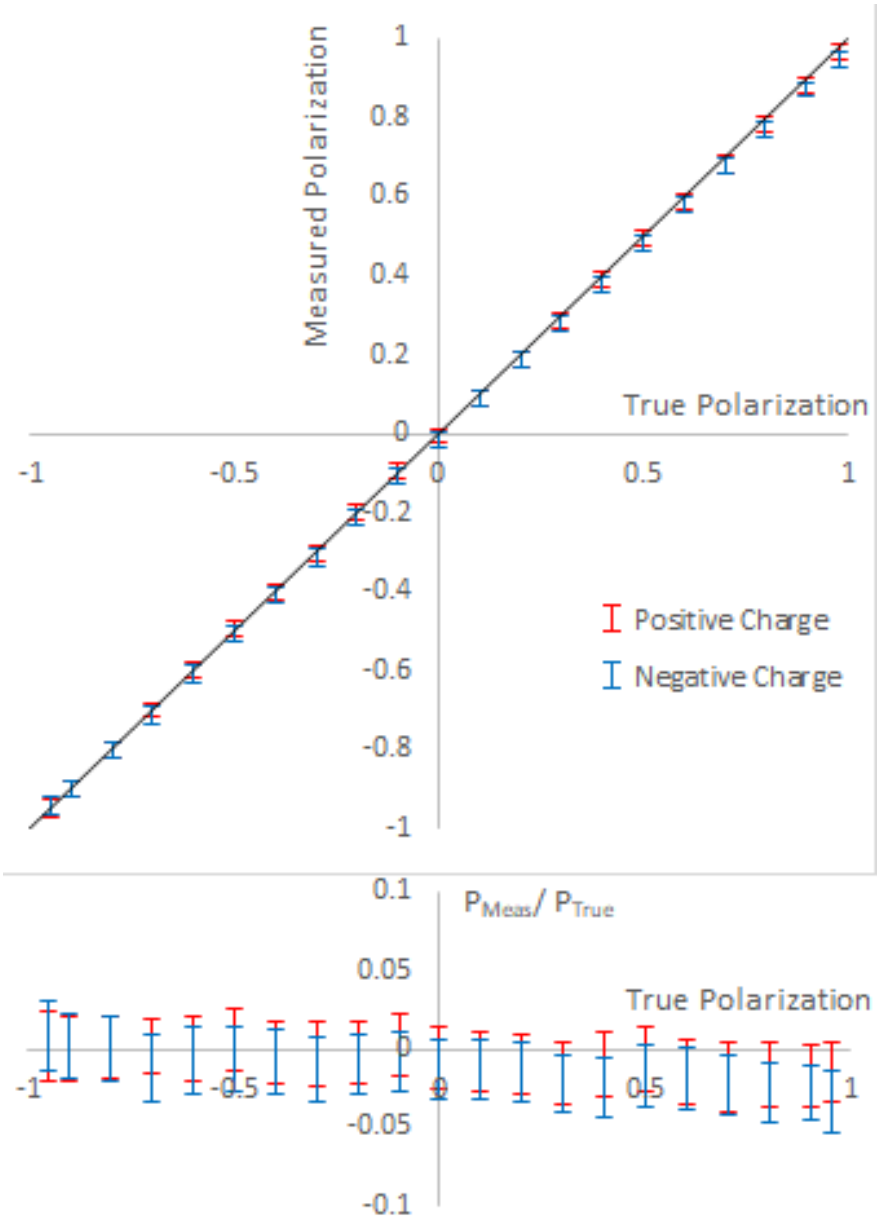

Figure B.5: Results from Table B.3 plotted. The line y=x also shown for reference. The lower plot shows the same points normalized by the true polarization.

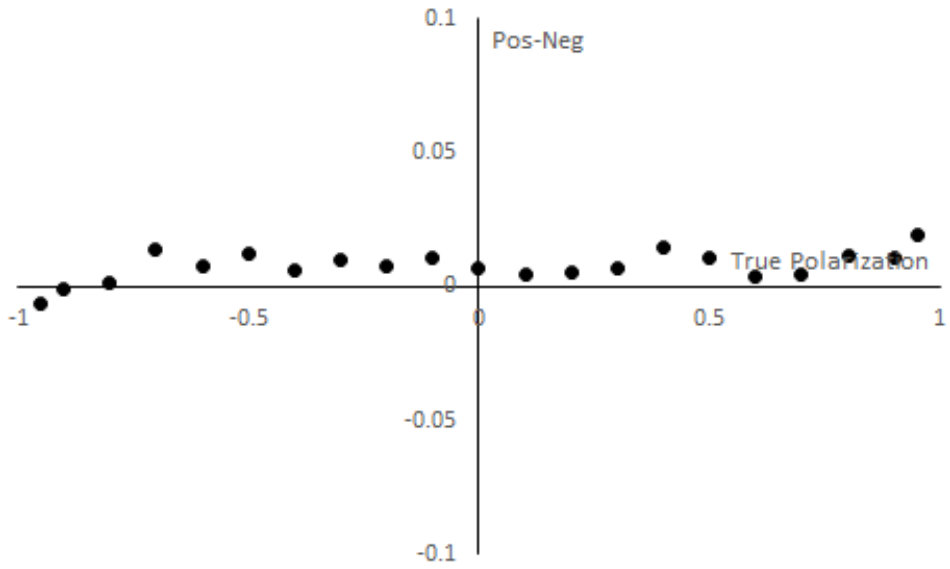

Figure B.6: The difference between the positive and negative run 3 polarization measurements as a function of the true polarization.

Run 4 Sensitivity

The run 4 results are see in Table B.4 and Figures B.7 and B.8.

Target	Positive Charge	Negative Charge	Combined Average	Deviation
-0.95	-0.9365 ± 0.0118	NAN	-	-
-0.9	-0.8914 ± 0.0099	NAN	-	-
-0.8	-0.7929 ± 0.0111	-0.7763 ± 0.0100	-0.7837 ± 0.0074	2.20 σ
-0.7	-0.6986 ± 0.0111	-0.6802 ± 0.0116	-0.6898 ± 0.0080	1.28 σ
-0.6	-0.6008 ± 0.0122	-0.5813 ± 0.0096	-0.5888 ± 0.0075	1.49 σ
-0.5	-0.5038 ± 0.0115	-0.4824 ± 0.0119	-0.4934 ± 0.0083	0.80 σ
-0.4	-0.4069 ± 0.0115	NAN	-	-
-0.3	-0.3048 ± 0.0109	-0.2855 ± 0.0110	-0.2952 ± 0.0077	0.62 σ
-0.2	-0.2055 ± 0.0116	-0.1881 ± 0.0109	-0.1963 ± 0.0079	0.47 σ
-0.1	-0.1083 ± 0.0116	-0.0881 ± 0.0108	-0.0975 ± 0.0079	0.32 σ
0	-0.0067 ± 0.0108	0.0143 ± 0.0107	0.0039 ± 0.0076	0.51 σ
0.1	0.0924 ± 0.0108	0.1131 ± 0.0106	0.1029 ± 0.0076	0.38 σ
0.2	0.1901 ± 0.0109	0.2138 ± 0.0093	0.2037 ± 0.0071	0.52 σ
0.3	0.2888 ± 0.0098	0.3068 ± 0.0105	0.2972 ± 0.0072	-0.39 σ
0.4	NAN	0.4055 ± 0.01	-	-
0.5	0.483 ± 0.0115	0.5008 ± 0.0109	0.4924 ± 0.0079	-0.96 σ
0.6	0.5807 ± 0.0115	0.5917 ± 0.0104	0.5868 ± 0.0077	-1.71 σ
0.7	0.6781 ± 0.0098	0.6888 ± 0.0107	0.6830 ± 0.0072	-2.36 σ
0.8	0.775 ± 0.0102	0.7867 ± 0.0108	0.7806 ± 0.0074	-2.62 σ
0.9	0.872 ± 0.0114	0.8835 ± 0.0107	0.8781 ± 0.0078	-2.81 σ
0.95	NAN	0.9313 ± 0.0109	-	-

Table B.4: Sensitivity to total polarization in Run 4 MC

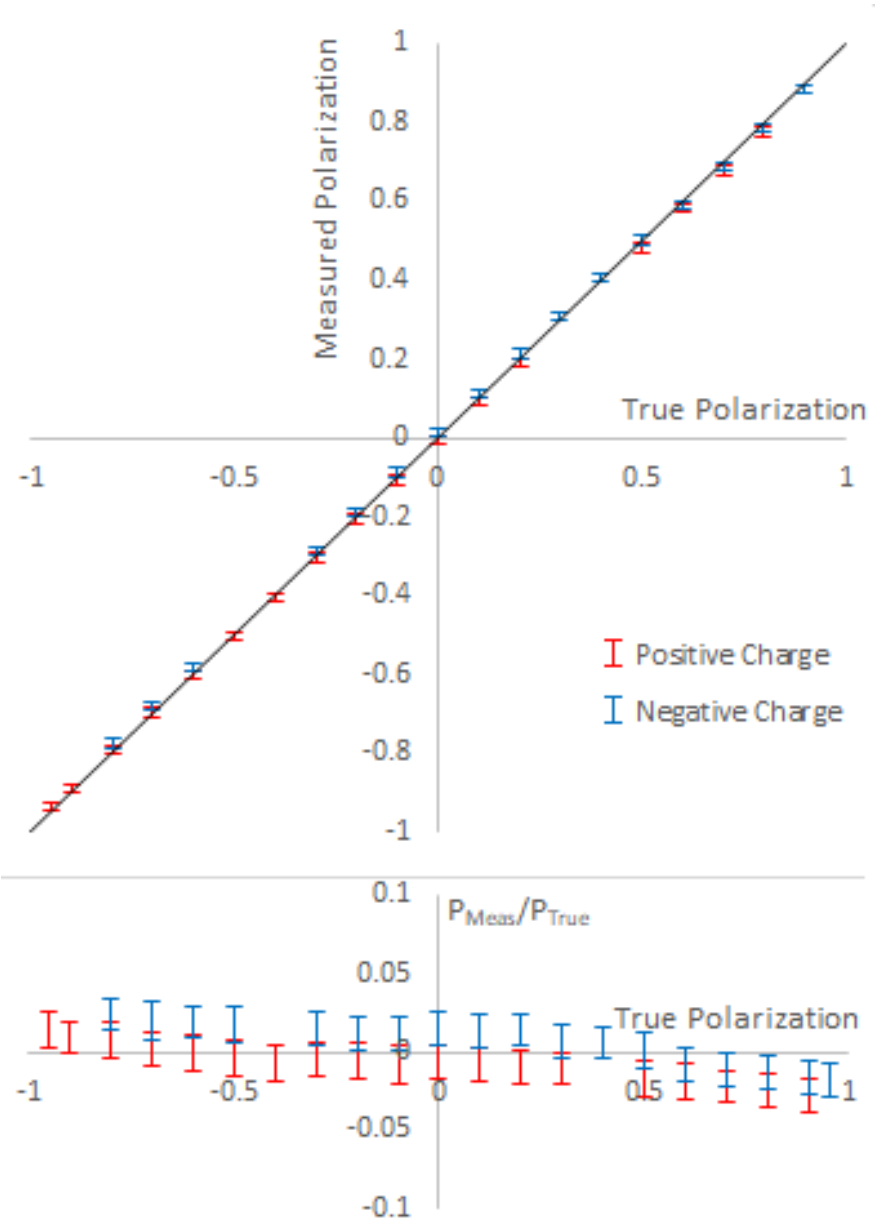

Figure B.7: Results from Table B.4 plotted. The line y=x also shown for reference. The lower plot shows the same points normalized by the true polarization.

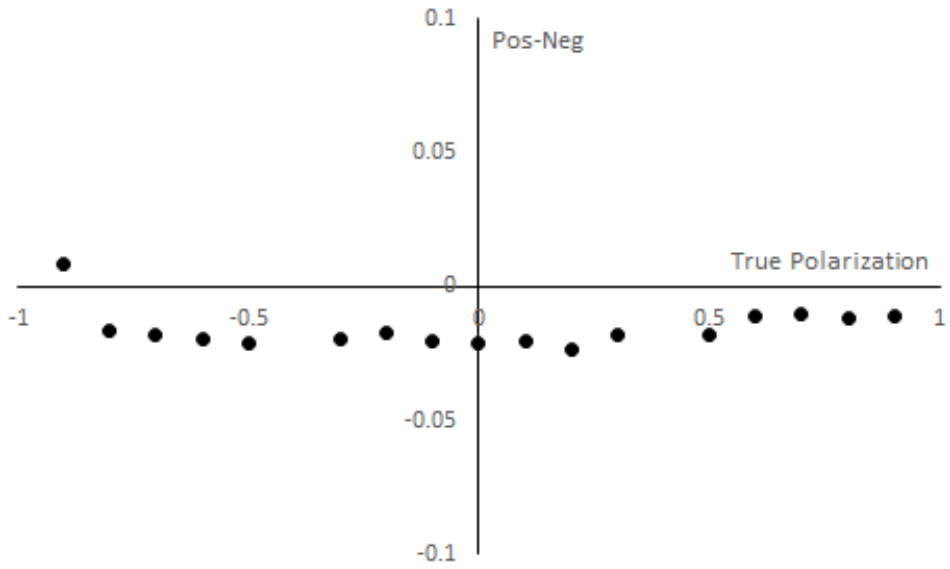

Figure B.8: The difference between the positive and negative run 4 polarization measurements as a function of the true polarization.

Run 6 Sensitivity

The run 6 results are see in Table B.5 and Figures B.9 and B.10.

Target	Positive Charge	Negative Charge	Combined Average	Deviation
-0.95	-0.8980 ± 0.0143	-0.8989 ± 0.0146	-0.8984 ± 0.0102	5.06 σ
-0.9	-0.8471 ± 0.0163	-0.8491 ± 0.0181	-0.8480 ± 0.0121	4.30 σ
-0.8	-0.7552 ± 0.0143	-0.7566 ± 0.0196	-0.7557 ± 0.0115	3.85 σ
-0.7	-0.6527 ± 0.0171	-0.6524 ± 0.0174	-0.6525 ± 0.0122	3.89 σ
-0.6	-0.5598 ± 0.0175	-0.5581 ± 0.0174	-0.5590 ± 0.0123	3.33 σ
-0.5	-0.4680 ± 0.0162	-0.4619 ± 0.0164	-0.4650 ± 0.0115	3.04 σ
-0.4	-0.3735 ± 0.0171	-0.3643 ± 0.0173	-0.3690 ± 0.0121	2.56 σ
-0.3	-0.2786 ± 0.0171	-0.2718 ± 0.0172	-0.2752 ± 0.0121	2.05 σ
-0.2	-0.1880 ± 0.0161	-0.1825 ± 0.0163	-0.1853 ± 0.0115	1.28 σ
-0.1	-0.0999 ± 0.0179	-0.0877 ± 0.0181	-0.0939 ± 0.0127	0.48 σ
0	-0.0094 ± 0.0169	0.0111 ± 0.0171	0.0008 ± 0.0120	0.07 σ
0.1	0.0892 ± 0.0169	0.1097 ± 0.0170	0.0993 ± 0.0120	-0.06 σ
0.2	0.1796 ± 0.0163	0.1948 ± 0.0163	0.1872 ± 0.0115	-1.11 σ
0.3	0.2746 ± 0.0168	0.2951 ± 0.0170	0.2847 ± 0.0119	-1.29 σ
0.4	0.3720 ± 0.0167	0.3897 ± 0.0169	0.3807 ± 0.0119	-1.62 σ
0.5	0.4651 ± 0.0167	0.4901 ± 0.0169	0.4774 ± 0.0119	-1.90 σ
0.6	0.5628 ± 0.0173	0.5882 ± 0.0175	0.5753 ± 0.0123	-2.01 σ
0.7	0.6570 ± 0.0175	0.6868 ± 0.0165	0.6728 ± 0.0120	-2.27 σ
0.8	0.7510 ± 0.0152	0.7830 ± 0.0165	0.7657 ± 0.0112	-3.06 σ
0.9	0.8490 ± 0.0157	0.8736 ± 0.0173	0.8602 ± 0.0116	-3.43 σ
0.95	0.8973 ± 0.0178	NAN	-	-

Table B.5: Sensitivity to total polarization in Run 6 MC

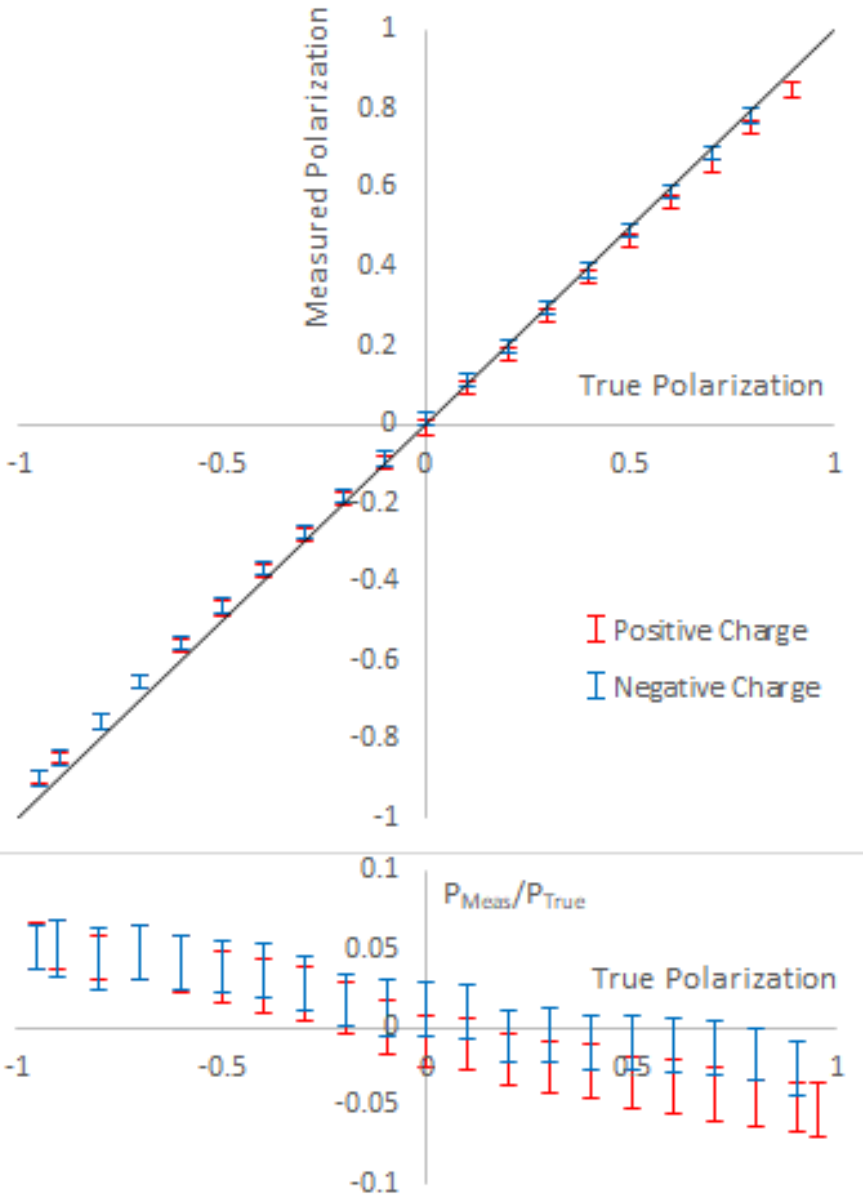

Figure B.9: Results from Table B.5 plotted. The line y=x also shown for reference. The lower plot shows the same points normalized by the true polarization.

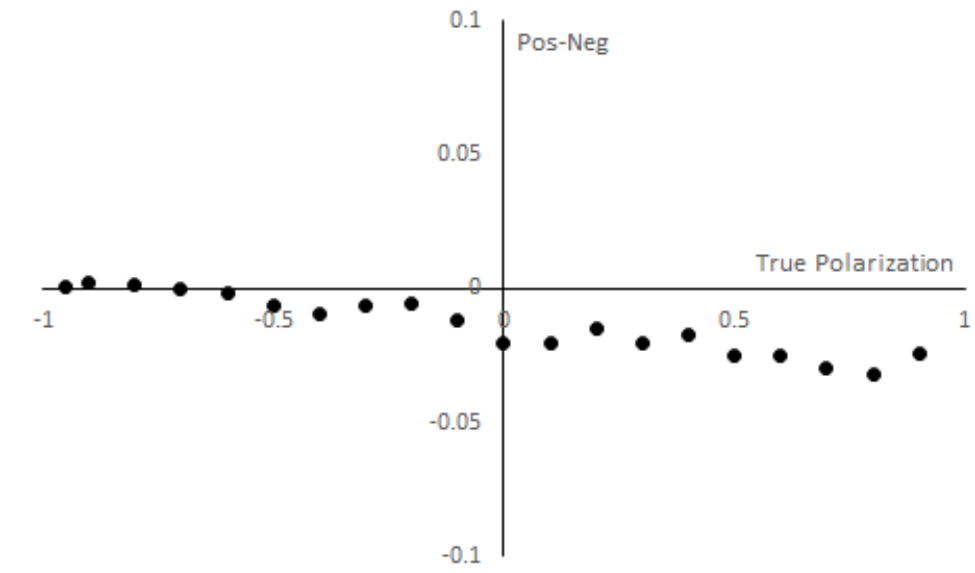

Figure B.10: The difference between the positive and negative run 6 polarization measurements as a function of the true polarization.

Appendix C

Electron-Tagged $\tau^{\pm} \to (\rho^{\pm} \to \pi^{\pm}\pi^{0})\overline{\nu}_{\tau}$ Analysis Plots

This Appendix displays a number of fit results and distributions for various parameters used in the electron-tagged $\tau^{\pm} \to (\rho^{\pm} \to \pi^{\pm}\pi^{0})\overline{\nu}_{\tau}$ analysis.

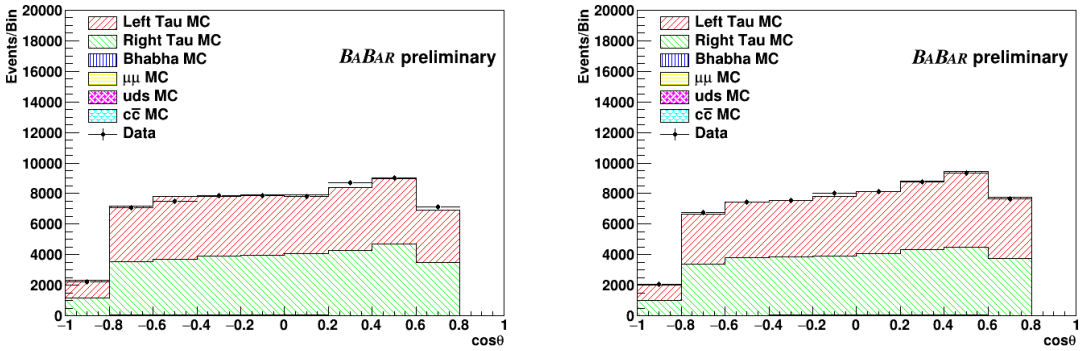

Figure C.1: One dimensional projection of fit performance for $\cos\theta$ in Run 1. Positively (left) and negatively (right) charged candidates.

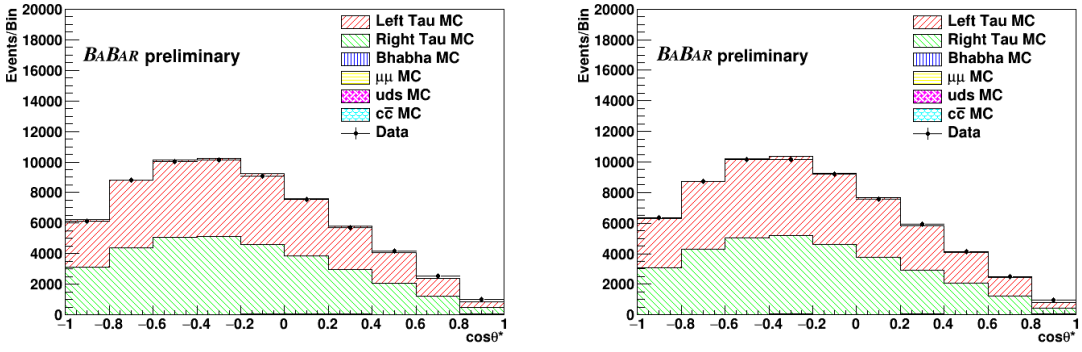

Figure C.2: One dimensional projection of fit performance for $\cos\theta^{\star}$ in Run 1. Positively (left) and negatively (right) charged candidates.

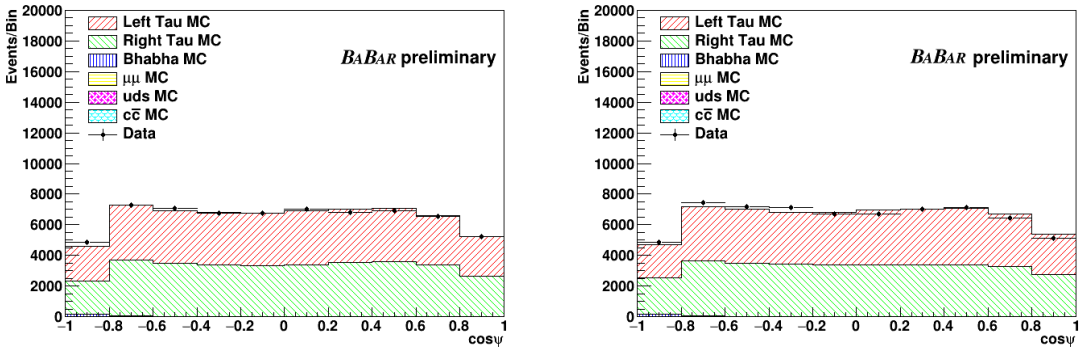

Figure C.3: One dimensional projection of fit performance for $\cos\psi$ in Run 1. Positively (left) and negatively (right) charged candidates.

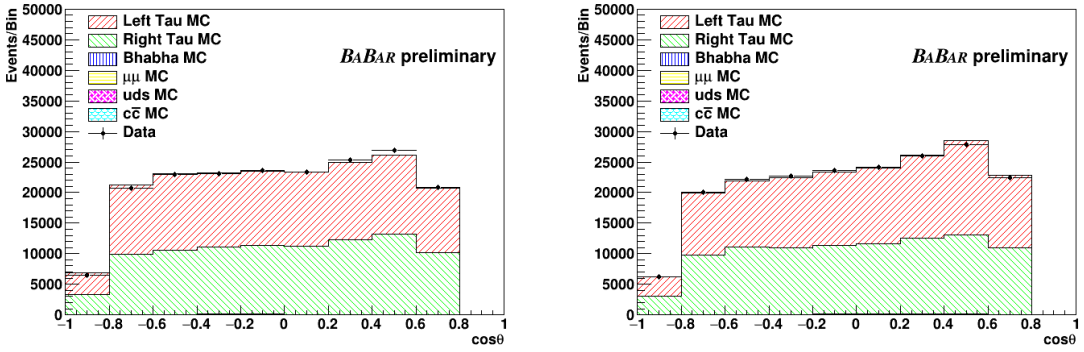

Figure C.4: One dimensional projection of fit performance for $\cos\theta$ in Run 2. Positively (left) and negatively (right) charged candidates.

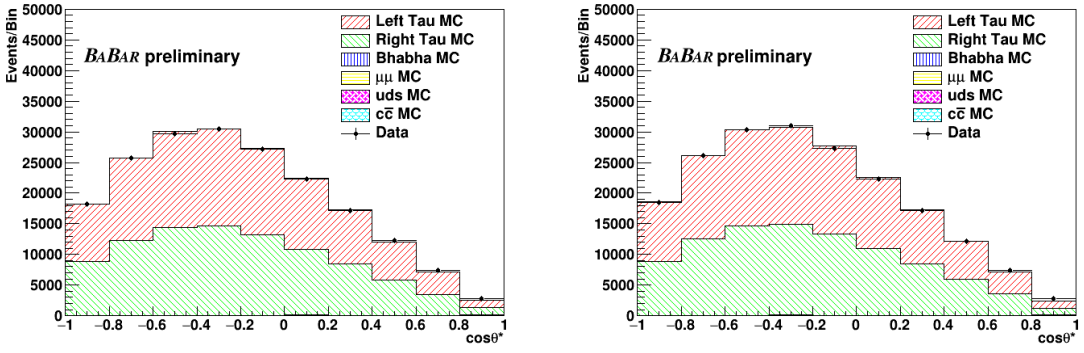

Figure C.5: One dimensional projection of fit performance for $\cos\theta^{\star}$ in Run 2. Positively (left) and negatively (right) charged candidates.

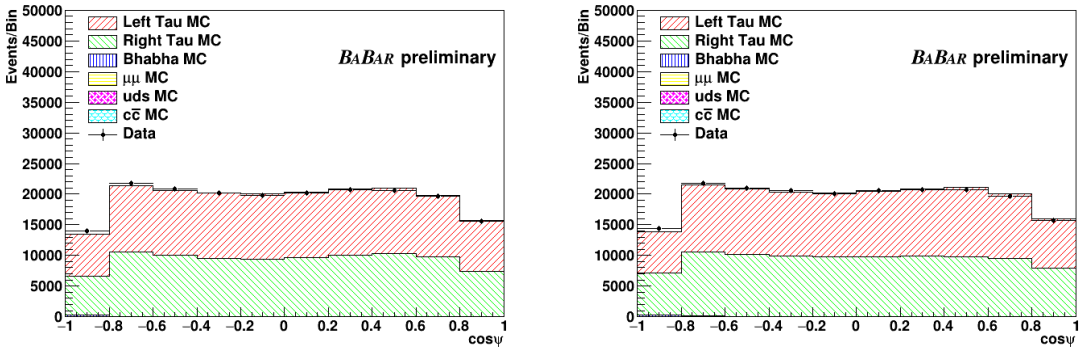

Figure C.6: One dimensional projection of fit performance for $\cos\psi$ in Run 2. Positively (left) and negatively (right) charged candidates.

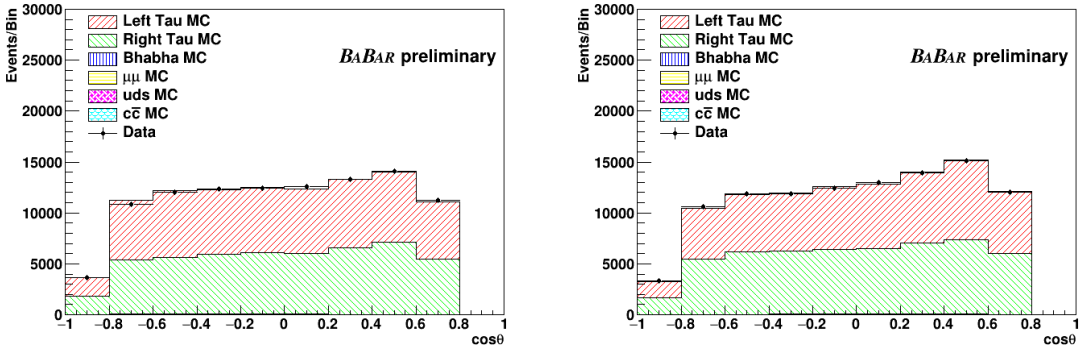

Figure C.7: One dimensional projection of fit performance for $\cos\theta$ in Run 3. Positively (left) and negatively (right) charged candidates.

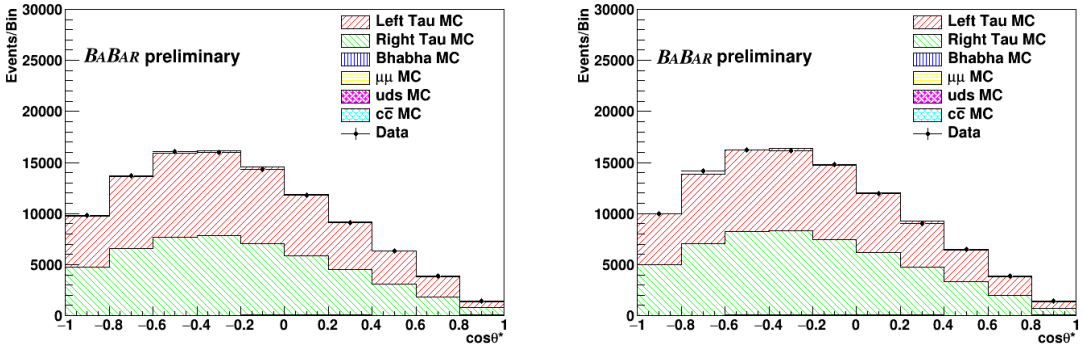

Figure C.8: One dimensional projection of fit performance for $\cos\theta^{\star}$ in Run 3. Positively (left) and negatively (right) charged candidates.

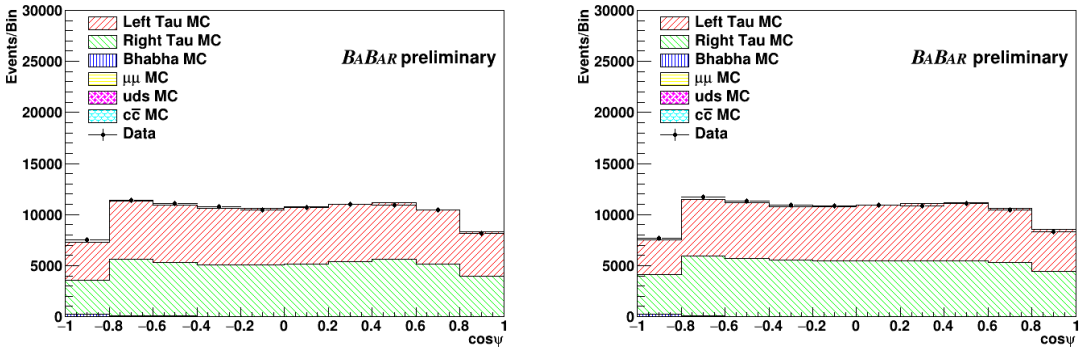

Figure C.9: One dimensional projection of fit performance for $\cos\psi$ in Run 3. Positively (left) and negatively (right) charged candidates.

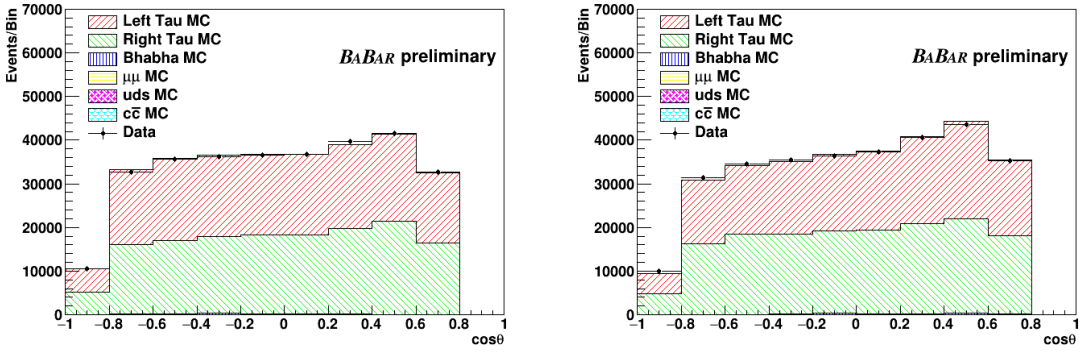

Figure C.10: One dimensional projection of fit performance for $\cos\theta$ in Run 4. Positively (left) and negatively (right) charged candidates.

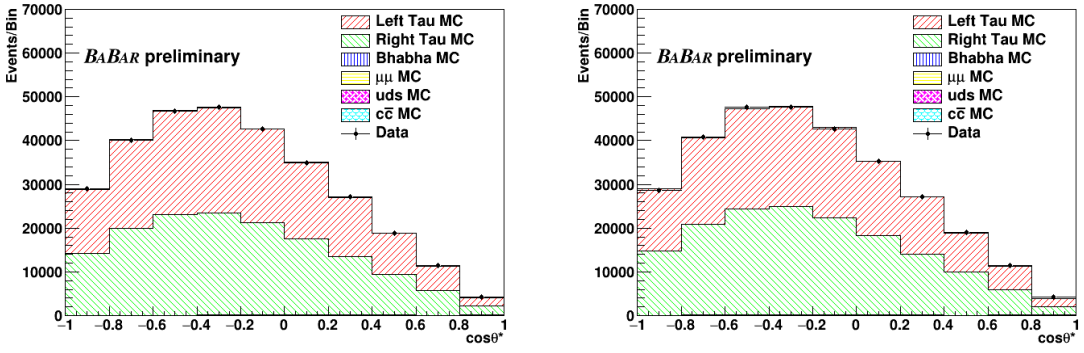

Figure C.11: One dimensional projection of fit performance for $\cos\theta^{\star}$ in Run 4. Positively (left) and negatively (right) charged candidates.

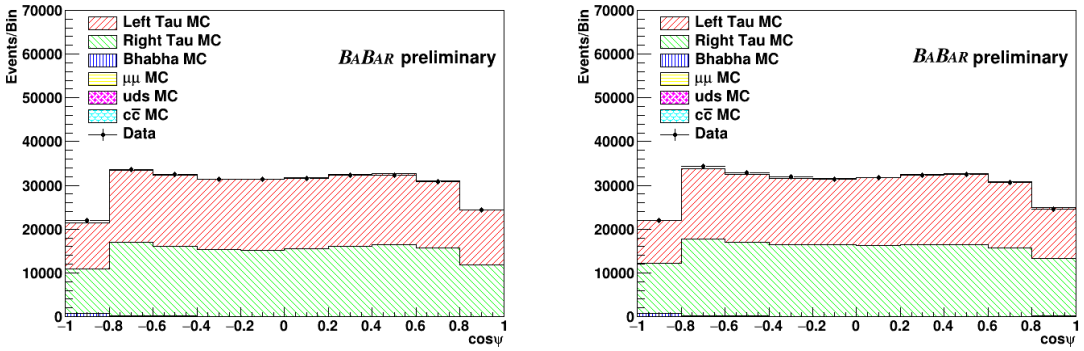

Figure C.12: One dimensional projection of fit performance for $\cos\psi$ in Run 4. Positively (left) and negatively (right) charged candidates.

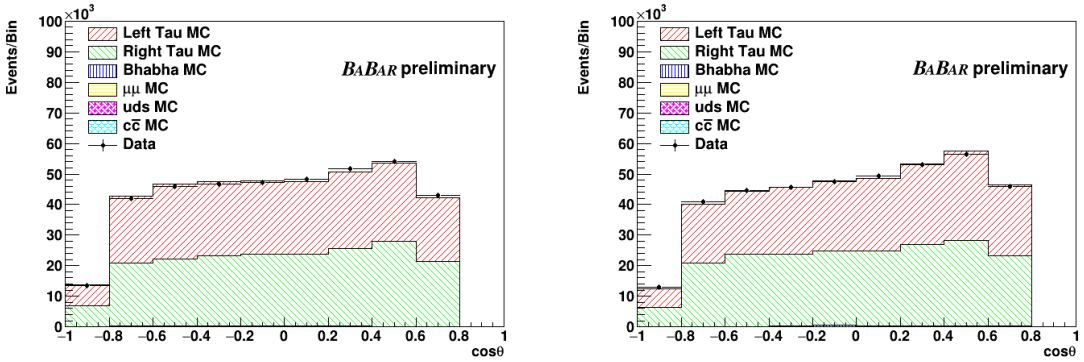

Figure C.13: One dimensional projection of fit performance for $\cos\theta$ in Run 5. Positively (left) and negatively (right) charged candidates..

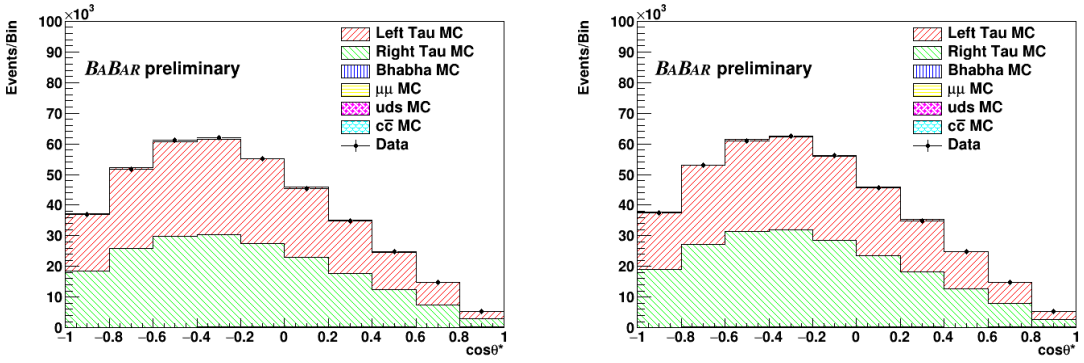

Figure C.14: One dimensional projection of fit performance for $\cos\theta^{\star}$ in Run 5. Positively (left) and negatively (right) charged candidates.

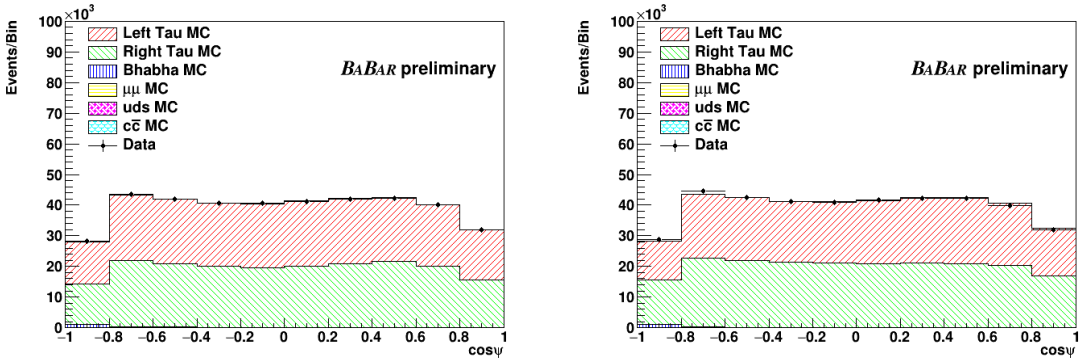

Figure C.15: One dimensional projection of fit performance for $\cos\psi$ in Run 5. Positively (left) and negatively (right) charged candidates.

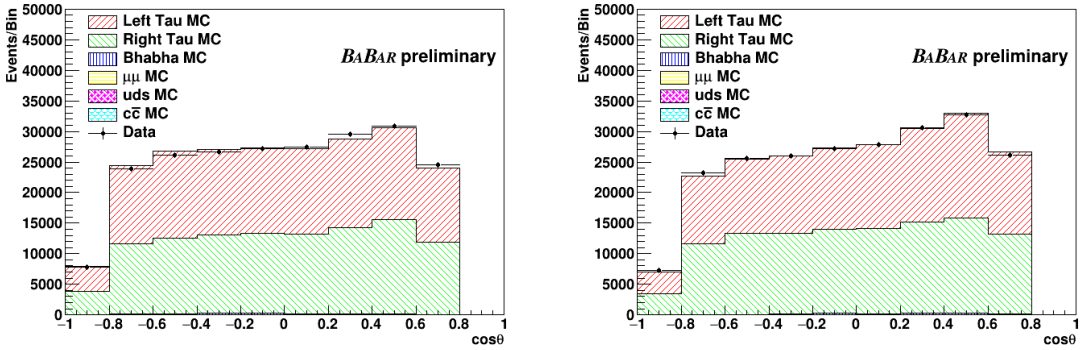

Figure C.16: One dimensional projection of fit performance for $\cos\theta$ in Run 6. Positively (left) and negatively (right) charged candidates.

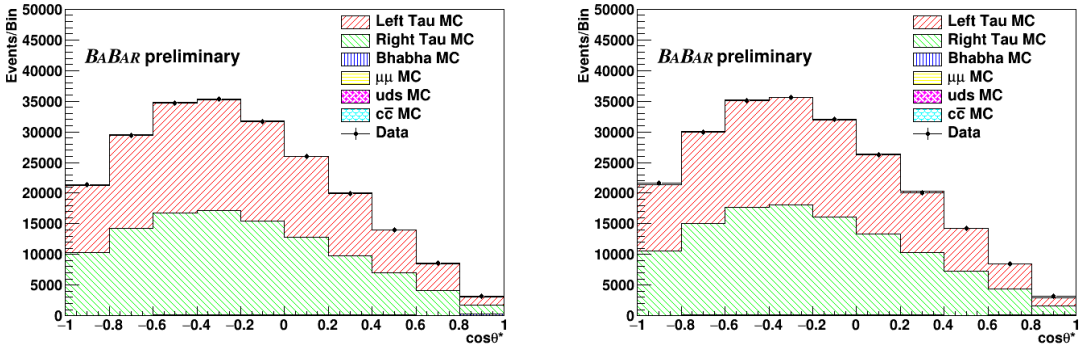

Figure C.17: One dimensional projection of fit performance for $\cos\theta^{\star}$ in Run 6. Positively (left) and negatively (right) charged candidates.

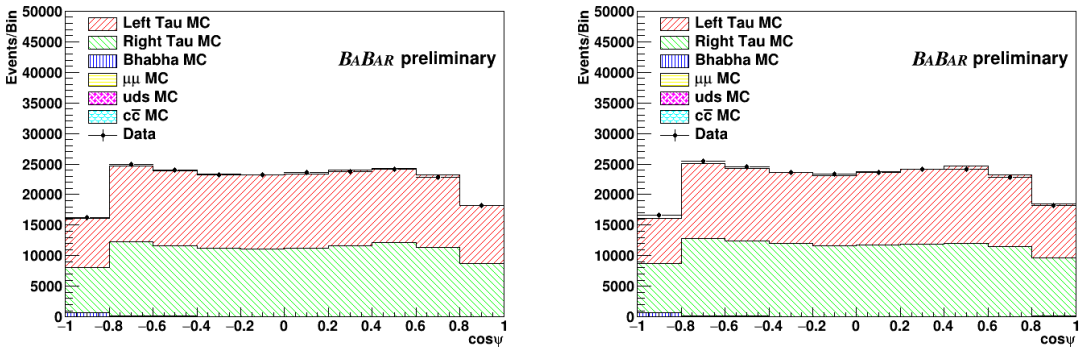

Figure C.18: One dimensional projection of fit performance for $\cos\psi$ in Run 6. Positively (left) and negatively (right) charged candidates.

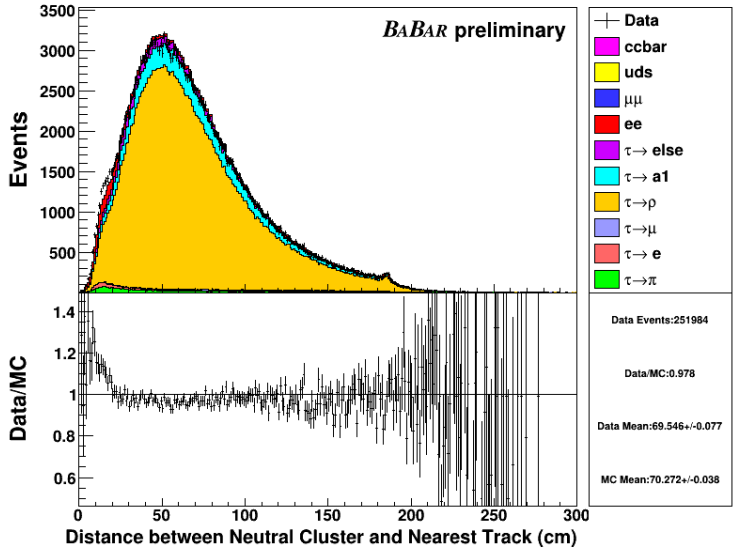

Figure C.19: Distance between neutral cluster and nearest charged track. No requirements on the π^0 mass or likelihood in this plot to highlight data/MC discrepancy at short distances

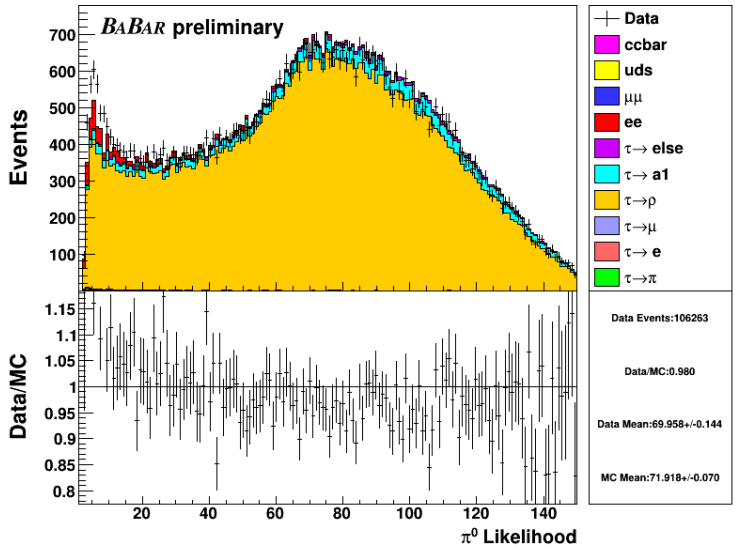

Figure C.20: π^0 likelihood of neutral clusters without likelihood requirement, all other analysis cuts in place.

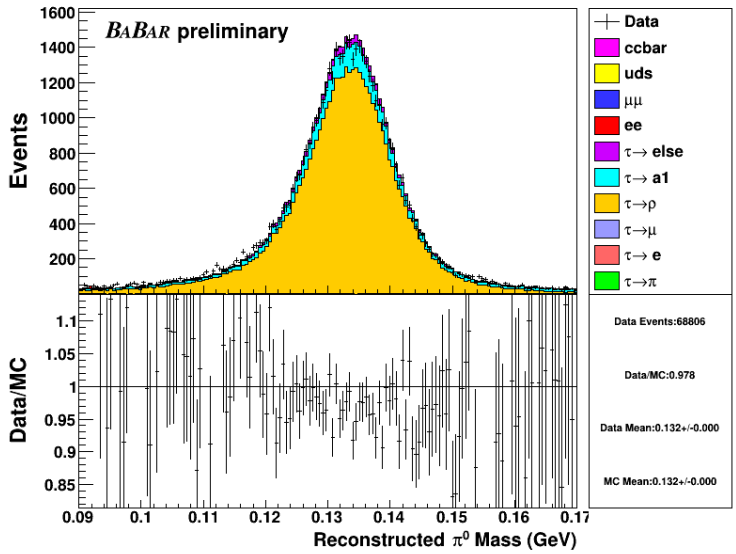

Figure C.21: π^0 mass of reconstructed neutral clusters without π^0 mass requirement, all other analysis cuts in place.

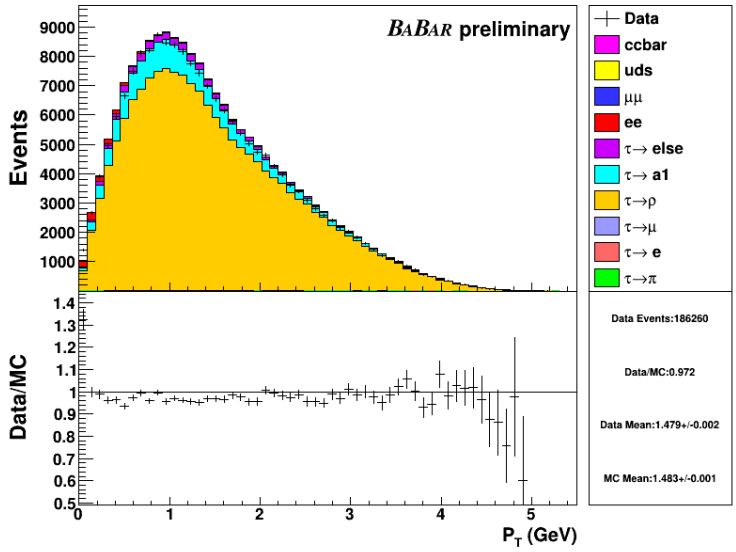

Figure C.22: Event transverse momentum before cut, all other analysis cuts in place.

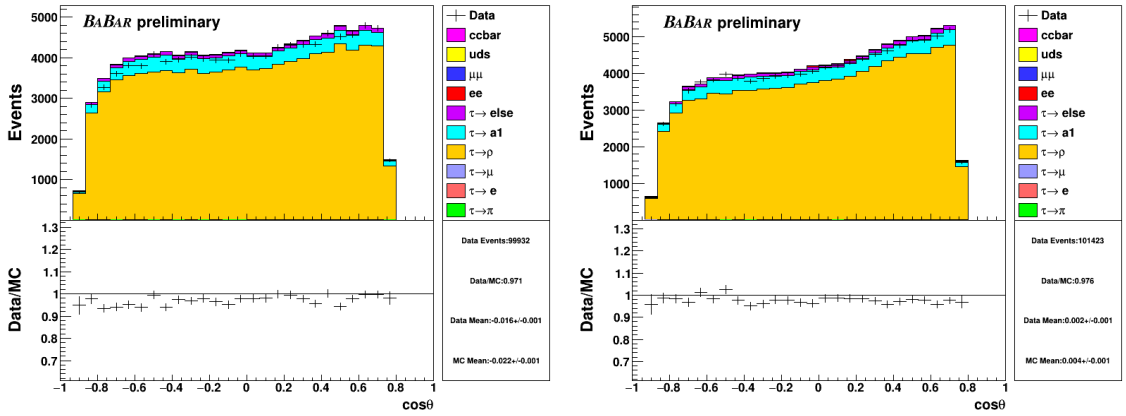

Figure C.23: $\cos\theta$ distribution for final state pions decaying from the rho. Positively (left) and negatively (right) charged candidates. All analysis cuts in place

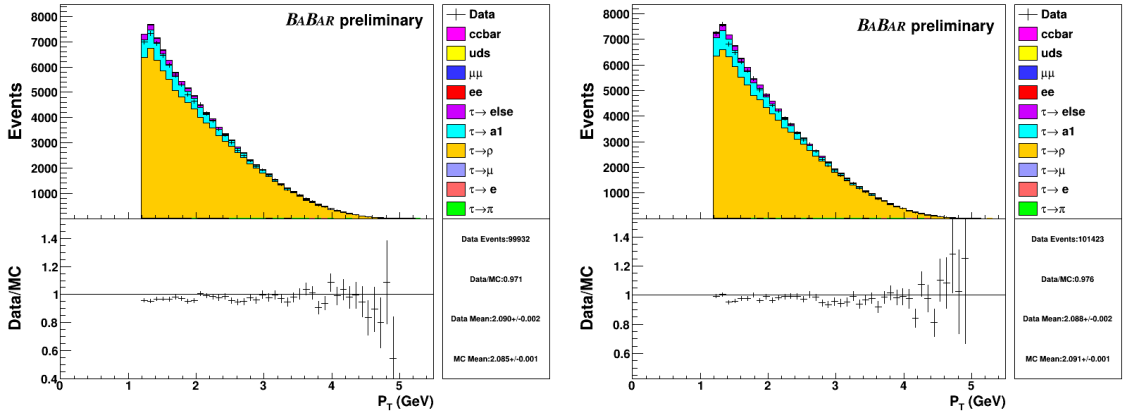

Figure C.24: Total event transverse momentum distribution. Positively (left) and negatively (right) charged candidates. All analysis cuts in place

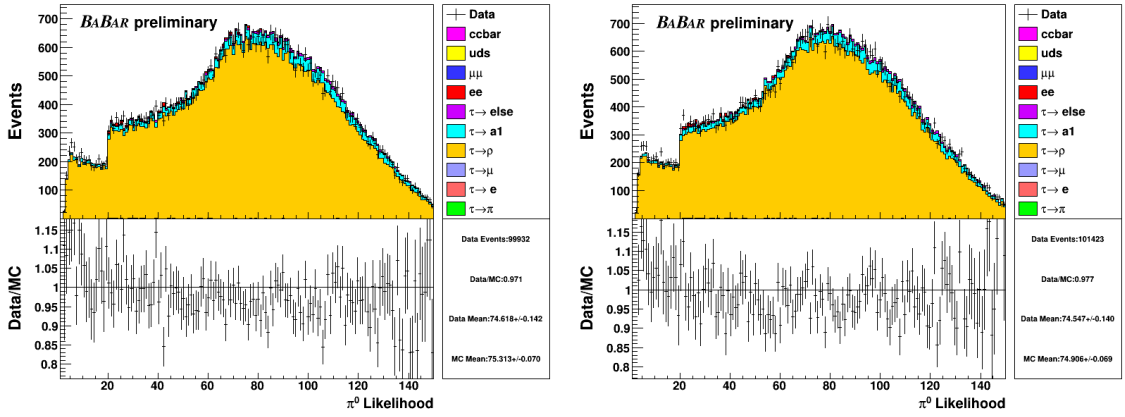

Figure C.25: π^0 likelihood distribution for selected neutral clusters. Positively (left) and negatively (right) charged candidates. All analysis cuts in place

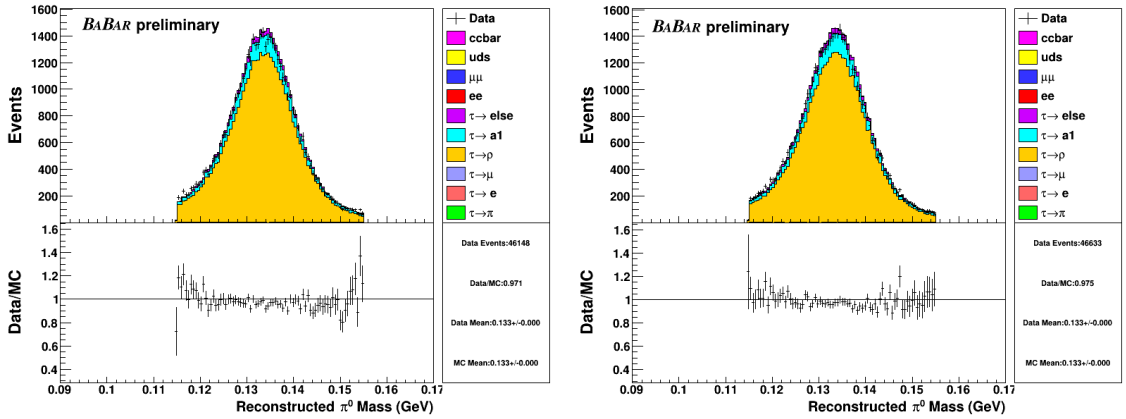

Figure C.26: π^0 mass distribution for reconstructed π^0's. Positively (left) and negatively (right) charged candidates. All analysis cuts in place

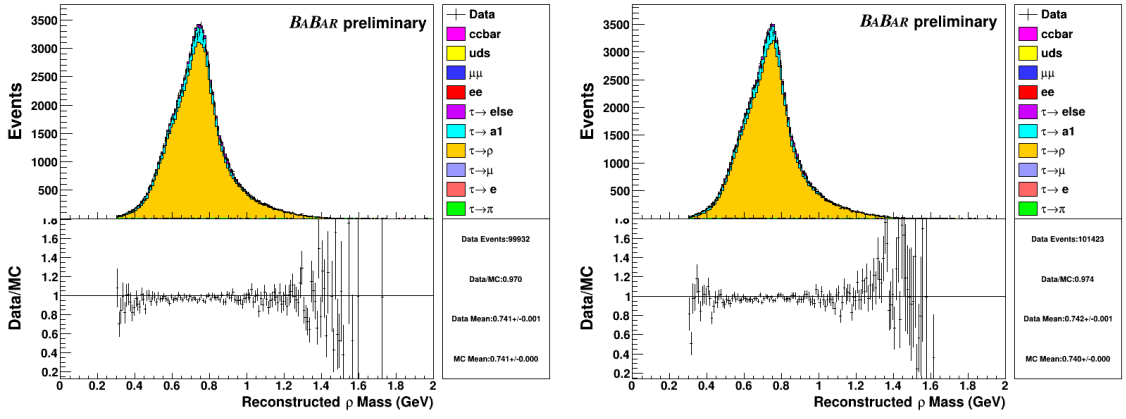

Figure C.27: rho mass distribution for reconstructed rho mesons. Positively (left) and negatively (right) charged candidates. All analysis cuts in place

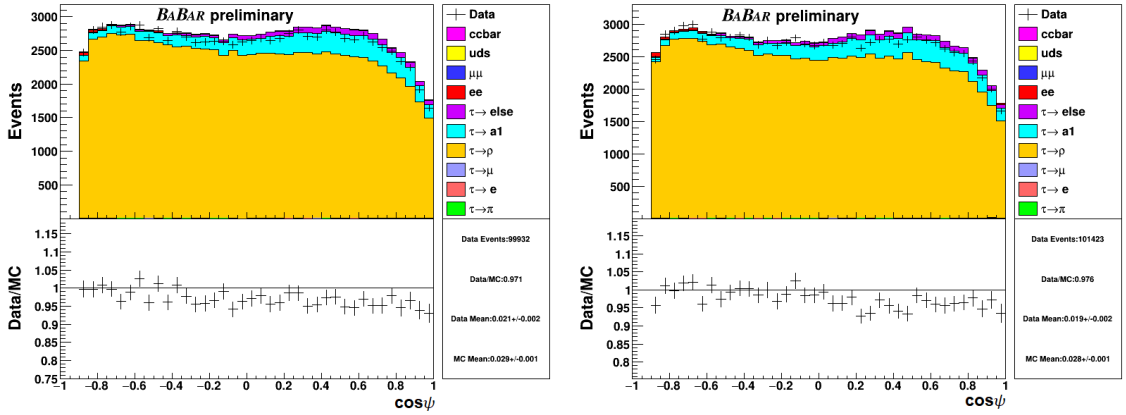

Figure C.28: $\cos\psi$ distribution. Positively (left) and negatively (right) charged candidates. All analysis cuts in place

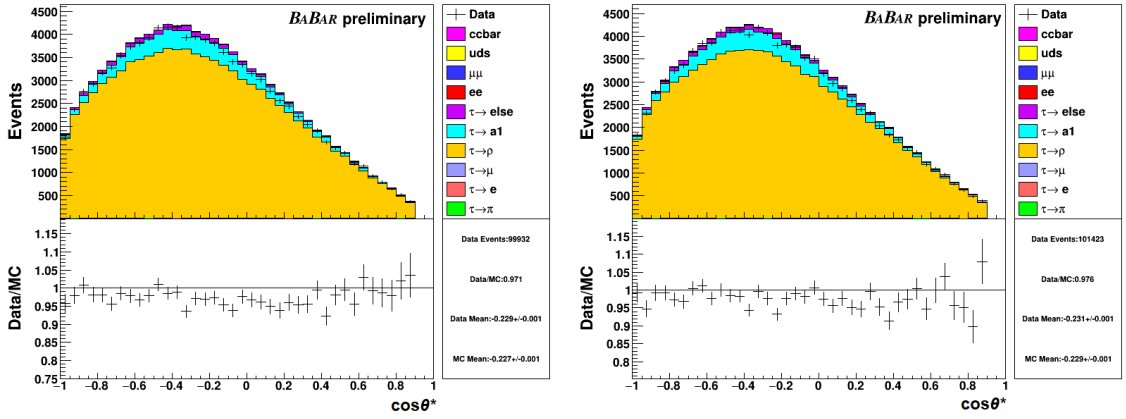

Figure C.29: $\cos\theta^{\star}$ distribution. Positively (left) and negatively (right) charged candidates. All analysis cuts in place

Source	Run 1	Run 2	Run 3	Run 4	Run 5	Run 6	Final
π^0 Likelihood	0.0032	0.0012	0.0013	0.0009	0.0010	0.0020	**0.0014**
Hadronic Split-off Modelling	0.0035	0.0012	0.0027	0.0015	0.0011	0.0005	**0.0012**
Minimum Neutral Energy	0.0006	0.0009	0.0013	0.0005	0.0006	0.0016	**0.0011**
π^0 Mass	0.0018	0.0005	0.0011	0.0009	0.0006	0.0014	**0.0009**
$\cos\psi$	0.0022	0.0012	0.0013	0.0006	0.0008	0.0010	**0.0009**
Angular Resolution	0.0010	0.0015	0.0010	0.0012	0.0002	0.0007	**0.0007**
Electron PID	0.0022	0.0008	0.0006	0.0007	0.0014	0.0010	**0.0007**
$\cos\theta^\star$	0.0012	0.0007	0.0002	0.0012	0.0009	0.0007	**0.0006**
Event Transverse Momentum	0.0013	0.0006	0.0006	0.0006	0.0002	0.0005	**0.0004**
Momentum Resolution	0.0005	0.0008	0.0002	0.0004	0.0003	0.0006	**0.0004**
π^0 Minimum Photon Energy	0.0008	0.0008	0.0011	0.0009	0.0003	0.0010	**0.0004**
Tau Branching Fraction	0.0007	0.0006	0.0001	0.0010	0.0006	0.0005	**0.0004**
Rho Mass	0.0007	0.0002	0.0002	0.0002	0.0004	0.0005	**0.0003**
Boost	0.0000	0.0002	0.0002	0.0001	0.0005	0.0004	**0.0002**
Background Modelling	0.0027	0.0002	0.0006	0.0002	0.0007	0.0009	**0.0002**
Total	0.0070	0.0033	0.0041	0.0032	0.0028	0.0039	**0.0029**

Table C.1: Summary of systematic uncertainties associated with polarization measurement, including Run 3.

Appendix D

Tau Polarimetry Paper Draft

Precision e^- Beam Polarimetry at an e^+e^- B-Factory using Tau-Pair Events

The *BABAR* Collaboration
(Dated: April 16, 2023)

We present a new technique for measuring electron beam polarization in an e^+e^- collider at $\sqrt{s} = 10.58$ GeV through the analysis of $e^+e^- \to \tau^+\tau^-$events. By exploiting the sensitivity of τ decay kinematics to the polarization of the beam, we demonstrate that the polarization can be measured with a 3 per mil systematic uncertainty at the e^+e^- interaction point using a technique that is independent of spin and beam transport modeling. Using 424.2±1.8 fb^{-1} of *BABAR* data, the average e^- beam polarization of the PEP-II e^+e^- collider has been measured to be $\langle P \rangle = 0.0035 \pm 0.0024_{\rm stat} \pm 0.0029_{\rm sys}$. A proposed e^- beam polarization upgrade to the SuperKEKB e^+e^- collider would benefit from this technique. The method and systematic uncertainty studies are described in detail, which can serve as a guide for future applications of Tau Polarimetry.

I. INTRODUCTION

Precision measurements of the weak mixing angle can be performed with experimental determinations of the left-right asymmetry, A_{LR}, for each of the $e^+e^- \to f\overline{f}$ processes, where f is a charged lepton or quark. The asymmetry is defined as the normalized difference between the production cross-section for a left and right handed process:

$$A_{\rm LR} = \frac{\sigma_{\rm L} - \sigma_{\rm R}}{\sigma_{\rm L} + \sigma_{\rm R}},$$

where the L and R subscripts refer to the chirality of the initial state electron in the $e^+e^- \to f\overline{f}$ process. In the past, the SLD experiment, operating at Z^0-pole, used $A_{\rm LR}$ to make the world's more precise measurement of $\sin^2\theta_W$ [1, 2]. At electron-positron colliders operating at $\sqrt{s} = 10.58$ GeV, a non-zero value of this asymmetry arises from $\gamma - Z$ interference [3] and the measured value of A_{LR} scales linearly with the average beam polarization [4, 5]:

$$A^f_{LR} \propto \left(\frac{sG_F}{\alpha}\right) g^e_A g^f_V \langle P_e \rangle,$$

where G_F is the Fermi constant, s is square of the center-of-mass energy, α is the fine structure constant, g^e_A is the neutral current axial coupling of the electron, $g^f_V = T^f_3 - 2Q_f \sin^2\theta_W$, is the neutral current vector coupling of fermion f, and $\langle P_e \rangle$ is the average beam polarization. It is defined as:

$$\langle P_e \rangle = \frac{1}{2}\left[\left(\frac{N^e_L - N^e_R}{N^e_L + N^e_R}\right)_{\mathbf{L}} - \left(\frac{N^e_L - N^e_R}{N^e_L + N^e_R}\right)_{\mathbf{R}}\right],$$

where $N^e_{L(R)}$ refers to the actual number of left (right) handed electrons in the data-set, and the **L(R)** subscript refers to the left (right) nominal polarization of the e^- beam. In order to significantly improve the precision with which the neutral current vector couplings, and hence $\sin^2\theta_W$, can be determined for electrons, muons, taus, c quarks, and b quarks, beam polarization can be introduced, such as is being considered for SuperKEKB in an upgrade refered to as 'Chiral Belle' [6]. A polarized beam also provides opportunities to make a number of world-leading precision measurements of other fundamental parameters, such as the anomalous magnetic moment form factor of the τ [6–8].

For the measurements that the Belle II upgrade proposes, it is expected that the knowledge of the average beam polarization will be the dominant systematic uncertainty. The proposed polarization upgrade includes the installation of a Compton polarimeter that will provide continuous measurements of the beam polarization as close to the interaction point(IP) as is feasible without disrupting the existing accelerator lattice. As the physics requires the beam polarization at the IP, the Compton polarimeter measurement will use spin and beam transport models to extrapolate the measurement to the IP. This extrapolation introduces unavoidable additional uncertainties. We present in this paper a novel, complementary, and independent method for measuring electron beam polarization in an e^+e^- collider, referred to as "Tau Polarimetry". Tau Polarimetry uses $e^+e^- \to \tau^+\tau^-$events measured in the detector at the IP and determines the average beam polarization by utilizing the sensitivity of the kinematics to the polarization. Compton polarimeters, which can also accurately measure the beam polarization, cannot occupy the same physical space as a general purpose detector such as *BABAR* or Belle II and therefore are accompanied with beam transport modelling uncertainties. Tau Polarimetry is free of these uncertainties as the polarization is extracted directly from the data collected at the IP.

Due to the similarities between the Belle II and *BABAR* detectors, and the fact that both involve e^+e^- collisions at $\sqrt{s} = 10.58$ GeV (Belle II at SuperKEKB and *BABAR* at PEP-II), *BABAR* is in a position to demonstrate the feasibility of the Tau Polarimetry technique, and establish the expected level of both statistical and systematic sensitivity that Belle II might achieve in a polarization-upgraded SuperKEKB collider. Tau Polarimetry relies on two convenient properties of nature. The first property is the linear relationship between the polarization of the initial state electron and the polarization of the τ leptons produced in the $e^+e^- \to \tau^+\tau^-$

process, where at $\sqrt{s} = 10.58$ GeV[9]:

$$P_\tau = P_e \frac{\cos\theta}{1+\cos^2\theta} - \frac{8G_F s}{4\sqrt{2}\pi\alpha} g_V^\tau \left(g_A^\tau \frac{|\vec{p}|}{p^0} + 2g_A^e \frac{\cos\theta}{1+\cos^2\theta} \right),$$

P_ℓ is the polarization of the τ or electron, θ is the angle between the τ^- and the electron beam, and $\vec{p}$ and p^0 are the 3-momenta and energy of the heavy lepton respectively. At $\sqrt{s} = 10.58$ the electroweak contribution to the polarization is on the order of 0.003, or 0.3% for an unpolarized beam. All of the parameters in the calculation are well measured, and any new physics in the electroweak sector will have an effect much smaller than the systematic uncertainties in the beam polarization measurement. The second property arises from the intrinsic left-handedness of neutrinos (and right-handedness of antineutrinos). As the ν_τ ($\overline{\nu}_\tau$) emitted in the $\tau^-(\tau^+)$ decay will always have a left-handed(right-handed) chiral state, the other decay products will exhibit a kinematic bias based on the τ spin state [4, 7]. This feature of τ decays has been exploited in the past by LEP to extract precision measurements of the weak mixing angle [10–14]. By combining the relationship between the beam polarization and tau polarization with the kinematic dependencies to polarization, *BABAR* is able to measure the average electron beam polarization present in the PEP-II accelerator, which operated without beam polarization. A major focus of this work is to evaluate the sensitivity of the Tau Polarimetry method, including the systematic uncertainties associated with the technique. In this paper we present the *BABAR* experiment (Section II), the relevant polarization sensitive variables (Section III), the polarization fitting method and a validation study utilizing simulated polarized beams (Section IV), the event selection process (Section V), the beam polarization fit results for PEP-II (Section VI), the systematic uncertainty evaluation (Section VII), and finally a discussion on future applications of Tau Polarimetry and the full measurement result (Section VIII).

II. PEP-II AND THE *BABAR* DETECTOR

The *BABAR* detector [15, 16] operated from 1999 to 2008 at the PEP-II asymmetric e^+e^- collider which collided 9.0 GeV electrons with 3.1 GeV positrons. The longitudinal beam polarization in *BABAR* data is expected to be near zero due to the beam rings at PEP-II being unsuited to build up transverse polarization, with less than 0.8% transverse polarization expected. Even if a polarized beam were to be injected into the HER, it would depolarize in less than 1.5 minutes[17]. Particles in the *BABAR* detector are identified by combining information from its sub-detectors. Charged-particle momenta are measured using tracks measured in both a five-layer silicon vertex tracker and a 40-layer drift chamber (DCH) operating in a 1.5-T solenoidal magnetic field. Photons and electrons have their full energy and angular coordinates measured in the electromagnetic calorimeter (EMC) consisting of 6580 Thallium doped Cesium Iodide [CsI(Tl)] crystals. Muons are identified by resistive-plate chambers and streamer tubes in the instrumented magnetic-flux-return iron (IFR). Charged-particle identification (PID) is based on energy-loss measurements in the silicon vertex tracker and DCH, and on information from a ring-imaging Cherenkov detector, the EMC, and the IFR. The studies reported in this paper use the data collected by *BABAR* at a center-of-mass energy of 10.58GeV, which corresponds to the mass of the $\Upsilon(4S)$ resonance, with an integrated luminosity of 424.2±1.8 fb^{-1} [18]. A total of 700 million polarized tau Monte Carlo (MC) simulated events, roughly a 643 fb^{-1} equivalent, were produced for each beam polarization state with the `KKMC` generator[19]. A number of MC generators are used to generate unpolarized *BABAR* MC samples of various processes of interest: the continuum $\mu^+\mu^-$ and $\tau^+\tau^-$ simulation is produced with `KKMC`, which invokes `TAUOLA` [20] to simulate the decay of final state tau leptons; the $e^+e^- \to e^+e^-$ Bhabha process is simulated using the `BHWIDE` [21] generator; and the `EvtGen` [22] generator provides the hadronic continuum MC. `PHOTOS` [23] is employed to calculate the final-state radiation effects. These raw processes undergo a detector response simulation implemented with GEANT4 [24, 25]. Roughly twice as much $\mu^+\mu^-$ and $c\overline{c}$ MC is produced compared to the number of data events, and roughly four times as many $u\overline{u}, d\overline{d}, s\overline{s}$, and $\tau^+\tau^-$ MC events are produced relative to the data. As *BABAR* relies more heavily on data-driven approaches to study and control Bhabha backgrounds, a smaller sample of Bhabha MC events is available to be used in low-statistics MC studies.

III. POLARIZATION SENSITIVITY

While all tau decay modes are sensitive to beam polarization, the hadronic decays are the most sensitive per event as there is only one neutrino carrying away spin information. In the case of the $\tau^\pm \to (\rho^\pm \to \pi^\pm\pi^0)\overline{\nu}_\tau$ decay, which has the largest tau branching fraction, three angular variables, including $\cos\theta$, are required to extract the beam polarization. The other two polarization sensitive variables are defined as [26]:

$$\cos\theta^\star = \frac{2z - 1 - m_\rho^2/m_\tau^2}{1 - m_\rho^2/m_\tau^2} \qquad z \equiv \frac{E_\rho}{E_{\rm beam}}$$

$$\cos\psi = \frac{2x-1}{\sqrt{1 - m_\pi^2/m_\rho^2}} \qquad x \equiv \frac{E_\pi}{E_\rho}$$

Where E_π and E_ρ are the reconstructed energies of the pion and rho respectively, and $E_{\rm beam} \equiv \sqrt{s}/2$. For the mass of the pion and the tau we use the PDG[27] values, while for the mass of the rho we used the event-by-event reconstructed $\pi\pi^0$ mass. $\theta^\star$ is defined as the opening angle between the between the tau flight path in the e^+e^-

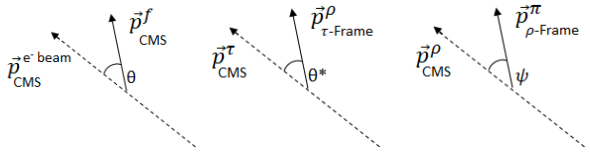

FIG. 1. Diagrams illustrating $\cos\theta$ (left, f represents a final state particle), $\cos\theta^\star$ (center), and $\cos\psi$ (right).

center-of-mass frame and rho direction in the tau rest frame. Similarly, ψ is the opening angle between the rho flight direction in the center-of-mass frame and the pion direction in the rho rest frame. The third angular variable is θ, the angle between the τ^- momentum and the electron beam direction. $\cos\theta^\star$ and $\cos\psi$ reverse their left-right behaviour depending on whether the τ^- decays in the forward ($\cos\theta>0$) or backward ($\cos\theta<0$) hemisphere. Figure 1 illustrates the angular definitions. The distributions of these variables are depicted in Figures 2 to 4 for both the left and right chiral states of the electron beam.

IV. FITTING

To extract the average beam polarization we perform a binned likelihood fit on the normalized distribution using the Barlow and Beeston method [28]. We fill three dimensional histograms of $\cos\theta^\star$, $\cos\psi$, and $\cos\theta$ for each of the data and MC modes. The 3D histogram for data is then fit as a combination of the MC histograms, where the weights of the non-tau MC is fixed based on the MC efficiency studies. The tau contributions from left and right beam polarization distributions are varied in the fit under the constraint that they sum to one, leaving a single parameter in the fit. We define this fitted parameter as $\langle P\rangle$=L-R, where L and R are the fitted fractions reported by the fit for the left and right polarized tau MC. As the polarization sign flips with electric charge, we perform the fit separately for positively and negatively charged signal candidates. A final fit result is then reported as the combined average of the two independent fits. As the *BABAR* datasets are split into six data collection periods with unique beam and detector conditions, referred to as Runs 1 through Run 6, we treat each sample independently. As such we obtain six measurements of the beam polarization and corresponding statistical and systematic uncertainties. A final measurement of the beam polarization is then obtained by combining these measurements and accounting for correlations in the systematic uncertainties.

A. Extracted vs Input Beam Polarization Study

In order to validate the Tau Polarimetry technique at different beam polarization states, we used polarized tau MC to study the extracted polarization from this analysis of the rho channel at multiple input beam polarization values. This was done by splitting each of the left and right polarized tau MC into two distinct samples, one reserved for fitting the beam polarization in MC "measurements" and the other for mixing beam polarization states. Specific beam polarization states can be created by combining left and right beam polarization MC samples with appropriate weights, e.g. 70% polarized is made with 85% left polarized MC and 15% right polarized MC. Using this technique we tested polarization states from -1 to 1 in steps of 0.1, the results of which are presented in Figure 5. The fit results to the MC are in good agreement of the input MC beam polarization states, which demonstrates the measurement technique will yield the correct polarization for any beam polarization.

V. EVENT SELECTION

We report on the measurement of the average beam polarization from the analysis of the kinematics of $\tau^\pm \to (\rho^\pm \to \pi^\pm\pi^0)\overline{\nu}_\tau$ decays. This decay mode was chosen because of its large branching fraction, 25.49%[27], as well as the high purity that can be achieved when the second τ lepton in the event decays via $\tau^\mp \to e^\mp\overline{\nu}_e\nu_\tau$ or $\tau^\mp \to \mu^\mp\overline{\nu}_e\nu_\tau$. Figure 6 shows the event topology for a signal event tagged with an electron. In order to select this topology, the event is required to contain two charged particles. These charged particles are required to originate within 2.5 cm along the beam axis of the collision point, and within 1.5 cm in the transverse plane. Neutral particles, such as photons, are identified as energy clusters in the EMC with no associated charged track, as identified by the DCH, and with deposited energy measured in excess of 50 MeV. From the thrust axis [29, 30] of the event we split the event into two hemispheres, the signal side and the tag side. On the tag side of the event we require a single charged particle and no neutral particles, while on the signal side a single charged particle and a neutral pion is required. Neutral pions are identified by the invariant mass of photon pairs, where each possible photon pair combination is considered and the pair with an invariant mass closest to 135 MeV is accepted as the neutral pion in the event. The invariant mass of the reconstructed neutral pion is required to be in a mass window of 115 MeV to 155 MeV. *BABAR* is also able to identify neutral pions where both photons are detected within the same EMC cluster (a "merged π^0 ") [15, 16] and pions identified this way are also included in the analysis. The identified π^0 is then combined with the momentum information from the charged particle in the same hemisphere, which is assumed to be a charged pion, to reconstruct a ρ candidate. If the reconstructed mass of the candidate is greater than 300 MeV, the event is kept. The tagging τ decay is then required to be consistent with a $\tau \to e\nu_e\overline{\nu}_\tau$ or a $\tau \to \mu\nu_\mu\overline{\nu}_\tau$ decay by requiring the charged particle be consistent with

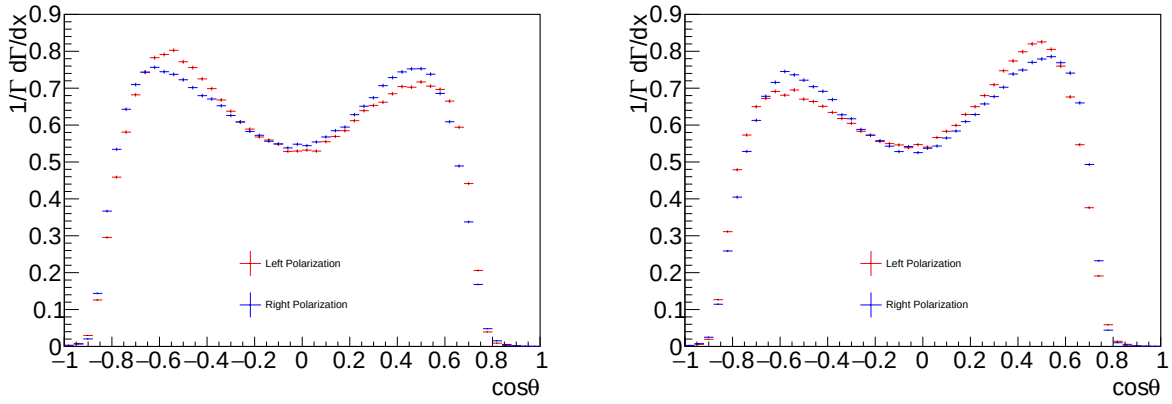

FIG. 2. $\cos\theta$ distribution in MC for positively(Left) and negatively(Right) charged τ decays to $\rho^{\pm} \to \pi^{\pm}\pi^{0}$.

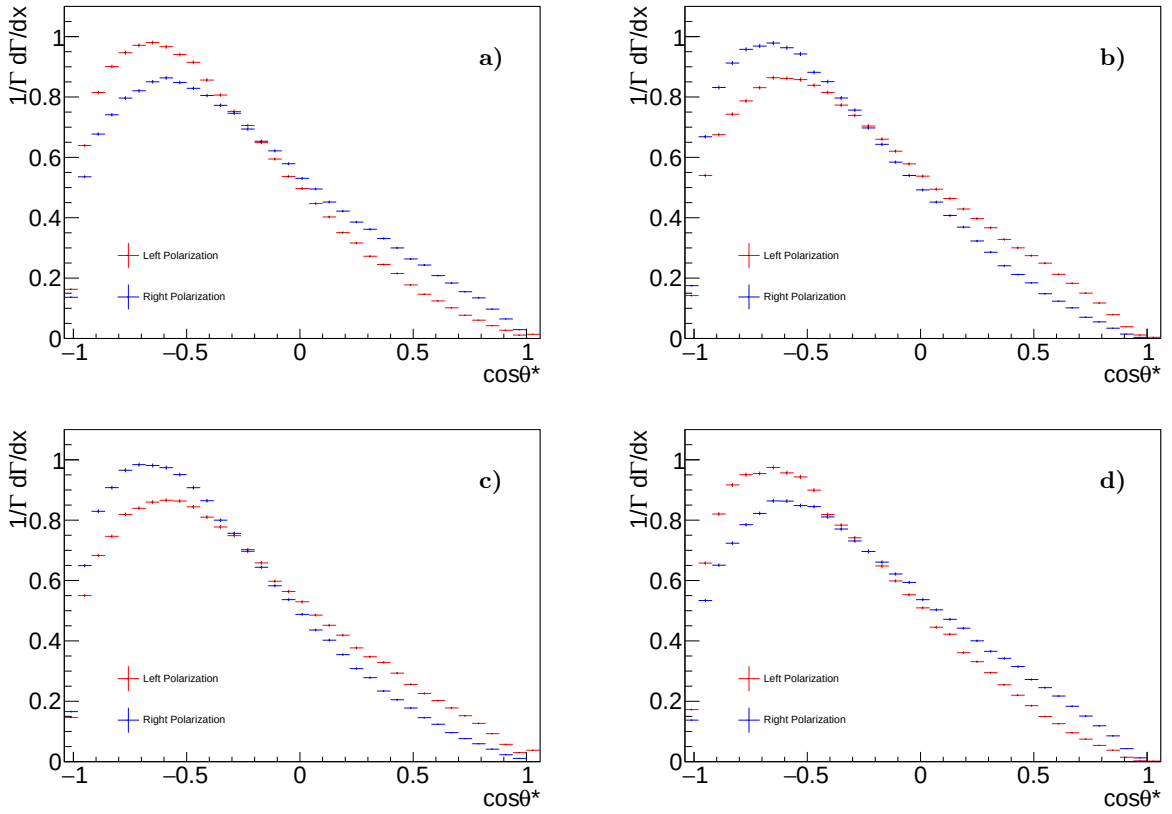

FIG. 3. $\cos\theta^{\star}$ distribution in MC for: positively charged τ decays for $\cos\theta < 0$ (**a**)) and $\cos\theta > 0$ (**b**)), and negatively charged τ decays for $\cos\theta < 0$ (**c**)) and $\cos\theta > 0$ (**d**)).

either a muon or electron via PID requirements on the track. Both the muon and electron selectors have been trained with machine learning techniques, a boosted decision tree for muons, and an error correcting output code utilizing bootstrap aggregate decision trees for the electrons. The angular acceptance for charged particle tracks is slightly reduced such that each track is within the calorimeter acceptance, $0.430 < \theta_{\rm lab} < 2.350$. This fiducial requirement improves PID performance, improves data/MC agreement, and reduces the Bhabha contamination. Combining both neutral and charged particles, the total event transverse momentum($p_{\rm T}$) is required to exceed 350 MeV in order to remove two photon events. The remaining Bhabha events are halved by requiring the EMC energy to not exceed 10 GeV, and reduced by an additional factor of three with the following requirements on polarization sensitive observables: $-1 < \cos\theta^{\star} < 0.9$, and $-0.9 < \cos\psi < 1$. These requirements result in a fi-

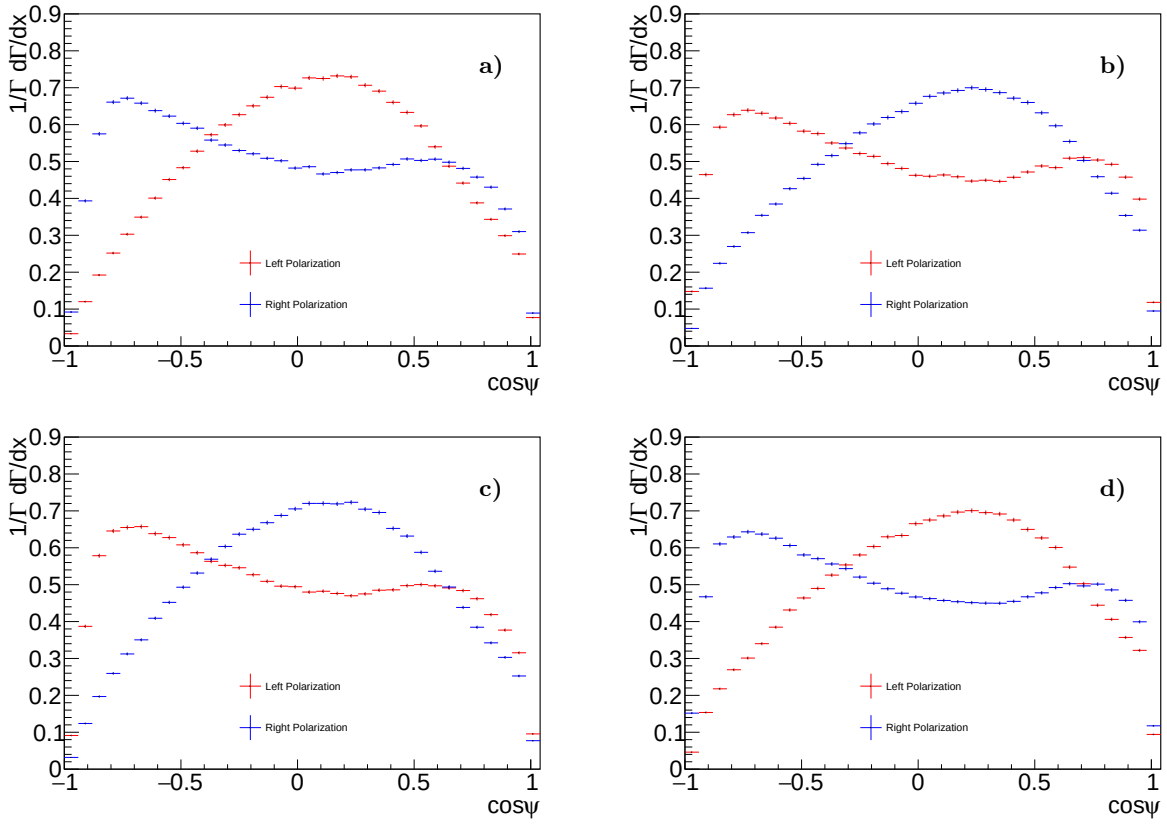

FIG. 4. $\cos\psi$ distribution in MC for: positively charged τ decays for $\cos\theta < 0$ (**a**)) and $\cos\theta > 0$ (**b**)), and negatively charged τ decays for $\cos\theta < 0$ (**c**)) and $\cos\theta > 0$ (**d**)).

nal $e^+e^- \to \tau^+\tau^-$ selection that is 99.9% pure and select 1.4% of all $\tau^+\tau^-$ events. This corresponds to a 7.8% efficiency for selecting $\tau^\pm\tau^\mp \to \rho^\pm\nu_\tau + \ell^\mp\nu_\ell\overline{\nu_\tau}$ $(\ell = e, \mu)$ events. The largest non-tau background sources are Bhabha and $\mu^+\mu^-$ events each of which make up 0.05% of the final sample. The final event selection breakdown as predicted by MC is shown in Table I. There is a small but statistically significant difference between the efficiency for selecting left and right polarized events, $\Delta\varepsilon = 0.011\% \pm 0.001\%$. This is expected to have little to no effect on the extracted polarization.

MC source	Fraction
Bhabha	0.046%
$\mu^+\mu^-$	0.046%
$u\overline{u}$,$d\overline{d}$,$s\overline{s}$	0.030%
$c\overline{c}$	0.006%
$b\overline{b}$	0.000%
$\tau^+\tau^-$	99.871%
Tau Signal	**Fraction**
$\tau^\pm \to e^\pm\nu_e\overline{\nu}_\tau$	0.018%
$\tau^\pm \to \mu^\pm\nu_\mu\overline{\nu}_\tau$	0.031%
$\tau^\pm \to \pi^\pm\overline{\nu}_\tau$	0.035%
$\tau^\pm \to (\rho^\pm \to \pi^\pm\pi^0)\overline{\nu}_\tau$	87.858%
$\tau^\pm \to (a_1^\pm \to \pi^\pm\pi^0\pi^0)\overline{\nu}_\tau$	9.785%
$\tau \to$ else	2.145%

TABLE I. Fraction of event types in MC in the final event selection. The tau pair events are further broken down to show the decay mode composition of the events selected on the signal side.

VI. RESULTS

The fit results for both charged fits as well as the combined average for all *BABAR* data sets is shown in Table II. Taking the weighted mean of these fit results gives the overall average beam polarization for PEP-II to be $\langle P \rangle = 0.0035 \pm 0.0024_{\rm stat}$. The two dimensional projections of $\cos\theta^*$ and $\cos\psi$ for positively charged events is shown in Figure 7 and the negatively charged events in Figure 8.

VII. SYSTEMATIC UNCERTAINTY STUDIES

The systematic uncertainties have been evaluated with a few distinct methods, depending on which methodology

Data Set (fb^{-1})	Positive Charge	χ^2/NDF	Negative Charge	χ^2/NDF	Average Polarization
Run 1 (20.4)	0.0018±0.014	756/833	-0.0047±0.014	819/835	-0.0014±0.010
Run 2 (61.3)	0.0075±0.0083	830/875	0.0007±0.0083	887/867	0.0041±0.0059
Run 3 (32.3)	0.0151±0.012	840/850	-0.0047±0.012	905/841	0.0048±0.0083
Run 4 (99.6)	-0.0035±0.0072	1033/878	0.0010±0.0067	987/877	-0.0011±0.0049
Run 5 (132.3)	-0.0028±0.0062	1367/881	0.0136±0.0064	1276/889	0.0052±0.0045
Run 6 (78.3)	0.0036±0.0089	1150/886	0.0133±0.0088	1065/877	0.0084±0.0062
424.18±1.8	0.0015±0.0034		0.0055 ± 0.0034		0.0035 ± 0.0024

TABLE II. Average beam polarization measured in each data set. The average for each run is found from the weighted mean of the positive and negative fit results.

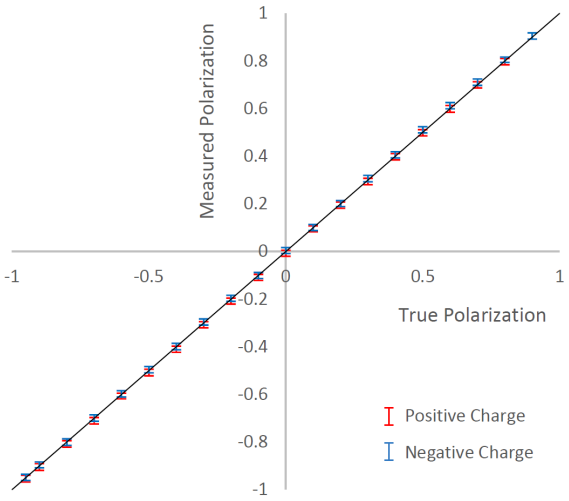

FIG. 5. Fit validation MC study: beam polarization outputs of fits as a function of input polarization, produced by mixing polarized tau MC as described in the text. The red points correspond to the measurements for positively charged signal candidates while the blue points correspond to the negatively charged candidates.

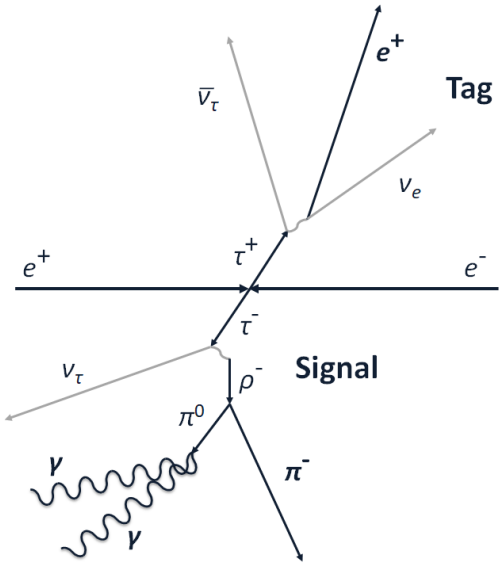

FIG. 6. Example signal type event, with signal $\tau^{\mp} \to (\rho^{\mp} \to \pi^{\mp}\pi^0)\nu_\tau$ decay tagged with a $\tau^{\pm} \to e^{\pm}\nu_e\overline{\nu}_\tau$ decay.

best suits the particular source of systematic uncertainty. The first method is a controlled variation of MC distributions in order to adjust the templates and determine the effect on the beam polarization measurements. The second method for evaluating the systematic uncertainties is a variation of the cut value applied to the variable, this is primarily used in regions where the cut is designed to remove uncontrolled sources of backgrounds or poor MC modelling. The final method is unique to evaluating the PID requirements, where different selectors are evaluated and the differing effects on the data and MC are used as an estimator on the bias introduced by the selectors. This section will discuss these methods in more detail and how they apply to each variable. For all of the approaches the intent is to capture an approximate 68% interval on the systematic variations.

A. Controlled variation of MC templates

1. π^0 *efficiency correction*

The π^0 efficiency is corrected as a function of lab-frame momentum and $\cos\theta$ distributions using a combined sample of π^0 from τ decays consisting of both charged states. This method uses the π^0 lab-frame momentum and $\cos\theta$ distributions split across 100 bins (10 in momentum $\times$ 10 in $\cos\theta$) to correct the efficiency in each bin. The statistical uncertainty in each bin is used to evaluate the polarization sensitivity by performing the fit with each bin varied up or down respectively. This process results in a systematic uncertainty of $\sigma = 0.0013$ being assigned. By combining both charged states in the correction procedure, the efficiency correction is independent of polarization effects which flip sign with the lepton charge. To verify the correction does not introduce a bias to the polarization measurement, the procedure is performed on a 70% polarized MC sample, and the corrections are found to have a negligible effect on the polarization measure-

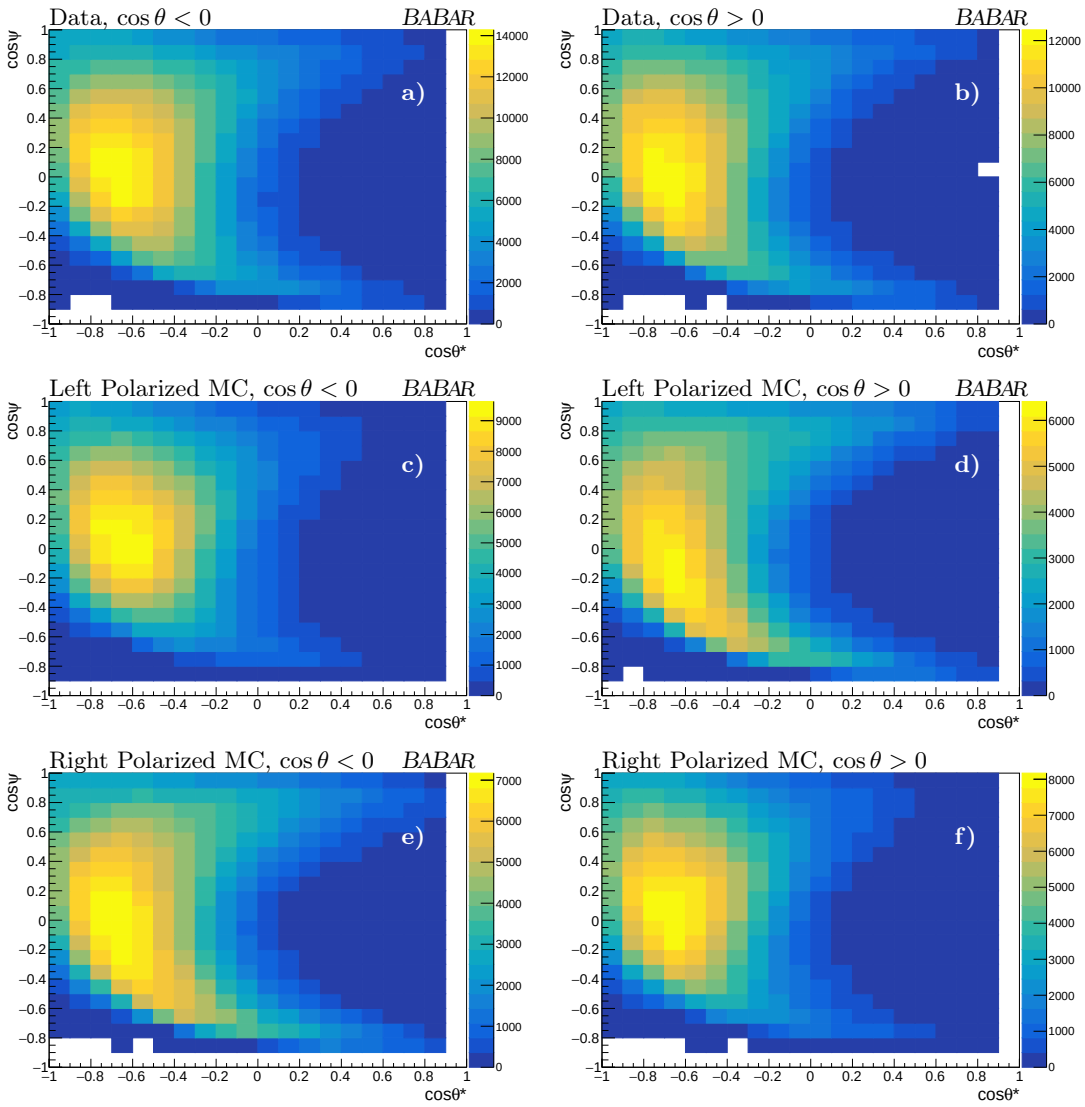

FIG. 7. 2-dimensional projection of $\cos\theta^*$ vs $\cos\psi$ for positively charged signal events. **a)**Data, $\cos\theta < 0$, **b)**Data, $\cos\theta > 0$, **c)**Left Polarized MC, $\cos\theta < 0$, **d)**Left Polarized MC, $\cos\theta > 0$, **e)**Right Polarized MC, $\cos\theta < 0$, **f)**Right Polarized MC, $\cos\theta > 0$.

ment. however if the corrections are carried out separately on each charge the polarization measurement is biased to measure only 49% polarization.

2. *Neutral Particle Energy Scale*

The energy scale of neutral particles in the *BABAR* detector is known to within 0.3% [16]. Increasing and decreasing the energy scale of all neutral particles in the MC results in a systematic uncertainty of $\sigma = 0.0010$ being associated with the polarization fluctuations due to the scaling. As a cross-check on the size of systematic uncertainties expected to be associated with the neutral particle energy scale a number of cut variation tests were performed as well. In particular, the 50 and 100 MeV neutral energy cut requirements were varied up and down by 1 MeV and if a systematic uncertainty were to be assigned would contribute $\sigma = 0.0005$ and $\sigma = 0.0004$ respectively. As having both approaches included in the analysis would double-count the effects of the neutral energy scale, this 0.3% EMC energy scaling approach is conservatively taken as the associated systematic uncertainty.

3. *Boost Correction*

In order to quantify the effect an incomplete understanding of the boost vector can have on the polarization measurement a sample of $e^+e^- \to \mu^+\mu^-$ events are studied. From the acollinearity of the muon pairs a small

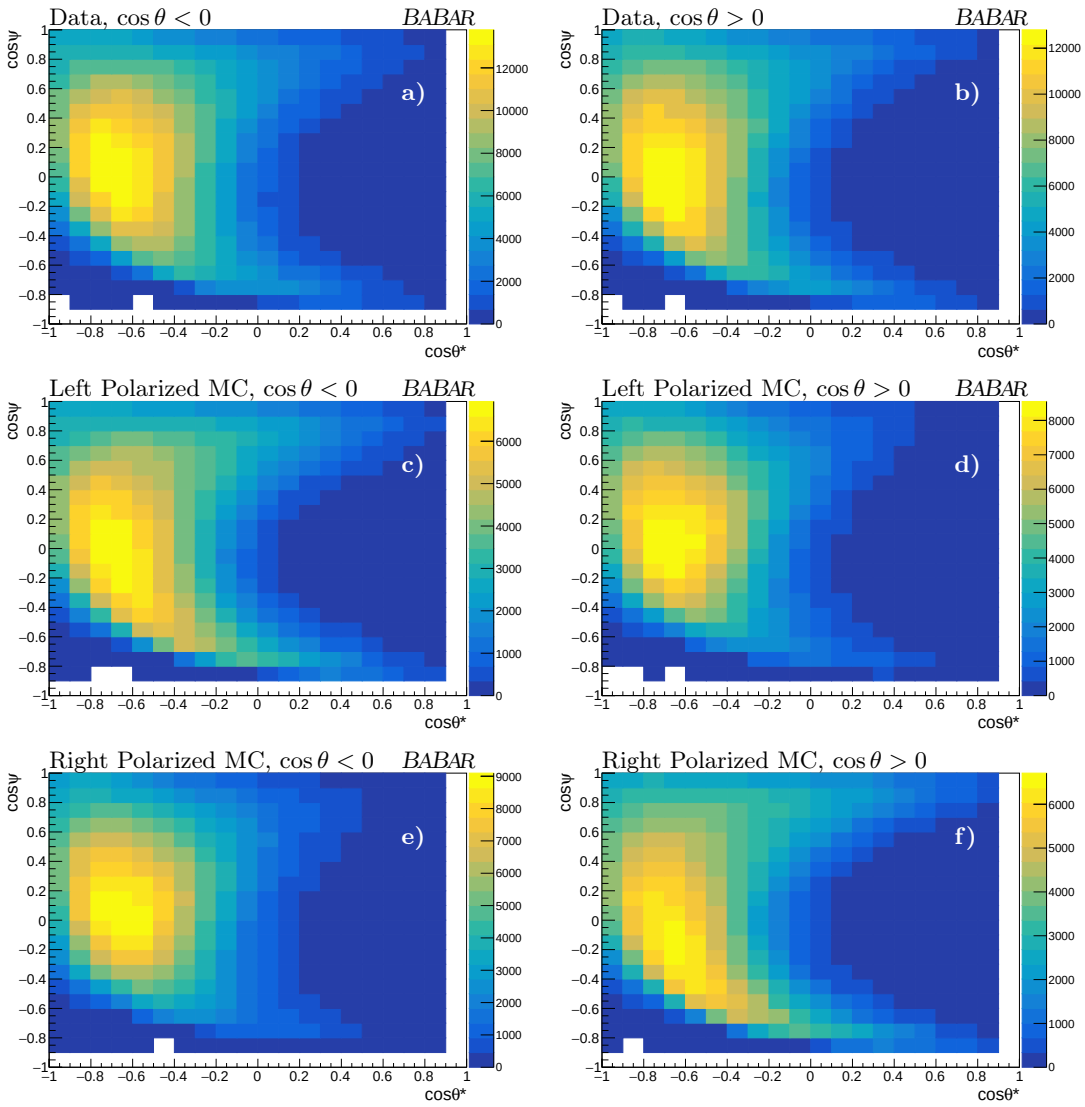

FIG. 8. 2-dimensional projection of $\cos\theta^*$ vs $\cos\psi$ for negatively charged signal events. **a)**Data, $\cos\theta < 0$, **b)**Data, $\cos\theta > 0$, **c)**Left Polarized MC, $\cos\theta < 0$, **d)**Left Polarized MC, $\cos\theta > 0$, **e)**Right Polarized MC, $\cos\theta < 0$, **f)**Right Polarized MC, $\cos\theta > 0$.

offset between data and MC was found corresponding to a 4 MeV difference in the boost vector along the Z-axis. Correcting this offset in the MC templates shifts the data polarization fit by 0.0004, and so a systematic uncertainty of $\sigma = 0.0004$ is assigned.

4. *Momentum Scale and Resolution*

The same sample of $e^+e^- \to \mu^+\mu^-$ events is used to correct and quantify the momentum scale and momentum resolution of the charged particles. This is done by first fitting the $p_{CM}/p_{CM}^{\rm Max}$ distribution with a crystal ball function, where $p_{CM}^{\rm Max}$ is the beam constrained maximum muon momentum ($\sqrt{s}/2 - 2m_\mu$). The fit is performed on both data and MC and from the results a scaling factor, S_p, and resolution factor, R_p, are defined. S_p is the ratio of the means of the fits ($S_p \equiv \overline{\mu}_{\rm data}/\overline{\mu}_{\rm MC}$), and R_p is the ratio of the widths ($R_p \equiv \sigma_{\rm data}/\sigma_{\rm MC}$). From these two factors the momentum can be re-scaled as:

$$p_{\rm recon}^{\rm corr} = (p_{\rm truth} - R_P(p_{\rm truth} - p_{\rm recon}))S_P \qquad (1)$$

Typical values of S_p differ from 1 by $\pm 0.1\%$ and the statistical uncertainties are $\sim$0.01%. The resolution factor is more significant,R_p $\sim$0.92, and has a statistical uncertainty of 0.1%. In order to evaluate a systematic uncertainty associated with the rescaling, the two factors are varied by their respective uncertainties found in the crystal ball fit. This results in a systematic uncertainty of $\sigma = 0.0004$ for the momentum scale, and $\sigma = 0.0003$ for the momentum resolution.

5. Tau Direction Definition

The reconstructed ρ direction was found to be the least biased estimator for the true τ direction. In order to evaluate the level of bias in the estimator we evaluate the acollinearity between the rho and lepton direction. This method results in adjusting the ρ direction templates by $\cos\theta_{\rm corr} = \cos\theta \pm 0.001$ and a systematic uncertainty of $\sigma = 0.0003$ being assigned.

6. Angular Measurement

The resolution of the the angular distribution is known with an accuracy of 0.897 mrad. Varying the angles by this factor and evaluating the effect of the polarization measurement results in a systematic uncertainty of $\sigma = 0.0003$.

7. Background Contributions

The effects of the background contributions, primarily Bhabha and $e^+e^- \to \mu^+\mu^-$ events, is evaluated conservatively by doubling and halving the weights of their respective templates in the polarization fit. This method results in a systematic uncertainty of $\sigma = 0.0003$ being assigned.

8. τ Branching Fraction

Similarly to the background weighting, the τ branching fraction uncertainty is evaluated by varying the weights of the templates in the fit. For the τ branching fraction the uncertainties on the fractions from the PDG[27] are used as the amount to vary the weighting by. Under this methodology a systematic uncertainty of $\sigma = 0.0002$ is assigned.

B. Variation of cut value

1. Photon Split-off Modelling

In order to reduce sensitivity to the modelling of low energy photons emitted by charged particles interacting hadronically in the EMC, all neutral depositions within 40 cm of the charged particle at the EMC surface are recombined with the charged energy deposition. At 40 cm the MC response is in good agreement with the Data and a ± 1 cm shift in the acceptance window was determined to be an appropriate value for the systematic uncertainty study. This results in a systematic uncertainty of $\sigma = 0.0011$ being assigned.

2. π^0 Mass Acceptance Window

The systematic uncertainty associated with the 115-155 MeV acceptance window for the reconstructed π^0 mass is expected to be partially related to the overall neutral energy scale. However the presence of two neutral particles in the reconstruction also introduces correlating effects and angular dependencies. At risk of partially double-counting systematic uncertainties a separate systematic uncertainty is conservatively assigned to the acceptance window as well. This is done by varying the acceptance window by 1 MeV which results in a systematic uncertainty of $\sigma = 0.0008$.

3. Rho Decay Product Collinearity Angle

The opening angle between the charged and neutral pion in the rho decay was a particularly sensitive variable in this analysis. Cutting out collinear events, $\cos\phi > 0.9$, improved data/MC normalization and reduced charge asymmetric bias observed in the polarization fits. A careful study of the modelling, fit response to this variable, and the cut threshold was carried out and an angle adjustment based on the ρ reconstructed mass uncertainty was used as the estimator for the systematic uncertainty. The relationship between fluctuations in the ρ mass and the angular separation of the decay products is given by $\Delta\cos\theta \approx m_\rho \Delta m_\rho/(E_\pi E_{\pi^0})$. Using this method a systematic uncertainty of $\sigma = 0.0007$ is assigned.

4. Merged π^0 Likelihood

The merged π^0 candidates, as previously described, are associated with a likelihood score. At low values of likelihood a significant amount of $\mu^+\mu^-$ and Bhabha events can mimic the presence of a π^0 in the final state. An appropriate acceptance value and systematic variation was established from by minimizing the ratio of the amount of signal to amount of background, and the level of data to MC agreement in the minimum. Varying the acceptance cut by this variation results in a systematic uncertainty of $\sigma = 0.0007$.

5. Track Event Transverse Momentum

The transverse momentum associated with the charged particle tracks is closely associated with the overall momentum scale and resolution factors. However at low values of p_T, Bhabha, and un-modelled two-photon final states can contaminate the data-set. In order to ensure these effects are controlled for, a 2 MeV variation, found from the level of agreement between data and MC, applied in both directions (248 and 352 MeV) in the 350 MeV minimum acceptance was applied. This results in a systematic uncertainty of $\sigma = 0.0008$.

6. Transverse Momentum

Similarly to the individual charged particle p_T, an additional systematic uncertainty is required for the total event p_T to account for any un-modelled effects contributing to the data-set. For the total event p_T a 1 MeV variation was determined to capture any relevant effects and a $\sigma = 0.0003$ uncertainty is assigned.

7. Maximum Calorimeter Response

The requirement for events to exhibit less than 10 GeV of EMC response cuts out 1/2 of the remaining Bhabha backgrounds after all other cuts are considered. This is a low statistics regime and as such the level of data-MC agreement is more variable and results in a 8 MeV variation being needed to fully capture the systematic behaviour. As such the cut is varied between 9.992 and 10.008 GeV, which results in assigning a systematic uncertainty of $\sigma = 0.0003$.

8. Rho Mass Acceptance

The requirement for the ρ mass to exceed 300 MeV is needed to ensure $\cos\psi$ remains a Real number. The level of data to MC agreement at this level suggests a 2 MeV variation is needed to evaluate the effects of the cut. This results in a systematic uncertainty of $\sigma = 0.0003$.

9. $\cos\theta^*$ and $\cos\psi$ Acceptance Cuts

The angular acceptance of $\cos\theta^\star$ and $\cos\psi$ is constrained to remove Bhabha events and remain in a well understood portion of the distributions. As the Bhabha behaviour is not well modelled a cut variation approach is taken. MC studies found appropriate variations for these cuts to be 0.002 and 0.01 respectively. Performing this variation gives the systematic uncertainties as: $\sigma_{\theta^*} = 0.0002, \sigma_\psi = 0.0002$.

C. Lepton Identification

The uncertainty due to the choice of lepton identification was evaluated by switching between *BABAR* predefined selection algorithms. For both the muon and electron selection algorithms the fit response was evaluated when a more strict requirement was used. This reduces the selection efficiency by ∼5% for the muons, and ∼1% for the electrons. Systematic uncertainties of $\sigma = 0.0012$ and $\sigma = 0.0005$ were assigned for the muon and electron identification respectively. Particularly for the muons this approach was limited by the change in statistical uncertainty associated with the different PID selectors. Due to this additional statistics would not improve the uncertainties and a new approach to evaluating the uncertainty would be required.

D. Other Effects

In addition to the prior systematic sources, the performance of the τ trigger decision, luminosity weightings, particle quality definitions, and effects of re-binning the histograms used in the fit are all evaluated. All of these effects demonstrate negligible effects for the analysis.

VIII. CONCLUSIONS AND DISCUSSION

An important assumption for Tau Polarimetry is that of purely Standard Model physics, and so the existence of Beyond the Standard Model (BSM) physics could potentially bias the final result. At PEP-II no beam polarization is expected so a significant deviation from 0 could have indicated a BSM bias. Though the measurement in this analysis is in good agreement with 0 polarization a number of potential BSM effects were considered. BSM effects related to the coupling of the electron and τ polarization through deviations from SM expectations in $g^\ell_{V,A}$ are one of the most likely sources potential BSM effects. However; any such effects are suppressed by the Fermi constant and as such any BSM effects would be $\mathcal{O}(10^{-7})$ which is entirely negligible for this measurement. A more important area (for Tau Polarimetry) where BSM effects could arise is in the τ Michel parameters, and specifically the chirality of ν_τ. In the SM $\xi = 1$, and has been experimentally constrained to $\xi = 0.985 \pm 0.030$. Any deviations from 1 in this parameter directly bias the average beam polarization measurement, and Tau Polarimetry would benefit from an future improved measurement of ξ.
In the development of this analysis a number of key features were identified from which any future deployment of Tau Polarimetry at other e^+e^- colliders would benefit. One of the strongest features of the analysis is the systematic cancellation obtained from combining the results of the fits from the two electric charges. This is due to the effects of beam polarization on the kinematic observables being inverted with a change in the sign of $\cos\theta_{\tau^-}$, or equivalently the electric charge. This means that any non-polarization sensitive biases present in the analysis will bias positive and negative charges in the opposite direction, which then largely cancel in the combination. A consequence of this behaviour is that a large discrepancy between the polarization fits on the separate charges can indicate an uncontrolled source of bias. While this bias may cancel in the average of the charges, the existence of the charge discrepancy allows the analyst to further study and control the source of the bias.
A major source of systematic uncertainty, and effort to understand and reduce it, in this analysis is related to MC modelling of neutral processes. The modelling issues

Source	Run 1	Run 2	Run 3	Run 4	Run 5	Run 6	Combined
π^0 Efficiency	0.0025	0.0016	0.0013	0.0018	0.0006	0.0017	**0.0013**
Muon PID	0.0018	0.0018	0.0029	0.0011	0.0006	0.0016	**0.0012**
Photon Split-off Modelling	0.0015	0.0017	0.0016	0.0006	0.0016	0.0020	**0.0011**
Neutral Energy Scale	0.0027	0.0012	0.0023	0.0009	0.0014	0.0008	**0.0010**
π^0 Mass	0.0018	0.0028	0.0010	0.0005	0.0004	0.0004	**0.0008**
$\pi - \pi^0$ Angular Separation	0.0015	0.0009	0.0016	0.0007	0.0005	0.0005	**0.0007**
π^0 Likelihood	0.0015	0.0009	0.0015	0.0006	0.0003	0.0010	**0.0006**
Electron PID	0.0011	0.0020	0.0008	0.0006	0.0005	0.0001	**0.0005**
Particle Transverse Momentum	0.0012	0.0007	0.0009	0.0002	0.0003	0.0006	**0.0004**
Boost Modelling	0.0004	0.0019	0.0003	0.0004	0.0004	0.0004	**0.0004**
Momentum Scale	0.0001	0.0014	0.0005	0.0002	0.0001	0.0003	**0.0004**
Max EMC Acceptance	0.0001	0.0011	0.0008	0.0001	0.0002	0.0005	**0.0003**
τ Direction Definition	0.0003	0.0007	0.0008	0.0003	0.0001	0.0004	**0.0003**
Angular Resolution	0.0003	0.0008	0.0003	0.0003	0.0002	0.0003	**0.0003**
Background Modelling	0.0005	0.0006	0.0010	0.0002	0.0003	0.0003	**0.0003**
Event Transverse Momentum	0.0001	0.0013	0.0005	0.0002	0.0002	0.0004	**0.0003**
Momentum Resolution	0.0001	0.0012	0.0004	0.0002	0.0001	0.0005	**0.0003**
Rho Mass Acceptance	0.0000	0.0011	0.0003	0.0001	0.0002	0.0005	**0.0003**
Tau Branching Fraction	0.0001	0.0007	0.0004	0.0002	0.0002	0.0002	**0.0002**
$\cos\theta^\star$ Acceptance	0.0002	0.0006	0.0004	0.0001	0.0001	0.0004	**0.0002**
$\cos\psi$ Acceptance	0.0002	0.0003	0.0002	0.0002	0.0002	0.0003	**0.0002**
Quadratic Sum	0.0058	0.0062	0.0054	0.0030	0.0026	0.0038	**0.0029**

TABLE III. Summary of systematic uncertainties associated with the Tau Polarimetry polarization measurement.

were observed in three related variables; the angular separation of the final state pion and neutral pion, the overall neutral pion efficiency, and modelling of the calorimeter response to neutral particles in close proximity to charged particles. These systematic sources could be significantly reduced by the choice of a final state without a neutral pion, such as a charged pion vs a lepton. However, we found the increased dependence on PID modeling as well as dilepton backgrounds to introduce more bias than is eliminated.

The final key insight obtained during the development of this technique is that a data-set of $\mathcal{O}(100\ \text{fb}^{-1})$ is required to fully identify and correct all the relevant sources of bias. A number of sources of systematic uncertainty were not fully appreciated in a 32 fb^{-1} data-set, and a larger study sample would allow the analysis to be carried out in a blinded approach. With all of these considerations the average beam polarization of PEP-II has been measured to be $\langle P \rangle = 0.0035 \pm 0.0024_{\text{stat}} \pm 0.0029_{\text{sys}}$. This measurement demonstrates that a 3 per mil systematic uncertainty in the average beam polarization measurement, with a comparable statistical uncertainty in half an inverse attobarn of data can be achieved in e^+e^- colliders. Knowing that such a polarization uncertainty can be achieved strongly motivates the addition of beam polarization to SuperKEKB for precision electroweak measurements.

[1] K. Abe et al. Direct measurement of leptonic coupling asymmetries with polarized Z bosons. *Phys. Rev. Lett.*, 79:804–808, Aug 1997.

[2] K. Abe et al. Improved direct measurement of leptonic coupling asymmetries with polarized Z bosons. *Phys. Rev. Lett.*, 86:1162–1166, Feb 2001.

[3] J. Bernabéu, F. J. Botella, and O. Vives. γ-Z interferometry at a ϕ-factory. *Nuclear Physics B*, 472(3):659–680, 1996.

[4] SuperB Collaboration. SuperB Technical Design Report, 2013. arxiv:1306.5655.

[5] A. G. Aleksejevs, S. G. Barkanova, Yu. M. Bystritskiy, and V. A. Zykunov. Electroweak Corrections with Allowance for Hard Bremsstrahlung in Polarized Bhabha Scattering. *Physics of Atomic Nuclei*, 83(3):463–479, September 2020.

[6] Swagato Banerjee and J. Michael Roney. Snowmass 2021 White Paper on Upgrading SuperKEKB with a Polarized Electron Beam: Discovery Potential and Proposed Implementation. In *2022 Snowmass Summer Study*, 5 2022.

[7] J. Bernabéu, F. J. Botella, and O. Vives. P-odd observables at the Υ peak. *The European Physical Journal C -*

Particles and Fields, 7(2):205–215, Feb 1999.

[8] Andreas Crivellin, Martin Hoferichter, and J. Michael Roney. Toward testing the magnetic moment of the tau at one part per million. *Phys. Rev. D*, 106(9):093007, 2022.

[9] O. Vives. Electroweak Observables at SuperB. In *XVII SuperB Workshop, Elba*, 2011.

[10] Precision electroweak measurements on the Z resonance. *Physics Reports*, 427(5):257–454, 2006.

[11] D. Decamp et al. Measurement of the polarization of tau leptons produced in Z decays. *Phys. Lett. B*, 265:430–444, 1991.

[12] P. Abreu et al. Measurements of the tau polarization in Z0 decays. *Z. Phys. C*, 67:183–202, 1995.

[13] O. Adriani et al. A Measurement of tau polarization in Z0 decays. *Phys. Lett. B*, 294:466–478, 1992.

[14] G. Abbiendi et al. and The OPAL Collaboration. Precision neutral current asymmetry parameter measurements from the tau polarization at LEP. *The European Physical Journal C - Particles and Fields*, 21(1):1–21, Jun 2001.

[15] Bernard Aubert et al. The BaBar detector. *Nucl. Instrum. Meth. A*, 479:1–116, 2002.

[16] Bernard Aubert et al. The BaBar detector: Upgrades, operation and performance. *Nuclear Instruments and Methods in Physics Research Section A: Accelerators, Spectrometers, Detectors and Associated Equipment*, 729:615–701, 2013.

[17] Y Nosochkov, M Minty, and A Chao. Expected polarization in the present pep-2 design. 1996. https://www.osti.gov/biblio/486213.

[18] J. P. Lees et al. Time-Integrated Luminosity Recorded by the BABAR Detector at the PEP-II e^+e^- Collider. *Nucl. Instrum. Meth. A*, 726:203–213, 2013.

[19] S. Jadach, B.F.L. Ward, and Z. Wąs. The precision monte carlo event generator kk for two-fermion final states in e+e- collisions. *Computer Physics Communications*, 130(3):260–325, 2000.

[20] N. Davidson, G. Nanava, T. Przedziński, E. Richter-Wąs, and Z. Wąs. Universal interface of TAUOLA: Technical and physics documentation. *Computer Physics Communications*, 183(3):821–843, 2012.

[21] S. Jadach, W. Płaczek, and B.F.L. Ward. BHWIDE 1.00: O(α) YFS exponentiated Monte Carlo for Bhabha scattering at wide angles for LEP1/SLC and LEP2. *Physics Letters B*, 390(1):298–308, 1997.

[22] David J. Lange. The EvtGen particle decay simulation package. *Nuclear Instruments and Methods in Physics Research Section A: Accelerators, Spectrometers, Detectors and Associated Equipment*, 462(1):152–155, 2001. BEAUTY2000, Proceedings of the 7th Int. Conf. on B-Physics at Hadron Machines.

[23] P. Golonka and Z. Wąs. PHOTOS Monte Carlo: a precision tool for QED corrections in Z and W decays. *The European Physical Journal C - Particles and Fields*, 45(1):97–107, Jan 2006.

[24] S. Agostinelli et al. Geant4—a simulation toolkit. *Nuclear Instruments and Methods in Physics Research Section A: Accelerators, Spectrometers, Detectors and Associated Equipment*, 506(3):250–303, 2003.

[25] J. Allison, K. Amako, J. Apostolakis, H. Araujo, P. Arce Dubois, et al. Geant4 developments and applications. *IEEE Transactions on Nuclear Science*, 53(1):270–278, 2006.

[26] K. Hagiwara, A.D. Martin, and D. Zeppenfeld. τ polarization measurements at LEP and SLC. *Physics Letters B*, 235(1):198–202, 1990.

[27] R. L. Workman et al. Review of particle physics. *PTEP*, 2022:083C01, 2022.

[28] Roger J. Barlow and Christine Beeston. Fitting using finite Monte Carlo samples. *Comput. Phys. Commun.*, 77:219–228, 1993.

[29] S. Brandt, C. Peyrou, R. Sosnowski, and A. Wroblewski. The Principal axis of jets. An Attempt to analyze high-energy collisions as two-body processes. *Phys. Lett.*, 12:57–61, 1964.

[30] Edward Farhi. A QCD Test for Jets. *Phys. Rev. Lett.*, 39:1587–1588, 1977.